Verticaal gealigneerd nematisch vloeibaar kristal in microbeeldschermen voor projectietoepassingen

Vertically Aligned Nematic Liquid Crystal Microdisplays for Projection Applications

---

Dieter Cuypers

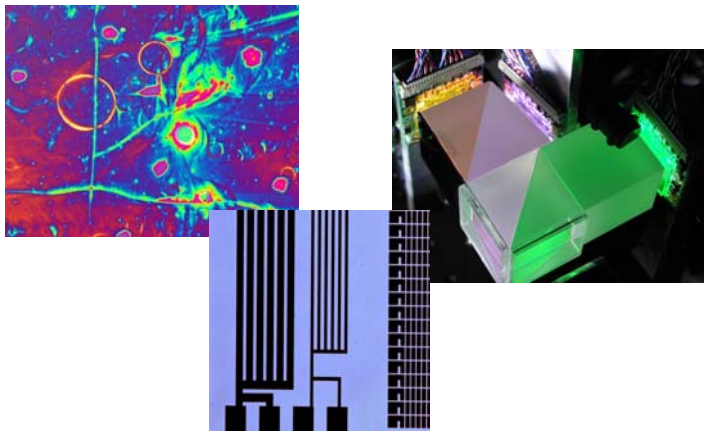

Proefschrift ingediend tot het behalen van de graad van
Doctor in de Toegepaste Wetenschappen: Elektrotechniek
Promotor: prof. dr. ir. H. De Smet

Vakgroep Elektronica en Informatiesystemen
Faculteit Toegepaste Wetenschappen
Academiejaar 2004–2005

UNIVERSITEIT GENT

ISBN 90-8575-025-X
NUR 959
Wettelijk depot: D/2005/10.500/26

Coverillustratie, vlnr. : polarisatiemicrografie van nauwelijks gealigneerd vloeibaar kristal; testpatronen in EXP99019V zwart polyimide; de projectorkern: ColorCorner kleurbeheereenheid met drie lichtkleppen.

Vanitas vanitatum, et omnia vanitas.

Ecclesiastes.

Dankwoord

Dit proefschrift is de neerslag van een stuk van mijn wetenschappelijke werk over microbeeldschermen uitgevoerd aan de vakgroep Elektronica en Informatiesystemen binnen de onderzoeksgroep TFCG sedert 1997. Het spreekt vanzelf dat een project van zo'n lange adem enkel gerealiseerd kan worden met de hulp en ondersteuning, in wat voor vorm dan ook, van heel wat mensen.

Mijn dank gaat in het bijzonder uit naar de volgende personen:

Allereerst natuurlijk mijn promotor, prof. dr. ir. Herbert De Smet, om voor de hand liggende redenen.

Daarnaast vanzelfsprekend ook prof. dr. ir. André Van Calster, groepsleider van TFCG; enerzijds voor de omkadering binnen zijn onderzoeksgroep, anderzijds voor de begeleiding en het de-facto promotorschap in de eerste jaren van mijn onderzoek.

De harde kern van de cleanroom adepten: Nadine Carchon voor zeer vele zaken, waaronder het mentorschap in het eerste jaar en de altijd geoliede samenwerking in al dan niet 'darce' tijden; Herbert De Pauw eveneens voor vele zaken, waaronder klankbord zijn tijdens ontelbare lunchpauzes en spitsbroeder bij de zoveelste oplapoperatie van aftandse en onwillige machines.

Mijn vele bureaugenoten, voor de aangename sfeer en amusante pauzes: Joeri De Vos, Dominique Wojchiechowski, Katrien Vanneste, Suixin Zhang, Nadine, An Gielen, Maarten Cauwe, Herbert en Bart Reekmans.

De collega's van het beeldschermgroepje: Jean Van Den Steen en Geert Van Doorselaer, een overduidelijk bewijs dat een team niet groot hoeft te zijn om serieus werk te verzetten.

Erik Coolsaet, maestro van het atelier, voor het realiseren van heel wat in huis ontworpen toestellen en hulpmiddelen en als lichtend voorbeeld van het feit dat vakmanschap en betrokkenheid niet per definitie onverenigbaar zijn met de status van administratief en technisch personeel.

Maurice De Caluwé; hoewel niet rechtstreeks meer betrokken bij dit werk zijn zijn inzichten en doorwrochte levensvisie altijd een waardevolle leidraad gebleken.

Melanie Klasen van Merck voor het ter beschikking stellen van vloeibare kristal mengsels, Jonathan Mayo van Brewer Science voor de vele gratis stalen polyimide en Rik Defever van Barco voor projectoronderdelen en -kennis.

Ten slotte, zeer vaak onterecht vergeten wegens nogal abstract: de gemeenschap die dit werk financiert. Vrijwel alle onderzoek aan universiteiten en instellingen wordt op een of andere wijze mogelijk gemaakt door geld dat door de gemeenschap aangedragen wordt; het kan geen kwaad daar af en toe eens bij stil te staan.

3 augustus 2005,

Dieter Cuypers

Inhoud - Contents

Tabellen - Tables

Figuren - Figures

Symbolen en afkortingen - Symbols and abbreviations

α	angle; absorption constant; polarisability
$\alpha_\star$	Leslie viscosity constant
β	retardation parameter; modulation parameter; polarisation ellipse rotation angle
c	speed of light
$C_\star$	reflection coefficient
CR	contrast ratio
γ	rotational viscosity; parameter in Yang and Lu's model
d	thickness; cell-gap
D	diameter
$\vec{D}$	electric displacement field vector
δ	phase angle
Δn	optical birefringence value
$\Delta\epsilon$	dielectric anisotropy value
E	Young's modulus; etendue
$\vec{E}$	electric field vector
$E_\star$	electric field component
$\epsilon, \epsilon_\star$	dielectric permittivity
$\widetilde{\epsilon}$	dielectric permittivity tensor
f_d	elastic deformation energy density
f_e	electric energy density
f_s	surface anchoring energy density
F	force
$\mathcal{F}$	Gibbs free energy
$\vec{h}$	propagation direction vector
$\eta_\star$	Miesowicz viscosity
θ	(azimuth) angle; rotation angle
I	intensity
$\vec{J}$	current density field vector

$\mathbf{J}$	Jones matrix
$\vec{k}$	wave vector
K	compressibility modulus
$K_\star$	elastic constant in the Frank-Oseen equation
λ	wavelength
$\lambda_\star$	coupling constant
μ	mean free path
$n, n_\star$	refractive index; director component
$\vec{n}$	director
N_A	Avogrado's number
ν	Poisson ratio
p	helix pitch; pressure
$\overline{Q}$	alignment tensor
r	radius
$\vec{r}$	position vector
R	Boltzmann's constant
ρ	density; charge density
$\rho_\star^\star$	phase angle
s	deformation
S	order parameter
σ	phase difference
t	time
T	transmission; absolute temperature
T_f	fall time
T_r	rise time
τ	thickness
U	driving voltage
$\upsilon_\star^\star$	phase angle
V	potential
V_{th}	threshold voltage
W	(anchoring) energy
$W_\star$	weighting factor
ξ	rotation angle
ζ	analyser rotation angle
ϕ, Φ	twist angle
φ	inclination angle
χ	ellipticity
Ψ	polariser angle
ω	cycle frequency
Ω	solid angle

AC	Alternate Current
AFLC	Anti-Ferroelectric Liquid Crystal
AMLCD	Active Matrix Liquid Crystal Display
ANSI	American National Standards Institute

AR	Anti Reflection
A.U.	Arbitrary Units
BCB	BenzoCycloButene
CdSe	CadmiumSelenide
CIE	Commission International d'Eclairage
CMOS	Complementary Metal Oxide Semiconductor
CMP	Chemical Mechanical Polishing
CRT	Cathode Ray Tube
DAP	Deformation of Aligned Phases
DOP	Degree of Planarisation
DC	Direct Current
D-ILA	Direct-drive Image Light Amplifier
DRAM	Dynamic Random Access Memory
ECB	Electrically Controlled Birefringence
FFT	Fast Fourier Transform
FLC	Ferroelectric Liquid Crystal
HAN	Hybrid Aligned Nematic
HBIMOS	High voltage Bipolar Metal Oxide Semiconductor
HDTV	High Definition Television
HFE	Hybrid Field Effect
IBM	International Business Machines Corporation
IC	Integrated Circuit
ILA	Image Light Amplifier
IPS	In-Plane Switching
ITO	Indium-TinOxide
JVC	Japan Victor Company
LC	Liquid Crystal
LCD	Liquid Crystal Display
LCOS	Liquid Crystal over Silicon
LCoS	Trademark of Brillian Corporation for their LCOS technology
lm	lumen
lm^*	modified lumen, disregards the acuity curve
MEMS	Micro Electro Mechanical System
MLC-XXXX	Product number of some liquid crystal mixtures provided by Merck
MPW	Multi-Purpose Wafer
MTN	Mixed Twisted Nematic
MOSAREL	Acronym for a European project aimed at the production of a 5 Mpixel lightvalve (Monocrystalline Silicon Active Matrix Reflective Lightvalve)
NCAP	Nematic Curvilinear Aligned Phase
NMP	n-methyl-pyrrolidone; codename for a polyimide used by Brewer Science
NB	Normally Black

NW	Normally White
OCB	Optically Compensated Bend
PBS	Polarising BeamSplitter
PCE	Polarisation Conversion Efficiency
PDLC	Polymer Dispersed Liquid Crystal
PECVD	Plasma Enhanced Chemical Vapour Deposition
PNLC	Polymer Network Liquid Crystal
RAM	Random Access Memory
Reflec	Acronym for the technology extensions developed at TFCG for the production of reflective lightvalves
RIE	Reactive Ion Etching
RTN	Reflective Twisted Nematic
SCTN	Self Compensated Twisted Nematic
SEM	Scanning Electron Microscopy
SMIC	Semiconductor Manufacturing International Corporation, Chinese silicon foundry
SOG	Spin-On Glass
SSFLC	Surface Stabilised Ferroelectric Liquid Crystal
STN	Super Twisted Nematic
TFT	Thin Film Transistor
TiN	TitaniumNitride
TiW	Titanium-Tungsten
TMDC	Taiwan Microdisplay Corporation
TN	Twisted Nematic
UHP	Ultra High Performance - Trademark of Philips' mercury-arc lamps
UMC	United Microelectronics Corporation, Taiwanese silicon foundry
UV	UltraViolet
VAN	Vertically Aligned Nematic
VGA	Video Graphics Array - VESA standard video mode with a resolution of 640×480
WXGA	Wide XGA - here a video mode with a resolution of 1280×768 (non VESA standard)
XGA	Extended Graphics Array - VESA standard video mode with a resolution of 1024×768

Hoofdstuk 1

Nederlandse samenvatting

1.1 Introductie

1.1.1 Lichtkleppen

Visualisatietechnologie speelt een grote rol in het leven van de modale westerling. Een zeer groot deel van deze technologie is vandaag reeds gegrondvest op elektronica, waarbij het ernaar uitziet dat dit aandeel enkel nog kan stijgen. Voorbeelden zijn er voldoende voorhanden: elke zaktelefoon is uitgerust met een steeds geavanceerder schermpje, er is bijna geen huishouden te vinden waar geen televisietoestel staat, computerbeeldschermen duiken zowat overal op en ook op straat wordt de reclame stilletjesaan door middel van elektronisch aangestuurde advertentiepanelen opgedrongen.

Nog niet zo lang geleden moesten vrijwel al deze beelden gegenereerd worden door kathodestraalbuizen. In de laatste decennia echter beleefde de vlakbeeldschermtechnologie uiteindelijk dan toch zijn doorbraak, en wordt het monopolie van de kathodestraalbuis langzaam aangetast. Dit is vooral duidelijk bij de computerbeeldschermen, waar vloeibaarkristalpanelen nu zowat standaard zijn en in veel mindere mate bij de televisietoestellen, waar groot formaat vloeibaarkristalbeeldschermen en nog grotere plasmapanelen de veeleisende consument verleiden.

Nog grotere schermformaten met behoud van hoge resolutie kunnen echter enkel op economische wijze bekomen worden door middel van projectietechnieken. Hierbij wordt het licht afkomstig van een sterke bron gemoduleerd zodat

een afbeelding ontstaat die vervolgens met behulp van een lenzensysteem op een geschikt medium zichtbaar gemaakt wordt. Doordat de afmetingen van de modulator of lichtklep niets van doen hebben met de afmetingen van het uiteindelijke geprojecteerde beeld zijn ook de fabricagekosten van de beeldgenerator ontkoppeld van de schermgrootte, wat een kostenbesparing betekent.

Pellicule is waarschijnlijk het best gekende voorbeeld van een klassieke lichtkleptechnologie. Elektronische lichtkleppen lijken heel wat exotischer maar hebben niettemin ook al een geschiedenis achter zich.

Een van de eerste elektronische lichtkleppen luisterde naar de naam Eidophor. Geconcipieerd door F. Fischer werd het principe voor het eerst gedemonstreerd in 1943; verscheidene varianten van het toestel bleven in dienst tot in 2000, voornamelijk voor projecties in openlucht met gigantische schermafmetingen. De modulatie van het licht gebeurt door diffractie, waarbij het continu veranderende diffractierooster gegenereerd wordt door in een oliefilm te schrijven met een elektronenstraal. Het voornaamste nadeel van de Eidophor is dan ook de complexiteit en de grootte van de benodigde installatie die onder andere een hoogvacuümpomp, een oliekoeler en een elektronenstraalgenerator omvat.

In de jaren 60 en 70 resulteerde de doorbraak van vloeibaarkristalbeeldschermpjes ook in een nieuw type lichtklep. Transmissieve vloeibaarkristalbeeldschermen zijn eigenlijk niets anders dan lichtkleppen, zodat hun toepassing in projectoren heel snel kwam. Actieve matrix aansturing maakt het mogelijk hoge resoluties te halen, terwijl de ontwikkeling van de dunnefilmtransistortechnologie het mogelijk maakte de lichtkleppen zelf steeds verder te miniaturiseren. De combinatie van die twee evoluties heeft aanleiding tot beeldschermpjes waarvan het beeld hoedanook vergroot moet worden, hetgeen de term microbeeldschermen rechtvaardigt. Het voorlopige eindpunt van deze evolutie zijn de lichtkleppen gebruikt in een aanzienlijk deel van de vandaag beschikbare projectoren, meestal gebaseerd op hoge temperatuur polysiliciumtechnologie, met resoluties tot 1920×1080 beeldpunten bij een schermdiagonaal van 1,3 inch.

Een groot nadeel bij transmissieve lichtkleppen is de eerder beperkte apertuur die effectief beschikbaar voor het licht ten opzichte van de totale beeldpuntgrootte. Dit is onvermijdelijk, aangezien de schakeltransistor in elk beeldpunt altijd een zekere oppervlakte zal afschermen. De meest voor de hand

liggende oplossing is over te stappen naar reflectieve lichtkleppen, waar elk beeldpunt een spiegel is.

Een kenschetsend voorbeeld van zo'n reflectieve vloeibaarkristallichtklep was de ILA, ontwikkeld door Hughes-JVC Technology Corporation. Naast een spiegel wordt bij deze lichtklep ook een fotogevoelige laag aangebracht op de achterzijde van het vloeibaarkristalpaneel. De inkomende lichtbundel wordt alzo gemoduleerd door het vloeibaar kristal dat op zijn beurt geschakeld wordt door een lichtbundel afkomstig van een kathodestraalbuis.

De vrij unieke aansturing van de ILA toont aan dat reflectieve lichtkleppen een grote vrijheid laten in de manier waarop het vloeibaar kristal geschakeld wordt. Een idee dat dan ook onvermijdelijk moest opduiken, is het gebruik van een siliciumchip als schakelend element en tweede elektrode. In 1987 werd door Ian Underwood een eerste 16×16 lichtklep voorgesteld gebaseerd op een statisch RAM geheugen. Terzelfdertijd duikt ook de term LCOS voor het eerst op als aanduiding voor wat een beeldschermtechnologie op zichzelf zou worden.

De voordelen van de LCOS technologie spruiten vooral voort uit de synergie die ontstaat tussen de aangewende technologieën, zijnde geïntegreerde schakelingen en vloeibaarkristalbeeldschermen, beide in een vergevorderd stadium van ontwikkeling. Zo zijn bijvoorbeeld zeer kleine beeldpunten en integratie van bijkomende functies vrij gemakkelijk te realiseren.

De interesse in LCOS lichtkleppen bereikte een hoogtepunt in de jaren 90 als gevolg van het marktpotentieel dat men meende te ontwaren in projectietoepassingen allerhande. Het op punt stellen van een gedegen LCOS technologie bleek echter heel wat ingewikkelder te zijn dan aanvankelijk in alle optimisme begroot werd. Een respectabel aantal LCOS lichtkleppen, evenals startende ondernemingen, zagen het levenslicht om na verloop van enige tijd stilletjes te verdwijnen.

Tot de mijlpalen behoren zeker de lichtkleppen gebaseerd op in polymeer gedispergeerd en nematisch curvilineair gealigneerd vloeibaar kristal van Hitachi en National Semiconductor. IBM's Display Research Group verzette heel wat werk om uiteindelijk met een indrukwekkende, op getwist nematisch vloeibaar kristal gebaseerde lichtklep met een resolutie van 2048×2048 beeldpunten naar buiten te komen, waarna IBM zijn onderzoek naar lichtkleppen stopzette. Ook anderen, zoals bijvoorbeeld Pioneer, stopten hun activiteiten vrij snel na

het lanceren van op het eerste zicht overtuigende producten.

Een alleenstaand geval in dit gebeuren is de D-ILA lichtklep van JVC. Afgeleid van, en rijkelijk profiterend van de ervaring opgedaan met de ILA lichtklep, is dit lange tijd het lichtend en quasi onklopbare voorbeeld geweest van de LCOS technologie. Technologische details bleven echter altijd versluierd achter fabrieksgeheimen, waardoor de bijdrage tot de ontwikkeling van de technologie uiteindelijk minimaal is geweest.

De grootste concurrent voor de LCOS technologie blijkt uiteindelijk de DMD-technologie van Texas Instruments te zijn. Deze puur optisch-mechanische benadering van het concept lichtklep gebruikt verstelbare miniatuurspiegeltjes om het licht te moduleren en wendt hiervoor micromechanische productieprocessen (MEMS) aan. Dit productieproces is echter vrij duur en moeilijk schaalbaar, waardoor de LCOS technologie uiteindelijk toch nog voordeliger kan uitvallen.

1.1.2 Onderzoeksonderwerp

In het voorliggend proefschrift wordt de ontwikkeling van een technologie voor vloeibaar-kristal-op-silicium-microbeeldschermen beschreven. Hierbij werden twee zaken voor ogen gehouden: enerzijds de kwaliteit van de uiteindelijke lichtklep, die het reeds beschikbare minstens moet evenaren, anderzijds de betrouwbaarheid en uitvoerbaarheid van alle benodigde processen. Er werd ook gestreefd naar een onafhankelijke ontwikkeling van de technologie, zodat alle deelprocessen controleerbaar zijn en men zich niet hoeft te baseren op oplossingen aangeboden door een specifieke producent.

Aldus wordt een technologie opgebouwd, vertrekkende van een geschikt substraat met geïntegreerde schakelingen, om uiteindelijk de lichtklep in een projector te demonstreren en de beeldkwaliteit te beoordelen.

1.2 Substraattechnologie voor microbeeldschermen

1.2.1 Vereisten voor de werking van microbeeldschermen

De siliciumsubstraten met de geïntegreerde schakelingen die dienst zullen doen als één van beide elektrodes zijn niet zomaar geschikt om in het vloeibaarkristalpaneel opgenomen te worden. Vooreerst is er een grote mate van planariteit vereist om de bovenste metaallaag als een efficiënte spiegel te doen werken. Anderzijds is silicium een goede fotogeleider en kan het substraat dus niet in een lichtrijke omgeving functioneren.

Voor beide problemen zal dus een aanpassing van de bestaande substraattechnologie nodig zijn. Hierbij kunnen twee pistes bewandeld worden: ofwel probeert men de nodige veranderingen te incorporeren in de siliciumprocestechnologie zelf, ofwel voegt men een aantal processtappen toe nadat het siliciumsubstraat op de klassieke wijze afgewerkt werd.

In het eerste geval bekomt men dan een geïntegreerde oplossing, in de zin dat de aanpassingen specifiek zijn voor de siliciumtechnologie van een bepaalde leverancier, waar men dan ook aan gebonden is. In het andere geval kan in principe eender welke siliciumtechnologie gebruikt worden, maar beslaat de productie nu twee vrij gelijkaardige cycli, hetgeen de uitval kan vergroten.

1.2.2 Geïntegreerde aanpak

Planarisatie

Bij de opbouw van geavanceerde geïntegreerde schakelingen zijn in principe reeds een aantal planarisatiestappen in het proces voorzien. De voornaamste reden voor hun aanwezigheid is de zeer geringe scherptediepte van de lithografiestappen, hetgeen dus gecompenseerd wordt door elke laag zoveel mogelijk in het beeldvlak te positioneren. Hoewel er dus geen enkele garantie bestaat dat deze planarisatie geschikt is om speculair reflecterende spiegels te produceren is het zowat de enige optie om binnen het productieproces tot vlakke substraten te komen.

CMP In de huidige siliciumtechnologie gebeurt de planarisatie door middel van het zogenaamd chemisch mechanisch polijsten (CMP). Hierbij wordt bovenop iedere isolatorlaag een bijkomende conforme laag gelegd die vervolgens door een anisotrope polijststap bijna volledig verwijderd wordt.

Het gebruik van CMP voor de productie van optisch vlakke spiegellagen werd voornamelijk onderzocht in het kader van het Mosarel project. Hierbij werd duidelijk dat het zeker mogelijk is lagen te bekomen met de gewenste optische kwaliteiten, maar dat heel wat nevenwerkingen kunnen optreden. In het bijzonder moet veel aandacht besteed worden aan mogelijke kortsluitingen, veroorzaakt door te grote variaties in de topologie van de onderliggende metaallaag. Dit kan opgelost worden door een doordachte invoeging van extra, anders nutteloze metaalvlakken.

Als bewijs voor de geschiktheid van deze aanpak kan aangevoerd worden dat tegenwoordig een aantal chipfabrikanten een aangepaste microbeeldschermtechnologie aanbieden waarin onder andere CMP figureert.

Lichtafscherming

Een afscherming van het licht voor het siliciumsubstraat kan gerealiseerd worden door het licht dat niet door de spiegels gereflecteerd worden te vangen in een tunnel waarvan de wanden uit absorberend materiaal bestaan. Hierbij kan dankbaar gebruik gemaakt worden van de antireflectielagen die sowieso bij elke metaallaag voorzien zijn om de lithografie te vergemakkelijken.

Optische simulatie van het lichtschild Het ontwerpen van een efficiënt labyrint voor de lichtabsorptie gebeurt met behulp van optische simulatiesoftware. Door de zeer kleine afmetingen van de openingen tussen de pixels en de hoogte van de tunnel tussen de lagen moet vooraf nagegaan worden of de strikt geometrische optica gebruikt in dergelijke simulatiepakketten nog wel geldig is. Met behulp van diffractietheorie en simulaties gebaseerd op Gaussiaanse bundels kan aangetoond worden dat een benadering door middel van geometrische optica nog steeds gerechtvaardigd is voor de beschouwde structuren.

Simulatiemodel Voor de eigenlijke simulatie wordt een geometrisch model opgesteld van de lagenstructuur op het siliciumsubstraat, uitgaande van negen pixels. Bij de optische eigenschappen van de materialen is vooral het titaniumnitride, het absorberende materiaal, belangrijk. Om problemen met de modellering van de exacte lichtinval te vermijden, worden twee extreme situaties beschouwd: een eerste waarbij alle lichtbronnen als lambertiaanse stralers beschouwd worden en een tweede waarbij de bron een uniforme intensiteitsverdeling heeft binnen een vastgelegde openingshoek. De lichtintensiteit op het substraat wordt zo gekozen dat, rekening houdend met alle mogelijke verliezen, een lichtstroom van 1500 lumens op het scherm bekomen wordt.

De berekeningen werden doorgevoerd voor twee lichtklepontwerpen die later ook effectief in productie genomen werden met onderscheidene beeldschermresoluties van 1024×768 en 1280×768. In het geval van lambertiaanse straling blijkt de afscherming onvoldoende in beide gevallen. Bij uniforme straling met realistische openingshoeken voldoet de afscherming in beide gevallen waarbij het ontwerp met de grootste beeldpunten ook de grootste marge vertoont.

Verificatie De simulatieresultaten konden geverifiëerd worden via een kleine omweg. Onvoldoende lichtabsorptie resulteert in een verstoring van de aanstuurspanning van de beeldpunten binnen een cyclus, hetgeen gedetecteerd kan worden in de hoeveelheid gereflecteerd licht met een snelle fotodetector. Fourier-analyse van deze signalen laat toe de minieme veranderingen waar te nemen die optreden wanneer de lichtklep bestraald wordt met schuin invallend licht van gepaste intensiteit, overeenkomend met de gesimuleerde condities.

1.2.3 Substraattechnologie onafhankelijke aanpak

Reflec

De zogenaamde Reflec technologie is de eerste versie van een reeks processtappen die ontwikkeld werden om een substraat met standaard afwerking geschikt te maken als lichtklep. Hierbij wordt intensief gebruik gemaakt van polyimides, zowel voor de planarisatie als de lichtafscherming.

Planarisatie De planarisatie gebeurt hoofdzakelijk door middel van een zeer visceus polyimide. Tijdens het aanbrengen in vloeistoffase van de polyimide-basiscomponenten kunnen hierdoor relatief grote niveauverschillen uitgevlakt worden, op voorwaarde dat de dikte van de laag vrij aanzienlijk is (~ 12 μm). Tijdens het uitharden krimpt deze laag al tot bijna de helft van de oorspronkelijke dikte. Om de latere processtappen te vergemakkelijken wordt daar nog eens 80 % van afgeëtst behulp van reactieve ionen.

Lichtschild Het lichtschild bestaat uit een laag zwart gepigmenteerde polyimide. De absorberende kwaliteiten van de zwarte pigmenten zijn aanzienlijk: een polyimide laag van 1 μm heeft reeds een optische densiteit van 2,3. Dit heeft ook als gevolg dat een aangepaste tweestapsprocedure nodig is om lithografie op deze laag toe te passen. Verder moet na het aanbrengen van de zwarte polyimide een dunne laag niet gepigmenteerd polyimide erbovenop gelegd worden om de ruwheid van de pigmenten te reduceren.

Spiegels De metaallaag voor de spiegels vereist ook nog enige zorg: enerzijds moet de depositie door sputteren gebeuren op lage temperatuur, anderzijds mag na de depositie geen sintering gebeuren. Het veronachtzamen van deze regels heeft een serieuze verruwing van de aluminiumlaag tot gevolg.

Zowel voor de planarisatie als voor het lichtschild voldoet deze technologie ruimschoots aan de gestelde doelen. Inzake lichtafscherming is het zelfs zo dat de Reflec technologie de aanpak met titaniumnitride evenaart, hoewel ze initieel niet voor grote lichtfluxen ontworpen werd.

Reflec II

De Reflec technologie heeft een aantal beperkingen, voornamelijk met betrekking tot de minimum grootte van de pixels. Voor een deel zijn deze beperkingen te wijten aan de gebruikte materialen en kunnen ze gereduceerd worden met doordachte aanpassingen aan de opbouw. Zo is het praktisch onmogelijk de grootte van de vias in het zwarte polyimide kleiner dan 4 μm te krijgen, hetgeen zijn weerslag heeft op de minimum pixelgrootte in de huidige opbouw.

Aangepaste processtappen Een aangepaste versie van de technologie, Reflec II, probeert deze beperkingen zoveel mogelijk op te heffen. Hiervoor wordt de zwarte polyimidelaag naar onderen verplaatst in de lagenstructuur. Hierbovenop komt een dunne contactmetaallaag, waarna de planarisatie gebeurt door middel van een niet gepigmenteerde versie van het zwarte polyimide om uiteindelijk de spiegels te sputteren. In een verdere ontwikkeling kan het originele zwarte polyimide nog vervangen worden door een fotogevoelige variant, die toelaat belangrijk kleinere vias te vormen.

Op deze manier wordt enerzijds de invloed van de via-grootte geneutraliseerd en anderzijds de werking van de zwarte polyimide nog beter geëxploiteerd door een tunneleffect te creëren.

1.2.4 Onderlinge vergelijking

Planarisatie Wat betreft planarisatie komen beide systemen vrij dicht in elkaars buurt. Zowel met de CMP als met de polyimide techniek kunnen planarisatiegraden van meer dan 90 % bereikt worden. Hierbij moet wel opgemerkt worden dat de te planariseren structuur voor beide technieken zeer verschillend is.

Lichtschild Voor een vergelijking van de werking van het lichtschild is het vooral interessant de evolutie van de kwaliteit van afscherming te bekijken in functie van een aantal procesparameters, ondermeer om een uitspraak te kunnen doen over de schaalbaarheid van beide systemen. Voor de polyimide route wordt uitgegaan van de Reflec II versie.

Beeldpuntgrootte Een eerste parameter is de beeldpuntgrootte. Voor beide systemen wordt een exponentieel dalende relatie gevonden tussen de nog doorgelaten lichthoeveelheid en de beeldpuntgrootte, maar de afschermingsgraad bereikt met polyimide is ettelijke grootteordes beter dan het titaniumnitride systeem.

Een mogelijkheid om de afscherming te verbeteren bij het gebruik van titaniumnitride is de introductie van een labyrint met twee verdiepingen, ten koste van een metaallaag die dan niet meer voor interconnectie gebruikt kan worden.

Dit levert een serieuze winst in afschermingskwaliteit op, hoewel nog steeds ver verwijderd van wat het polyimide systeem aankan. Een nadeel van dit drie-metaal systeem zijn de grote parasitaire capaciteiten die gecreëerd worden tussen de beeldpunten.

Openingshoek Om de lichtopbrengst van het systeem te vergroten is de enige uitweg vaak het vergroten van de maximale openingshoek van de lichtbundel. Het spreekt vanzelf dat dit ook de kwaliteit van de lichtafscherming beïnvloedt. Opnieuw kan voor beide systemen eenzelfde exponentiële relatie opgesteld worden, dit keer tussen de cotangens van de halve openingshoek en de doorgelaten lichthoeveelheid. Als gevolg hiervan kan een kleine reductie van openingshoek soms een vrij grote verbetering in lichtafscherming opleveren.

Laagdikte Een laatste belangrijke parameter is de laagdikte, te interpreteren als de tunnelhoogte in het geval van titaniumnitride. Voor realistische tunnelhoogtes kan eens te meer een exponentieel dalende relatie gevonden worden tussen de reciproke tunnelhoogte en de doorgelaten lichthoeveelheid. Voor de polyimide oplossing ligt dit wat anders: tot aan een bepaalde laagdikte blijft de doorgelaten lichthoeveelheid constant, waarna ze exponentieel daalt met toenemende laagdikte. De ongevoeligheid voor de laagdikte is natuurlijk een interessante eigenschap daar ze toelaat op eenvoudige wijze een betrouwbare lichtafscherming te vormen.

Conclusie Samenvattend kan gesteld worden dat beide systemen geschikt zijn voor het beoogde doel, waarbij het onmiskenbaar is dat de polyimide oplossing qua lichtafscherming superieur is. Een geïntegreerde aanpak heeft echter het voordeel van een mogelijke kostreductie.

1.3 Verticaal gealigneerd nematisch vloeibaar kristal

1.3.1 Selectie van een vloeibaar kristal mode

Bij de keuze van een geschikt vloeibaar kristal type voor een hoog kwalitatieve lichtklep zijn een aantal factoren van belang. Allereerst zij er natuurlijk de optische karakteristieken van een bepaalde mode, zoals maximale contrastverhouding, schakelsnelheid en optische efficientie. Daarnaast zijn er ook randvoorwaarden verbonden aan de specifieke toepassing, bijvoorbeeld een zeer lichtsterke omgeving, maar ook de eenvoud van fabricage en de betrouwbaarheid op lange termijn. Ook de manier van aansturen (analoog of digitaal, benodigde spanning) is een bijkomend criterium.

Vloeibaar kristal types

Op basis van de analoge aansturing, de verwachte fabricage- en betrouwbaarheidsproblemen en de relatief lage algemene performantie werden in een eerste ronde de polaire vloeibare kristallen (ferro- en antiferroelektrische) uitgesloten.

De overblijvende klasse, de nematische vloeibare kristallen, kent een grote verscheidenheid aan modes, onderscheiden van elkaar door de initiële oriëntatie en de schakelmechanismes. Hieronder worden kort diegenen besproken die het meest geschikt zijn voor gebruik in reflectieve lichtkleppen.

RTN De reflectieve getwist nematische mode (RTN) is een aangepaste versie van de welbekende getwist nematische mode. De twisthoek wordt beperkt tot 45°. Zowel een 'normaal-zwart' als een 'normaal-wit' werking zijn mogelijk waarbij in het eerste geval een redelijk goede contrastverhouding mogelijk is en in het tweede geval een korte schakeltijd. De zogenaamde polarisatieconversie-efficiëntie, die aangeeft hoeveel van het invallende gepolariseerde licht maximaal bruikbaar is, is echter in beide gevallen lager dan 100 %, wat dus een serieus nadeel is.

MTN Veel gebruikt voor lichtkleppen is de gecombineerde getwist nematische mode (MTN). Hierbij worden de parameters zo gekozen dat het twisteffect

slechts gedeeltelijk benut wordt en dus een combinatie met het dubbelbrekingseffect nodig is om het licht volledig te kunnen moduleren. Klassieke parameterwaarden zijn een twisthoek van 90° tezamen met een polarisatiehoek van 20°. Meestal wordt de 'normaal-wit' werking gebruikt, waarbij zeer korte schakeltijden bekomen worden. Ook voor deze mode is de polarisatieconversie-efficiëntie beperkt tot 88 %.

SCTN De intern gecompenseerde getwist nematische mode (SCTN) is een verdere variant op de gecombineerde getwist nematische mode. De twisthoek bedraagt nu 60° en de polarisatiehoek 30°. Een polarisatieconversie-efficiëntie van 100 % is nu mogelijk, evenals een zeer lage aanstuurspanning, maar kleine afwijkingen op de gespecifiëerde celdikte hebben nefaste gevolgen voor de goede werking.

HAN De hybried gealigneerde mode (HAN) is niet getwist maar berust volledig op dubbelbreking. Aan één zijde wordt het vloeibaar kristal horizontaal georiënteerd, aan de andere zijde verticaal. Snelle schakeltijden zijn het voornaamste kenmerk van deze mode, de nadelen zijn de hoge aanstuurspanningen en de kleine tolerantie voor afwijkingen op de celdikte.

PDLC Een compleet andere aanpak wordt gevolgd bij de in polymeer gedispergeerde vloeibare kristallen (PDLC). Ultrakleine druppeltjes nematisch vloeibaar kristal bevinden zich in een polymeermatrix en kunnen daar vrij bewegen. Omdat deze mode gebruikt maakt van lichtverstrooiing zijn geen polarisatoren nodig en komt er dubbel zoveel licht ter beschikking. Nadelig zijn de lange schakeltijden, de hysteresis op de schakelkarakteristiek en de noodzaak voor het gebruik van Schlieren optiek.

VAN Als laatste komt de verticaal gealigneerde nematische mode (VAN). Ook dit is een pure dubbelbrekingsmode, waarbij het vloeibaar kristal initieel zo goed als verticaal georiënteerd wordt. Het belangrijkste voordeel van deze mode is de enorme contrastverhouding die mogelijk is, tezamen met een relatief grote tolerantie voor allerhande afwijkingen op celparameters. Nadelen bevinden zich in de afwijkende methodes die gebruikt worden voor de alignering en

de beperkte beschikbaarheid van vloeibaar kristal met negatieve diëlektrische anisotropie, nodig voor de goede werking van deze mode.

Conclusie

De criteria opgelegd door de toepassing kunnen samengevat worden als: hoge contrastverhouding, hoge lichtefficiëntie, beperkte analoge aanstuurspanningen en voldoend korte schakeltijd. Uit bovenstaande bespreking van mogelijke modes kan afgeleid worden dat in bijna alle gevallen er punten zijn waarop een mode minder goed presteert. Enkel de verticaal gealigneerde mode voldoet aan vrijwel al de criteria en lijkt daarom de uitgelezen kandidaat. Om deze keuze verder te rechtvaardigen wordt in de volgende paragrafen een aantal eigenschappen van de verticaal gealigneerde mode verder uitgediept en vergeleken met directe concurrenten.

1.3.2 Verticaal gealigneerd vloeibaar kristal

Zoals reeds vermeld komt bij de verticaal gealigneerde vloeibaar kristal mode de rusttoestand overeen met een verticale oriëntatie van de moleculen. Een kleine afwijking, de pre-tilt, is nodig om ervoor te zorgen dat bij het aanleggen van een elektrisch veld de moleculen uniform dezelfde richting kiezen voor het omklappen.

Hierdoor ontstaan in principe twee mogelijke VAN configuraties: één waarbij de pre-tilt richting aan beide substraatzijden parallel is en een tweede waar ze anti-parallel is. Het tweede geval heeft aanleiding tot instabiliteiten tijdens het schakelen en wordt daarom niet gebruikt.

Celdikte- en golflengte-afhankelijkheid

De theoretische minimum celdikte voor de VAN mode ligt rond de 1,5 μm met de vandaag beschikbare materialen. In de praktijk worden zulke cellen echter nooit gebruikt, omdat de benodigde aanstuurspanningen dan zeer groot worden en het assemblageproces onevenredig moeilijk wordt.

In principe hoeft er geen maximumwaarde voor de celdikte opgelegd worden. Dunnere cellen hebben echter altijd kortere schakeltijden, waardoor het

nodeloos vergroten van de celdikte absoluut niet aan te raden is. Bovendien wordt de elektro-optische responsiecurve op de duur zo steil dat ze niet meer bruikbaar is voor de reproductie van grijswaarden.

De cellen die tijdens dit onderzoek geproduceerd werden, hadden alle een celdikte van 3 μm. Dit resulteert in een maximale aanstuurspanning van 3,5 V en een modulatiespanning van 1 V.

Contrastverhouding

De meest tot de verbeelding sprekende eigenschap van de VAN mode is zonder twijfel de mogelijke contrastverhouding. In de rusttoestand is er enkel dubbelbreking afkomstig van de minieme pre-tilt. Voor een pre-tilthoek van bijvoorbeeld $88,5°$, een zeer representatieve waarde, ligt een contrastverhouding van 50000:1 gemakkelijk binnen bereik. Dit terwijl een zeer goede polariserende bundelsplitser, het traditionele polariserende element in een lichtklepprojector, slechts een verhouding van 5000:1 laat optekenen.

De bereikte constrastverhouding is vanzelfsprekend sterk afhankelijk van de pre-tilthoek. Veranderingen in de pre-tilthoek hebben echter ook gevolgen voor de elektro-optische curve. Bij lagere waarden verschuift zowel de maximale benodigde aanstuurspanning als de drempelspanning naar lagere waarden. Daarnaast speelt de pre-tilthoek nog een rol in de lengte van de schakeltijd en het optreden van zones met inverse tilt.

Contrastverhouding onder schuine lichtinval Reeds eerder werd opgemerkt dat grote lichtfluxen onder andere gerealiseerd worden door grote openingshoeken voor de lichtbundel toe te laten. Het is dan ook belangrijk de contrastverhouding bij schuine lichtinval te bekijken. Het meest in het oog springend is hier de vrij snelle val van de contrastverhouding met toenemende inclinatiehoek. Afhankelijk van de berekenigswijze is de contrastverhouding bij een invalshoek van 15° nog nauwelijks meer dan 100:1. Hierbij dient opgemerkt te worden dat ten eerste de effectieve contrastverhouding de integratie is over alle invalshoeken en dus nog steeds veel hoger zal zijn, en ten tweede dat een invalshoek van 15° overeenkomt met een f/# getal van 1,86 hetgeen toch al een extreme waarde is.

In vergelijking met andere modes, die in het beste geval een contrastverhouding van enkele honderden kunnen leveren blijft VAN dan ook een buitenbeentje.

Aanstuurspanning

De benodigde aanstuurspanning is natuurlijk afhankelijk van de celdikte. Deze wordt dan ook vastgelegd rekening houdend met de maximaal beschikbare spanning, maar ook met de schakelsnelheid en de eenvoud van fabricatie. Daarnaast is de aanstuurspanning ook nog afhankelijk van de pre-tilthoek en de verankeringsenergie. De mogelijke variatie veroorzaakt door deze parameters is echter vrij beperkt.

Schakelsnelheid

De schakelsnelheid van een vloeibaar kristal wordt bepaald door de elastische en visceuze eigenschappen van het materiaal. De mathematische beschrijving van dit gedrag is vrij complex daar de anisotropie van het materiaal zich ook manifesteert in de elasticiteits- en viscositeitsconstanten.

Simulatiemodellen Het simuleren van het schakelgedrag is dan ook heel wat minder nauwkeurig dan wat mogelijk is bij de simulatie van statische evenwichtskarakteristieken. Een veelgebruikt ééndimensionaal model houdt rekening met drie elasticiteitsconstanten, overeenkomend met drie mogelijke vervormingstoestanden, maar combineert het visceuze gedrag in slechts één parameter, de rotationele viscositeit. Een meer geavanceerd model vervangt de rotationele viscositeit door zes zogenaamde Leslie-viscositeitsconstanten die overeenkomen met de mogelijke oriëntaties van de moleculen in een stroming. Een probleem hierbij is echter de zeer beperkte beschikbaarheid van meetgegevens waarmee de waarde van die constanten zou bepaald kunnen worden. Meestal neemt men dan ook zijn toevlucht tot benaderende schattingen, hetgeen de waarde van dergelijk model wel enigszins vermindert. Niettemin levert dit geavanceerd model vrij behoorlijke resultaten.

Resultaten Uit simulaties en metingen blijkt dat de VAN mode in ieder geval snel genoeg schakelt om bewegende beelden aan de gebruikelijke verversingsfrequenties te tonen. Een kleursequentiële aanpak ligt echter niet direct binnen bereik.

Parameters De schakelsnelheid kan sterk beïnvloed worden door de pre-tilthoek. Lagere waarden voor de pre-tilthoek resulteren in kortere schakeltijden. Vooral de uitsteltijd, zijnde de schijnbare wachttijd tussen het aanleggen van het elektrisch veld en een zichtbare heroriëntatie, verkort sterk bij kleinere pre-tilthoeken.

Tolerantie voor afwijkende parameters

Doordat vele celparameters bepaald worden tijdens het assemblageproces is de nauwkeurigheid en reproduceerbaarheid ervan beperkt. Een zekere tolerantie ten opzichte van de gespecificeerde waarden is dan ook gewenst. Hoe groter de tolerantie voor afwijkingen van een bepaalde mode is, hoe gemakkelijker het fabricageproces verloopt.

Pre-tilthoek Afwijkingen op de pre-tilthoek beïnvloeden de contrastverhouding bijna niet, een vrij unieke eigenschap van de VAN mode. De variaties die optreden tengevolge van pre-tilthoekveranderingen in een uniforme grijswaarde zijn substantiëler, maar zijn vergelijkbaar met andere modes; de RTN mode is nog gevoeliger, de MTN mode een stuk minder.

Celdikte Variaties in celdikte hebben opnieuw zo goed als geen invloed op de behaalde contrastverhoudingen. De elektro-optische responsiecurve wordt echter vanzelfsprekend wel beïnvloed. De variatie op de intensiteitswaarde rond het 50 % grijsniveau tengevolge van celdiktevеranderingen is vergelijkbaar met die in de MTN mode.

Celdiktevеranderingen leiden in de meeste andere modes tot een sterke reductie van de contrastverhouding, waardoor de toleranties veel nauwer genomen moeten worden. Dit is ondermeer het geval bij de RTN mode. De MTN mode heeft hier wat minder last van, maar boet dan weer in aan maximale helderheid.

Twisthoek De VAN mode is een niet-getwiste mode en heeft dan ook zeer weinig last van een kleine bijkomende twist, zowel wat betreft contrastverhouding, grijsniveaus als maximale helderheid.

De getwiste modes RTN en MTN presteren hier integendeel vrij slecht, de ene voornamelijk op het gebied van helderheid, de andere op contrastverhouding.

Het optreden van een negatieve invloed op de schakelsnelheid bij de introductie van (zeer) kleine twisthoeken bij de verticaal gealigneerde mode wordt door één auteur gerapporteerd. Dit blijkt echter een uitzonderingsgeval te zijn dat zich enkel voordoet bij vrij hoge aanstuurspanningen.

Conclusie

De eigenschappen van de verticaal gealigneerde mode zijn uitermate geschikt voor de productie van lichtkleppen van hoge kwaliteit. Naast de hoge contrastverhouding is ook de grote tolerantie voor vele mogelijke afwijkingen in het fabricageproces een grote troef. Enkel wat betreft schakelsnelheid kan enige verbetering nog wenselijk zijn.

1.4 Aligneringmethodes voor vloeibaar kristal

Zoals reeds eerder vermeld onderscheiden de modes zich onder andere door de initiële oriëntatie van de vloeibaar kristal moleculen. Deze oriëntatie wordt gerealiseerd door de aligneringlagen, zeer dunne lagen uitgelezen materiaal met speciale verankeringseigenschappen. Doordat ze rechtstreeks de kwaliteit van de gekozen mode beïnvloeden moet er ook evenredig aandacht aan besteed worden.

1.4.1 Aligneringsmethodes

Alignering met organische materialen

Gewreven polyimides Deze klassieke methode maakt gebruik van dunne polyimidelagen die aangebracht worden met behulp van de 'spin-on' techniek. Na imidisatie van het polyimide wordt de laag gewreven met een op een rol aangebrachte doek. Hierdoor ontstaan microscopisch kleine groefjes waarop het vloeibaar kristal zich kan aligneren.

Hoewel op zich een vrij complex proces, is de wrijfmethode toch de standaardmethode van de industrie. Het belangrijkste nadeel is de mogelijke schade die kan aangebracht worden tijdens het wrijven: krassen, contaminatie en elektrostatische ontladingen.

Voor verticale alignering moeten speciale polyimides gebruikt worden. Het wrijven dient hier voornamelijk om de kleine pre-tilthoek te bekomen.

Foto-alignering Om de nadelen verbonden aan het mechanisch contact te vermijden werden ook contactloze aligneringsmethodes onderzocht. De meest succesvolle hiervan is de zogenaamde foto-alignering, waarbij polymeer films met fotogevoelige componenten gedopeerd worden en vervolgens belicht met gepolariseerd ultraviolet licht. Dit veroorzaakt een alignering van de vloeibaar kristal moleculen loodrecht op de polarisatierichting. Om goed gedefinieerde pre-tilt hoeken te bekomen worden dubbele of schuine belichtingen gebruikt. Grootste nadeel van deze techniek is de geringe stabiliteit van de polymeermaterialen.

Langmuir-Blodgett films Langmuir films zijn ultradunne, mono-moleculaire lagen van amfifilisch organisch materiaal die op een vloeistofoppervlak gevormd worden. Deze lagen kunnen met speciale technieken getransfereerd worden op vaste substraten, hetzij als monolaag, hetzij als multilaag en worden dan Langmuir-Blodgett films genoemd. Eén van de vele interessante eigenschappen van deze films is hun vermogen om vloeibaar kristal te aligneren. Hun toepassing beperkt zich echter voornamelijk tot theoretisch en laboratoriumwerk.

Oppervlakte-aktieve stoffen Een aantal oppervlakte-aktieve stoffen kunnen rechtstreeks gebruikt worden om een vloeibaar kristal te aligneren op een substraat. Voor verticale alignering worden meestal silaanderivaten of alcoholen met lange koolstofketens gebruikt. Om een voorkeursrichting te introduceren wordt bovendien vaak eerst een anorganisch aligneringslaagje gelegd. Ook hier is de stabiliteit van de lagen een probleem, evenals de onvoorspelbaarheid van de uiteindelijke oriëntatie.

Alignering met anorganische materialen

Schuin opdampen De lagen bekomen door de schuin invallende, directionele bundel van bepaalde anorganische materialen in de dampfase zijn in staat vloeibaar kristal te aligneren. Deze ontdekking leidde tot heel wat onderzoek, voornamelijk geconcentreerd op het materiaal siliciummonoxide, teneinde hiermee een betrouwbare aligneringsmethode te ontwikkelen.

Met de anorganische materialen kunnen zeer dunne, uiterst stabiele aligneringslagen aangebracht worden op een contactloze manier. In principe is het ook mogelijk een waaier aan pre-tilthoeken te bekomen door de procesparameters te variëren. Het succes van deze methode werd echter niet zo groot als verwacht, waarbij vooral de complexiteit van de voorgestelde technieken en de soms geringe reproduceerbaarheid een rol speelden.

Schuin sputteren Opdampen als depositietechniek wordt meestal beschouwd als een weinig efficiënte techniek. Om de capaciteit van het productieproces wat op te drijven werd dan ook geprobeerd de opdamptechniek te vervangen door de sputtertechniek.

Aangezien de sputterdepositiemethode van nature een omnidirectioneel proces is moeten heel wat aanpassingen doorgevoerd worden om de benodigde directionele materiaalbundels te verkrijgen. Praktisch gebeurt dit door een groot aantal schoepen in de materiaalstroom te plaatsen, waardoor slechts een beperkte hoeveelheid materiaal met de juiste invalshoek uiteindelijk het substraat bereikt.

Hierdoor wordt het voordeel van de sputtertechniek natuurlijk grotendeels teniet gedaan. Bovendien gaat ook een flink deel van de flexibiliteit van de opdampmethode verloren.

Gebruik van ionenbundels Een zeer recente ontwikkeling is het gebruik van ionenbundels om aligneringslagen te 'schrijven'. Als aligneringsmateriaal wordt koolstof gebruikt, echter afgezet in de bijna-diamantfase. Vervolgens wordt de laag afgerasterd met een schuin invallende ionenbundel, hetgeen een uniforme alignering met een variabele pre-tilthoek tot gevolg heeft.

Naast een zeer controleerbaar proces heeft deze methode het bijkomende voordeel het vloeibaar kristal in te sluiten tussen twee identieke geleidende materialen, wat de productie van flikkervrije lichtkleppen vergemakkelijkt. Het zeer bewerkelijke en kostelijke proces is daarentegen het grootste nadeel.

1.4.2 Schuin opgedampte lagen

Principe

Opdat schuin opgedampte lagen kunnen gebruikt worden om vloeibaar kristal moleculen te oriënteren zijn twee zaken vereist: enerzijds moet een zekere anisotropie aanwezig zijn om effectief een voorkeursrichting te doen ontstaan, anderzijds moet er natuurlijk een zekere interactie bestaan tussen de vloeibaar kristal moleculen en het oppervlak teneinde een verankering te bekomen.

Morfologie Schuin opdampen van materiaal introduceert anisotropie in de morfologie van de afgezette laag. De opgedampte moleculen groeperen zich in een kolommenstructuur, waarbij de hoofdas van de kolom eveneens schuin staat, echter met een hoek tussenin de invalshoek van het materiaal en de verticale. De kolommen zelf vormen rijen of bundels loodrecht op het invalsvlak, waarbij

dus de afstand tussen kolommen binnen een rij merkelijk kleiner is dan tussen de rijen onderling.

Om de groei van dergelijke lagen te beschrijven kunnen een aantal modellen gebruikt worden. Hierna volgt een kort overzicht.

Gediscretiseerd continuum model Bij dit oudste model vertrekt men van de vaststelling dat lagen slechts kunnen groeien in discrete stappen, zijnde de grootte van een atoom. Hierdoor kan bij schuine inval de rand van de laag niet eender waar stoppen en groeit de laag in een richting die verschilt van de invalshoek. Uit dit model volgt de veelgebruikte tangensregel, die stelt dat de tangens van de invalshoek het dubbele is van de tangens van de groeihoek.

Zelfafscherming Een andere verklaring voor de kolomgroei volgt uit het zelfafschermingsmodel. Initiële groeikernen die in elkaars buurt liggen schermen de zone vlak achter zich af voor invallende atomen waardoor opnieuw de groeirichting afwijkt van de invalsrichting. Ook het bundelen van de kolommen volgt hier op natuurlijke wijze uit.

Behoud van parallelle bewegingshoeveelheid Aangezien het onwaarschijnlijk is dat de impact van een invallend atoom volkomen inelastisch is, zal in veel gevallen het atoom na de botsing nog een zeker momentum parallel aan het substraatoppervlak bezitten. Hierdoor kan het nog wat doorschuiven in die richting en zal dus de groeirichting afwijken van de invalsrichting.

Verankering Uit het bovenstaande kan afgeleid worden dat het ontstaan van anisotropie in de aligneringslagen op adequate wijze kan gemodelleerd worden. Een beschrijving van de eigenlijke verankering van de vloeibaar kristal moleculen op dergelijke lagen is echter veel moeilijker te formuleren. Een vrij algemene theorie steunt op het bestaan van Van der Waals krachten tussen de moleculen en het alignerende oppervlak.

Reeds eerder werd aangetoond dat aan bepaalde grensvlakken spontaan een bepaalde oriëntatie aangenomen wordt door de vloeibaar kristal moleculen. Dit tengevolge van een netto polarisatie in het vloeibaar kristal die ontstaat aan dit grensvlak en in de totale energiebalans van het systeem opgenomen moet

worden. Er van uit gaande dat de de mogelijke aantrekkingskracht tussen het vloeibaar kristal en de aligneringslaag veroorzaakt wordt door geïnduceerde dipool - dipool bindingen, moet bij een aligneringsoppervlak dan ook een Van der Waals potentiaalterm toegevoegd worden aan de energiebalans. Aldus bepaalt die potentiaalterm tezamen met de polarisatieterm de oriëntatie aan het aligneringsoppervlak, overeenstemmend met een minimale energie-inhoud van het systeem.

Daar de anisotropie van de vloeibaar kristal moleculen zich ook uitstrekt tot hun elektrische polariseerbaarheid, volgt uit het Van der Waals krachtenmodel dat materialen met positieve diëlektrische anisotropie zich horizontaal zullen aligneren, terwijl negatieve anisotropie tot verticale alignering moet leiden.

De (ruwe) voorspellingen die kunnen gedaan worden met bovenstaand model stemmen grotendeels overeen met experimentele resultaten. Er zijn echter een voldoend aantal anomalieën die er op duiden dat het model nog verre van compleet is.

Aligneringsmaterialen

Een grote waaier aan materiaaltypes kan in se gebruikt worden als aligneringsmateriaal. Zowel metalen als metaalsulfides, nitrides en vooral oxides zijn op een bepaald ogenblik gebruikt geweest. Om verscheidene redenen concentreerde het onderzoek zich echter voornamelijk op siliciumoxides.

Siliciummonoxide en niet-stoechiometrisch siliciumoxide zijn lange tijd de uitverkoren materialen geweest. Ze hebben echter een aantal nadelen, zoals een beperkte chemische stabiliteit en een moeilijke reproduceerbaarheid. De afkeer van de industrie voor de anorganische aligneringsmethodes is deels te wijten aan deze materiaalproblemen.

Siliciumdioxide elimineert vrijwel al deze problemen. De stabiliteit van de ontwikkelde aligneringstechnologie is dan ook voor een stuk gebaseerd op deze materiaalkeuze.

Een eigenschap van siliciumoxides waar sowieso rekening mee moet gehouden worden is hun hoge adsorptievermogen voor bijvoorbeeld watermoleculen en koolstoffracties. Vooral dit laatste kan de alignerende eigenschappen van het materiaal vernietigen. Het is dan ook noodzakelijk de blootstelling van de

aligneringslagen aan de atmosfeer relatief kort te houden.

Aligneringstechnologie

Bestaande technieken Gedurende de vele jaren onderzoek werden een groot aantal voorgesteld op het principe van schuin opgedampte lagen. Hierna volgt een summier overzicht.

Statisch opdampen In het originele proces werd het substraat simpelweg in de opdampklok bevestigd zodanig dat het op te dampen materiaal onder een zekere hoek op het substraat toekomt. Bijna scherende inval werd aanbevolen met laagdiktes rond de 2 nm. Het grote probleem bij deze opstelling is dat de effectieve invalshoek verandert met de plaats op het substraat, terwijl de bekomen pre-tilthoek juist erg afhankelijk blijkt te zijn van de invalshoek.

Om dit wat te verhelpen worden in sommige varianten schoepen in de materiaalstroom geplaatst, waardoor ongewenste invalshoeken geweerd kunnen worden.

Een andere, relatief simpele oplossing voor dit probleem is het gebruik van lineaire opdampbronnen. Dit veronderstelt echter dat het opdampen uit lineaire bronnen zeer uniform verloopt, hetgeen niet zo vanzelfsprekend is.

Een alternatief voor de schoepen is het gebruik van een apertuur waardoor het op te dampen materiaal moet passeren. Om goed te werken vereist dit systeem echter vrij lange opdampweglengtes, waardoor de opdampapparatuur zeer kostelijk wordt.

Roterend opdampen Om de afhankelijkheid van de invalshoek wat te milderen werden ook andere wegen bewandeld. Eén mogelijkheid is het substraat te laten roteren om zijn eigen as terwijl de materiaalbundel nog steeds schuin invalt. Door de rotatiesnelheid te variëren tijdens een omwenteling kunnen verschillende pre-tilthoeken bekomen worden. Met deze methode werden vrij behoorlijke resultaten geboekt maar de benodigde apparatuur en sturing is dermate ingewikkeld dat snel afgezien werd van het procédéé.

Een tweede mogelijkheid is het gebruik van dubbele opdampstappen, waarbij twee verschillende invalshoeken gebruikt worden. Ook hier bleek de finale

reproduceerbaarheid echter veel slechter dan verwacht.

Eigen technologie De uiteindelijke bedoeling van de ontwikkeling van een eigen opdamptechnologie is een compacte, weinig aanpassingen vergende opdampmethode op punt te stellen waarbij op een reproduceerbare manier aligneringslagen met de gewenste pre-tilthoek kunnen verkregen worden.

De aanpassingen aan de opdampklok zijn minimaal. De substraten worden in een carrouselhouder gemonteerd, waarbij één hoek in principe instelbaar is. De carrouselhouder roteert boven de opdampbron en laat aldus elk substraat kort in de materiaalstroom verblijven. Net onder de houder is een afschermplaat gemonteerd die slechts een smalle sector vrijlaat. Op deze manier is de directionaliteit van de opdampbundel verzekerd.

Het opdampen gebeurt bij een zodanige druk dat de vrije weglengte van de opgedampte partikels veel groter is dan de afmetingen van de opdampklok. De invalshoeken op de substraten worden dan ook enkel door de geometrie van de opdampinrichting bepaald.

Er kan aangetoond worden dat de mogelijke variatie op de invalshoeken op deze wijze zeer beperkt blijft, ook voor substraatafmetingen die als uitzonderlijk beschouwd kunnen worden voor microbeeldschermen. Metingen van de effectieve pre-tilthoeken tonen aan dat op deze substraten geen afwijkingen te vinden zijn. Voor zeer grote substraten zoals bijvoorbeeld complete siliciumplakken gaat dit natuurlijk niet op.

Resulterende aligneringslagen Door de procesparameters te variëren is het mogelijk de eigenschappen van de aligneringslaag te beïnvloeden.

Het variëren van de invalshoek heeft een rechtstreekse invloed op de pretilthoek. Steeds wordt een quasi-verticale alignering bekomen, maar een variatie van 40° op de invalshoek heeft een kleine 3° verschil in de pre-tilthoek tot gevolg. Dit is ideaal voor het nauwkeurig vastleggen van de pre-tilthoek.

Het variëren van de laagdikte heeft weinig gevolgen in het beschouwde - vrij beperkte - interval. Laagdiktes rond de 6 nm lijken een optimale instelling te zijn.

De verankeringssterkte van de opgedampte lagen is aan de lage kant verge-

leken met polyimide aligneringslagen. Dit is een normaal, welbekend fenomeen. De variatie op de verankeringssterkte met de depositieparameters is zeer miniem.

De eigenschappen van de aligneringslagen die afgezet werden gebruik makend van geoptimaliseerde parameterwaarden (45° invalshoek, 6 nm laagdikte) blijken zeer reproduceerbaar te zijn. Zowel procesvariaties als externe omstandigheden hebben weinig invloed op de kwaliteit van de alignering. Er kan dan ook gesteld worden dat het doel bereikt is.

1.5 Cel assemblage

Hoewel het assembleren van vloeibaar kristal cellen een triviale zaak lijkt, is er toch een aanzienlijke hoeveelheid technologie gemoeid bij het produceren van kwalitatief hoogstaande reflectieve microbeeldschermen. De hierna beschreven technologie is een zogenaamde celgebaseerde aanpak, waarbij het assemblageproces van in het begin stuksgewijs verloopt, in tegenstelling tot de wafergebaseerde aanpak, waarbij zolang mogelijk met de volledige siliciumplak gewerkt wordt.

1.5.1 Procesverloop

Tabel 1.1 bevat een bondig overzicht van het assemblageproces.

Hierna worden de belangrijkste stappen kort becommentarieerd.

Spatieerders

De spatieerders dienen om de celdikte exact op de gewenste waarde te houden. Ze zijn zowel in de afdichtingsrand als in het vloeibaar kristal aanwezig. Traditioneel gebruikt men in de afdichtingsrand harde spatieerders en in het vloeibaar kristal zachte spatieerders om schade aan de actieve matrix te voorkomen.

In dit geval werd er geopteerd om overal zachte, op divinylbenzeen gebaseerde spatieerders te gebruiken. Dit vergemakkelijkt het proces ietwat en heeft als enig gevolg dat er rekening gehouden moet worden met de samendrukbaarheid

Reinigen substraten
Aanbrengen aligneringslaag
Aanbrengen spatieerders m.b.v. spinner (enkel glaszijde)
Afzetten UV-hardende lijm voor de afdichtingsring
Uitlijnen en tegen elkaar zetten van beide substraten
Aandrukken en fixeren van de cel
Uitharden van de afdichtingsrand
Vullen van de cel met vloeibaar kristal
Afzetten UV-hardende lijm voor de afdichtingsprop
Uitharden van de afdichtingsprop

Tabel 1.1: Procesverloop assemblage

van de spatieerders bij het bepalen van de celdikte.

De spatieerders in het vloeibaar kristal worden aangebracht door ze in suspensie te brengen met methanol en vervolgens op het glassubstraat te 'spinnen'. De spatieerders voor de afdichtingsring worden eenvoudig in de lijm gemengd.

Aantal spatieerders Het aantal spatieerders per oppervlakte eenheid bepaalt natuurlijk de mechanische eigenschappen van de assemblage.

Voor het aantal spatieerders in de afdichtingsrand kunnen twee criteria vooropgesteld worden: enerzijds moeten er voldoende aanwezig zijn om de hoogste optredende druk tijdens het assemblageproces te kunnen overleven, anderzijds mag ook de uiteindelijke celdikte niet te veel afwijken van de vooropgestelde diameter van de spatieerders. Het tweede criterium heeft vrijwel altijd de doorslag. Voor de beschouwde lichtkleppen heeft een dichtheid van 20000 spatieerders per vierkante millimeter bijvoorbeeld aanleiding tot een afwijking op de celdikte van minder dan 1%.

In de actieve matrix geldt dat in principe minder spatieerders altijd beter is omdat dan mogelijke optische artefacten vermeden worden. Anderzijds moet hun aantal hoog genoeg liggen om nog enige mechanische stabiliteit te garanderen. Een mogelijke berekeningswijze gaat uit van een maximale afwijking op de celdikte die nog toegelaten wordt waaruit dan een minimum aantal spatieerders volgt.

Alternatieven In plaats van losse spatieerders te gebruiken zoals hierboven beschreven is het ook mogelijk 'geplaatste' spatieerders aan te wenden. Hierbij worden met behulp van processtappen uit de silciumtechnologie kleine kolommen gefabriceerd tussenin de beeldpunten waarop de tegenelektrode kan rusten. Twee problemen duiken hierbij op: regelmatige patronen worden veel sneller opgemerkt door het menselijke oog dan willekeurige puntenverzamelingen en de kolommen kunnen danig in de weg staan tijdens het aanbrengen van de aligneringslaag.

Het is ook mogelijk de spatieerders op de actieve matrix in het geheel weg te laten. Dit verschuift alle moeilijkheden in verband met de uniformiteit van de celdikte naar de spatieerders in de afdichtingsrand, eventueel geholpen door de onsamendrukbaarheid van het vloeibaar kristal. Het spreekt vanzelf dat dit

technologisch een veel moeilijker route is.

Afdichtingsring

De afdichtingsring dient enerzijds om het vloeibaar kristal te beschermen tegen contaminaties en invloeden van buitenaf en is anderzijds een stuk van de mechanische structuur van de cel die de juiste celdikte moet behouden. De keuze van de juiste lijmsoort is dan ook cruciaal. De verschillende lijmtypes worden verderop besproken. Door de zeer kleine afmetingen is het aangewezen de lijm aan te brengen met de druppelafzettingstechniek.

Laminatie

Tijdens het lamineren worden de twee substraten aan elkaar verbonden; terzelfdertijd wordt ook de celdikte en de uniformiteit ervan goeddeels vastgelegd.

Voor het eigenlijke lamineren wordt een pers gebruikt. Doordat de gebruikte lijm een UV-hardend type is moet ervoor gezorgd worden dat tijdens het aandrukken de cel ook kan belicht worden. In de gekozen uitvoering bestaat de pers uit een zeer vlakke glasplaat aan de bovenzijde en een rubber kussen aan de onderzijde. Door de luchtdruk onder het kussen te regelen kan een willekeurige en zeer uniforme belasting op de cel ingesteld worden.

De uiteindelijke uniformiteit van de cellen kan beoordeeld worden met behulp van interferogrammen. Bij een belichting met quasi-monochromatisch licht kunnen door reflectie aan de boven- en onderzijde van de vloeibaar kristal laag zogenaamde 'franjes van gelijke dikte' ontstaan. Elke volledige franje stemt overeen met een hoogteverschil van een kwart van de golflengte van het gebruikte licht.

Met de gebruikte techniek is het mogelijke een uniformiteit te behalen overeenkomend met nauwelijks één franje.

Vullen

Het vullen van cellen met vloeibaar kristal gebeurt vrijwel altijd met de vacuum methode. Hierbij wordt een lege cel in een vacuümklok geplaatst tezamen met een kleine hoeveelheid vloeibaar kristal in een speciaal houdertje. Nadat

de klok leeggepompt is laat men de cel zakken tot de zijde waar de vulopening zich bevindt in contact komt met het vloeibaar kristal. Als de druk in de vacuümklok nu weer langzaam stijgt wordt het vloeibaar kristal naar binnen geduwd.

Deze methode is heel geschikt om op een betrouwbare wijze vele cellen in één keer te kunnen vullen, indien aangepaste houders voor de cellen ter beschikking zijn. Voor laboratoriumgebruik is het beter een zekere flexibiliteit ten aanzien van de substraatgrootte aan te houden. In plaats van het in contact brengen van de cel met de meniscus van het vloeibaar kristal wordt dan de substraathoek waar de vulopening zich bevindt volledig ondergedompeld in het vloeibaar kristal. Dit verhoogt de kans op contaminatie weliswaar, maar laat toe op zeer betrouwbare wijze zeer uiteenlopende cellen te vullen.

Voor laboratoriumwerk kunnen ook nog andere vulmethodes gebruikt worden. De capillaire vulmethode is zeer eenvoudig maar levert weinig betrouwbare resultaten. De zogenaamde ééndruppel methode, waarbij vooraf de juiste hoeveelheid vloeibaar kristal op een substraat aangebracht wordt en de cel vervolgens in één stap geassembleerd wordt is een zeer interessante techniek, maar stelt hoge eisen aan de compatibiliteit tussen het vloeibaar kristal en de afdichtingslijm.

Afdichtingsprop

Na het vullen moet de vulopening nog afgedicht worden. Dit is een kritische stap omdat de kans op interactie tussen het vloeibaar kristal en de nog niet uitgeharde lijm op dat moment het grootst is. Een zorgvuldige selectie van de lijm is dan ook noodzakelijk. Meestal wordt ook geprobeerd de mogelijke interactiezone zover mogelijk uit de buurt van de actieve matrix te houden.

Voor de mechanische sterkte van de afdichting is het te verkiezen dat de lijm zich tussen de twee substraten bevindt. Dit gebeurt door eerst een lichte, gecontroleerde druk uit te oefenen op de substraten waardoor een kleine hoeveelheid vloeibaar kristal uitgedreven wordt, waarna bij het wegnemen van de druk de lijm naar binnen getrokken wordt. Hierbij moet er over gewaakt worden dat de uniformiteit van de celdikte niet in het gedrang komt.

1.5.2 Lijmtechnologie

Lijmtypes

De lijmen die in aanmerking komen voor gebruik in de celassemblage zijn over het algemeen thermohardende polymeren. De gezochte eigenschappen zijn ondermeer een hoge adhesiesterkte, hoge breuksterkte, ductiliteit, chemische inertie en ondoordringbaarheid voor water. Veelgebruikte lijmen zijn siliconen, cyanoacrylaten, polyurethanen, mercapto-esters en epoxies.

Siliconen Siliconen zijn excellente afdichtingsmaterialen; ze hebben zowel een grote weerstand tegen vele chemicaliën als een grote adhesiesterkte en dit bovendien over een breed temperatuurbereik. Jammer genoeg zijn ze ook zeer elastisch, wat ze ongeschikt maakt voor de beoogde toepassing.

Cyanoacrylaten De welbekende contactlijmen gebaseerd op cyano-acrylaten hebben vanzelfsprekend een zeer hoge adhesie. Het uitgeharde materiaal is echter vrij bros en slecht bestand tegen vochtigheid.

Polyurethanen Veelgebruikt als afdichtingsmateriaal in de electronica-industrie hebben poly-urethanen vrij goede mechanische eigenschappen. Weerstand tegen chemicaliën en temperatuurbereik zijn echter vrij beperkt. Desondanks is een UV-hardende variant, urethaanacrylaat, toch zowat de standaard geworden onder de UV-lijmen. Een bekend nadelig fenomeen bij dit type UV-lijm is de zogenaamde zuurstofremming waarbij de polymerisatie deels verhinderd wordt door de zuurstof in de atmosfeer.

Mercapto-esters Mercapto-esters zijn lange tijd de standaardkeuze voor UV-hardende lijmen geweest maar zijn nu wat gedateerd. De uithardingstijden kunnen extreem lang zijn, van de orde van meerdere uren. Niettemin wordt het materiaal nog courant gebruikt.

Epoxies Epoxies hebben over het algemeen excellente mechanische eigenschappen. Ook de chemische inertie is vrij groot. Door hun specifieke systeem van vernetting is de krimp gedurende de polymerisatie zeer miniem. Bij de

UV-hardende variant gebeurt de polymerisatie door kationen gegenereerd door de foto-initiator. Dit heeft als positief neveneffect dat de polymerisatie niet noodzakelijk stopt als de UV-bestraling ophoudt, hetgeen gebruikt kan worden om moeilijk te belichten lagen uit te harden.

Lijmkeuze voor de afdichtingsrand

Uit bovenstaande opsomming en rekening houdend met een sterke voorkeur voor UV-hardende lijmen om productiviteitsredenenen, lijken de meest aangewezen lijmtypes de urethaanacrylaten en de epoxies te zijn. In het specifieke geval van anorganische aligneringslagen blijkt de keuze van lijmtype echter niet zo rechttoe rechtaan te zijn.

Voor een zeer groot aantal lijmsoorten blijkt na vrij korte tijd een degradatie van de alignering op te treden, startende aan de lijmranden en zich naar het midden uitbreidend in de loop van enkele dagen. Uit experimenten is af te leiden dat het fenomeen specifiek is voor anorganische aligneringslagen, aangezien ze nooit optreedt bij identisch geproduceerde cellen waar een polyimidelaag voor de alignering zorgt. Verder speelt ook de graad van polymerisatie van de lijm geen rol.

De oorzaak van de degradatie van de aligneringslagen lijkt te liggen in het verdringen van de vloeibaar kristal moleculen aan de aligneringslaag door koolstoffracties afkomstig van de lijm. Dit is gelijkaardig aan de oorzaak van de beperkte houdbaarheid van de aligneringslagen.

Voor de afdichtingsprop stelt het probleem zich in nog grotere mate, daar de lijm nog volledig onuitgehard is. Omdat informatie over de samenstelling van de lijm bijna niet te verkrijgen is, kan de compatibiliteit van de lijmsoorten enkel experimenteel vastgesteld worden. De resultaten tonen aan dat inderdaad elke lijmsoort bijna individueel geverifieerd moet worden, zelfs binnen families van eenzelfde fabrikant kan de compatibiliteit erg verschillen. Uiteindelijk werd voor een epoxielijm geopteerd waarvoor de interactie zo goed als nihil is.

1.6 Karakterisatie

1.6.1 Meetmethode voor celparameters

Een adequate meetmethode om de celparameters van reflectieve lichtkleppen met verticaal gealigneerd vloeibaar kristal vast te stellen is niet echt voorhanden. Daarom werd een meetprocedure ontworpen specifiek voor dit soort lichtkleppen.

De meetopstelling bestaat, in volgorde, uit een monochromatische lichtbron, een hoogkwalitatieve polarisator van het Glan-Thompson type, een halfdoorlatende spiegel, een optioneel kwartgolflengteplaatje, een analysator en een snelle fotodetector met groot dynamisch bereik. De te testen lichtklep komt na de halfdoorlatende spiegel te staan.

Een eerste meting waarvoor deze opstelling uitermate geschikt is, is het bepalen van de inherente contrastverhouding van de cel. De Glan-Thompson polarisatoren zijn één van de weinige types waarvan de uitdovingsverhouding groot genoeg is om de contrastverhouding van een VAN-cel te overtreffen en dus te kunnen meten. Uit de gemeten contrastverhouding kan ook een eerste schatting voor de pre-tilthoek geëxtraheerd worden.

Het bepalen van de celdikte heeft wat meer voeten in de aarde. In principe kan men de celdikte berekenen uit de fasevertraging tussen de twee polarisatiecomponenten van een lichtbundel gereflecteerd vanop een cel waarin alle moleculen volledig horizontaal liggen.

Het bepalen van fasevertragingen tussen de polarisatiecomponenten gebeurt door de intensiteitsvariatie op te meten van de bundel als het kwartgolflengteplaatje in het optisch pad geplaatst wordt en roteert. Het aldus bekomen verband intensiteit - rotatiehoek is karakteristiek voor de polarisatietoestand van de gereflecteerde bundel. Met behulp van 'curve-fitting' software is het dan ook mogelijk de initiële parameters, waaronder de fasevertraging, te bepalen uit de vorm van de grafiek.

Om nauwkeurige metingen te verkrijgen moeten echter nog een aantal andere zaken in acht genomen worden. Allereerst moet rekening gehouden worden met de pre-tilthoek, die op zichzelf reeds een kleine fasevertraging veroorzaakt die dus in mindering moet gebracht worden. Het bepalen van de fasevertra-

ging door de pre-tilthoek gebeurt op identieke wijze als hierboven beschreven, nu echter met de cel in rusttoestand. Dit levert meteen ook een nauwkeurige meting van de pre-tilthoek op, aangezien die rechtstreeks uit de fasevertraging volgt.

De veronderstelling dat alle moleculen volledig horizontaal komen te liggen bij de meting is moeilijk te realiseren in de praktijk. Niet alleen zal er altijd een dunne zone zijn tegenaan de aligneringslagen waar de moleculen niet omklappen, het is meestal simpelweg niet mogelijk een voldoend grote aanstuurspanning te genereren om een volledig horizontale toestand te bekomen.

In de meetprocedure kan hiermee rekening gehouden worden door een model voor het verloop van de molecuuloriëntatie in functie van de aangelegde spanning te incorporeren. De Franck-Oseen theorie laat toe een directorprofiel te voorspellen indien de pre-tilthoek, aanstuurspanning en verankeringsenergie gekend zijn. Indien deze simulatiestap in het model ingebouwd wordt introduceert de verankeringsenergie een bijkomende vrijheidsgraad waarvoor een bijkomende voorwaarde opgelegd moet worden. Dit is eenvoudigweg de conditie dat de elektro-optische respons die volgt uit de simulatie moet overeenstemmen met de werkelijkheid. Op deze manier bekomt men bovendien een idee van de sterkte van de verankeringsenergie.

Verder kan in de meetprocedure ook nog rekening gehouden worden met de mogelijkheid dat de te testen cel niet volledig juist gealigneerd is met de invallende polarisatie van het licht, evenals met een mogelijke twisthoek in het vloeibaar kristal.

Typische waarden van de lichtkleppen die geproduceerd werden en opgemeten met bovenstaande procedure zijn: contrastverhouding 80000:1, celdikte 2,865 μm, pre-tilthoek 88°.

1.6.2 Schakelsnelheid

Zowel de opgemeten stijg- als daaltijden liggen beneden de 10 ms. De uitsteltijd bij het aanschakelen bedraagt ongeveer 3 ms. Dit is ruimschoots voldoende voor de vooropgestelde doelen.

In tegenstelling tot vele andere modes blijven de schakeltijden tussen grijsniveaus bij de verticaal gealigneerde mode ook zeer beperkt. Het is zelfs zo dat

de klassieke stijg- en daaltijden ook de maximale transitietijden zijn.

1.6.3 Franjevelden

Bij het vastleggen van de procesparameters van het vloeibaar kristal werd enkel rekening gehouden met één dimensie. Door de zeer kleine beeldpunten is dit echter niet altijd gerechtvaardigd. Aan de rand van het beeldpunt zullen de elektrische veldlijnen niet meer loodrecht invallen en bijgevolg ook de lokale richting van de director beïnvloeden.

In extreme gevallen kunnen de franjevelden de directorconfiguratie zo verstoren dat disclinaties optreden. Dit zijn 'fouten' in de algemene oriëntatie van het directorveld. In eerste instantie induceert een franjeveld zones waarin de tiltrichting van de vloeibaar kristal moleculen tegengesteld is. Indien de tilthoek niet te groot is kunnen de twee zones nog in elkaar overgaan middels een inversiegebied met verticale oriëntatie. Wordt de tilthoek echter te groot dan is dit niet meer mogelijk en is een overgang door middel van een horizontaal georiënteerd gebied meer voor de hand liggend. Dit is echter alleen mogelijk door de introductie van twee incompatibiliteitszones, de disclinaties, waar de horizontale oriëntatie abrupt overgaat in de verticale van de aligneringslagen.

In het optische domein kunnen de disclinaties of het inversiegebied aanleiding geven tot twee types artefacten. Allereerst is door de verandering in de directorconfiguratie de optische transmissie verstoord, bij VAN resulteert dit in een zwarte lijnen binnenin een wit beeldpunt. Dit vermindert de helderheid van dat beeldpunt en geeft het een onscherp aanzien.

Een tweede artefact doet zich voor indien het franjeveld plots verdwijnt, zoals voorkomt bij bewegende beelden. Hoewel de oorzaak van de verkeerde directorconfiguratie dan ogenblikkelijk weg is blijft de configuratie zelf nog enige tijd in stand; het heroriënteren neemt immers energie en tijd in beslag. Het zichtbare gevolg hiervan zijn naijlende contouren rond bewegende objecten.

Aan de franjevelden op zich valt natuurlijk weinig te veranderen maar de gevolgen ervan kunnen mogelijk geminimaliseerd worden. Een studie over de invloed van de celparameters op de vorming van de disclinaties dringt zich dan op. Dit gebeurt het best via simulaties van de directorconfiguratie in een tweedimensionaal domein.

Tweedimensionale simulatie van de directorconfiguratie

Binnen het kader van deze simulaties werd een vectorrepresentatie voor de director gebruikt. Dit maakt de simulaties rekentechnisch eenvoudiger, bovendien kan (achteraf) aangetoond worden dat er in dit geval geen noodzaak is om de ingewikkelder tensorrepresentatie te gebruiken.

De vergelijkingen voor de director oriëntatie worden opgesteld op basis van het principe van virtuele arbeid. Dit principe stelt dat de arbeid verricht door alle externe krachten tijdens een virtuele verplaatsing noodzakelijkerwijs teruggevonden moet worden hetzij als gedissipeerde warmte, hetzij als een verhoging van de inwendige energie van het systeem. In onderhavig geval zijn de externe krachten op te vatten als de viscositeitskrachten die zich verzetten tegen beweging, terwijl de inwendige energie van het systeem bestaat uit bijdragen van de elastische vervormingsenergie, de elektrische energie en de verankeringsenergie aan de randen.

Na uitwerking bekomt men uiteindelijk de Euler-Lagrange vergelijkingen van het systeem, die de tijdsevolutie van de director geven voor een gekend elektrisch veld. In de praktijk is echter de potentiaal over de beeldpunten gekend, dus moet eerst een Poissonvergelijking opgelost worden om het elektrisch veld te kennen.

De uiteindelijke directorconfiguratie is aldus de oplossing van een iteratief systeem, waarbij vertrekkende van een startconfiguratie een nieuwe configuratie bekomen wordt met de Euler-Lagrange vergelijkingen, vervolgens het elektrisch veld herberekend wordt om aan de nieuwe omstandigheden te voldoen, waarna opnieuw de directorconfiguratie herzien moet worden en dit tot convergentie bereikt is.

Simulatieresultaten

De invloed van een aantal celparameters op de optische distortie tengevolge van disclinaties kan nu gemakkelijk nagegaan worden.

Vormfactor De vormfactor is de verhouding beeldpuntgrootte tot celdikte. Het reflectieprofiel van een beeldpunt waarin zich een disclinatie bevindt wordt enigszins beïnvloedt door die vormfactor. Meest belangrijke feit is dat voor

grotere waarden van de vormfactor het profiel rechthoekiger wordt, dus meer aan de verwachtingen voldoet. De plaats van de zwarte lijn hangt ook af van de vormfactor: hoe lager de waarde, des te meer schuift de lijn naar het midden van het beeldpunt toe.

Pre-tilthoek De pre-tilthoek heeft een vrij grote invloed op het reflectieprofiel. Lagere pre-tilthoeken doen de zwarte lijn sterk opschuiven naar de beeldpuntrand toe, waarbij ook de intensiteit in het afgesplitste stuk van het beeldpunt sterk daalt. Voor extreme pre-tilthoek waarden, bijvoorbeeld 85°, kan het profiel er zelfs bijna ongeschonden uitzien.

Verankeringssterkte De verankeringssterkte heeft een vergelijkbare invloed als de pre-tilthoek, maar de effecten zijn veel bescheidener. Doordat een vermindering van de verankeringssterkte een vermindering van de benodigde aanstuurspanning tot gevolg heeft moet een groot deel van de positieve invloed van een lagere verankeringsenergie rechtstreeks toegeschreven worden aan de lagere veldsterktes.

Een optimale parameterset kan gevonden worden door een geschikte combinatie van bovenstaande invloeden. Hierdoor kunnen cellen gemaakt worden die weinig last ondervinden van disclinatie effecten en toch een voldoend grote contrastverhouding hebben.

1.6.4 Projector

Het uiteindelijke doel is natuurlijk de lichtkleppen in een projector te demonstreren. Wars van alle metingen is dit immers nog altijd de ultieme, zij het subjectieve test. Om echter een minimaal kwalitatieve projectie te kunnen realiseren is het bijna onvermijdelijk de projectie-optica af te stemmen op de lichtkleppen. Er werd dan ook een prototype projector ontworpen en gebouwd.

Er werd geopteerd voor een vrij klassieke opbouw. De lichtbron is een hogedrukkwikboogontladingslamp met een elliptische reflector. Het gecollecteerde licht wordt door een integratorpijp geüniformiseerd en omgezet naar een rechthoekig beeldveld. Met behulp van lenzen wordt dit vervolgens afgebeeld

op de lichtkleppen, doorheen de componenten voor kleurbeheer. De gevormde afbeeldingen worden tenslotte door de projectielens getransfereerd naar het projectievlak.

Het kleurbeheer behelst het uitsplitsen van het licht in drie basiskleuren, deze naar de juiste lichtklep te sturen en de gereflecteerde en gemoduleerde kleurenbundels opnieuw te recombineren tot één beeld. Dit kan op vele manieren geïmplementeerd worden en de keuzes die hiervoor gemaakt worden zijn bepalend voor de performantie van de projector. Aangezien het hier om een prototype ging, werd voor een geïntegreerde, kant-en-klare component gekozen, de commercieel verkrijgbare ColorCorner. Dit vergemakkelijkt het uitlijnen van het geheel aanzienlijk; de negatieve kanten zijn de relatief beperkte prestaties, vooral op gebied van contrastverhouding.

Bij het ontwerp wordt extensief gebruikt gemaakt van software die de stralengang doorheen de projector simuleert. Eén van de belangrijke concepten hierbij is het begrip etendue. Dit is een maat voor de hoeveelheid licht die door een component kan gesluisd worden. De lichtklep zelf is vrijwel altijd de limiterende factor in dit verband. Het ontwerp van de projector spitst zich dan ook voor een groot deel toe op het zodanig aanpassen van de stralengang dat de etendue van de lichtklep optimaal benut wordt.

De gebouwde projector levert uiteindelijk een lichtstroom van 800 lumens op het scherm met vrij goede uniformiteit. De sequentiële contrastverhouding bedraagt 300:1 en de contrastverhouding volgens de ANSI normen 30:1; hierbij moet echter benadrukt worden dat deze lage getallen volledig te wijten aan factoren extern aan de lichtklep, met name de ColorCorner zelf en de projectielens.

1.7 Besluit en verdere onderzoeksmogelijkheden

1.7.1 Besluit

In de voorgaande tekst werd een technologie beschreven die werd samengesteld voor de productie van vloeibaarkristalmicrobeeldschermen.

Startende van een aangepaste geïntegreerde schakeling werden eerst de mogelijkheden onderzocht om deze schakeling geschikt te maken voor gebruik als lichtklep. Hierbij is vooral de planarisatie van de schakeling en de lichtafscherming van belang. Twee routes kunnen hiervoor gevolgd worden: een geïntegreerde aanpak gebaseerd op antireflectielagen en polijstprocedures of een fabrieksonafhankelijke technologie-extensie gebaseerd op planariserende en gepigmenteerde polyimides. Er werd aangetoond dat beide systemen goede prestaties kunnen leveren binnen de grenzen van hun toepassing.

Vervolgens werd de selectie van een geschikt vloeibaar kristal type uitgevoerd. De voor- en nadelen van verschillende vloeibaar kristal modes werden gedocumenteerd en vergeleken met de gewenste eigenschappen inzake contrastverhouding, aanstuurspanning, schakelsnelheid en efficiëntie. Op basis hiervan werd geopteerd voor de verticaal gealigneerde mode. Deze mode werd dan verder gekarakteriseerd en in detail vergeleken met zijn dichtste concurrenten. Enkel op gebied van schakelsnelheid blijkt de VAN mode niet het meest aangewezen te zijn.

De keuze voor de verticaal gealigneerde mode heeft een directe weerslag op de manier van aligneren. Een verticale alignering is immers verre van standaard. Na afweging van voor- en nadelen werd gekozen voor een aligneringsmethode met schuin opgedampte anorganische lagen. Na een verkenning van de bestaande technieken werd een eigen technologie ontwikkeld waarvan de voornaamste eigenschap de robuustheid van het proces is, dit in tegenstelling tot de bestaande systemen.

In een volgende stap werd de assemblage van de lichtkleppen behandeld. Een gedetailleerd overzicht van het proces wordt gegeven, waarbij speciaal aandacht wordt geschonken aan de uniformiteit van de cellen. Door de interacties die ontstaan tussen de afdichtingsrand en de aligneringslaag bij het gebruik van anorganische materialen werd ook veel belang gehecht aan de lijmtechno-

logie. Een zorgvuldige materiaalkeuze laat uiteindelijk toe hoogkwalitatieve lichtkleppen te assembleren.

Tenslotte werden in een laatste deel de geproduceerde lichtkleppen geëvalueerd. Hiervoor werd allereerst een meetmethode ontwikkeld om de celparameters te bepalen, specifiek voor de verticaal gealigneerde mode. Ook de mogelijke beeldkwaliteitsvermindering ten gevolge van franjevelden werd onderzocht waarbij ondermeer simulatiesoftware werd geschreven. De resultaten van die simulaties lieten toe de lichtkleppen nog wat verder te optimaliseren. Als afsluiter werd een projectiesysteem ontworpen en gebouwd om de lichtkleppen in 'levensechte' omstandigheden te demonstreren.

1.7.2 Verdere onderzoeksmogelijkheden

De wereld van de beeldschermtechnologie evolueert razendsnel. Het onderwerp van dit onderzoek, microbeeldschermen gebaseerd op geïntegreerde schakelingen, situeerde zich bij aanvang in een als zeer pril te omschrijven domein. Vandaag zijn televisietoestellen die gebruik maken deze beeldschermtechnologie reeds mondjesmaat te koop in de winkels.

Niettemin is er nog steeds ruimte voor verder onderzoek in dit domein. Een fundamentele studie van het gedrag van de anorganische aligneringslagen vormt nog steeds een grote uitdaging gezien de beperkte reeds aanwezige kennis. Ook bij de interacties tussen deze aligneringslagen en de lijmen gebruikt voor de afdichting blijven nog heel wat vragen onbeantwoord.

Voor de beeldschermtechnologie in nauwe zin is het vooral de markt die de richting van het onderzoek aangeeft. Hier lijken twee trends de toon aan te geven: snellere schakeltijden om kleursequentiële architecturen mogelijk te maken en een groter aantal beeldpunten om de hoge-definitiestandaarden te kunnen volgen.

In het eerste geval kunnen 'intelligente' aanstuurschema's een uitkomst bieden, naast natuurlijk materiaaltechnische verbeteringen aan het vloeibaar kristal. In het tweede geval bieden vooral een geavanceerde assemblagetechnologie en inzichten in de rol van de franjevelden perspectieven.

Chapter 2

Introduction

2.1 Lightvalves

Visualisation technology plays an important role in the western world. A large and still increasing part of this visualisation technology deals with electronic imaging. From the tiny screens on portable phones over countless computer monitors, omnipresent TV-sets up to giant billboards and large-venue projectors, the presence of electronically generated imagery cannot be overlooked.

Up to very recently, cathode ray tubes were a key component in the generation of this imagery. In the last decade several flat-panel technology have successfully challenged this monopoly, mainly in the computer monitor business, where LCD-panels are now practically standard items. Inroads have also been made to the immense TV-set market, featuring both large LCD-panels and very large plasma displays.

Although these flat-panels can be impressive on their own, really large screen sizes with high resolution can only be obtained with projection methods.

In a projector, the light from a bright lightsource is modulated to represent an image which is then made to appear by the projection lens. The size of the device that modulates the incoming light (the lightvalve) is not related to the screen size, hence the manufacturing cost does not scale with that size.

The best known lightvalve is probably 35 mm film as used in cinema projectors. Electronic lightvalves are less frequently encountered but have nevertheless been around for quite some time.

One of the first electronic lightvalves was probably the Eidophor. It was developed by F. Fischer and first demonstrated in 1943 [1]. It uses diffraction to modulate the light, with the diffraction grating created on the fly in an oil film using an electron beam. Improved versions of the Eidophor have been in use till 2000, but the huge installation (high vacuum generator, oil cooler, e-beam generator) prevented it from being really successful.

The breakthrough of liquid crystal displays in the 70's and 80's resulted in a new type of lightvalve. Transmissive LCD panels can modulate the light in a very straightforward fashion, so putting them in a projector seems a natural thing to do. Active matrix addressing [2] and thin film transistor technology made it possible to realise high resolution, tiny lightvalves of this type. Quite some projectors nowadays use far-developed versions of such panels, operated by high-temperature polysilicon transistors and featuring resolutions up to full HDTV (1920×1080) at panel sizes of 1.3 inch diagonal [3]. The combination of these high resolutions with small outer dimensions justifies the term microdisplay, as their image needs to be magnified to be of any use.

A serious drawback of transmissive panels is the attainable aperture ratio of the pixels. The area that is available for transmitting light is always considerable smaller than the total pixel area, because the switching transistor takes up space and is not transparent. A convenient way around this is to reflect the light after passing through the liquid crystal layer. Each pixel becomes a mirror and can thus cover all available area.

A particular successful liquid crystal lightvalve of the reflective type was the ILA device [4]. Developed by Hughes-JVC Technology Corporation, it consists of a classic liquid crystal panel backed by a mirror, lightblocking layer and a photosensitive amorphous silicon coating. The output light is modulated by the liquid crystal layer, which in turn is switched through the photosensitive coating by the light coming from a CRT. As such, it can be seen as an amplifying system, hence the name Image Light Amplifier.

The ILA device illustrates that the turnover to a reflective mode of operation gives a large amount of freedom in choice of what to put behind the mirror to drive the liquid crystal. The idea of using a silicon chip for addressing the liquid crystal then emerged halfway the 80's. In 1987, Ian Underwood and coworkers presented a 16×16 pixels lightmodulator based on a static RAM cell. He also coined the term Liquid Crystal over Silicon (LCOS) for it, which later became the common designator for this type of display technology.

The potential advantages of this technology are numerous. It is a synergy of two mature technologies, so the resulting product should benefit from both sides. The high degree of miniaturisation reached in CMOS technology easily allows very small pixels on one side and integration of additional functionality on the other side.

In the 90's LCOS lightvalves started to enjoy quite some attention, largely because of the growing market potential for small and medium sized projectors. Applications include both front and rear projectors, covering business data projectors, home cinema, simulator screens, computer monitors, and TV-sets.

The development of a mature LCOS technology turned out to be a lot more involved than initially foreseen. Several devices have been developed and proposed, but none actually could force a breakthrough. Early versions often were based on polymer dispersed liquid crystal or NCAP material, such as the

devices of Hitachi [5, 6] and National Semiconductor [7].

A lot of work was done by the Display Research Group of IBM [8], resulting in an impressive 2048×2048 lightvalve based on the twisted nematic mode [9]. It never left the status of demonstrator however. A whole suit of companies and research groups contributed with sometimes very convincing devices, e.g. Pioneer [10], but for different reasons none of them proved to be lasting.

An exception to the lot is JVC's D-ILA chip (Direct-drive ILA), a derivative of the ILA device. The addressing with the CRT is replaced by a CMOS backplane [11], making it an LCOS. The D-ILA highly benefits from the experience gained with the ILA, an advantage that allowed it to be the forerunner in the technology for many years. However, the proprietary nature of its technology prevents other parties from collaborating to its advancement.

Lastly, when talking about lightvalves, it is impossible not to mention the Digital Micromirror Device from Texas Instruments. This opto-mechanical approach to the lightvalve concept uses a matrix of movable mirrors to modulate the light. The MEMS-technology behind it is a fascinating piece of engineering work but may also be the weak spot of the concept in the long run, being a difficult to scale, highly complex proprietary process.

2.2 Research scope

In this text, the development of a complete technology for the fabrication of LCOS lightvalves is described. The aim was to provide a reliable technology that does not rely on company secrets, yet provides lightvalves of the highest quality.

The different aspects of the technology are addressed, starting from a given silicon active-matrix chip. This comprises among others the selection of the liquid crystal, enhancements to the silicon processing and device assembly engineering.

Quite some effort is also put in the characterisation of the produced lightvalves, involving both the development of measurement techniques and simulation tools as well as the creation of a suitable prototype projection environment.

2.3 Liquid crystal over silicon

Although the upcoming chapters should be self-explanatory for a reader with some experience in the field, a very concise description of the LCOS concepts is given here to facilitate the understanding and provide some reference guide.

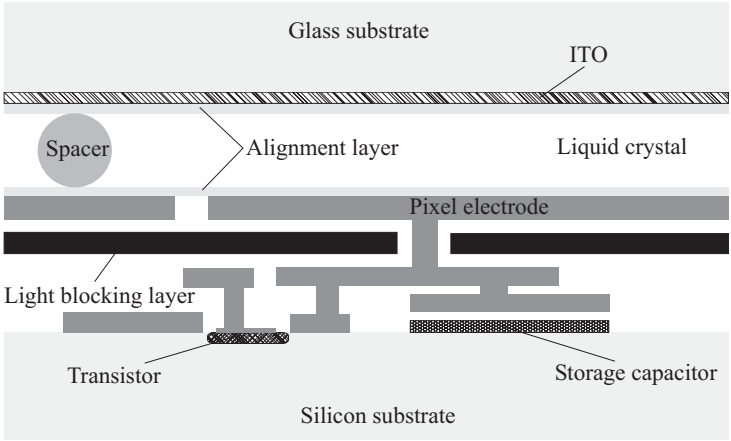

Figure 2.1: Cross-sectional view of a generic LCOS device.

2.3.1 LCOS devices

In figure 2.1 a cross-sectional view of a pixel in a generic LCOS device is shown. At the bottom is the silicon substrate, with its characteristic alternation of metal and insulator layers forming the circuit.

A typical but very basic configuration is shown: a transistor and a storage capacitor. Also shown is a layer that is normally not present in an IC: a light blocking layer. It is a crucial part of the device, but must not necessarily be implemented as suggested in the drawing. The top layer of the IC is the pixel mirror.

On top of the pixel the liquid crystal is found. Most commonly it introduces selective phase retardations between different polarisation directions of the light passing through it, making it possible to modulate the light flux.

The desired orientation of the liquid crystal molecules is obtained through two very thin alignment layers at both sides of the liquid crystal. The distance between the silicon substrate and the glass that covers it is maintained with spacers, usually tiny spheres or rods. The cover glass itself is coated with a uniform conducting layer, indium-tinoxide (ITO) that serves as common electrode for all pixels.

2.3.2 LCOS driving

All LCOS devices use active matrix addressing, which means that for each pixel there is a non-linear element in the driving circuitry; the pixel can thus be addressed individually and independently. Figure 2.2 shows one of the simplest implementations of this active matrix: the DRAM-like structure, with one transistor and a storage capacitor per pixel.

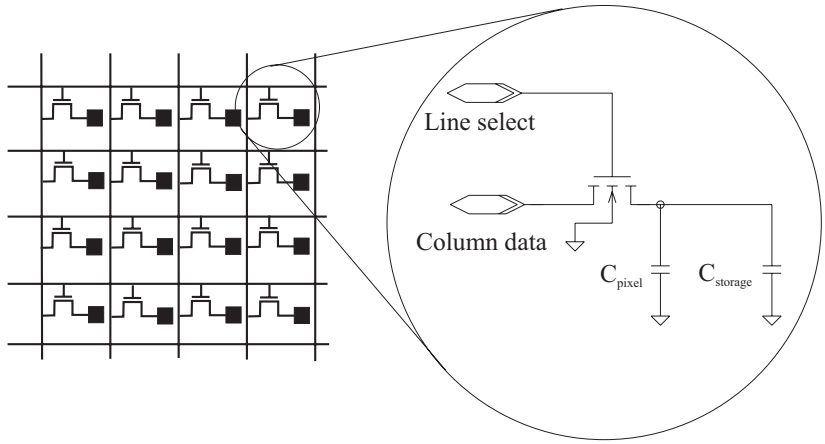

Figure 2.2: Active matrix addressing. Left an excerpt from a matrix featuring the line and column busbars and the active element for each pixel in every corner. Right a somewhat more detailed electronic schematic of a single pixel.

To drive a certain pixel, its line is selected (all the gates of the transistors on that line are activated) and the desired pixel voltage present on the column electrode charges the pixel capacitor. Complete images are thus generated progressively, line by line.

Liquid crystals cannot be driven in a unipolar fashion at the risk of degrading them. Hence, the driving voltage is intermittently reversed. For the actual implementation of the reversing several options exist, but LCOS devices virtually always go for the simplest solution: frame inversion, for which the polarity is the same for all pixels in the matrix and is reversed every frame.

2.3.3 Projection

The most important component used in projection with polarisation-changing LCOS lightvalves, apart from the lenses of course, is probably the polarising beamsplitter (PBS). It enables 'on-axis' projection, meaning here that the overall propagation direction of the light to and from the lightvalve is parallel.

A classic PBS consists of two 45 °-prisms glued together, with some coatings in between. It splits incoming light by polarisation; p-polarised light passes straight through the coating, s-polarised light is deflected by 90 °. This works regardless of the entrance face of the PBS, so if the lightvalve is placed opposite of the incoming p-polarised light, the reflected light will either return to the source if the polarisation direction is unaltered at the lightvalve or exit at a side face of the PBS if it is rotated. This is exactly the modulating behaviour needed.

2.4 Context

Virtually all research performed today, be it fundamental or applied, has to find its funding in projects of some kind, initiated by government or industry. As a consequence, research is often driven by short-term economical motives rather than considerations of technical or scientific desirability. This piece of work makes no exception to that rule.

The development of the polyimide based microdisplay backplane technology was largely covered by the internal research project Reflec, which in turn was backed up by the government initiatives IUAP and ITA-II. Several core aspects of the technology have been developed in the frame of the European-funded Mosarel project.

The further elaboration of the base technology was possible through the cooperation with Taiwan Microdisplay Corporation (TMDC). Although their initial interest was the design of the backplane, eventually they decided to cover the total production cycle. As a result, the microdisplay technology described in this text was transfered to their production fab, where it runs in a slightly modified (upscaled) version. At later stages, several other companies, most of them who value their anonymity, entered some form of collaboration as well.

Virtually all research is also performed in teams nowadays. In this case, the team is probably surprisingly small. Supervised by Herbert De Smet, and apart from our omnipresent group leader André Van Calster, the 'display team' indeed consisted of only three people.

The designs of the subsequent generations of microdisplays (quite some of them of the rather rare 'first time right' type) were all done by Jean Van den Steen. The thorough description of his work is to be found in another thesis; in this text the result of his work, the silicon backplane is in fact taken for granted.

Geert Van Doorselaer took care of the peripheral driving electronics and everything related to it. Again, the results of his work (basically the fact that, given a video source, there is actually something to watch on the screen) are taken for granted.

My own contribution to the research is then best described as 'the rest'. As will become clear further on, this is indeed a very mixed bag. The highlights certainly include the following: the development of a back-end technology for the production of lightvalves, predictions of lightshielding performance based on ray-tracing simulations, a thorough characterisation of the VAN liquid crystal, the development of an inorganic alignment layer technology, implementation of a laboratory-scale lightvalve assembly process, the development of two-dimensional simulation code for the director motion of liquid crystals and the design and implementation of a prototype projector system.

2.5 Practical remarks

- The different stages in the development of the technology have been grouped in chapters according to the field of research they belong to and are presented in the order of a sequential build up of the device, although actual research evolves far more chaotic.
- A list of mathematical symbols used in the text, along with acronyms and abbreviations can be found at the very beginning of this book. Many standard abbreviations are not explained anymore in the text itself, but can be looked up in this list.
- Material properties and other detailed processing information can be found in the appendices; they are not always explicitly referred to in the text.
- All optical ray-tracing simulations were performed with the ZEMAX-EE program from ZEMAX Corporation.
- A number of one-dimensional simulations on the liquid crystal behaviour, in particular the ones including back-flow phenomena or oblique incidence, are carried out with the DIMOS progam from autronic-Melchers GmbH. All other simulations are performed using own-developed software.
- The 1/16th VGA device was produced by Alcatel Mietec in their 2 μm HBIMOS technology. The Mosarel devices were also processed by Alcatel Mietec, this time in a 0.7 μm technology with high-voltage extensions and several other adaptations. Both the XGA and the WXGA displays have been processed for TMDC at UMC using their 0.35 μm technology along the microdisplay route. The WXGA was subsequently ported to fit the requirements of the SMIC foundry.
- If not mentioned otherwise, optical characteristics of liquid crystals are simulated or measured with monochromatic light at 550 nm.
- The vertically aligned liquid crystal mixture used is always MLC-6610 from Merck, unless otherwise specified.

Chapter 3

Microdisplay backplane technology

3.1 Microdisplay requirements

3.1.1 General

Unlike ordinary integrated circuit designs, a silicon microdisplay backplane is not finished once the electrical part is done. Being an opto-electronic device, operated under circumstances out of the ordinary compared to the average chip, some adaptations to the manufacturing process must be included. The need for these modifications are rooted in two requirements specific to microdisplays: planarisation and lightshielding.

3.1.2 Planarisation

The stacking of patterned layers, as used in virtually every semiconductor process, normally results in a rather bumpy top surface. Since the top metal layer is intended as a mirror, this poses a lot of problems if the die would be left as such. Problems can occur at three levels: on the largest scale, it is possible that the chip as a whole is not flat. This will cause trouble during the assembly, especially to keep the width between top and bottom surface constant. Ultimately, the top surface could become a concave or convex instead of a flat mirror. On the second level, looking at pixel scale, underlying circuitry can cause a single pixel to be not flat or oriented the wrong way. This will show up as uneven brightness and contrast among pixels that are supposed to give identical output. Thirdly, at an intra-pixel level, the nature of the depositions generally causes surfaces to be not optically flat, giving some unpredictable diffusing effect, which is generally not wanted (when a controlled amount of

diffusivity is needed this is achieved in other ways).

As lateral feature sizes have shrunk, while the layer thickness did not follow proportionally, registering layers and connection reliability became a problem, forcing IC process technologists to introduce planarising steps in the process flow. These steps may enhance the planarisation at the largest and medium level. However, they are not always available throughout the entire process and are aimed at alleviating electrical problems, not optical ones. A dedicated solution will thus still be needed.

3.1.3 Lightshielding

The base material for the backplane is quite sensitive to the introduction of photo-electrons . Contrary to ordinary circuits, which are shielded by their package or glob-top, a microdisplay intended for projection bears a lot of light on a small surface. Hence, measures will have to be taken to shield the circuitry from impinging photons, because they ruin the operation of the transistors and capacitors [12].

3.1.4 Solutions

The issues outlined above can be dealt with in two ways. Either we try to adapt the semiconductor process in such a way that it accommodates for the microdisplay requirements, or we take the chip as it is and add some additional process steps to make it fit for the purpose. The former option has the advantage of being an integrated approach, with the possible benefits of better yield, a familiar environment to do the design, one supplier and so on. The disadvantages are accordingly: dependence on the solution offered by the CMOS foundry (so no portability), and it remains to be seen if the requirements can actually be met within the frame of a semiconductor process. The latter option offers total freedom in the choice of foundry and technology but requires a separate process facility and additional handling, possibly influencing the yield.

Both approaches have been pursued and both were successful in their domain. In practice, the technology independent option was developed first, because when microdisplays were still in the conceptual phase, no foundry would even consider adapting anything for a potential product the feasibility and merchantability of which were quite uncertain.

3.2 An integrated microdisplay CMOS process

3.2.1 General

With the advancement of IC technology, it became apparent that planarising was mandatory. Newer technologies, with feature sizes below 0.5 μm incor-

porate one or more planarising steps to smooth out underlying topology. As their prime intention is providing a level surface for the next lithographic step, it should not be taken for granted that these layers also provide optical quality surfaces. If they do, or can be modified to do so, a first hurdle in the manufacturing process is taken.

Lithographic steps on highly reflecting layers, such as metals, pose a lot of problems when performed without further measures. To prevent multiple reflections from ruining the masking process, anti-reflective coatings are deposited along with every layer. Normally they only serve once at the time of the masking and then become obsolete, but as they remain in the stack, they can still be used for other purposes. If the design is such that light entering below the pixel mirror gets trapped in a tunnel with these anti-reflective coatings, the attenuation may be so large that the final energy of the ray is harmless when reaching the substrate.

3.2.2 Planarisation by CMP

Principle

The chemical mechanical planarisation procedure (CMP) has become the standard practice for planarising circuitry in advanced semiconductor processes (0.5 μm and below), where it has replaced the SOG (Spin-on Glass) planarisation common in older technologies. At regular intervals in the process, generally on every insulator, an additional layer of insulating material is deposited and then polished back. The deposition of the material is tuned so that it produces highly conformal coatings. This means that smaller topology differences, such as the dimples in via holes or the spacings between metal tracks, will gradually close down.

Of course, the polishing process on the contrary has to be anisotropic, otherwise the just deposited layer is simply removed again. The polishing occurs at wafer level, using chemically active slug while applying mechanical force. The process performs better if topology differences are not too deep and are localised, i.e. there are no larger areas where the average height is consistently different than elsewhere. For this reason, dummy metal surfaces are sometimes inserted in the layout to achieve a better CMP performance.

Feasibility

An early attempt to use CMP for planarising display devices started from a conventional two-metal IC process and appended a separate CMP step and third metal layer deposition at the end [13]. This resulted in optically smooth surfaces at the pixel level.

In the Mosarel project, the CMP steps were integrated in the process. It was demonstrated that this approach works and is capable of producing both op-

tically smooth surfaces and die-level planarisation [14]. The project also made clear that the introduction of CMP for this kind of purpose is not straightforward at all. After the introduction of the CMP steps, numerous shorts popped up, some of which were very persistent and hard to track down. Virtually all problems occurred in the periphery of the matrix. Being the area of the drivers and interconnection, it exhibits a lot more topological variation than the matrix area, making it very difficult to obtain a uniform planarisation. This is where the introduction of dummy metal surfaces can make things a lot easier. However, even with these present, the project research showed that even then the CMP process must be carefully tuned to obtain reliable results, especially on the exceptionally large substrates used in the project.

In conclusion, it can be stated that planarisation by CMP is feasible, although it requires some additional know-how. This is further evidenced by the fact that today some select foundries offer a 'microdisplay process' featuring CMP planarisation.

3.2.3 Lightshielding based on AR coatings

Principle

A metal layer in an IC process actually consists of a stack of materials itself, usually of the type anti-reflective coating - adhesion layer - actual metal (e.g. Al) - adhesion layer - anti-reflective coating. As for the anti-reflective coating, titaniumnitride is mostly the material of choice. It provides a high absorption in a broad band of wavelengths around the UV.

Labyrinth If the metal layers in the circuit are arranged in such a way that they form a kind of labyrinth for a light ray impinging from the top, a possibly very effective light shield may be formed. A typical layer stack is shown in figure 3.1. Light entering in the inter-pixel gap can be reflected back and forth between the pixel mirror electrode and the underlying metal layer which is exclusively used to generate the tunnel effect.

Of course the underlying layer must also be pixelated, so eventually the light will be able to get down to the next metal layer. The process essentially repeats itself, but as these lower layers are used for interconnection, large continuous areas of metal are not possible anymore and the distances the light must travel to get down another level are substantially smaller. The light will finally be able to reach the silicon substrate itself, where the energy of the photons could be used for the harmful charge carrier generation.

Optical modelling This crude model needs some refinements before it can be used to evaluate the performance of the labyrinth lightshield. A first complication is the fact that the size of the obstacles the light encounters is in the

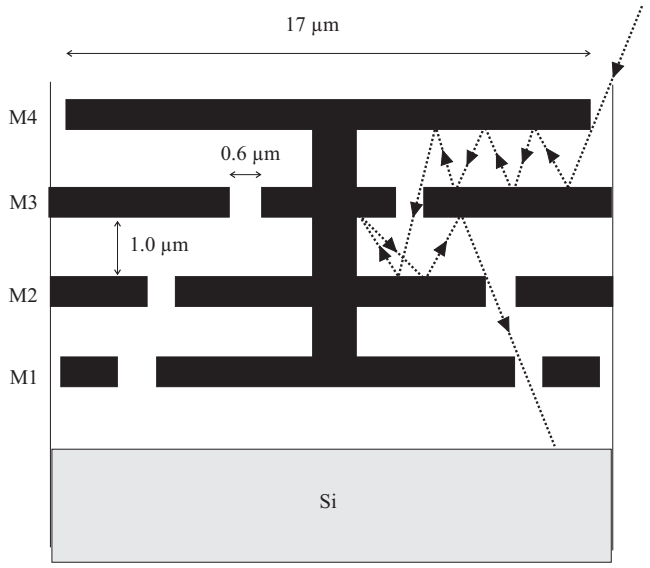

Figure 3.1: Schematic layer build-up for a four metal process, showing one pixel with some typical dimensions and a possible path down to the substrate for a light ray. Drawing not to scale.

range of the wavelength of the light. This means that geometrical optics is normally not valid.

Inter-pixel gap The first obstacle the light encounters is the inter-pixel gap itself. It is only slightly larger than the considered wavelengths, so diffraction phenomena are to be expected. The classical diffraction theory (Fresnel and Fraunhofer) is however not valid here, as the distance from the slit to where the diffraction pattern is to be calculated, is hardly two wavelengths. To obtain an exact solution, a rigorous diffraction theory, directly based on Maxwell's equations is required. The analytical solution of such a boundary value problem is highly complicated and can only be performed for a limited set of highly idealised cases. Born and Wolf [15] have summarised a number of these cases. Two of them may be useful here: the diffraction of a light beam by a semi-infinite plane and an infinitely long strip, both considered infinitely thin and perfectly conducting. The resulting analytical expressions are still very complicated and hard to interpret, but some general conclusions can be drawn from the instances where a numerical evaluation has been done. The most important conclusion may be that although some oscillation in the field strength over the aperture is induced, the amplitude variation is moderate enough to approximate it as a constant.

Although theoretically not entirely appropriate, some additional insight can

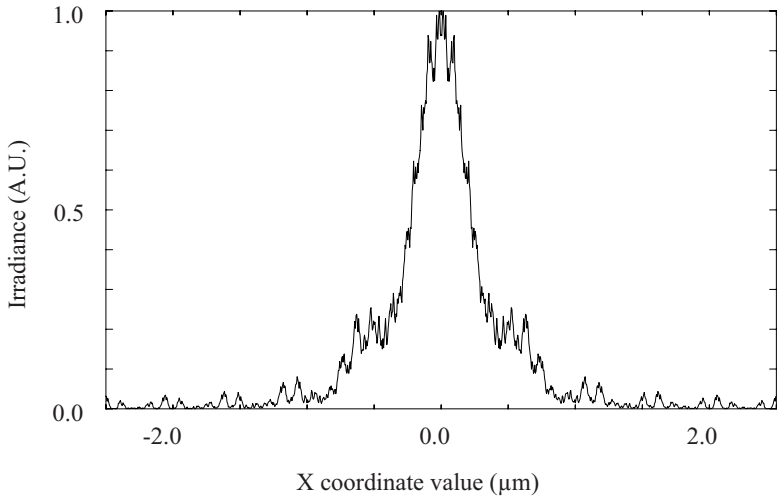

Figure 3.2: Calculated cross-sectional irradiance profile 1.0 μm behind a 0.6 μm wide slit. The slit itself is 0.6 μm thick and the light enters it perpendicular.

be gained by employing optical simulation software based on Gaussian beams. Figure 3.2 shows the calculated irradiance profile using this technique at a distance of 1.0 μm from a 0.6 μm wide rectangular slit. The profile indeed has some oscillations and is smeared out somewhat, but is still easily recognisable. The important conclusion is that the irradiance remains localised and does not differ too much from what is obtained with ray-tracing. This means that we can safely neglect the entire diffraction phenomenon and proceed as if it was not there.

Inter-layer distance The distance between two subsequent metal layers is also small compared to the wavelength, so again only a treatment of the propagation via the electro-magnetic equations produces exact results. It is however more obvious over here that the geometrical approach will still produce reliable results, as it closely resembles the propagation through thin films. In summary, despite the apparent objections, geometrical optics can be used to analyse the behaviour of the lightshield. This is in concordance with the approach taken in literature.

Via plugs As shown in figure 3.1, the path that has to be travelled by the light consists of several stages and the propagation direction has to reverse a couple of times. This may seem an additional difficulty for the light penetration, but one has to take into account the role of the via plugs. These are nearly vertical, metal walls that may very well act as good mirrors.

Shielding performance simulation

It is very worthwhile to have an estimate of the effectiveness of the shield design before it is actually processed. This can be achieved with optical simulation software. Based on the previous paragraph, it is already clear that a geometrical ray-tracer will suffice for a first order approximation. The simulation model is derived from the schematic layout presented in figure 3.1. Figure 3.9 shows the model for a particular design in more detail.

Light path For symmetry reasons, a 9 pixel excerpt from the active matrix is used. Inter pixel spacings and layer thicknesses are of course determined by the design rules of the technology. Careful observation of figure 3.1 learns that, if no special measures are taken, the shortest path for the light to travel will in general not be much longer than half of the pixel width. This leads to the approximation that for a worst case analysis, it is justifiable to take only the upper light-guide into account if the exit port is placed halfway beneath the pixel mirror. The light sources from which the rays are launched are placed between the pixel electrodes, aligned with the bottom side. This removes the necessity to model the behaviour of the side walls of the pixel electrodes, a very tricky task. Top and bottom metal are covered with a 100 nm TiN layer, as are the via walls. The detectors at the exit port represent the spots where the light can reach the underlying level. They record the intensity of the rays falling on them.

Anti-reflection layer A prerequisite for useful simulations is an adequate model for the anti-reflection layer. The commonly used titaniumnitride serves two purposes in the semiconductor stack: an anti-reflection layer to improve the definition of the photo-masking by reducing multiple reflections of the UV light and a diffusion barrier layer between the metal interconnection and the silicon layers. Because of this, the properties of the layer are chosen to satisfy both purposes. In literature, widely differing values for the complex refractive index of titaniumnitride can be found [16, 17], depending on actual stoichiometry and deposition method. We use the one published by Sony [18] because the resulting reflectivity characteristic matches best the measured one. In figure 3.3 the reflectivity versus wavelength of a 100 nm titaniumnitride layer is shown. Because the layer is intended to perform best in the UV region, reflectivity goes up towards the red part of the spectrum. Fortunately, the transparency of silicon also rises towards the (far) infrared. As a side note, it may be clear that the reflectivity of a single layer of TiN is by now means as low as the commonly encountered alternating TiN - SiO_2 stacks on e.g. CRTs.

Lightsource For the lightsources, several models can be used. The light beam coming from the illumination optics is commonly characterised by its f/# number, representing the maximum angle of incidence the light can have. The

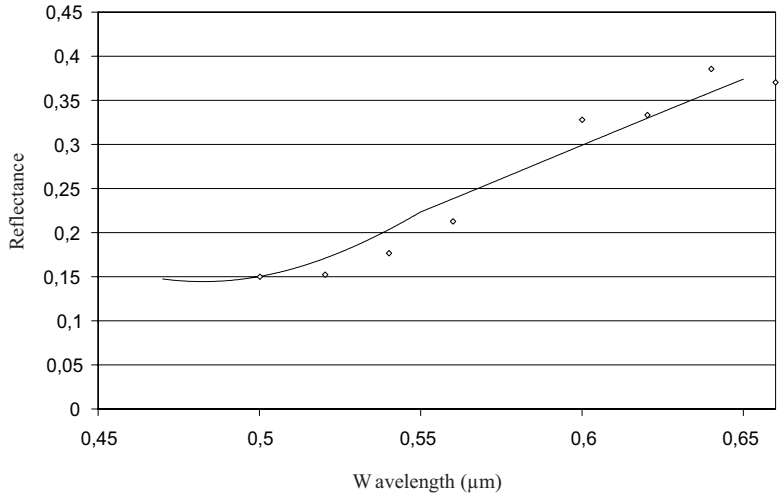

Figure 3.3: Reflectivity of a perpendicularly illuminated layer of titaniumnitride. Solid line shows the calculated reflectivity for a 100 nm layer with complex refractive index as given by Sony [18]. Diamond markers indicate the measurement points on a 100 nm titaniumnitride layer on a silicon substrate, deposited in our laboratory.

distribution of the energy among the incidence angles can still vary, depending on the nature of the illumination optics. A first reasonable approximation is to assume a uniform, isotropic distribution. Consequently, the inter-pixel gaps may then be represented by light emitting bars, from which rays start at random positions and have random direction cosines between preset boundaries. A different approach is to consider the lightsource as a diffusely radiating source with a lambertian profile. The justification for this can be found in the fact that the metal walls of the pixel electrodes are rough and will scatter the light that impinges on it. Taken to the extreme, all light will then be diffusely scattered, thus effectuating a lambertian source. The actual light distribution will arguably be a combination of both, so a realistic prediction will be in between these two extremes.

Light flux The amount of light incident on the inter-pixel gaps can be calculated starting from the amount of light expected on the screen. Currently available projectors in the envisaged product group feature a light output in the range of 1000 to 1500 ANSI lumens. Typical examples are reasonably sized rear-projection television sets and small data-projectors. For applications that have requirements outside of this range, the results can easily be scaled.

Setting the screen luminance to 1500 lumens, the amount of light actually needed on the lightvalve can be calculated using table 3.1. Rounded off, 3500 lumens will be needed on the surface of the active area.

geometrical aperture loss	0.9
analyser	0.8
colour recombination	0.8
projection lens	0.8

Table 3.1: Typical optical efficiencies of the projector components going from the lightvalve to the screen [19].

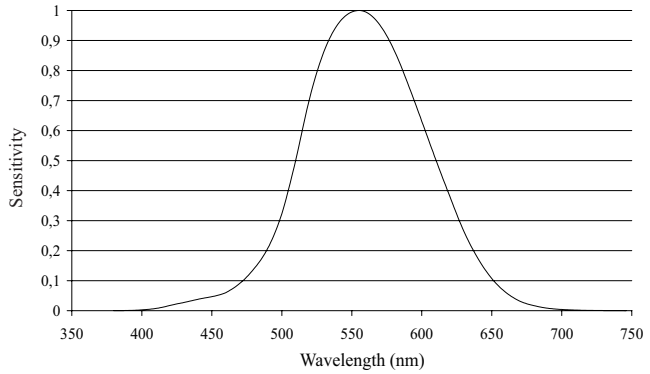

Figure 3.4: Acuity curve for photopic vision of a CIE Standard Observer.

Two particular matrix designs will be considered. They were designed in the same technology, so the design rules are identical. The first is a 1024×768 (XGA) device with 17.6 μm pitch, the other a 1280×768 (WXGA) matrix with a 11.9 μm pitch. For the XGA, the active area is about 18.5 mm $\times$ 14.0 mm = 259 mm^2. For the WXGA, we have 15 mm $\times$ 9.5 mm = 142.5 mm^2. This gives 13.5 lm/mm^2 and 25 lm/mm^2 respectively. Of course, only the light falling on the inter-pixel gaps must be taken into account. In the simulation model, the gaps at the four sides of the pixel are each considered as a separate source. So the amount of light emitted per source is proportional to the surface of the inter-pixel gap, being 17.6 μm $\times$ 0.6 μm $= 10.56 \times 10^{-6}$ mm^2 for the XGA and 11.9 μm $\times$ 0.6 μm $= 7.14 \times 10^{-6}$ mm^2 for the WXGA, yielding 158.4×10^{-6} lm and 178.5×10^{-6} lm per source, respectively.

Up to now the required amount of light has been given in photometric units (lumens), since humanly perceived brightness levels are being specified. This means the acuity curve (see figure 3.4) has been taken into account to modulate the intensity spectrum of the light source.

The spectral distribution of the amount of radiant energy absorbed by the silicon and the number of charge carriers eventually created are of course not related to this acuity curve. The photoelectric sensitivity of silicon depends on a number of parameters, like the thickness of the layer, the amount and type of foreign dopants and surrounding materials. A typical example is given in

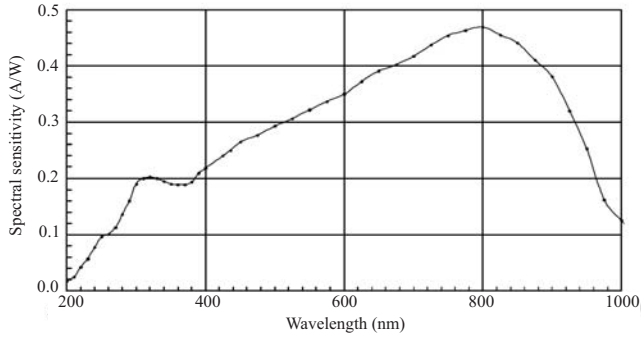

Figure 3.5: Typical spectral photoelectric sensitivity curve of silicon. This material is intended for use as an avalanche photodiode and was tuned to have peak sensitivity at 800 nm. Data taken from [20].

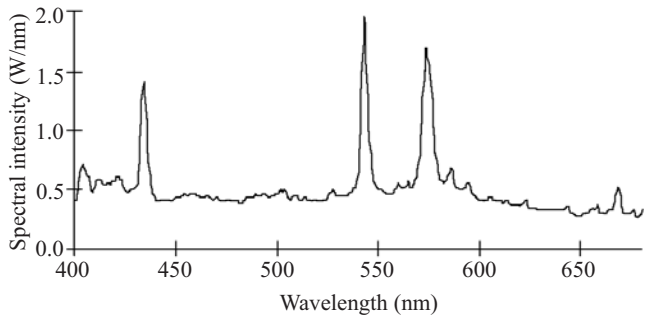

Figure 3.6: Typical emission spectrum of a metal-halide arc lamp.

figure 3.5. Even if only the visible part of the spectrum (470 nm to 650 nm) is considered, it is clear that the two curves are not interchangeable.

Additionally, the spectral intensity distribution emitted by the source can also show some variation. Figures 3.6, 3.7 and 3.8 show the spectra of the light source most frequently used in projection applications.

To perform a globally valid simulation it is desirable to eliminate the uncertainties created by both the sensitivity curve and the light source. A fair approximation of the combined spectral modulation of the silicon sensitivity and the emission of the light sources seems to be a simple constant function. Consequently, the simulations have been carried out using a uniform wavelength spectrum in the visible range (470 nm to 650 nm) instead of the photopic distribution for the standard CIE observer. This means the unit of illuminance in these simulations is not lumens anymore; instead a 'modified lumens' is introduced and denoted as lm*, indicating the acuity curve is not used.

A final noteworthy observation is that for projectors that use three sepa-

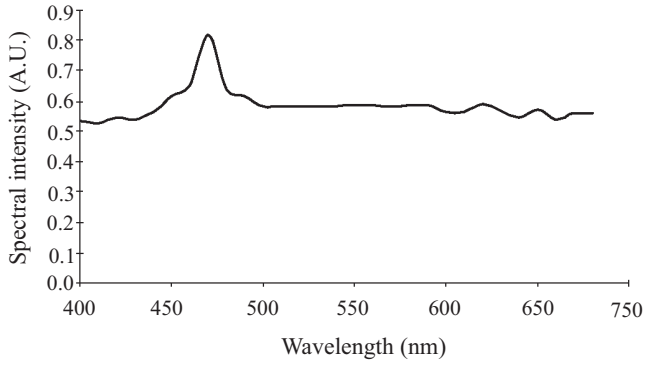

Figure 3.7: Typical emission spectrum of a xenon arc lamp.

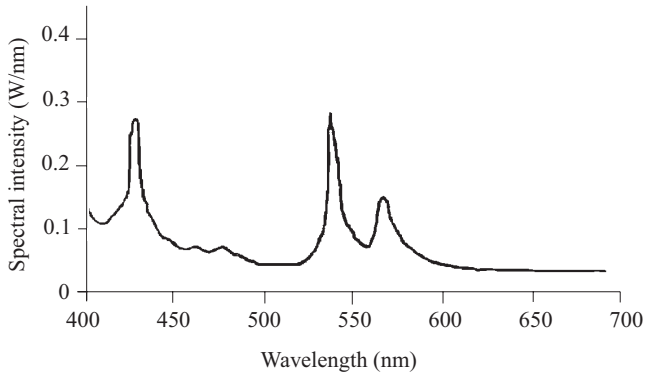

Figure 3.8: Typical emission spectrum of a high pressure mercury (UHP) arc lamp.

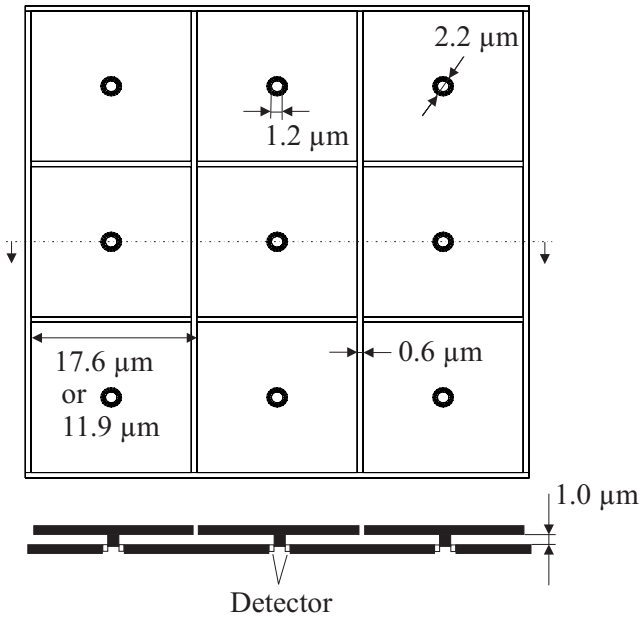

Figure 3.9: Model of the pixel layout used for simulating the shielding performance of a tunnel with anti-reflective coatings. Light enters via the inter-pixel gaps and may travel to the detector areas around the vias. The dimensions of the pixels can vary with the design, spacings and inter-layer distances are fixed by the chosen semiconductor technology.

rate colour-channels, the light flux is distributed over three lightvalves and the demands on the lightshielding are thus reduced to only one third of the original.

Results The following section gives some results of the ray-tracing simulations for the two matrix designs. Figure 3.9 shows a schematic of the model used in the ray-tracer. As explained above, only the two topmost metal layers are taken into account for the labyrinth and a nine pixel configuration is used to eliminate side effects. All inter-pixel gaps act as sources, while the areas where the light can pass to the underlying circuitry, the annuli around the vias, are all detectors. Only the central detector is considered for the simulation results.

Figure 3.10 shows the graphical result of the simulation for the XGA chip when illuminated with light having a maximum entrance angle of 45 °. Figure 3.11 does the same under the assumption of perfectly diffusing lambertian sources.

Because an analytical prediction of the influence of light on the circuitry is very complicated and experiments showed that in some cases even moderate lightsources can cause malfunction, it is required that the silicon 'stays in the dark'. In illumination terms, this translates to a light level of 10^{-9} – 10^{-10}

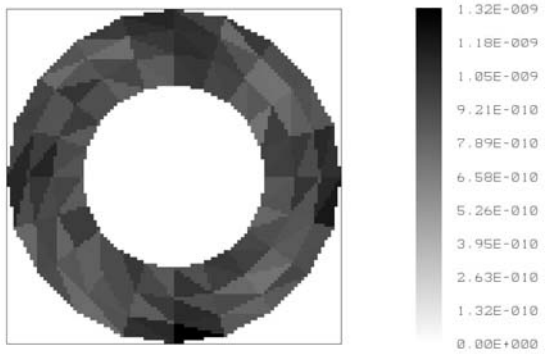

Figure 3.10: Registered illuminance at the detector for a 17.6 μm pixel pitch TiN route design with 45 ° half light-cone angle isotropic illumination. Detector area inner diameter 1.2 μm, outer diameter 2.2 μm, unit is $\mathrm{lm}^*/\mathrm{mm}^2$.

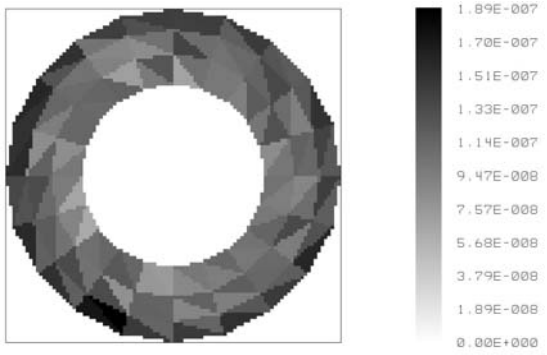

Figure 3.11: Registered illuminance at the detector for a 17.6 μm pixel pitch TiN route design and illumination with a diffuse lambertian source. Detector area inner diameter 1.2 μm, outer diameter 2.2 μm, unit is $\mathrm{lm}^*/\mathrm{mm}^2$.

f/#	Illuminance
3.0	$< 10^{-14}$ lm*/mm^2
2.0	$< 10^{-14}$ lm*/mm^2
1.0	$< 10^{-14}$ lm*/mm^2
0.5	10^{-9} lm*/mm^2

Table 3.2: Simulated illuminance levels for the 17.6 μm layout at different f/# numbers.

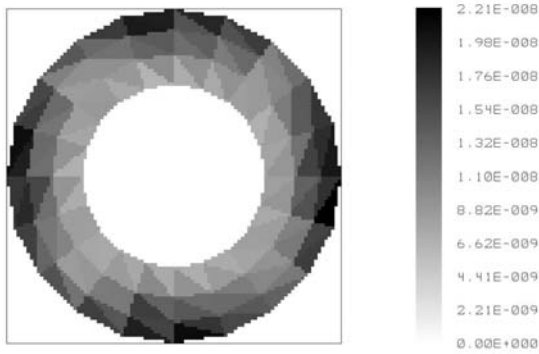

Figure 3.12: Registered illuminance at the detector for an 11.9 μm pixel pitch TiN route design with 45 $^\circ$ half light-cone angle isotropic illumination. Detector area inner diameter 1.2 μm, outer diameter 2.2 μm, unit is lm*/mm^2.

lm*/mm^2 [21].

For the first simulation, the condition is just met. Of course, the maximum incidence angle has been chosen unrealistically large, especially because the energy distribution with angle is supposed to be uniform. In table 3.2, the results for more realistic incidence angles, presented as f/# numbers, are summarised. There should be no problems for these.

As for the simulation with lambertian sources, the threshold is already passed. Again, this simulation represents a very unlikely border-case: it was assumed that all energy is diffusely scattered into a lambertian sphere. It can be expected that in practice, only a small percentage of the energy will effectively been scattered, and the lambertian nature will probably not be fully met, especially at the largest scatter angles.

Figure 3.12 and 3.13 show the results for the same type of simulation, this time for the 11.9 μm pitch WXGA layout. As can be expected, the shielding efficiency is slightly worse and the threshold is passed in both cases. However table 3.3 again shows that for realistic circumstances, the shielding is still more than adequate.

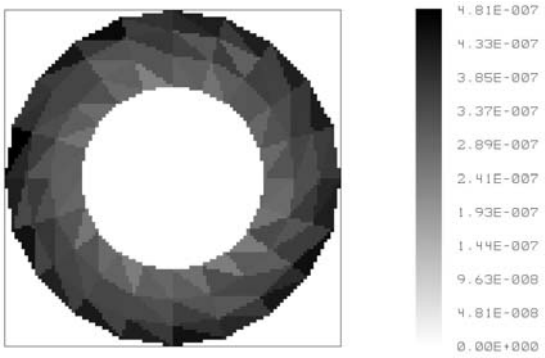

Figure 3.13: Registered illuminance at the detector for an 11.9 μm pixel pitch TiN route design and illumination with a diffuse lambertian source. Detector area inner diameter 1.2 μm, outer diameter 2.2 μm, unit is $\mathrm{lm}^*/\mathrm{mm}^2$.

f/#	Illuminance
3.0	$< 10^{-14}$ $\mathrm{lm}^*/\mathrm{mm}^2$
2.0	$< 10^{-14}$ $\mathrm{lm}^*/\mathrm{mm}^2$
1.0	5.10^{-12} $\mathrm{lm}^*/\mathrm{mm}^2$
0.5	$1.8.10^{-8}$ $\mathrm{lm}^*/\mathrm{mm}^2$

Table 3.3: Simulated illuminance levels for the 11.9 μm layout at different f/# numbers.

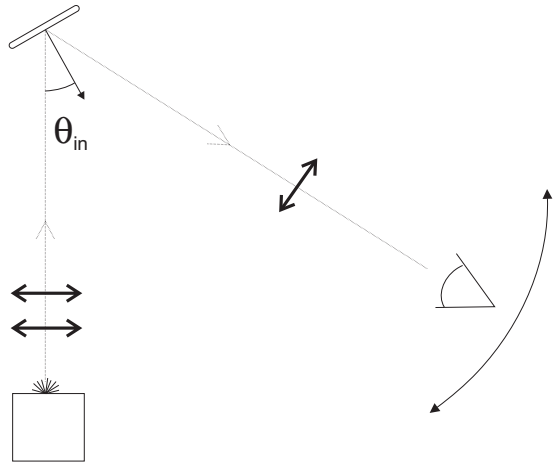

Figure 3.14: Optical setup for verifying the quality of the light shield. The collimated light of a xenon arc-lamp is polarised and then focused by a lens onto the display which is mounted on a pivot. The reflected light passes through an analyser before being picked up by a silicon photodiode.

Verification

The results from these simulations have been confirmed by the experience with functional cells used in projectors. If the light shield would not be sufficient, the electrical charge on a pixel would leak away during a frame time, resulting in fainting imagery. This was never observed in any projector, under any circumstances.

A more direct attempt at determining the light shield quality was performed using the setup depicted in figure 3.14. The display is operated at a nominal frame rate and obliquely illuminated with a strongly collimated light source with a stabilised output. The reflected light is picked up by a fast photodetector. If the display is made to show a uniform level of brightness, the time-varying part of the signal picked up by the detector for $\theta_{in} = 0$ will generally look like the waveform in figure 3.15. The slight output variation is caused by a virtually always present DC offset in the driving signal combined with the frame inversion driving scheme. The base frequency of the signal is thus half the frame rate and the signal is ideally a square wave, smoothed out through the reaction time of the liquid crystal.

When obliquely illuminated, the light can more easily pass the lightshield and introduce some leakage in the pixel capacitors. If the leakage is large enough, the voltage over the pixel will change within a frame time and influence the signal picked up by the detector.

Figures 3.16, 3.17 and 3.18 show the signals picked up at increasing angles of incidence. The light source produces 500000 lux, which results in 71.25

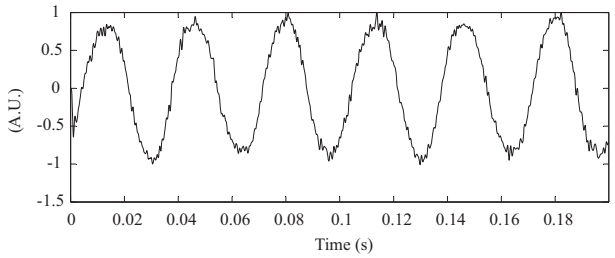

Figure 3.15: Time-varying part of the brightness level of the light reflected by a frame-sequential driven display for perpendicular illumination ($\theta_{in} = 0\,^\circ$).

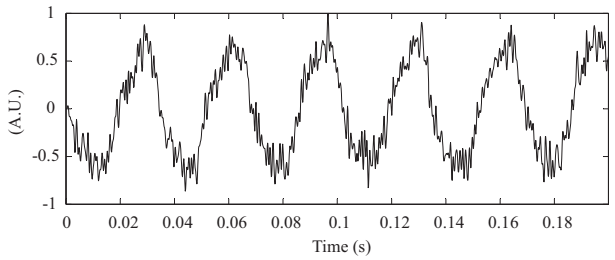

Figure 3.16: Time-varying part of the brightness level of the light reflected by a frame-sequential driven display for oblique illumination ($\theta_{in} = 45\,^\circ$.)

lumens on the WXGA surface. This may seem substantially lower than the proposed 3500 lumens in the earlier calculations, but this time the light is highly collimated. Comparing this collimated light source with the uniformly distributed source used in the simulations, it is obvious that in the latter case only a small fraction of all light rays, those with near-maximum inclination, will actually contribute to the penetrating power of the source. As a result, it can be shown that around 45 ° (either maximum incidence or fixed incidence angle), the two sources are nearly equivalent.

From the graphs, it is clear that the signals recorded at oblique incidence are influenced by the illumination. More information is obtained by inspecting the frequency spectra of the signals. Figures 3.19, 3.20, 3.21 and 3.22 show the lower-frequency parts of the spectra as calculated with FFT.

The reference spectrum (fig. 3.19) features a main peak at 30 Hz and a secondary one at 90 Hz. As the frame rate was 60 Hz, this corresponds to the oscillation at half the frame frequency and its third harmonic . The even harmonics are virtually absent, indicating the signal resembles a square wave

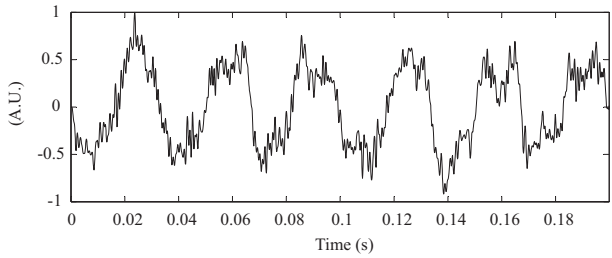

Figure 3.17: Time-varying part of the brightness level of the light reflected by a frame-sequential driven display for oblique illumination ($\theta_{in} = 65\,^{\circ}$).

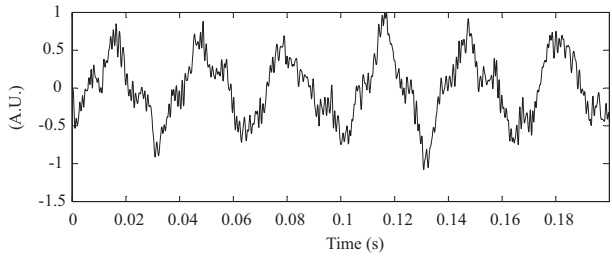

Figure 3.18: Time-varying part of the brightness level of the light reflected by a frame-sequential driven display for oblique illumination ($\theta_{in} = 75\,^{\circ}$.)

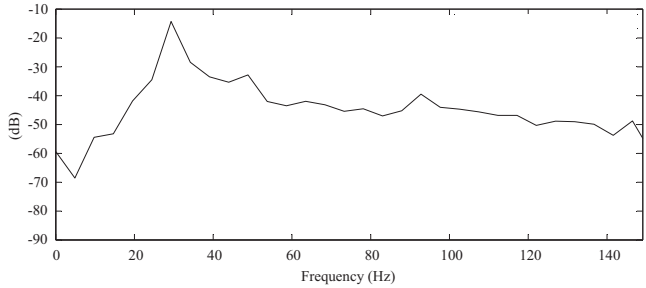

Figure 3.19: Frequency spectrum of the brightness level of the light reflected by a frame-sequential driven display for perpendicular illumination ($\theta_{in} = 0\,^{\circ}$).

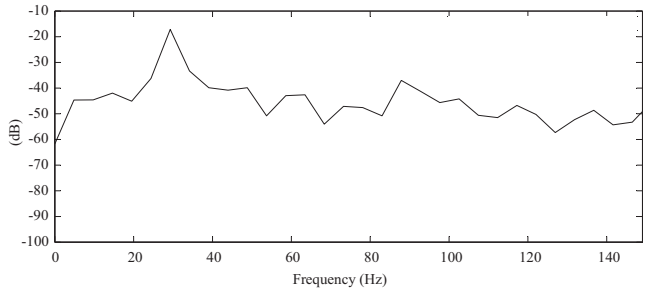

Figure 3.20: Frequency spectrum of the brightness level of the light reflected by a frame-sequential driven display for oblique illumination ($\theta_{in} = 45\,^{\circ}$.)

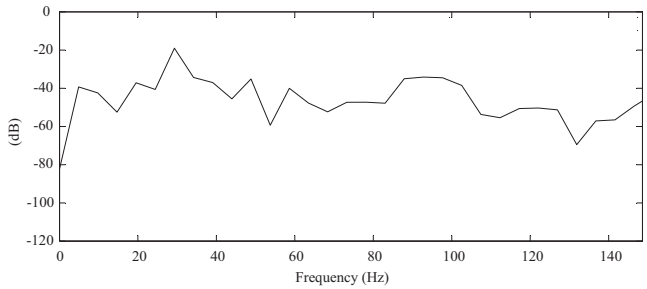

Figure 3.21: Frequency spectrum of the brightness level of the light reflected by a frame-sequential driven display for oblique illumination ($\theta_{in} = 65\,^{\circ}$).

quite well.

In the other spectra, the second harmonic at 60 Hz does pop up. This means the light is able to penetrate the lightshield and starts influencing the electrical circuitry. A typical leak mechanism that has a base frequency equal to the frame rate is symmetrical leak over the storage capacitor toward the backplane voltage. This will distort the original signal introducing even harmonics.

This proves that the simulations produce meaningful results. In conclusion, it can be stated that the performance of the lightshield can be predicted in a reliable way.

3.3 A CMOS technology independent microdisplay process

3.3.1 Introduction

In the early nineties, the TFCG research group undertook its first steps in microdisplay research. CMOS technologies available and affordable at that time

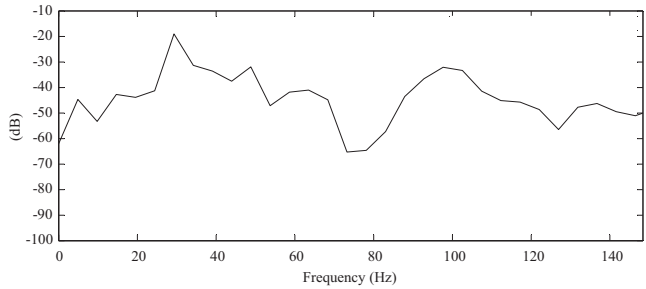

Figure 3.22: Frequency spectrum of the brightness level of the light reflected by a frame-sequential driven display for oblique illumination ($\theta_{in} = 75\,^{\circ}$.)

did not offer any options for planarisation nor lightshielding. Based on the experience gained in thin-film processing during the activities around CdSe active matrix devices, a so-called back-end processing suitable for the first generation microdisplays was developed, providing these very steps. This work was largely carried out by Mrs Carchon and published in display related symposia [22, 23, 24, 25, 26]. Starting from this basis, some refinements to the technology were carried out, mostly towards reliability and resolution. Additionally, a second generation of this technology was conceived, in which we tried to optimise it towards attainable resolution without compromising the excellent planarising and lightshielding properties of the original approach.

3.3.2 Reflec technology

The Reflec technology is the original processing sequence that was developed to produce the first microdisplay demonstrator of the lab. The process flow outlined here describes the way the first working prototypes were produced, later improvements are discussed further on. Table 3.4 shows the detailed process flow. Figure 3.23 shows a schematic cross-sectional view of the finished back-end processing for one pixel, while figure 3.24 can be used as a visual aid while traversing the different steps.

Silicon chip

The substrates for which this technology was developed were 1/16th VGA resolution (160 × 120), 80 μm pixel pitch miniature displays with a 12.8 mm × 9.6 mm active area and a total chip size of 24.6 mm × 19.6 mm. They were processed as an MPW-run using Alcatel's 2 μm HBIMOS process. Due to the MPW nature of the run, a 4"wafer contained only 2 displays in a dedicated area. The Reflec processing started after dicing out this area and treats it as one huge chip up to the very end, after which the two displays are sawn apart and packaged.

Incoming inspection
Gentle cleaning
Dehydration bake
Deposition of Si_3N_4 by PECVD
Spin coating of planarising polyimide
Drying of the planarising polyimide
Illumination through TRANSIMIDE EXTRA mask
Full crosspolymerisation bake of the planarising polyimide
Uniform back-etching of the planarising polyimide
Spin coating of black polyimide
Beta-stage bake of the black polyimide
Spin coating of transparent polyimide
Beta-stage bake of the transparent polyimide
Spin-on of photo-resist
Illumination through ZWARTIMIDE EXTRA mask
Developing
Illumination through ZWARTIMIDE mask
Developing
Reactive Ion etching of the planarising polyimide
Reactive Ion etching of the Si_3N_4
Photo-resist removal
Full crosspolymerisation bake of black and transparent polyimide
Sputtering TiW/Al mirror electrode layer
Spin-on of photo-resist
Illumination through the METAL3 mask
Wet etching of the TiW/Al layer
Photo-resist removal
Final inspection

Table 3.4: Original Reflec process flow.

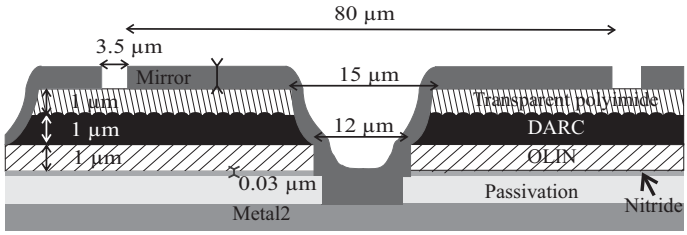

Figure 3.23: Cross-sectional view of the back-end processing in the Reflec technology.

The chip contains all electrical circuitry in its 2 metal layers, no functionality will be added in the subsequent steps. As the chip is considered finished by the wafer fab, it is completely covered with a passivation layer except for the bondpad area. By introducing bondpad areas in the middle of the chip, one can achieve that the passivation is opened at every pixel, avoiding a tedious job doing it oneself.

Process start

After incoming inspection the run is started with a so called gentle clean. This involves an acetone, acetone/isopropyl alcohol, de-ionised water sequence and is aimed at removing organic residues. After this a dehydration bake is performed to remove absorbed moisture. The polyimides used in the upcoming steps are quite sensitive to the presence of moisture, hence this precaution.

The first layer applied is a thin, barely 30 nm, coating of siliconnitride . This coating will serve as a simple protective cover for the exposed metal contact area in each pixel. It ensures that the metal is not attacked by etchants used in later process steps. The siliconnitride is deposited using Plasma Enhanced Chemical Vapour Deposition.

Planarisation

The first polyimide serves as the main planarising layer. In the original flow HTR3-200 from OCG was used for this purpose. This is a very viscous imide precursor with photo-sensitive properties. It is applied using the spinning technique, preferably after the application of an adhesion promoter. Right after spinning, the imide precursor layer is around 12 μm and has levelled out any topology beneath. Next, the precursor is dried in an oven to remove the larger part of the solvent content and make it suitable for contact photo-lithography.

The applied mask (TRANSIMIDE EXTRA) is a very rudimentary one, only to clear out the areas of the mask alignment structures. This is highly advisable because otherwise the thick, smooth layer on top of these structures

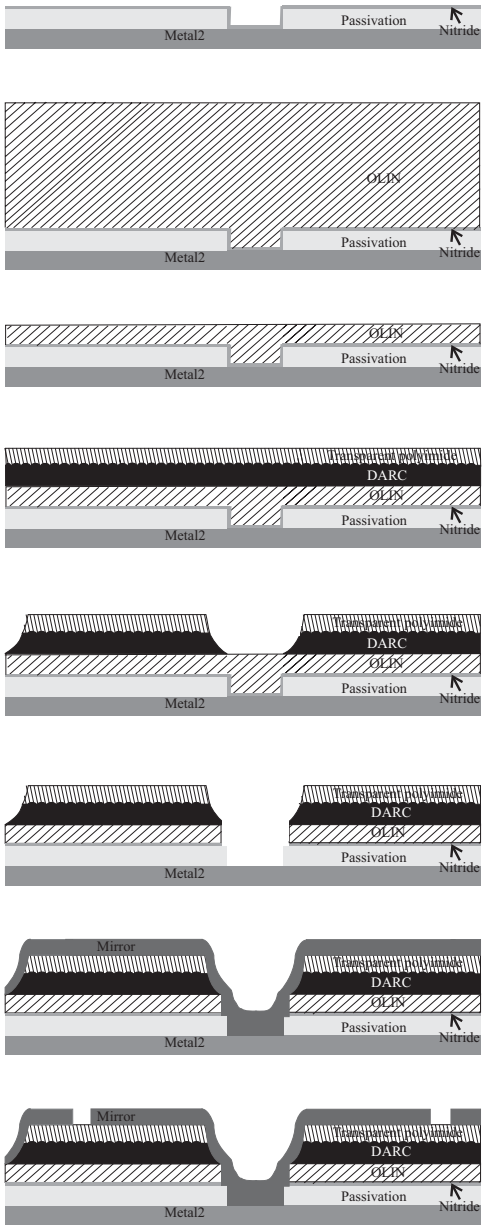

Figure 3.24: Cross-sectional view of the layer structure at several intervals in the Reflec back-end processing. From top to bottom, images are shown right after the, respectively: deposition of the protective nitridelayer; application of the planarising polyimide (OLIN); thinning of the OLIN; application of the black and replanarising polyimide; wet etching (developing) of the top polyimides; dry etching of the OLIN and nitride layer; sputtering of the top metal; patterning of the pixel mirrors.

will make it very difficult to achieve accurate alignment. As the precursor is photosensitive, it suffices to simply illuminate it through the mask and develop it with a dedicated solvent based developer. After this, the precursor can be fully imidised in a vacuum oven.

The fully cured polyimide layer shrinks during the imidisation process but is still around 5 μm thick. If this layer would be kept in the stack unaltered, the vias connecting the pixel mirror to the driving circuitry would be exceptionally deep. Therefore, the layer is uniformly back-etched in a Reactive Ion Etcher (RIE) until it is 1 μm thick. If properly performed, this back-etch does not introduce any additional roughness. It should be noted that although the planarisation of the HTR3-200 is exceptional, it does not provide an optically smooth surface. This is not a problem, since the black polyimide does not have this feature either.

Lightshielding

The following layer is the black polyimide layer for the lightshield. Throughout the research, the DARC300 pigmented polyimide from Brewer Science has been used for this purpose. It is applied by spin-coating, again preferably using an adhesion promoter. Making the layer fit for photo-lithography requires two baking steps: a first alpha bake on a hot-plate removes the solvents, a second beta bake in an oven solidifies the film to a certain extent.

As stated above, the pigment content of this polyimide prevents it from having an optically smooth surface after the cure. Therefore, an additional replanarising layer is needed on top of the stack. This is achieved using a dedicated transparent polyimide layer, originally the T15010 also from Brewer Science. This polyimide features an identical processing scheme as the DARC300, ensuring perfect compatibility. The beta stage of the first polyimide makes it possible to apply the second polyimide on top of it without adverse effects. There is also no problem in subjecting the DARC to a second beta bake needed to solidify the transparent polyimide.

The polyimides are not photo-sensitive, so a photo-resist will be required. However, the polyimides are compatible with standard photo-resist developer, so the stack will be completely patterned during the developing process. The photo-lithography is done in two steps. A first mask, ZWARTIMIDE EXTRA, is very similar to the mask previously applied to the planarising polyimide: it only clears out the alignment structures. This is again mandatory, since the black layer absorbs so much light it is impossible to distinguish the alignment features sufficiently for any positioning with a higher accuracy than 20 microns. After a first developing round, it is then possible to re-illuminate the photo-resist through the second mask, ZWARTIMIDE, basically containing the via holes for the pixels. The second developing, again assisted with ultrasonic agitation to ease the release of the pigments, then yields the desired result.

The via holes however only extend down to the planarising polyimide yet.

The same photo-resist mask is used once more to etch through the planarising polyimide. This is done using RIE, in what comes down to a so-called ashing of the polyimide in a highly oxidising atmosphere. Once this is done, the photo-resist mask is used a last time to remove the protective Si_3N_4 layer, which has now served its purpose. This is again done using RIE.

Now that the patterning is complete, the photo-resist is removed with a dedicated solvent to prevent damaging the polyimide layers. The black and transparent polyimide precursors can then be fully imidised in a vacuum oven.

Metallisation

The remaining step is the application of the top mirrors. Aluminium, already the material of choice in the semiconductor industry, is also ideally suited for the production of mirrors, because of its high reflectivity in the complete visible spectrum. The aluminium is applied by sputtering, in a 1 μm thick layer with a 20 nm TiW adhesion enhancement layer beneath, deposited in the same vacuum cycle.

During the sputtering of thicker layers a lot of heat builds up and the substrate becomes quite hot. This is very disadvantageous for the production of mirrors because the deposition mechanism of the aluminium then slightly changes, usually resulting in matte, diffusely reflecting layers. This phenomenon is prevented using the technique of cold sputtering , in which the layer is deposited in several short sequences, avoiding a significant temperature rise of the substrate. The commonly applied sintering bake after the deposition of metals should also be avoided, because it roughens the metal surface and may cause the formations of hillocks .

The pixels are formed in the metal layer in the conventional way, using the METAL3 mask. The aluminium is wet-etched with acids, the thin TiW layer is opened up with RIE. The removal of the photo-resist and a final inspection complete the process run. Figure 3.25 shows a SEM photograph of some pixels after the back-end processing.

3.3.3 Comments and enhancements

- The planarising polyimide HTR3-200 was originally marketed by OCG. It later moved on to OLIN which then became Arch Chemicals. Under this firm it was discontinued and replaced with the Probimer series of polyimides. Although this required some readjustments of the processing parameters, there was no real difference in performance, both in planarising capabilities or compatibility with other materials. Current material is Probimer 7510.

- Although the T-series polyimides have identical features and requirements for processing as the DARC polyimide, there is a serious material

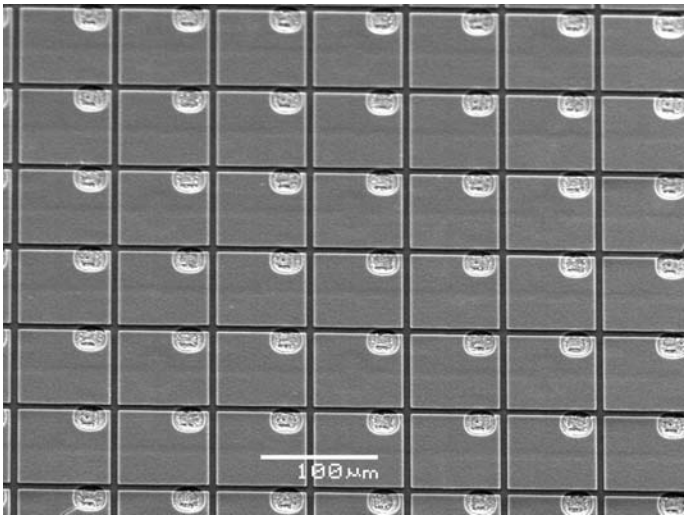

Figure 3.25: SEM photograph of some pixels in the active matrix after the back-end processing according to the Reflec technology.

incompatibility between the two, originally not identified by the manufacturer. If processed on top of each other, in the way described above, larger surfaces will exhibit massive cracking during the final curing step. This is most probably caused by an internal build up of thermal stresses and can be alleviated somewhat by varying the processing conditions. The definitive solution comprised the replacement of the T-polyimide by the base material for the imide precursor of the DARC300, called NMP, which is normally not commercially available. This ensured the compatibility between the two materials, while the absence of the pigments in the NMP resulted in optically smooth surfaces.

- The wet etching of the aluminium top mirrors is not ideal and introduces quite some over-etch. The use of RIE for this etch is strongly recommended, but this requires a chlorine based gas system, which was not available at the laboratory. The original design rule implemented a 5 μm spacing between the pixels, which could later on be reduced to 3.5 μm.

- The double polyimide stack (total 2 μm) together with the combined develop & wet-etch step limit the minimum size of the vias. As the area of the via hole should be considered lost for the reflective surface, this limits the actual geometrical aperture of the pixel. In the Reflec design, the via size was chosen extremely conservative, initially 25 μm and later on 15 μm squares. This is related to the limited position accuracy of the aligner available at the laboratory. The top via, made in the triple stack of polyimides, has to coincide with the contact window in the passivation.

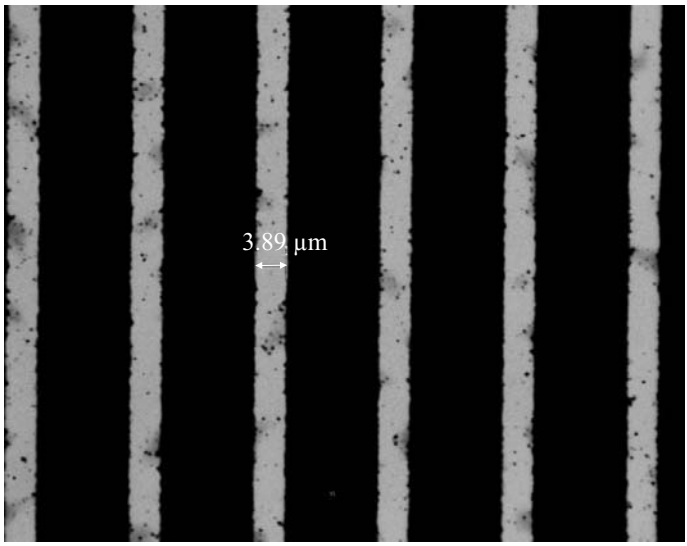

Figure 3.26: Micrograph of line structures in a DARC + T polyimide layer, each 1 μm thick. The spacing between lines is 5 μm on the photo-mask.

This is of course easier if the via and thus the chance for an overlap is larger. The technology is however capable of smaller sizes, 5 μm is certainly possible as is shown in figure 3.26.

- Splitting the patterning of the photo-resist and the polyimides may open a path to better via definition. This split-up is possible by first fully imidising the uniform polyimide layers, potentially copying the photoresist mask onto a dummy metal layer for better performance, and then dry etch through the polyimides. This poses no problems for the transparent polyimide, but unfortunately the pigments in the DARC prevent it from being dry etched by any means except for the expensive and rather exotic ion milling technique.

3.3.4 Reflec II

Limitations of the Reflec technology

The most obvious limitation of the Reflec technology is the attainable resolution. The minimum via size is restricted by several factors and effectively limits the pixel size via the geometrical aperture ratio .

The attainable resolution is in general limited by two kinds of factors: material capabilities on the one side and processing machine capabilities on the other. The material capabilities determine the real limits of a certain technology, whereas the machine capabilities are specific for the laboratory. Of course,

machine capability here is to be interpreted as relative to the state of the art. It is obvious that e.g. the resolving power of a photoresist system ultimately also depends on the quality of the illuminating optics, which is a machine capability, but at any fixed moment in time there will always be a limit that is considered as state of the art.

In the description of the Reflec technology, a limit that is clearly machine dependent is the inter-pixel spacing. Because the gases for dry-etching aluminium are not available in the laboratory, we have to revert to wet etching which limits the minimum spacing that can be obtained. With dry etching and a projection aligner, the spacings can be readily shrunk to the commonly encountered 1.0 - 0.5 μm.

The minimum via size in the polyimide stack is determined by a combination of limitations. As indicated above, the via size is in part determined by the need to accommodate for a certain registration error. This is for the larger part again a machine limitation, although the thick stack is not a favourable condition either. However, the minimum attainable via size in the DARC - T stack is still only 5 μm and is clearly material related. The dry etching of the planarising polyimide through this via will of course increase this value still somewhat.

Adapted technology

The Reflec II technology is a revised version of the original one in an attempt to overcome the limitations of the former as much as possible.

The via size in the black polyimide is one of the main limiting factors. It would be already advantageous if the patterning of the black and transparent polyimide could be separated. Moreover, if the planarising on top of the DARC could be such that the dimple caused by the via is flattened out, concerns about the via size are in fact eliminated. This requires among others that the influence of the registration error is reduced, so that there is no need for oversized vias, a serious obstacle for good planarisation.

The proposed stack is shown in figure 3.27. It realises the goals just set forth and has some additional benefits, as explained below.

The black polyimide layer is moved to the bottom of the stack. As it can now be patterned as a single layer, the via size can be reduced to 4 μm. Because it is now directly above the contact window, the registration problem is greatly alleviated. For most designs, the last metal covers most of the pixel area; in that case it is also feasible to skip the passivation step and apply the black polyimide directly on the last metal.

On top of the black polyimide a thin contact metal layer is sputtered. This layer is patterned in pixels just as the top mirrors will be, only slightly shifted. Again, this provides the entire pixel surface as contact area for the next via, eliminating the registration error.

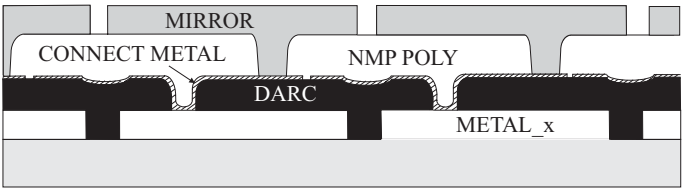

Figure 3.27: Proposed layer build-up for the Reflec II technology. METAL_x is the last metal layer provided by the foundry. Directly on top of it comes a DARC layer, followed by a thin metal layer and a planarising polyimide. The pixel mirrors finish the stack.

The next layer planarises the complete surface. Because the imidisation temperature of the HTR3-200 is much higher than the maximum allowed temperature for the DARC, this material cannot be used anymore. Instead, the NMP polyimide is used. The basic delivery form of this material is also a very viscous liquid, which has to be diluted for its use as replanarising layer in the original technology. In pure or somewhat diluted form, it can also planarise larger topology differences. Just as with the HTR3-200, the resulting layer is too thick and must be thinned off. The back-etching with RIE introduces some micro-roughness, so a replanarising is necessary to get optically smooth surfaces. The same NMP polyimide, this time in highly diluted form, is conveniently used for this.

Lastly, the mirrors are sputtered and patterned, finishing the process. Because the vias in the previous layer have been dry etched, the via size is minimal and the dimple in top mirror is relatively small.

Reflec II features

Sandwiching the black polyimide directly between two metal layers, has a very beneficial effect on the light shielding properties of the stack. Although the shielding efficiency of the original technology is anything but bad, as will become clear later on, the performance of the black polyimide was not optimally exploited. By capturing the light in a tunnel similar to the one presented in the integrated approach, but this time filled with the highly absorbing polyimide, exceptional shielding is attained.

The via size in the DARC300 layer is somewhat smaller than before, but there is still room for improvement. One option to reduce the via size further is simply shrinking the layer thickness. In the original technology, this has a negative impact on the quality of the lightshielding. In the Reflec II technology however, the shielding efficiency is unaffected, as will be explained further on.

In later stages of the research, experiments with advanced derivatives of the DARC300 polyimide were conducted. The EXP99019V material is such an evolved system, designed to outperform DARC300. It is a photo-sensitive

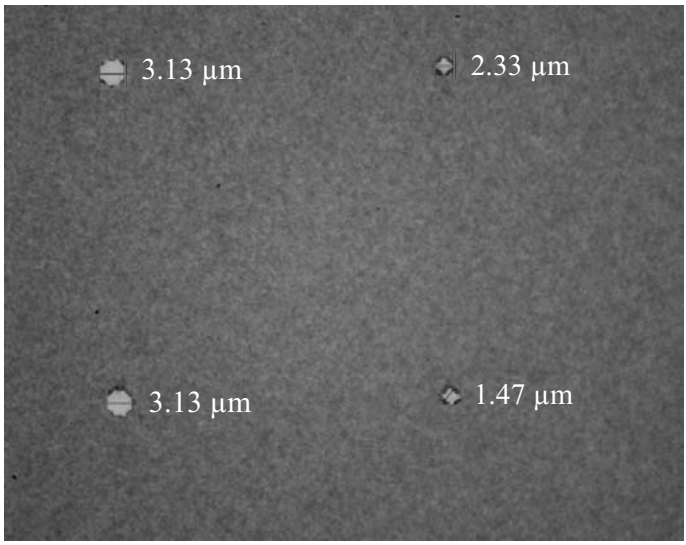

Figure 3.28: Micrograph of 3 μm (left) and 2 μm (right) vias in a 1 μm EXP99019V layer.

polyimide system, which should allow it to attain higher resolutions. Via sizes as small as 2 μm have been realised with this material, while the layer thickness was kept at 1 μm (see figure 3.28).

3.3.5 Polyimide planarisation

Concept

The principle of planarisation with polyimides or, more general with polymers, is quite similar to CMP. The organic material, in the form of a viscous liquid, is spin-cast on top of the topology. The rheology of the liquid makes it act as a spatial low-pass filter, with a 'cut-off frequency' related to the viscosity. Depending on the initial thickness of the film, height differences over larger distances can also be flattened out. Crosslinking fixes the layer. The polymers are preferably thermosets with high glass transition temperature. This ensures that during and after the cure the surface is not altered anymore by plastic flow or creep. The resulting layer can be quite thick if the topological variation was particularly bad. In that case, the layer must be back-etched.

Both benzocyclobutene (BCB) and polyimides have been used to achieve planarisation [27, 28, 29]. The former attracted quite some attention because it is believed to produce good planarisation for not so thick layers. On the other hand, this has only been demonstrated for relatively dense underlying topologies. Certain polyimides, as used in this research, attain comparable

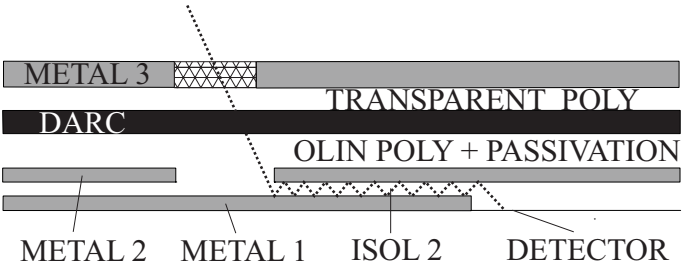

Figure 3.29: Schematic layer build-up of the Reflec technology, showing one pixel. Before light can reach the silicon substrate (the detector area), it must pass through the absorptive DARC layer and travel a short distance between the METAL1 and METAL2 layers. Picture not to scale.

planarisation, also on sparsely occupied topologies. This is achieved through the high initial thickness of the layer, which is subsequently reduced by the large shrinkage during the imidisation.

3.3.6 Black polyimide lightshielding

The design of the lightshield in the original Reflec technology is quite different from the concept laid out earlier on. The chip is now processed in a 2 metal technology, so there are no spare metal layers available.

In figure 3.29 a cross-sectional view of the buildup layers is shown. METAL1 and METAL2 are still patterned in the foundry. Typical layer thickness is 600 nm, as is the insulating layer between them. The spacing between the METAL2 layers belonging to neighbouring pixels is 4 μm. On top of the passivation layer provided by the foundry, a planarising OLIN polyimide, the DARC polyimide and a replanarising T-polyimide of 1 μm each is applied. The mirrors provided by METAL3 are also 1 μm thick, while the spacing between two pixels is 3.5 μm. In the drawing the spacings between METAL3 and METAL2 respectively are shown as coincident for clarity. As is evident from figure 3.30, the spacings actually cross each other, resulting in a 3.5 μm $\times$ 4.0 μm rectangle where the light can pass through.

Light entering via this opening hits METAL1. It then still has to propagate via multiple reflection through a METAL1 / METAL 2 tunnel before reaching silicon. To make sure this tunnel is always the longest possible, shorter paths are blocked off by means of dedicated via walls. In figure 3.30, these walls show up as vertical and horizontal black lines near the pixel borders. The resulting

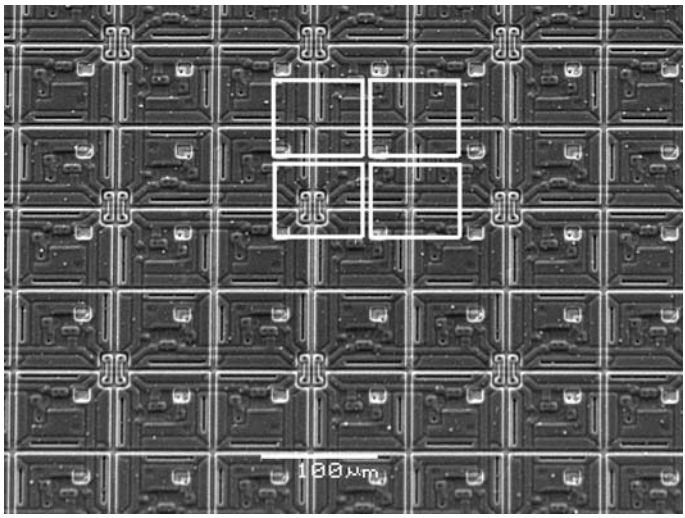

Figure 3.30: SEM photograph of the active matrix of a Reflec display as processed by the foundry. Both METAL1 and METAL2 are visible (the contours of the latter are brighter). The white squares indicate the position of the METAL3 mirrors. Pixels appear rectangular due to a tilt of the substrate.

lightshield thus comprises an absorptive part and a short (approximately 8 μm) light tunnel.

Black polymeric resins have been introduced to replace the chromium-oxide black layers used throughout the AMLCD industry as black matrix material. Chromiumoxide is a very efficient lightshield, but is harmful to the environment and quite costly in deposition. Polyimide films are frequently used as base material, but other organics such as acrylic resins are also in use [30]. For the actual lightshielding, several, often proprietary solutions are in use, ranging from carbon black [31], over pigments [32, 33], dyes, to latent pigments [34]. The black polyimide material used in this research uses such a proprietary system, resulting in high optical densities.

Performance

Although the Reflec chips were originally not intended to bear the amount of light associated with the above mentioned projection applications, it is interesting to see how well they perform under such circumstances. Taking up the model developed for the AR lightshield and adapting it to the new situation, the active matrix size is now approximately 13 mm $\times$ 10 mm and the needed light flux becomes 27 lm/mm^2. The inter-pixel region where light can enter is now 3.5 μm $\times$ 80 μm large so a single source has 0.00756 lumens.

Table 3.5 shows that the performance is not at all bad; it is even still slightly

Light source half cone angle	Illuminance (lm^*/mm^2)
45 ° (with TiN layer)	10^{-13}
45 ° (without TiN layer)	2.5×10^{-10}
22.5 ° (with TiN layer)	$<< 10^{-14}$
22.5 ° (without TiN layer)	1.5×10^{-10}
diffuse lambertian source (with TiN layer)	$< 10^{-14}$
diffuse lambertian source (without TiN layer)	1.8×10^{-10}

Table 3.5: Simulated average illuminance levels at the detector for the original Reflec layout using different illumination conditions.

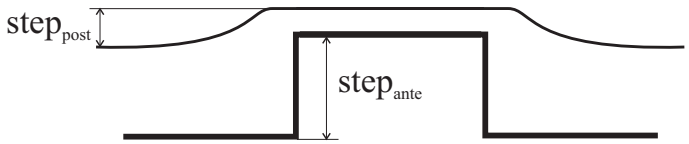

Figure 3.31: A definition of the step heights before and after planarisation as used in equation (3.1). It is obvious that this definition is particularly meaningful when dealing with the planarisation of relatively narrow, isolated tracks.

better than the TiN solution for 17.6 μm pixels. For completeness, both the results with and without a TiN layer inside the light tunnel are given.

3.4 Performance comparison

3.4.1 Planarisation

The quality of planarisation is usually characterised using the degree of planarisation (D.O.P) [35], as defined in (3.1). The actual implementation of the step to be measured before and after the planarisation can vary according to what is envisaged; a frequently used definition is shown in figure 3.31.

$$\text{D.O.P.} = 1 - \frac{\text{step}_{post}}{\text{step}_{ante}} \tag{3.1}$$

For the CMP technique, D.O.P. values of 95 % to almost 99 % have been reported [36]. BCBs have D.O.P values ranging from 83 % to 96 % [37, 29], while non-dedicated polyimides end up in the 20 % to 30 % range [38]. With the polyimide used in the Reflec technology, a D.O.P. of 85 % to 95 % has been achieved.

It should be noted however, that the D.O.P. is only useful in the comparison of different materials or techniques insofar identical reference substrates are used to obtain the D.O.P. values. In the particular case of display planarisation, it is already clear that the design, and thus the topology of the chip,

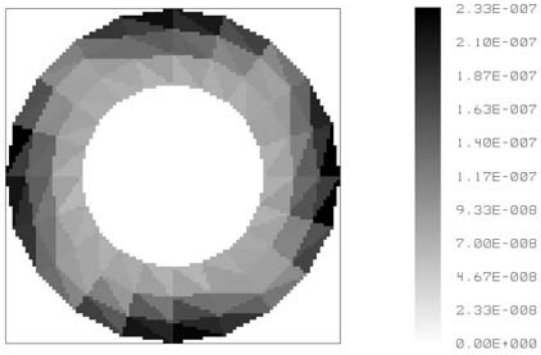

Figure 3.32: Registered illuminance at the detector for a 8.0 μm pixel pitch TiN route design at 45 ° half light-cone angle isotropic illumination. Detector area inner diameter 1.2 μm, outer diameter 2.2 μm, unit is $\mathrm{lm}^*/\mathrm{mm}^2$.

is customised, among others for the envisaged type of lightshielding, so that a correct comparison is difficult.

This is the more true since the cited values often are not accompanied with specifications of how they were obtained. On the other hand, as all values are already quite high and not far apart, it is fair to assume that all technologies meet the requirements. Performance comparison then comes down to a cost comparison.

3.4.2 Lightshielding

In order to compare the two lightshielding approaches to each other, their behaviour for varying design parameters is explored and evaluated in the following sections.

TiN

Pixel size An ongoing trend is the search for smaller pixels. This will ultimately be stopped by problems with diffraction patterns [39]; the current limit seems to be around 8 to 7 μm. Figure 3.32 shows the detected intensity for a 8 μm pixel pitch design, to be compared with the pictures 3.10 and 3.12. It can be seen that the irradiation levels have again increased with an order of magnitude, so problems become quite probable.

Figures 3.33 and 3.34 show how the light extinction evolves with the pixel pitch for a light source that radiates isotropically within a cone with 45 ° half top angle and a diffuse lambertian source, respectively. For both, a rather simple exponential relation with the pixel pitch can be found. This illustrates the difficulties that can be expected with the light shielding when pixel pitch is

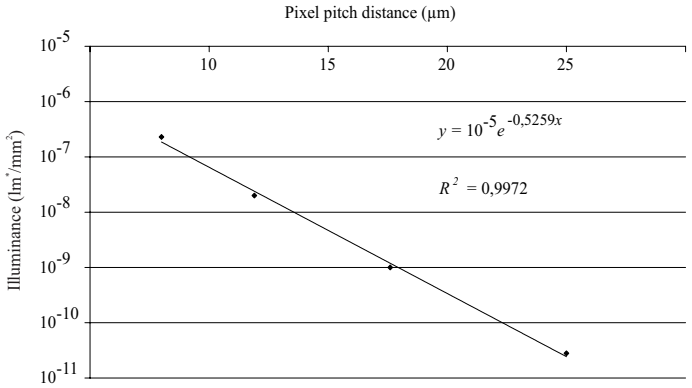

Figure 3.33: Light shield efficiency (as registered average illuminance at the detector) versus pixel pitch for the TiN route design with isotropic illumination within a fixed half light-cone angle of 45 °.

substantially reduced. Of course, the relation is only true if the same technology is used for all pitch values, i.e. the minimum inter-pixel distance and layer thicknesses are assumed to be constant. Using highly advanced technologies may alleviate the problem somewhat, but it should be noted that although the current semiconductor research features critical dimensions of 45 nm and below, the minimum allowed spacings between metals in a top layer are far less impressive.

Two-stage labyrinth A way out of the dilemma is to enlarge the number of reflections by extending the labyrinth to a metal level underneath. This sacrifices another metal layer that could otherwise be used for the implementation of circuitry. The most efficient light shielding enhancement with this additional layer generally implies that serious parasitic capacitances are created between pixels, thus giving rise to other concerns. Figure 3.35 shows a cross-section of the layout used for simulating the behaviour of this construction.

Figures 3.36 and 3.37 show the resulting performance of the structure, by means of an illuminance plot at the detector, again for uniformly radiating 45 ° sources and diffuse lambertian sources, respectively. The detector area, where the light can pass to the underlying circuitry is now the thin, rectangular inter-pixel gap at the bottom metal layer. The chosen layout here is the best possible light shielding, i.e. the light is forced to travel form the pixel side to the centre where it can enter the lower light pipe and is sent back to the pixel side again. A significant improvement is gained in both cases.

Maximum incidence angle A way to increase the light throughput of a projector system is to enlarge the maximum accepted cone angle of the light that falls on the lightvalve. For liquid crystal lightvalves, the limit is usually

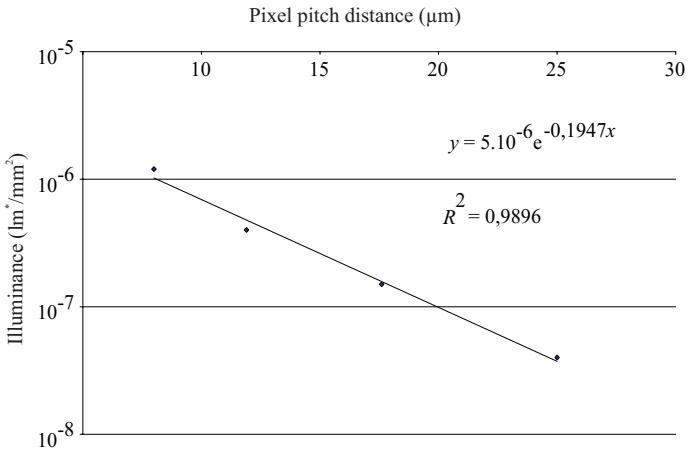

Figure 3.34: Light shield efficiency (as registered average illuminance at the detector) versus pixel pitch for the TiN route design with a diffuse lambertian source as illumination.

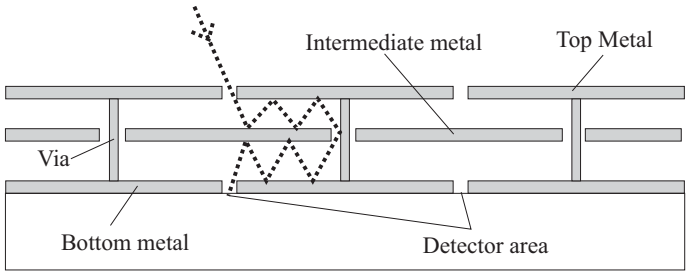

Figure 3.35: Schematic representation of the build-up for a three metal layer labyrinth arranged for optimum lightshielding. To reach the underlying circuitry, the light now has to travel a distance of half the pixel width at the first level, get down to the lower level and travel back the same distance.

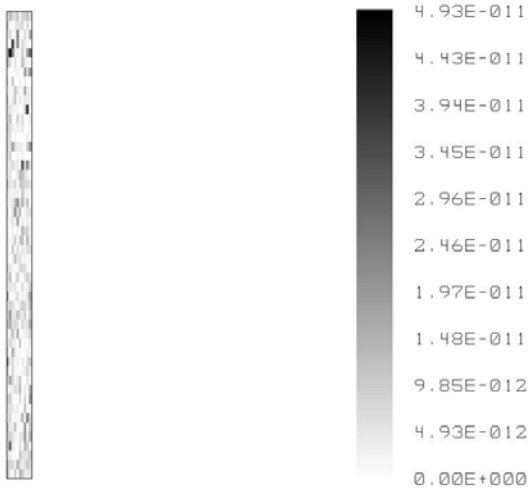

Figure 3.36: Registered illuminance at the detector for a 11.9 μm pixel pitch 3 layer TiN structure with 45 ° half light-cone angle isotropic illumination. Detector area is 11.9 μm by 0.6 μm, unit is lm*/mm^2.

Figure 3.37: Registered illuminance at the detector for a 11.9 μm pixel pitch 3 layer TiN structure with a diffuse lambertian source as illumination. Detector area is 11.9 μm by 0.6 μm, unit is lm*/mm^2.

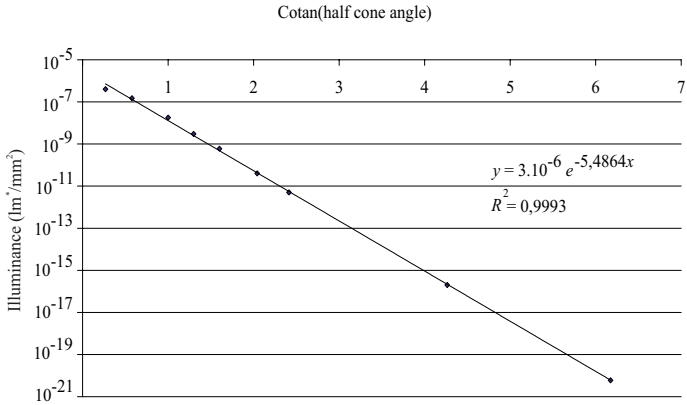

Figure 3.38: Light shield efficiency (as registered average illuminance at the detector) versus illumination light-cone angle for the TiN route design at a fixed pixel pitch of 11.9 μm.

imposed by the contrast ratio that has to be achieved. The behaviour of the lightshield under various incidence angles is shown in figure 3.38 in the case of a 11.9 μm pitch design. If the half cone angle value is converted into an equivalent distance the light can travel per reflection, again a rather simple exponential relationship between shield efficiency and this distance can be obtained. Basic geometry shows that an equivalent distance is obtained by taking the cotangent of the maximum cone angle. One consequence of this is that, for reasonable values (15 to 20 degrees) a relatively small additional reduction of the cone angle can result in a relatively large gain in shielding efficiency.

As a side remark, it should also be noted that the reflectivity of the TiN layer depends on the incidence angle. Figure 3.39 shows the reflectivity coefficient for the two polarisation directions. In the expected operating region the discrepancies still remain very moderate.

Tunnel height A last crucial parameter is of course the thickness of the insulating layer between the two TiN reflectors. In principle this is determined by the semiconductor technology and there is not so much variation possible, even across different technologies. A foundry may however consider to introduce a dedicated microdisplay process where this thickness is adjusted, provided the reliability is not endangered. Since the obvious goal is to go for thinner layers, the reliability issue will be mainly concerned with accidentally short-circuiting two metal levels. Adjustments of this kind have been pursued during the research project Mosarel.

Figures 3.40 and 3.41 show how the shield efficiency evolves with the layer thickness over a broad range. The graphs feature three distinct areas: a rapidly rising part ending in a first plateau, a transition region and a second plateau.

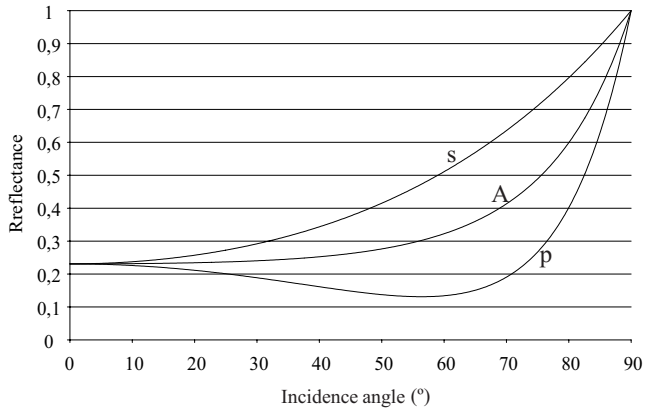

Figure 3.39: Reflectivity of a 100 nm TiN layer under different incidence angles at 550 nm. S and P denote s- and p-polarisation respectively, A represents the average of the two.

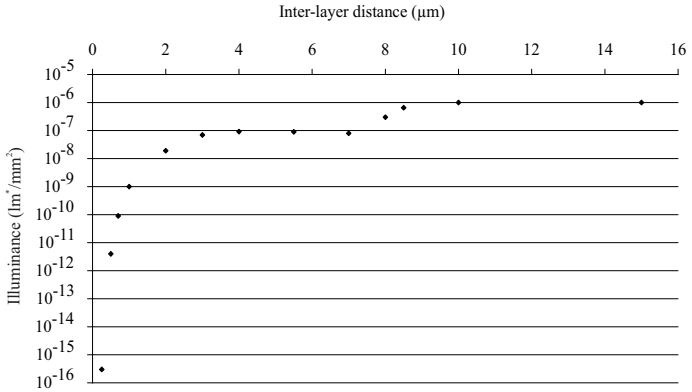

Figure 3.40: Light shield efficiency (as registered average illuminance at the detector) versus inter-layer distance for the TiN route design with 17.6 μm pixel pitch layout and 45 ° half light-cone angle isotropic illumination.

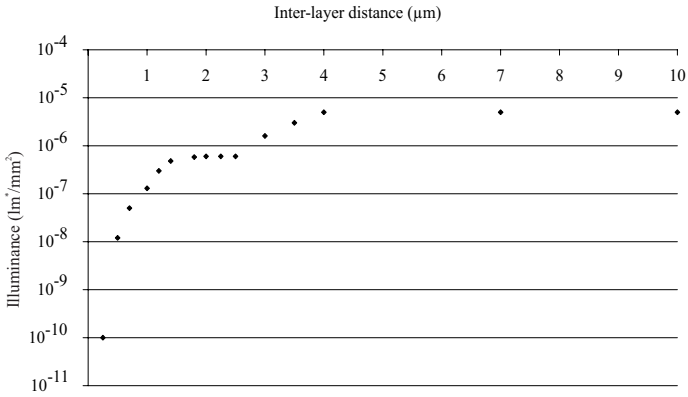

Figure 3.41: Light shield efficiency (as registered average illuminance at the detector) versus inter-layer distance for the TiN route design with 8.0 μm pixel pitch layout and 45 ° half light-cone angle isotropic illumination.

The first part of the graph, up to the beginning of the first plateau, comprises the thicknesses for which multiple reflections actually still take place. Similar to the previous cases, an exponential relation with the shielding efficiency can be demonstrated if the inter-layer distance is converted into an equivalent distance travelled per reflection. Simple geometry again quickly reveals that the inverse of the inter-layer distance can serve as such an equivalent distance. Figures 3.42 and 3.43 illustrate this for the 17.6 and 8.0 μm pitch layout.

The first plateau marks the region where only very few reflections are needed to reach the detector area, typically only two. In this situation, a small change in layer thickness does not change the amount of captured light in a significant way, as the extinction ratio stays fixed by the two reflections. Once the thickness is large enough to eliminate the need for reflections, the extinction ratio rapidly drops.

The second plateau corresponds with the situation where the layer thickness is so large light can directly fall onto the detector area. The extinction ratio is then only determined by the size of the inter-pixel gap and the detector area. The layer thicknesses for which this happens are of course excessively thick and will never be encountered in reality.

The layer thickness around which the first plateau occurs is therefore dependent on the maximum incidence angle and the pitch. In the designs considered, the minimum distance the light has to travel to reach a detector is approximately half the pitch. So in the case of a 45 ° opening angle, the first plateau is expected around a quarter of the pitch. This is confirmed in the graphs already shown.

Of course, if the opening angle becomes more moderate, the occurrence of

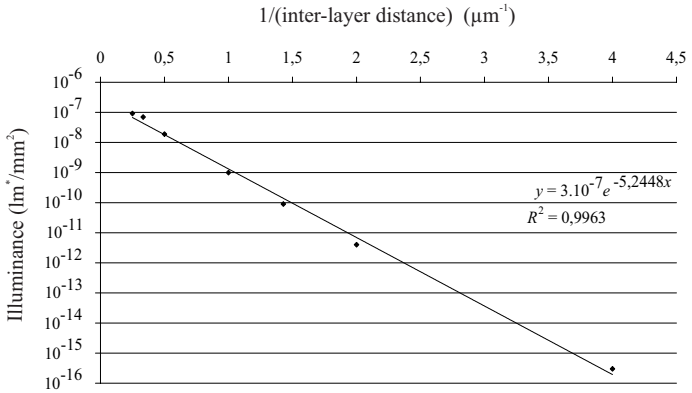

Figure 3.42: Light shield efficiency (as registered average illuminance at the detector) versus the inverse of the inter-layer distance for the TiN route design with 17.6 μm pixel pitch layout and 45 ° half light-cone angle isotropic illumination.

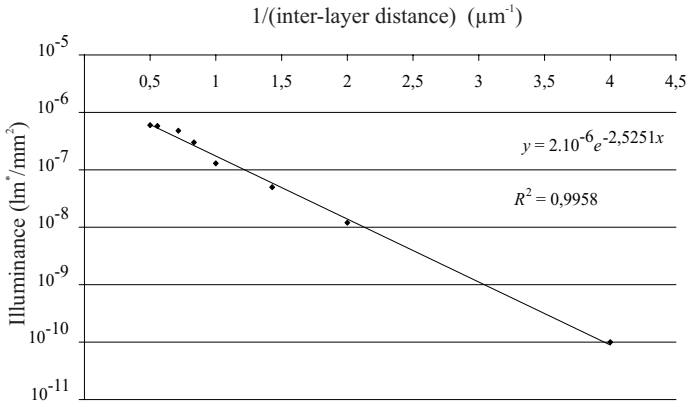

Figure 3.43: Light shield efficiency (as registered average illuminance at the detector) versus the inverse of the inter-layer distance for the TiN route design with 8.0 μm pixel pitch layout and 45 ° half light-cone angle isotropic illumination.

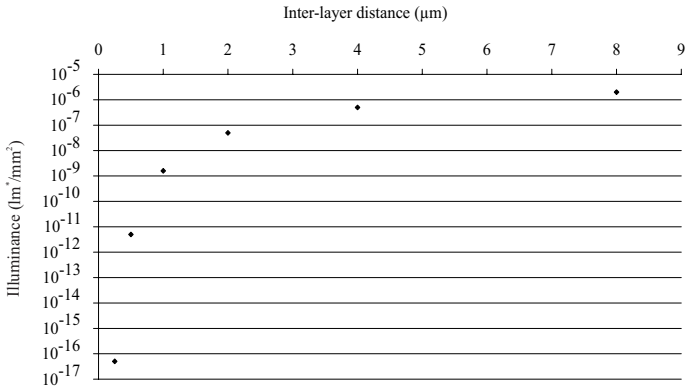

Figure 3.44: Light shield efficiency (as registered average illuminance at the detector) versus inter-layer distance for the TiN route design with 8.0 μm pixel pitch layout and 22.5 ° half light-cone angle isotropic illumination.

the plateau is shifted to thickness values beyond what is remotely realistic. Figure 3.44 shows the situation for a 22.5 ° opening angle. The plateau is expected at 8 μm, a very unlikely value for a thin-film process. Before the plateau value is reached, the relation extinction - thickness follows the exponential law already set forth (figure 3.45).

DARC

The performance of the DARC layer set out in the previous paragraphs is not a good basis to compare the two technologies, as the capabilities were not fully exploited. With the technology improvements outlined for Reflec II, it is possible to make a fair comparison, where the two technologies are at their best. For the simulation modelling, this basically means the layout from the TiN route is kept, but the standard insulating layer between the two metals is replaced with the DARC polyimide layer. The current technological limitations of the DARC layer, mainly the minimum via size, are also taken into account.

Pixel size The resulting light-blocking system is extremely efficient. Figure 3.46 shows the efficiency versus pixel pitch for illumination with a 45 ° half opening angle under the same conditions as for the TiN route. The achieved extinction ratios are several orders of magnitude better than for the TiN route. Even for extremely tiny pixels at 5.0 μm pitch, no problems are to be expected, given that the extinction ratio is still better than the one for the 17.6 μm TiN version. It can also be demonstrated that the exponential relation between extinction ratio and pitch distance is still valid.

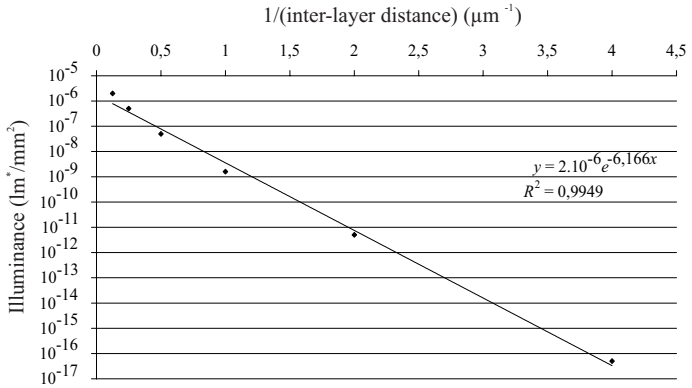

Figure 3.45: Light shield efficiency (as registered average illuminance at the detector) versus the inverse of the inter-layer distance for the TiN route design with 8.0 μm pixel pitch layout and 22.5 ° half light-cone angle isotropic illumination.

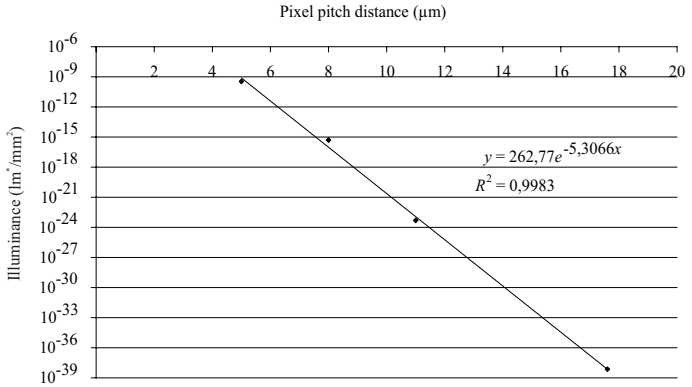

Figure 3.46: Light shield efficiency (as registered average illuminance at the detector) of a 1.0 μm DARC layer versus pixel pitch with isotropic illumination within a light-cone of 45 ° half opening angle.

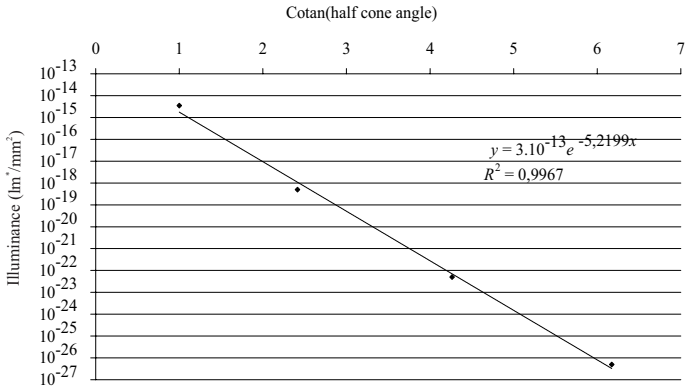

Figure 3.47: Light shield efficiency (as registered average illuminance at the detector) of a 1.0 μm DARC layer versus the light-cone half opening angle of the isotropic illumination at 5.0 μm pixel pitch.

Maximum incidence angle A similar result is seen for the behaviour with varying opening angles. Achieved extinction ratios are very high, especially in the region of the currently employed f/# numbers. Also over here, a similar exponential relation can be established between the extinction ratio and an equivalent distance travelled by the light per reflection. Unsurprisingly, the same function as for TiN can be used as equivalent distance. Figure 3.47 illustrates this.

Layer thickness Finally the evolution of performance with thickness (figure 3.48) shows some deviant behaviour compared to the TiN route, apart from the systematically higher performance. All of the thicknesses below 1 μm show a constant extinction. Outside of this area, again an exponential relation can be demonstrated, but this time directly between shielding efficiency and layer thickness.

The mechanism becomes clear considering the physical properties of the layer. As an absorptive medium, the DARC layer obeys the Beer's law (3.2), where d is the distance travelled through the medium.

$$I = I_0 e^{-\alpha d} \tag{3.2}$$

For a fixed incidence angle, this distance is normally constant, regardless of the thickness of the layer, as illustrated in figure 3.49. The number of segments to get out of the tunnel is given by (3.3), whereas the distance travelled for each segment is given by (3.4). Obviously, in the product of the two, the thickness t gets cancelled out.

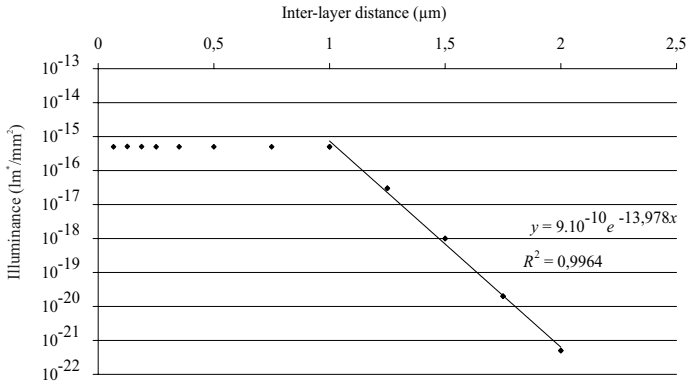

Figure 3.48: Light shield efficiency (as registered average illuminance at the detector) of a DARC layer versus its thickness for a 8.0 μm pixel pitch layout at 45 ° half light-cone angle isotropic illumination.

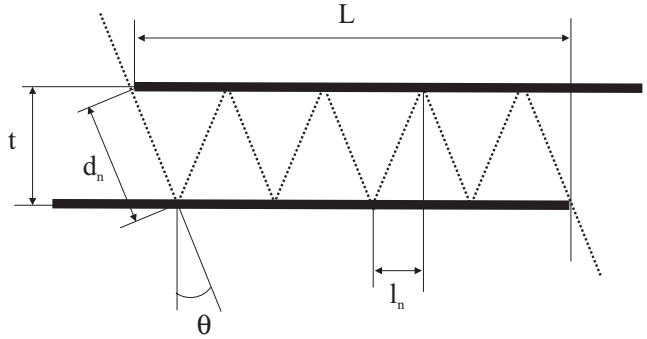

Figure 3.49: Schematic representation of a light tunnel and the path a light ray has to follow to get from one end to the other.

$$N = \begin{cases} n & \text{if n is odd} \\ n+1 & \text{if n is even} \end{cases} \qquad n = Int\left(\frac{L}{l_n}\right) = Int\left(\frac{L}{t\tan\theta}\right) \tag{3.3}$$

$$d_n = \frac{t}{\cos\theta} \tag{3.4}$$

This explains the flat curve. Once the thickness becomes so large the light can directly strike the detector, the relationships (3.3) and (3.4) do not hold anymore and the travelled distance becomes directly proportional to the thickness. Thus the intensity drops exponentially following (3.2) with d proportional to the layer thickness.

The constant extinction for smaller layer thicknesses is of course a nice feature of the system, making it fairly easy to produce a reliable lightshield.

3.4.3 Conclusion

In conclusion, it can be stated that both technology routes for the production of microdisplays are viable and perform well. Looking at the planarisation, with the present availability of CMP steps, it may be favourable to opt for this route. As for the lightshield, it is undeniable that the DARC route, if properly applied, is superior in terms of light-blocking efficiency. Whether future developments will necessitate its use, remains to be seen.

Chapter 4

Vertically Aligned Nematic Liquid Crystal

4.1 Outlook on liquid crystals

4.1.1 State of matter

Commonly, three states of matter are distinguished: solid, liquid, and gas. Liquid crystal can be regarded as a fourth state, intermediate between a normal liquid and a solid, that is exhibited by certain kinds of materials under the right conditions. The molecules in solids exhibit both positional and orientational order: they are in fixed positions with respect to each other and cannot turn around themselves. In liquids, the molecules do not have positional nor orientational order: the positions are random and molecules can turn freely.

As for liquid crystal, the molecules do not exhibit any positional order (at least for the most general case), but they do possess a certain degree of orientational order. If the long axis of the molecule is taken as a reference, then the axes of all molecules will not point in the same direction at a given time, but on average there will be a preferred direction. This direction is referred to as the director of the liquid crystal.

The amount of order can be quantified by an order parameter S, defined as in equation (4.1); the brackets are to be interpreted as an average over the considered volume and θ is defined as the angle between the long axis of each individual molecule and the director.

$$S =< \frac{3\cos^2\theta - 1}{2} > \tag{4.1}$$

The order parameter is highly dependent on the temperature of the sample.

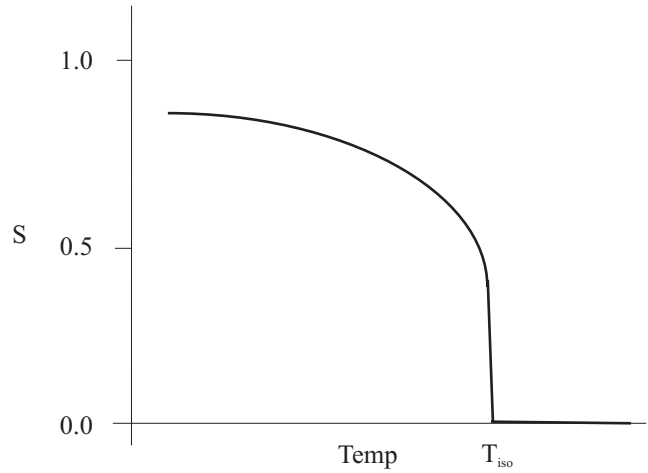

Figure 4.1: Typical behaviour of the order parameter as a function of temperature for a liquid crystal with a single nematic phase.

Values of S will generally range between 0.9 and 0.3. At the nematic-isotropic transition, the liquid crystal becomes an ordinary liquid and S drops to 0. Figure 4.1 illustrates this.

Not all substances can have a liquid crystal phase. Molecules that are likely to be candidates are long and have a rigid central region and ends that are slightly flexible: they are more or less cigar shaped, though other shapes are possible, most notably discs and bowls. The first are termed nematogens , the latter discotic and bowlic liquid crystal, respectively.

The important fact is that liquid crystal molecules are always geometrically highly anisotropic. This leads to anisotropy showing up in other physical properties as well (e.g. electric, magnetic, etc), contrary to normal fluids, where the anisotropy has no influence on a macroscopic scale. This property is the key to all functionality of liquid crystals.

Thermotropic and lyotropic

Liquid crystals can generally be divided into two classes: thermotropic and lyotropic. The first comprises all conventional liquid crystals, as known from the opto-electronic industry: their crystallinity phase only depends on temperature. Otherwise said, for the given substance, only temperature determines whether the phase will be solid, ordinary liquid, or liquid crystal.

On the other hand, certain materials form ordered fluids when dissolved in a solvent (often water); these systems constitute the lyotropic liquid crystals. Materials that have this property are widely present in nature and include DNA, certain viruses, soap, etc. The liquid crystal phases that are exhibited

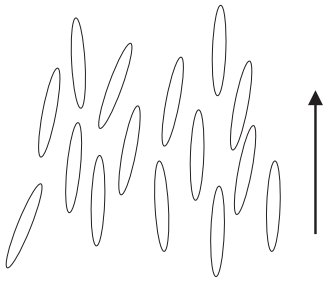

Figure 4.2: Ordering of molecules in the nematic phase.

depend on the concentration of the lyotropic solution as well as on the temperature. Certain materials can have both thermotropic and lyotropic liquid crystal phases. Obviously, this text will disregard the lyotropic systems, since they are not used in the opto-electronics industry.

4.1.2 Phases

The designation liquid crystal is still rather broad, as several phases (mesophases) can be distinguished within the state, with varying amounts and kinds of order present. The specific phase the liquid crystal is in will depend on temperature and the type of liquid crystal considered: some have only one phase, others can exhibit different phases as temperature changes.

Nematic phase

The nematic phase is the most common one. It always appears in the highest temperature range, so heating the liquid crystal above the nematic temperature range will cause it to become isotropic. Consequently, the nematic phase is the least ordered: there is only orientational ordering, no positional. This is visualised in the schematic drawing of figure 4.2.

The long axis of the molecules all point more or less in the same direction, no other restrictions are imposed, the molecules can float freely around. Note that the orientational alignment of the molecules is not rigid, only on average the molecules keep their axes locally parallel. The name for this phase (nematic = thread-like) stems from the thread-like defects that occur in this phase.

Smectic phases

Another very common phase, the smectic one, exhibits, besides the orientational ordering present in the nematic phase, also some kind of positional ordering. Several smectic phases exist, of which the smectic A and smectic C are

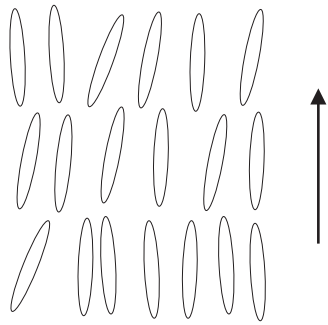

Figure 4.3: Ordering of molecules in the Smectic A phase.

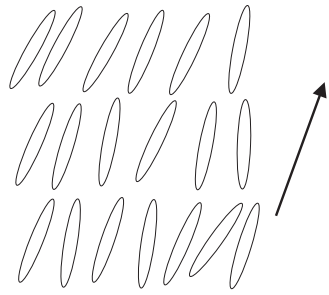

Figure 4.4: Ordering of the molecules in the Smectic C phase.

the most important. Smectic is the Greek word for soapy, which refers to the general appearance of this phase.

Smectic A Smectic A is the phase that occurs below the nematic temperature range, if the phase exists for the considered material. The difference with the nematic phase is an additional positional ordering in one dimension: the molecules are arranged in layers, as shown in figure 4.3. Within the layers they can move around, but translation across layers is very difficult. In a way, this can be considered a two dimensional fluid. As shown in the drawing, the director in the smectic A phase is orthogonal to the layer plane.

Smectic C Most materials having a smectic A phase, also have a smectic C phase at still lower temperatures. The main difference with the former phase is the tilted director: the molecules are not longer standing upright with respect to the layer plane, but have an inclination, see figure 4.4. The lower the temperature, the more the molecules tilt towards the layer plane.

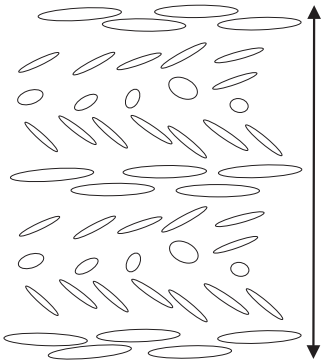

Figure 4.5: Ordering of molecules in a the chiral nematic phase. The arrow indicates the pitch.

Others As for the other smectic phases, they all show an even higher degree of ordering and crystallinity. Besides the ordering in layers, extra restrictions are imposed by the molecular packing. Most of these phases are of course very exotic and seldomly used.

4.1.3 Chirality

Some molecules are chiral: they lack mirror symmetry. Otherwise put, the mirror image of such a molecule cannot be made to look exactly as the original if only rotations are allowed. A simple analogon is a left and right glove. If the molecules of a certain liquid crystal happen to be chiral this will have some consequences on the way they will arrange themselves and hence on the macroscopic properties of the liquid crystal.

The chirality causes the molecules to arrange themselves in a twisted fashion, forming a helix . Note that this arrangement concerns the direction of the molecules, not the position: it is the local director that turns around. For liquid crystals with chiral molecules or liquid crystal mixtures with a chiral dopant added to them, the phases mentioned above get another name. The nematic phase is usually termed cholesteric, while the smectic phases get an asterisk appended to them, e.g Smectic A*.

Chiral nematic or cholesteric

In the cholesteric phase, the helix axis lies perpendicular to the local director, as shown in picture 4.5. Every half turn of the helix, the molecules are oriented the same way. The distance travelled along the helical axis for one full turn is called the pitch. If this pitch is in the range of the wavelength of visible light, interesting optical phenomena can occur.

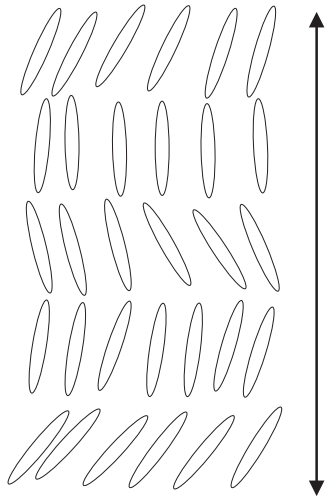

Figure 4.6: Ordering of the molecules in the chiral smectic phase. The arrow indicates the pitch.

Chiral smectic

In the smectic phase, the formation of a helix similar to the one in the cholesteric phase is normally not possible since within a layer no twist can be allowed; this would mean breaking the layer. The chiral nature expresses itself in a twist across the layers: the helical axis is perpendicular to the layer plane and the orientation of the molecules changes from one layer to the next, as illustrated in figure 4.6. Even for Smectic A* this produces a visible difference compared to Smectic A, apart from the change in physical properties. In a Smectic C* texture, it normally takes around a hundred layers to complete one revolution.

Materials with very high chirality may form additional phases in a very small temperature range close to the upper transition. These are so called frustrated phases, with very high concentrations of defects or dislocations.

4.1.4 Behaviour in electric fields

Almost all liquid crystal molecules are dipoles, or dipoles can be induced in the molecules by an electric field. Despite this, the mechanism behind the behaviour of liquid crystals in an electric field is most commonly not directly based on the torque exerted on such dipole.

In most liquid crystals, the molecules are organised in such way that the local dipoles compensate each other everywhere, forming a quadrupolar structure. On average there are always as much molecules head-up as there are head-down and this tendency is so strong it is even maintained in external

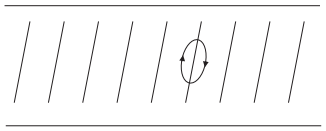

Figure 4.7: Rotational symmetry in a smectic C* layer.

electric fields, up to extremely high field strengths.

The fact that an electric field can turn the molecules in a particular direction is then based on the anisotropy of the molecules: the dielectric constant differs, depending on whether it is measured along the director or perpendicular to it. Normally the dielectric constant is larger along the director (positive anisotropy); for a constant dielectric displacement field minimisation of energy occurs if the larger dielectric permittivity gets in line with the applied field as much as possible, hence the orienting power.

The family of the polar liquid crystals however has a different orienting mechanism.

Polar liquid crystal

Ferroelectric LC For the smectic C* phase, it was demonstrated on symmetry grounds that a polarisation must exist parallel to the smectic layers and perpendicular to the director [40].

The smectic C* phase has a two-fold rotational symmetry along an axis perpendicular to the plane of drawing 4.7. A polarisation vector may go out or into this plane and remain unchanged under this two-fold rotation. Since there is chirality, this plane also cannot be a mirror plane and the polarisation can therefore not be cancelled out by reflection symmetry. Thus the symmetry of the smectic C* phase permits a polarisation perpendicular to both the tilt plane and the director.

The chirality ensures that the tilt direction precesses helically across the layers so that the polarisation also rotates, allowing the net macroscopic polarisation to remain zero. This is illustrated in figure 4.8. Thus, in the C* phase, within each layer the molecules will show a ferroelectric response, but the material as a whole is 'helical anti-ferroelectric' rather than ferroelectric.

Applying an electric field will ultimately align all polarisations of the layer and thus break the helix, but this is not the way these crystals are used in displays. It was found out that the formation of the helix can be suppressed by making the LC layer sufficiently thin (less than the pitch of the helix) and imposing an initial alignment with the outer substrates [41]. This yields the so-called bookshelf geometry, with the smectic layers perpendicular to the substrates and a net polarisation present between the substrates (figure 4.9).

These surface stabilised ferroelectric liquid crystal devices (SSFLC) based

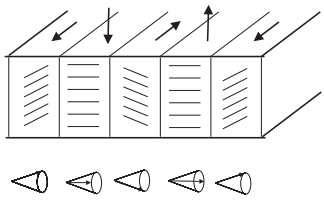

Figure 4.8: Helical arrangement of resulting dipole moments per layer in ferroelectric liquid crystal.

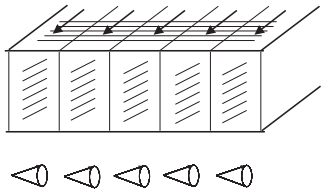

Figure 4.9: Bookshelf arrangement in ferroelectric liquid crystal.

on the bookshelf geometry are bistable and can be switched between the two possible polarisation states (up or down) in a very fast way. Typical times for switching from one state to the other are in the microseconds range. This is the main advantage of all ferroelectric devices.

The bistable nature however necessitates the use of digital driving. This can be considered advantageous from the point of view of the driving electronics, as digital circuits are in general smaller, cheaper and easier to design. On the other hand, creating grey levels with a bistable device can only be accomplished with pulse-width modulation techniques, which complicates the circuitry and can introduce optical artifacts. Despite major research efforts, both the available materials themselves and the manufacturing techniques are still not mature.

Anti-ferroelectric LC The anti-ferroelectric ordering can be thought of as a ferroelectric one where the pitch of the helix is reduced such that there is already a half turn by proceeding from one layer to the next. Consequently, there is no real helical structure anymore: the tilt simply reverses for each layer, thereby cancelling the polarisations present in the layers [42], see figure 4.10.

In this arrangement no macroscopic polarisation is present anymore, which can be advantageous in some cases. The configuration is now tristable . Special arrangements can make this device suitable for analog addressing, resulting in the so-called V-shape switching [43]. Apart from the analog driving in the case of the V-shape switching, the anti-ferroelectric materials suffer from the same drawbacks as the ferroelectric ones.

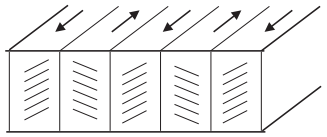

Figure 4.10: Configuration of anti-ferroelectric liquid crystal.

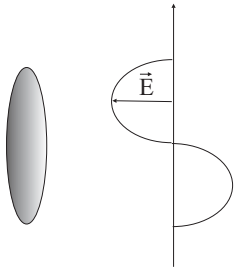

Figure 4.11: Ordinary index of refraction

4.1.5 Optical behaviour

The anisotropy encountered in the electrical behaviour, namely the dependence of the dielectric constant upon the direction it is measured in, also extends into the optical frequency range. This enables liquid crystals to modulate light in various ways. The anisotropy also implies that the molecules have an optic axis and thus behave like a uniaxial optically birefringent crystal. Although it is not strictly necessary, the optic axis almost always coincides with the director.

If light travels along the optic axis, the refractive index is given by: $n_o = \sqrt{\epsilon_\perp(\omega)}$ where $\epsilon_\perp(\omega)$ should of course be the dielectric constant for frequencies in the optical range.

Note that the correct dielectric constant to be used is the one measured for a field perpendicular to the director, since light is a transverse wave; the field vectors are perpendicular to the propagation direction, as illustrated in figure 4.11. This refractive index, for light travelling along the director, is termed the ordinary index.

For light travelling perpendicular to the director and polarised parallel to it (figure 4.12), the refractive index becomes $n_e = \sqrt{\epsilon_\parallel(\omega)}$ and is called extraordinary index.

Any other combination of polarisation and travel direction can be decomposed into the above two cases, where-after the effective refractive index for the situation considered can be calculated. This can be visualised by using the ellipsoid of refractive indices or indicatrix (see figure 4.13).

The indicatrix consists of an ellipsoid of which the length of half the long axis has been normalised to the value of the extraordinary index, while the

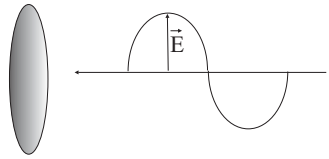

Figure 4.12: Extraordinary index of refraction

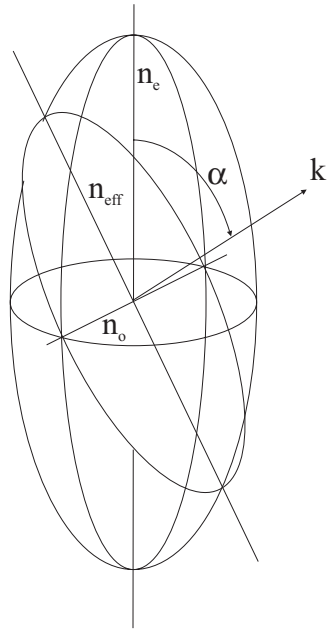

Figure 4.13: Ellipsoid of refractive indices.

length of half of the other axis is normalised to the value of the ordinary index. The ellipsoid represents the molecule in a certain way: the long axis points along the director. The vector $\vec{h}$ represents the direction of propagation of the light.

To determine the desired effective refractive index, a plane is inserted through the centre-point of the ellipsoid and perpendicular to $\vec{h}$. The intersection of this plane with the ellipsoid will be an ellipse, having a short half-axis with length n_o and a long half-axis with length n_e^{eff}, exactly the effective index of refraction for light polarised along this axis and travelling in the direction of $\vec{h}$. This geometrical construction can of course be translated in algebraic terms, the expression for n_e^{eff} is given by (4.2).

$$n_e^{eff}(\alpha) = \frac{n_e n_o}{\sqrt{n_o^2 + (n_e^2 - n_o^2)\cos^2\alpha}} \tag{4.2}$$

As such the phase velocities of light entering under any angle and having any kind of polarisation can be determined. The component of the electrical field vector along the direction of the ellipse's long axis deals with refractive index n_e^{eff} and thus has phase velocity $\frac{c}{n_e^{eff}}$, the other component encounters n_o and has phase velocity $\frac{c}{n_o}$.

Jones calculus

To calculate the behaviour of polarised light through different media, the compact Jones calculus is often used [44]. Consider the scalar equation for a planar harmonic electrical wave as in (4.3),

$$E(t,\vec{r}) = E_0 \cos\left(\omega t - \frac{\omega \vec{r}\vec{m}}{c_m} + \delta\right) \tag{4.3}$$

where c_m is the speed of light in the considered medium and $\vec{m}$ is a unit vector indicating the propagation direction. Often the wave vector $\vec{k}$ and wavenumber $k = |\vec{k}|$ is defined as in (4.4),

$$\vec{k} = \frac{\omega \vec{m}}{c_m} \tag{4.4}$$

so (4.3) becomes (4.5).

$$E(t,\vec{r}) = E_0 \cos\left(\omega t - \vec{k}\vec{r} + \delta\right) \tag{4.5}$$

Introducing complex notation, this can be transformed into (4.6).

$$E(t,\vec{r}) = E_0 Re\left(e^{i\omega t} e^{i\delta} e^{-i\vec{k}\vec{r}}\right) = E_0 Re\left(A_1 A_2 e^{-i\vec{k}\vec{r}}\right) \tag{4.6}$$

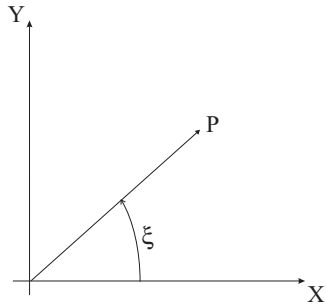

Figure 4.14: Phasor in X-Y reference system.

For a given wave, A_1 and A_2 are constant, so they are not essential for the calculation. What is left is a complex phasor of the form (4.7).

$$P = E_0 e^{-i\vec{k}\vec{r}} \tag{4.7}$$

If a reference axis system is introduced as in figure 4.14, then the two components along these axes can be written as in (4.8).

$$\begin{aligned} P_x &= E_0 \cos(\xi) e^{-i\vec{k}\vec{r}} = E_x e^{-i\vec{k}\vec{r}} \\ P_y &= E_0 \sin(\xi) e^{-i\vec{k}\vec{r}} = E_y e^{-i\vec{k}\vec{r}} \end{aligned} \tag{4.8}$$

These two components can be combined in a column vector (4.9), the Jones vector, which completely describes the light wave.

$$\mathbf{J} = \begin{pmatrix} P_x \\ P_y \end{pmatrix} \tag{4.9}$$

If the light beam hits an anisotropic medium, the wave vector $\vec{k}$ will be different depending on the orientation of the $\vec{E}$ field vector. Suppose the reference axes are aligned with the chief directions of the uniaxial anisotropic medium, then the Jones vector of the light after passing through the medium can be calculated as in (4.10).

$$\mathbf{J_{exit}} = \begin{pmatrix} P_x e^{-i\vec{k_x}\vec{r}} \\ P_y e^{-i\vec{k_y}\vec{r}} \end{pmatrix} = \begin{pmatrix} e^{-i\vec{k_x}\vec{r}} & 0 \\ 0 & e^{-i\vec{k_y}\vec{r}} \end{pmatrix} \begin{pmatrix} P_{x,entry} \\ P_{y,entry} \end{pmatrix} \tag{4.10}$$

In this way, the optical activity of any medium can be represented by 2×2 Jones matrix. If the properties of the medium vary as the beam travels through it, the layer can be sliced into thin sub-layers in each of which the properties

remain constant. If the reference axes are not oriented in the most convenient way, a coordinate transformation can be applied by left-multiplying the Jones matrix with an appropriate transformation matrix and right-multiplying with the one that transforms it back to the original reference system. Rotation from one coordinate reference into the other can be achieved by the rotation matrix $R(\alpha)$ in (4.11) which performs a counterclockwise rotation over α radians.

$$\mathbf{R}(\alpha) = \begin{pmatrix} \cos(\alpha) & \sin(\alpha) \\ -\sin(\alpha) & \cos(\alpha) \end{pmatrix} \tag{4.11}$$

The simple Jones calculus outlined above is only valid for perpendicular incidence and it does not take any reflections at interfaces into account. Modifications have been proposed, leading to extended Jones matrices [45, 46] that can deal with oblique incidence. A full description of all phenomena, including multiple reflections is offered by the 4×4 Berreman method [47].

4.2 Modes

4.2.1 General

The larger part of the optical applications of liquid crystal is in some way based on their birefringence. The most notable exceptions are the dye-doped modes or Guest-Host systems [48], which rely on the absorptive nature of foreign dopants. The others use birefringence in several, sometimes very ingenious ways, including use as a tunable phase retarder (ECB), employing the polarisation rotation effect (TN, STN), a combination of both (MTN), exploiting Bragg-reflection at repetitive structures (cholesteric texture) or scattering at randomly aligned molecules (PDLC).

The working principle of virtually all modes assumes that an initial alignment can be imposed upon the liquid crystal molecules, i.e. even in the absence of electrical fields the director must be predetermined and uniform throughout the cell. This is achieved by putting special alignment layers on the substrates constituting the cell. See the chapter on liquid crystal alignment for more details.

Survey of modes

The upcoming paragraphs contain short descriptions of a selection of modes. They serve as background material to clarify and justify the choice of the vertically aligned mode for this research.

Only modes that are based on nematogens have been retained, based on the considerations outlined in the paragraph on ferroelectric liquid crystals. Even within the nematic liquid crystals, the selection is not at all exhaustive.

Emphasis is of course laid on modes that are suitable for use in projection environments, although this is a somewhat fuzzy criterion.

Both transmissive (if appropriate) and reflective operation are considered. In general, a reflective cell can be treated as a transmissive one with double cell-gap and an additional jump of 180 ° in the phase angle of the light wave. For optimal performance, it is however advisable to take the reflective nature directly into account. Therefore, some modes are specifically designed for one type of operation and do not work very well in the other.

Mathematical description

For a number of reflective modes a mathematical description and classification based on the Jones Matrix formalism can be performed after Yang and Lu [49]. The Jones matrix they use is shown in (4.12).

$$\mathbf{J}(\Phi,\beta) =$$

$$\begin{pmatrix} \left(\frac{\Phi}{\gamma}\right)^2 + \left(\frac{\beta}{\gamma}\right)^2 \cos 2\gamma - i\left(\frac{\beta}{\gamma}\right)\sin 2\gamma & \frac{-i\Phi\beta(1-\cos 2\gamma)}{\gamma^2} \\ \frac{-i\Phi\beta(1-\cos 2\gamma)}{\gamma^2} & \left(\frac{\Phi}{\gamma}\right)^2 + \left(\frac{\beta}{\gamma}\right)^2 \cos 2\gamma + i\left(\frac{\beta}{\gamma}\right)\sin 2\gamma \end{pmatrix}$$

$$\beta = \frac{\pi d \Delta n}{\lambda} \qquad \gamma = \sqrt{\Phi^2 + \beta^2} \tag{4.12}$$

The parameter Φ is the twist angle, measured from the top to the bottom substrate and positive if counterclockwise. The retardation parameter β is of course voltage dependent. To make the description complete, a third parameter Ψ is needed, defining the angle for the polarisation direction of the incident light. It is measured from the LC director at the side where the light enters and is considered positive if counterclockwise (see figure 4.15).

With this Jones matrix, the polarisation conversion function can be computed. This function describes how the intensity of the light output varies with the LC parameters, assuming a proper linearly polarised beam is used as input and the reflected light is analysed by a polariser with polarisation orientation perpendicular to the input. The maximum of this function in the considered operation interval is the Polarisation Conversion Efficiency (PCE), a measure of how much of the polarised input light can actually be used as output.

Finally, to be complete, equation (4.13) formally defines the contrast ratio in terms of the minimum and maximum light intensity transmitted or reflected by the cell.

$$CR = \frac{I_{max}}{I_{min}} \tag{4.13}$$

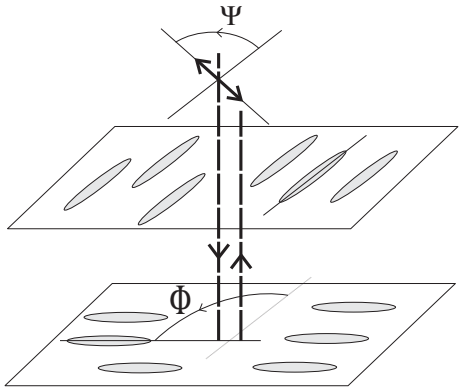

Figure 4.15: Illustration of the definition of the parameters used in the Jones matrix (4.12), describing the behaviour of some reflective liquid crystal modes. Polarised light enters from the top and is reflected at the bottom substrate. The polariser angle Ψ is measured between the orientation of the top liquid crystal molecules and the polarisation plane. The twist angle Φ is measured between top and bottom orientation of the liquid crystal molecules.

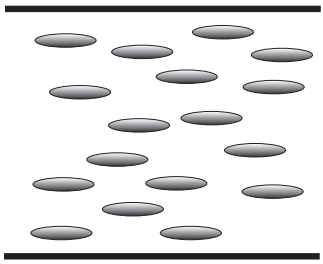

Figure 4.16: Homogeneous alignment.

4.2.2 Untwisted modes

Homogeneous

This is probably the most simple way of making practical use of the liquid crystal properties and therefore also one of the oldest [50]. The transmissive cell, which is composed of the symmetrical stack polariser - glass - LC layer - glass - polariser, is usually termed Freedericksz cell.

The molecules in the LC layer are aligned parallel to the substrates (figure 4.16) and make a 45 ° angle with respect to the optical axis of the polariser. A small pre-tilt of 1 ° to 5 ° away from the substrate plane is usually added to make sure the molecules all tilt in a known direction if an electrical field is present.

If no field is applied, light rays will be linearly polarised by the first polariser

and then be split in two distinct modes, with equal amplitude but different phase velocities, since each mode deals with another refractive index. This speed difference results in a phase difference when exiting the LC layer given by (4.14).

$$\frac{2\pi\Delta nd}{\lambda} \qquad \begin{array}{l}\Delta n = n_e - n_o \\ d : \text{LC layer thickness} \\ \lambda : \text{wavelength}\end{array} \tag{4.14}$$

If the thickness of the cell is chosen so that (4.15) is satisfied, the recombination of the two modes upon exiting the LC layer shows that the original polarisation direction of the light has been turned by 90 °.

$$\Delta nd = \left(m + \frac{1}{2}\right)\lambda \qquad m = 0, 1, 2, \ldots \tag{4.15}$$

If the outer polarisers are parallel, all light will be blocked by the second polariser and the cell looks black. For crossed polarisers the light will easily pass and the cell will look white.

Application of an electrical field results in an reorientation of the molecules along the field lines, the molecules stand upright with respect to the substrate plane. The linearly polarised light entering the cell now passes the LC layer unmodified since no birefringence is present. Hence the polarisation direction of the light remains unchanged and light will pass in the case of parallel polarisers and be blocked in the case of crossed ones.

In reflective operation, the bottom polariser is replaced by a mirror. If a polariser is laminated on top of the cell, the cell is normally black. For projection applications, the polarising device usually is a polarising beamsplitter, which behaves as a pair of crossed polarisers, so the cell is normally white. In either case, (4.14) and (4.15) must be changed into (4.16) and (4.17) to accommodate for the double pass through the LC layer.

$$\frac{4\pi\Delta nd}{\lambda} \tag{4.16}$$

$$\Delta nd = \left(m + \frac{1}{2}\right)\frac{\lambda}{2} \qquad m = 0, 1, 2, \ldots \tag{4.17}$$

Referring to the parameters defined above, for this reflective mode we have $\Phi = 0\,°$ and $\Psi = 45\,°$. The polarisation conversion function can be obtained from (4.12) or, since the configuration is quite simple, be derived directly based on some insight in the physics of the device. It is shown in (4.18) and represented graphically in figure 4.17.

$$I = \sin^2\left(\frac{2\pi d\Delta n}{\lambda}\right) \tag{4.18}$$

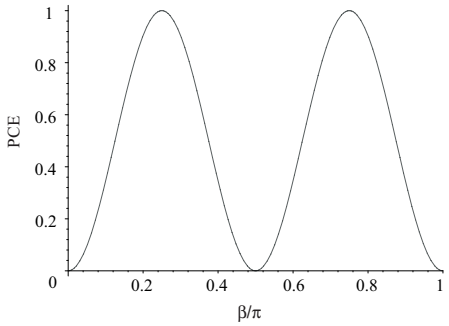

Figure 4.17: Polarisation conversion efficiency for the homogeneous and the homeotropic mode as function of $\frac{d\Delta n}{\lambda}$.

A PCE of 100 % is possible and the normally white cell is quite fast because it is thin (if $m = 0$ in (4.17)) but good contrast requires large voltages in order to eliminate the residual birefringence at the boundary layers as much at possible. It is also possible to make the cell normally black by having the cell thickness value satisfying (4.19) instead of (4.17). The contrast ratio however remains problematic, since now the cell-gap tolerance becomes very small: the slightest deviation of either cell thickness or wavelength will cause considerable light leakage in the dark state.

$$\Delta nd = \left(m + \frac{1}{2}\right)\lambda \qquad m = 0, 1, 2, \ldots \tag{4.19}$$

Homeotropic

The natural counterpart of the homogeneous cell is the homeotropic cell, also known as Vertically Aligned Nematic cell (VAN), or Deformation of Aligned Phases (DAP).

The initial orientation is now perpendicular to the substrates, again with a small pre-tilt (fig 4.18). Upon application of an electric field, the molecules must now tilt to a horizontal position, parallel to the substrates. This requires an LC material whose dielectric constant perpendicular to the director is larger than the one along, i.e. a negative dielectric anisotropy.

Homeotropic alignment is almost never used in combination with parallel polarisers, because its main strength, high contrast, is then completely wasted. With crossed polarisers, it is of course only suited for operation as normally black. Transmissive operation for direct view flat panel displays frequently employs the multi-domain technique to achieve wide viewing angles [51, 52, 53].

Equations (4.14), (4.15) and (4.16), (4.17) are still valid for transmissive and reflective operation, respectively, but (4.15) and (4.17) now both refer to normally black operation.

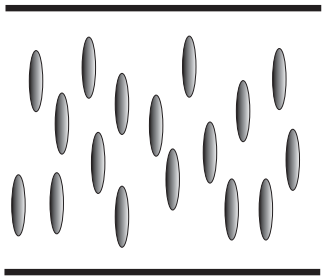

Figure 4.18: Vertical alignment.

Since the physics is the same, the polarisation conversion function is identical to the one for the homogeneous cell, so expression (4.18) and figure 4.17 can still be used. Combining (4.18) and (4.2) gives us an expression for output light intensity versus tilt angle. As the PCE is still 1 as well, the expression for the contrast ratio versus initial tilt angle is then as in (4.20).

$$CR = \frac{1}{\sin^2\left(\frac{2\pi d}{\lambda}\left(\sqrt{\frac{n_e n_o}{n_o^2+(n_e^2-n_o^2)\cos^2\alpha}} - n_o\right)\right)} \tag{4.20}$$

High contrast ratios are certainly achieved for initial tilt angles larger then 85 °. Additional advantages include a large tolerance for deviations in cell-gap and wavelength. The features of this mode are treated in detail further on in this chapter.

Optically Compensated Bend

The Optically Compensated Bend cell (OCB) [54], also known as π-cell, uses tilted parallel alignment whereby the tilt angles on both substrates converge, resulting in a bent LC director profile (fig 4.19). This mode features a very high response speed and has some inherent advantages for wide viewing angle applications [55, 56]. Instability can be a problem, since there is a second possible molecular configuration, the splay mode, where the molecules converge to a horizontal position in the middle of the cell. This may be a lower energy state, unless the pre-tilt is very high [57], which is not easy to realise or unless there is a bias voltage present, which is also an unfavourable solution. This mode is mostly used in direct view applications.

Hybrid Aligned Nematic

The Hybrid Aligned Nematic cell (HAN) uses a combination of the alignment conditions of homeotropic and homogeneous cells [58], see figure 4.20. It can also be considered as an OCB cell with a mirror put halfway the stack [59].

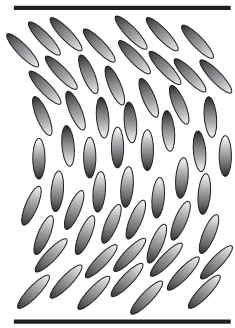

Figure 4.19: Pi cell alignment

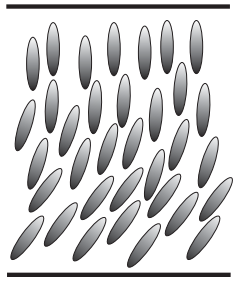

Figure 4.20: Hybrid alignment.

Consequently, this is the reflective counterpart of the OCB cell. The polarisation conversion function can easily be deduced by noting that the cell can be considered as a stack of homogeneous or homeotropic cells with constantly changing refractive index. So, (4.18) can still be used if Δn is replaced by $\frac{1}{2}\Delta n$. The cell is very fast, but both the normally white and normally black modes suffer from the same problems encountered in the homogeneous cell: high voltage requirements and the need for stringent cell-gap control [60].

4.2.3 Twisted modes

Instead of a homogeneously aligned cell where all molecule directors are oriented the same way throughout the sample, the directors can also be made to twist if moving from one substrate to the other. This enables the use of the polarisation rotation effect.

Twisted Nematic

The cell configuration is quite similar to the one of the Freedericksz cell, except that the initial orientations imposed at the substrates make a 90 ° angle with

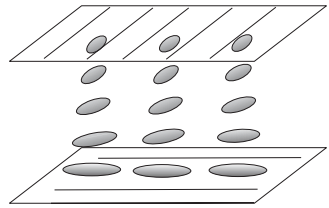

Figure 4.21: Twisted nematic alignment

respect to each other. The first polariser has its optical axis aligned with the director orientation at the first substrate.

Since the axis of birefringence is now constantly turning, the behaviour of light entering the cell is not so straightforward anymore and the calculation of the transmittance is a lot more complex.

For sufficiently thick layers that satisfy the Mauguin condition (4.21), it was shown that the polarisation direction of the light simply rotates along with the nematic director [61]. This is called the Polarisation Rotation Effect ; the liquid crystal layer acts as an optical waveguide.

$$\Delta nd \gg \frac{\phi\lambda}{\pi}, \qquad \phi\text{: twist angle} \tag{4.21}$$

If crossed polarisers are used, the cell will be normally white: without an electrical field the light will easily pass, since the waveguide effect turns the polarisation direction exactly the required quarter turn. In the presence of an electrical field, the molecules will re-orientate to a more or less vertical position. The wave-guiding function disappears and all light is blocked. With parallel polarisers the cell will off course be normally black.

Real displays are never made to meet (4.21), since it yields too thick and consequently too slow cells. A detailed calculation of the transmission of light through a TN cell was carried out by Tarry and Gooch [62] and yielded expression (4.22) for operation between parallel polarisers. It shows that thin cells can be used as displays, provided the cell thickness is correctly chosen.

$$T = \frac{1}{2}\frac{sin^2\left(\frac{\pi}{2}\sqrt{1+u^2}\right)}{1+u^2}, \qquad u = 2\frac{\Delta nd}{\lambda} \tag{4.22}$$

Most displays are either operated in the first or second minimum, i.e. d is chosen so that T is zero when no electric field is present. The first minimum appears for $\frac{\Delta nd}{\lambda} = \frac{\sqrt{3}}{2}$ and is named after Tarry-Gooch.

Together with the Super Twisted Nematic, the TN mode is probably the most widely used of all available liquid crystal modes. Its invention by Schadt and Helfrich [63] started the advent of liquid crystal displays in numerous

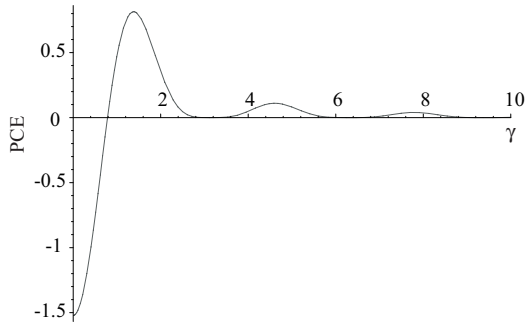

Figure 4.22: Polarisation conversion efficiency for the Hybrid Field Effect mode as function of the parameter γ

applications, culminating in today's abundant presence of e.g. flat panel laptop screens.

Super Twisted Nematic This is a variant of the normal twisted nematic, featuring a steeper response curve which makes it more suitable for passive addressing [64]. The twist angle is increased to somewhere in between 180 ° and 270 ° (most commonly 240 °), necessitating the use of chiral dopants to stabilise this high twist. The optimum cell thickness is proportional to the twist angle, so STN cells are relatively slow and thus not so suited for fast moving imagery.

Hybrid Field Effect For reflective operation, the classical twisted nematic cell is not very suited because of a very low PCE [65]. With a slight adaptation, reducing the twist angle to 45 °, a much better performance is obtained. This is the classic Reflective Twisted Nematic (R-TN), sometimes also called Hybrid Field Effect mode (HFE) which has been the standard choice for reflective devices for many years. In this case $\Phi = 45\,^\circ$ and $\Psi = 0\,^\circ$ or $90\,^\circ$. The polarisation efficiency function can be calculated using (4.12) and simplifies to (4.23). A plot of this function for varying γ is shown in figure 4.22. Since $\Phi = 45\,^\circ$, meaningful values of γ only start at $\pi/4$.

$$I = \left(1 - \frac{\pi^2}{16\gamma^2}\right) \frac{\pi^2 \sin^4 \gamma}{4\gamma^2} \tag{4.23}$$

A normally black mode can be achieved by choosing $\frac{d\Delta n}{\lambda} = \sqrt{\frac{15}{16}}$ so that $\sin \gamma = 0$, corresponding with the first minimum on figure 4.22. The cell-gap tolerance of this mode is rather large, as the polarisation function is pretty flat in the proximity of the minimum, so that reasonable contrast ratios can be obtained. On the other hand, the PCE is well below 100%, a serious disadvantage. The normally white version can be obtained by choosing $\gamma = 1.38339$

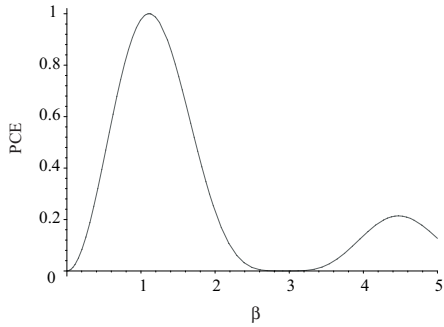

Figure 4.23: Polarisation conversion efficiency for the 63.6 ° twist mode as function of β

or $\frac{d\Delta n}{\lambda} = 0.3625$ corresponding with the maximum on the polarisation curve. This makes the cell faster because of the thinner cell-gap but requires high voltages to achieve acceptable contrast ratios. Furthermore, the PCE stays at the low value of 0.81.

Alternative twist angles Attempts to improve the PCE of the normally black HFE mode have been made by trying to optimise the twist angles. Several versions have been proposed [66, 67] resulting in 52.5 °, 53 ° and 54 ° twist modes. The penalty for this increased light output is usually a decrease in cell-gap or wavelength tolerance.

63.3 ° Twist mode

This mode is still quite similar to the 45 ° twist mode. Now $\Phi = \pi\frac{\sqrt{2}}{2}$ and $\Psi = 0\,°$or $90\,°$. The polarisation conversion function then looks as in (4.24) and is graphically shown in figure 4.23.

$$I = \Phi^2\beta^2\frac{(1-\cos 2\gamma)^2}{\gamma^4} \tag{4.24}$$

The most apparent improvement is the possibility of a PCE of 100 %. A normally black behaviour is obtained for $\frac{d\Delta n}{\lambda} = 0.935$ ($\beta = 2.937$), normally white if $\frac{d\Delta n}{\lambda} = 0.354$ ($\beta = 1.112$). The normally white mode has quite good cell-gap tolerance, but still requires high voltages to achieve good contrast ratio.

Mixed Twisted Nematic

In order to obtain a twisted reflective mode with characteristics as nice as the twisted nematic mode has in transmissive operation, a combination of the polarisation rotation effect and the birefringence effect was also considered.

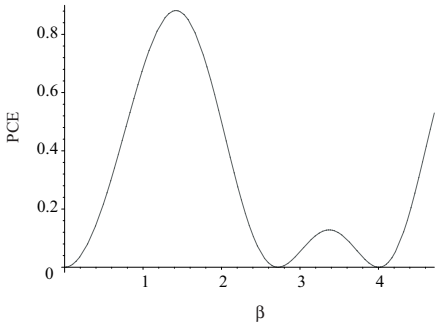

Figure 4.24: Polarisation conversion efficiency for 90 ° the Mixed Twisted Nematic mode as function of β

Such modes use a twisted configuration but generally operate below the Tarry-Gooch first minimum. Rotating the polarisers away from their position in the conventional approach then allows to use the birefringence effect as well.

The Mixed Twisted Nematic mode is the best known example of this approach. It has $\Phi = 90\,°$ and $\Psi = 20\,°$. In this case, the polarisation conversion function does not have a mathematically simple form anymore, but the plot has to be calculated directly from (4.12). It is shown in figure 4.24.

The MTN mode can be used as normally white by choosing $\frac{d\Delta n}{\lambda} = 0.45$ ($\beta = 1.412$)) and as normally black if $\frac{d\Delta n}{\lambda} = 0.866$ ($\beta = 2.721$). The latter is however seldomly used because the cell-gap tolerance is very poor. The normally white has better cell-gap tolerances and the low value for β results in very thin and thus fast cells. The main drawback is the PCE which is still no more than 0.88. Some adapted MTN modes have been proposed to correct this, resulting in 80 ° and 70 ° MTN modes, indicating the reduction of the twist angle. This way, a PCE of 97 % and almost 100 %, respectively, can be achieved, at the price of higher driving voltages.

Self Compensated TN

The Self Compensated Twisted Nematic (SCTN) is a variation of the MTN mode. The twist angle may vary between 60 ° and 65 °, but most of the time $\Phi = 60\,°$ is used. The input polarisation angle is determined as $\Psi = \frac{1}{2}\Phi$. The same considerations as for the MTN mode concerning the use of normally black and normally white apply. For normally white operation, $\frac{d\Delta n}{\lambda} = 0.62$ ($\beta = 1.948$) is chosen. The PCE has improved to almost 100 %, as shown in figure 4.25. On top of that, the driving voltage is very low, due to the self-compensating nature of this mode [68]. The cell-gap tolerance is however lower than for the normally white MTN.

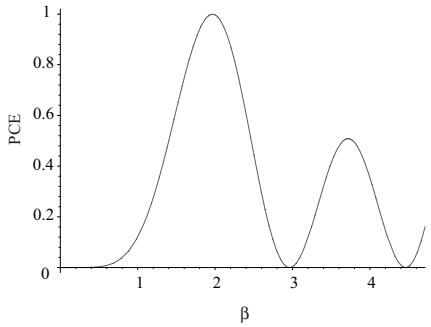

Figure 4.25: Polarisation conversion efficiency for the Self Compensated Twisted Nematic mode as function of β

4.2.4 Diffraction modes

All the modes listed above require that the input light beam is already polarised. This implies that, unless special measures are taken in the illumination optics, only half of the light of the source will actually be used. One way to overcome this limitation is by using liquid crystal phase gratings. In this case the liquid crystal layer is used as a tunable diffraction grating. In the transmissive version, the input light is sent through a first set of louvers, before being sent through the LC grating. If the grating does not diffract, the light is blocked by a second set of louvers. To let light pass, the grating has to be tuned so that it diffracts the light in between the second set of louvers. The reflective version is similar, except that one set of louvers suffices.

For the realisation of the phase grating with liquid crystal, several propositions have been made [69, 70]. The phase modulation is performed by one of effects listed above, usually the homogeneous or twisted nematic mode. Each pixel now contains at least two zones, one of which is addressable. Depending on the system, either inter-pixel electrodes or patterned alignment techniques are needed to achieve this. The first complicates the active matrix circuitry substantially, the second is still not common practice.

Diffraction modes are attractive because they are potentially very performant and can be inherently polarisation independent. Efficiently manufacturing the phase grating itself may be the obstacle that prevents its wide application on the shorter term.

4.2.5 Others

Cholesteric texture

This type of cell uses a single layer of a cholesteric liquid crystal, mostly with the helix axis perpendicular to the substrates. No polarisers are needed, but the

LC layer should be thick enough to accommodate for a fully periodic structure - the pitch must be small compared to the cell thickness. The periodicity of the alternating refractive indices in this structure can cause the occurrence of multiple constructive reflections within a certain wavelength band [71]. Only circularly polarised light with the same handedness as the helix is reflected. The exact position of the band where this Bragg-reflection occurs is determined by the refractive indices and the pitch p of the LC material: $n_o p$ and $n_e p$. Light waves with wavelengths outside of this band are absorbed by an absorber at the back of the cell. If an electrical field is applied, the molecules reorient in what is called the focal conic configuration, which is slightly scattering, thus effectuating a black state.

The properties of this mode make it hardly useful for projection: the thick LC layer makes the switching very slow, and very complicated high voltage waveforms are needed to reliably switch the liquid crystal from one state into the other [72, 73]. The bistable nature however makes it a very attractive system for low-power applications where the image data does not change frequently.

PDLC and PNLC

Polymer Dispersed and Polymer Network Liquid Crystal employ scattering as optical mechanism. They consist of a matrix of a polymer wherein small cavities are filled with liquid crystal.

The ordinary refractive index of the LC is matched with the one of the polymer, but the extraordinary index is highly different. Since in the absence of an electrical field there is no way to control the directors in the isolated LC drops, they tend to have a random distribution, turning the layer as a whole into a highly scattering medium. On the other hand, an electric field will align all directors, resulting in an optically inactive, transparent layer.

For reflective direct view operation, the scattering state is used as white, while the a perception of black is created either by putting an absorber behind the cell or, better, a mirror. In the case of the mirror, the light is specularly reflected away from the viewer, giving the impression of black. This works because the mirrors are very small [74].

For projection, the transparent state is used as white (the incident light is simply reflected into the projection lens). With Schlieren optics, the scattering state is turned into an effective black state on the screen.

Like the diffraction modes and the cholesteric texture, no polarisers are needed for this mode. A further advantage may be the ease of manufacture of PDLC layers, since alignment layers are also not required. Disadvantages are the need for the Schlieren optics, the response speed of the liquid crystal and the hysteresis on its electro–optical response.

Hitachi has a commercial XGA projector product on the market based on

this technology [6].

4.3 Features of the vertically aligned nematic mode

4.3.1 Introduction

Selection process

The benefits of a certain mode have to be outweighed to what is available in other modes. A choice for a certain liquid crystal mode is always a compromise, tailored to the needs of the specific application.

In this research, we concentrate on reflective devices for projection purposes. This already puts forward two criteria: contrast will be important and the mode should be fast enough to show live video imagery. The actual speed requirement is of course dependent on the colour-recombining architecture chosen. Additionally, it is advantageous if the mode has no inherent light loss.

The choice of LC mode is also tangled up with the way the electrical driving is envisaged to be, so with the design of the backplate. If for example the circuitry is to be fully digital, the only way of introducing grey scale values is by some form of pulse-width modulation, which may not be the optimal approach for some modes. Reversely, choosing for a classic ferro-electric liquid crystal automatically implies the use of pure digital driving.

The considered driving circuitry here is always a simple analog DRAM-like structure. This means the pixel matrix resembles a memory cell, with one transistor and one storage capacitor per pixel. At the write time, the pixel electrode is put at an analog voltage corresponding with a grey level via the transistor; during the rest of the frame time when the transistor is non-conducting, the voltage level is maintained by the combined capacitance of the storage and pixel capacitor .

Consequently, the voltage required to fully drive the pixels is also an important selection factor. Although, if the backplane is based on CMOS based integrated circuitry of a recent generation, it is virtually impossible to squeeze the full driving span of any LC mode into the maximum specifications of the IC, any reduction in voltage requirement can still be beneficial. Larger voltages are accommodated for by special high voltage transistors, which tend to be both more bulky and costly as the maximum voltage goes up.

Nematic liquid crystals are always driven with symmetrical pulses to avoid electrolysis of the material itself during operation. This means that for the simple DRAM structure considered here, the actual available driving voltage is less then half the maximum voltage specification of the IC technology. Special techniques to use the full span of a transistor by changing the external reference

voltage of the counter electrode (counter-electrode toggling) are possible, but result in more complicated circuitry. An example of such an advanced driving scheme is the so-called bucket-brigade pixel [75]. The use of more complicated circuitry can only be accounted for if the high-voltage transistors then actually become redundant, so the maximum needed modulation voltage remains important, even in the case of counter-electrode toggling.

For the different panel designs the final LC technology has been applied to, the available voltage ranges varied slightly, but all were capable of outputting at least a 12V signal on the pixel electrode.

Candidates

From the above, the selection criteria can be summarised as: analog addressing, modest addressing voltage (< 6 V), high contrast, high efficiency and fast response.

As already implicitly indicated above, the polar liquid crystals have been excluded quite early in the process. This is partly based on the analog nature of the backplane, partly on the manufacturing issues cited earlier and partly on the additional consideration that some of the problems associated with polar liquid crystals will be enhanced in the high light flux environment of a projector (image sticking, ionic content, ...).

Within the nematic family, the merits and drawbacks of the different modes have been briefly covered in the previous section. Of those, the modes that have already been considered for projection include PDLC, the reflective twisted nematic modes (RTN, MTN, SCTN), the hybrid aligned and vertically aligned mode.

From the short descriptions given above, there is already quite some indication that the vertically aligned mode will perform well on the formulated criteria. This is now further elaborated.

In the remainder of this section, the features of the vertically aligned mode are covered in more detail and compared to the other possible modes, in particular the Mixed Twisted Nematic mode, as it is in widespread use today.

4.3.2 Molecular tilt configuration

In principle, there are two possible configurations for a vertically aligned cell. In the first one, which is the most natural, the directions of the pre-tilt angle at the top and bottom substrates are anti-parallel, see figure 4.26. Analogously to the terminology used for homogeneous cells, this is called the 's'-configuration. If an electrical field is applied, there can be no doubt as to how all the molecules will tilt.

The alternative is to keep the tilt directions parallel, resulting in the 'p'-configuration as shown in figure 4.27. For the quiescent state, there is not much

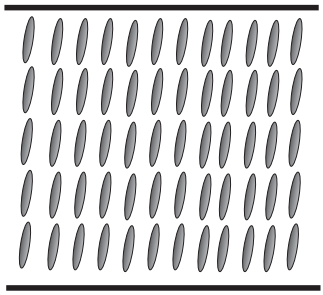

Figure 4.26: Molecular tilt distribution in the 's'-configuration.

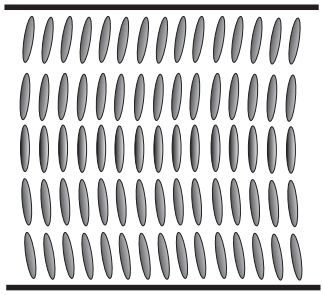

Figure 4.27: Molecular tilt distribution in the 'p'-configuration.

difference, the total birefringence will be a little less due to the presence of some truly vertical molecules. The behaviour when an electrical field is applied is however not obvious anymore. In figure 4.28 the results of a simulation of the electro-optical response curve for a cell in 'p'-configuration is shown. The curve is not very smooth and features a distinct jump.

More insight is obtained when looking at the evolution of the tilt and twist angle while the electrical field is applied. Figure 4.29 shows the local tilt and twist angles across the cell under these circumstances. The jump of the previous graph now translates into discontinuities in the tilt and twist distribution. At zero field, the slightly curved distribution of the 'p'-configuration can be recognised as the A zones in the graphs. The tilt of the molecules gradually increases towards the middle of the cell where it reverses (i.e the twist angle changes from $0\,^\circ$ to $180\,^\circ$) and decreases again to the value imposed by the alignment layer. When the field strength is increased, at first not much happens. The middle portion of the molecules tries to tilt, but since the top and bottom portion impose a tilt in the same direction, the middle molecules cannot move without introducing a mismatch (a disclination plane) over the entire cell surface. If the field becomes too strong, the distribution suddenly changes into a new equilibrium state, which is largely the 's'-configuration, but with a reversing of the tilt direction close to one of the substrates (zone B in the

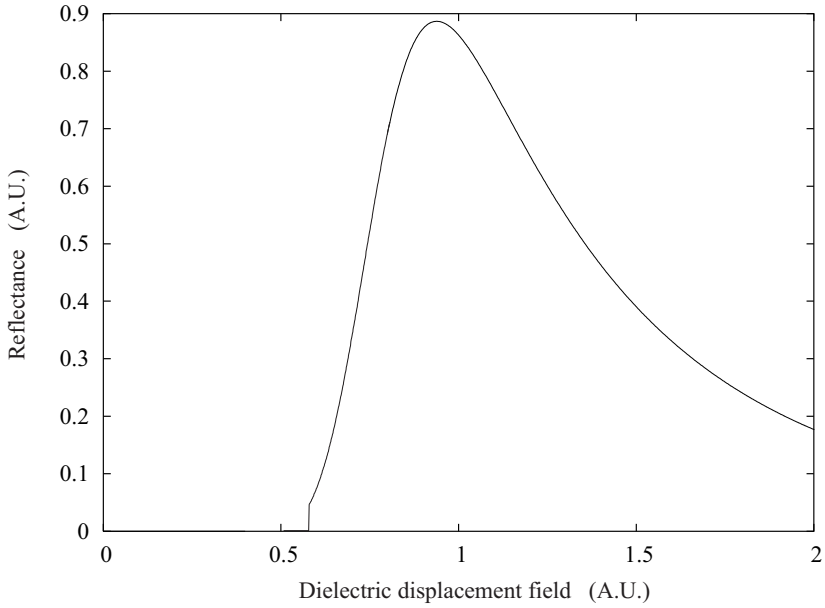

Figure 4.28: Simulated electro–optical response of a vertically aligned cell in 'p'-configuration for a 3 μm cell with MLC-6610 at 88 $^\circ$ pre-tilt and 550 nm wavelength. The discontinuity at the beginning of the slope is indicative of some instability.

graphs). Further increasing of the field strength can still push the location of the reversal a little bit more to the side.

The description above is based on results from simulation programs. These programs have their inadequacies, like the impossibility to treat disclinations correctly. Although the exact internal mechanism maybe therefore be somewhat different, it is clear that 'p'-configuration cells certainly have no advantages over the 's'-configuration. This coincides with experimental observations on some test cells. It is implicitly assumed that all vertically aligned cells are 's'-configuration.

4.3.3 LC layer thickness

The layer thickness is the crucial parameter for the optical behaviour of the stack once the mode has been chosen. The theoretical minimum value for which the optical activity can still be complete is dictated by the material properties. For the vertically aligned mode, equation (4.17) can be used, giving (4.25).

$$d_{min} = \frac{\lambda}{4\Delta n} \tag{4.25}$$

For the material used, MLC-6610, this comes down to 1.380 μm for 550 nm wavelength. The electro-optical response curve then looks as in figure 4.30.

A maximum value is not available on theoretical grounds; however, as the switching speed heavily depends on the layer thickness, it is advisable to keep the thickness as small as possible. Figure 4.31 shows a simulation of the expected electro optical curves for some layer thicknesses above the theoretical limit. With increasing layer thickness the transition from black to white becomes steeper and steeper and for 5.0 μm there is already a second maximum.

It may be quite clear that bigger layer sizes are not advantageous: besides the concern about switching speed, which will be dealt with in its own paragraph, it also becomes more difficult to get lots of grey values on a very steep curve. Very thin cells on the other hand complicate the assembly process and require larger voltages, especially for thicknesses near the theoretical minimum.

At the beginning of this research, the smallest spacer size that was available off the shelf was 3.0 μm, anything smaller required special orders and a premium price. From figure 4.31 it is clear that the 3.0 μm curve is certainly not a bad compromise: the steepness is acceptable, the modulation range is about 1 V and the maximum required voltage is very reasonable, 3.5 V should do. Considering this, the 3.0 μm LC layer thickness has been used throughout this research. Unless otherwise mentioned, the LC layer thickness is assumed to be 3.0 μm in the remainder of this text.

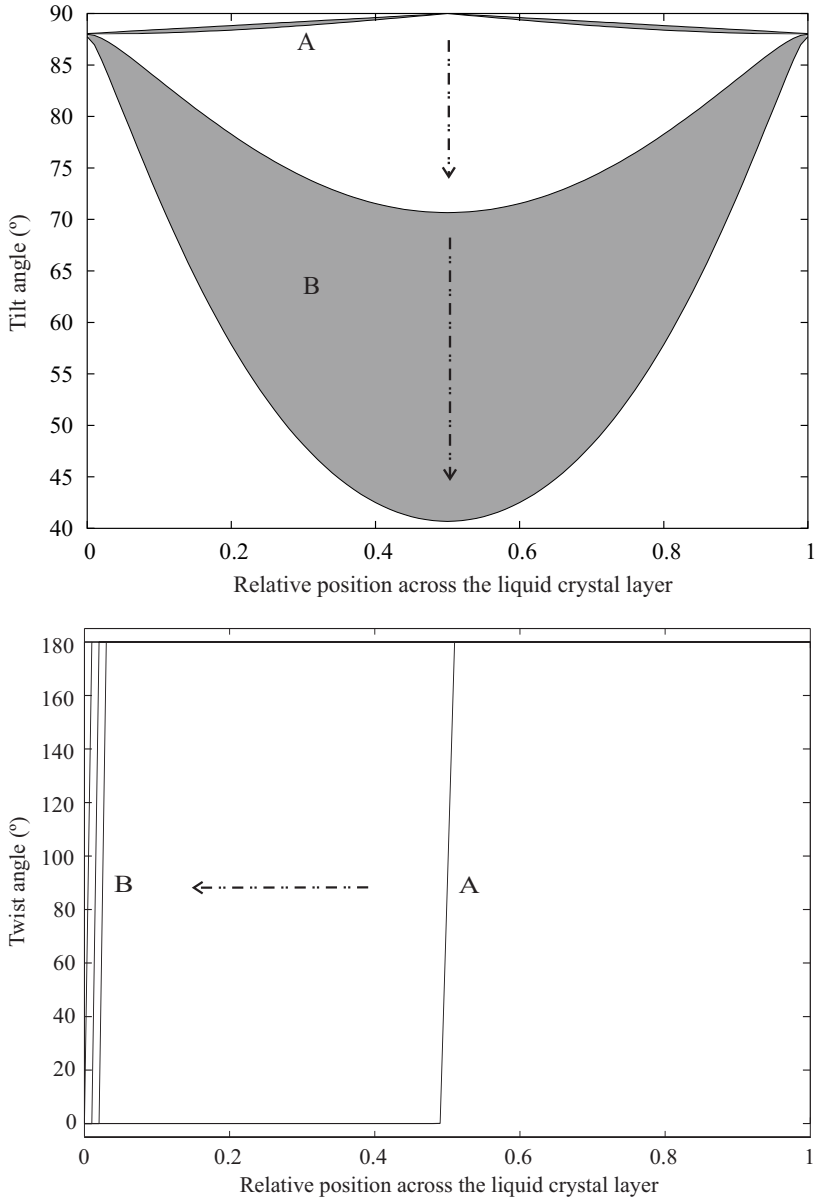

Figure 4.29: Tilt and twist angle distribution across the liquid crystal layer for a continuously increasing electrical field in a 'p'-configuration VAN cell. The original 'p'-configuration corresponds with zone A. Above a certain field strength the configuration suddenly jumps into a state corresponding with zone B, where the total amount of twist is concentrated at one side of the layer, leaving the rest of the layer in the 's'-configuration. The arrows indicate the progression with increasing electrical field. Simulation for MLC-6610.

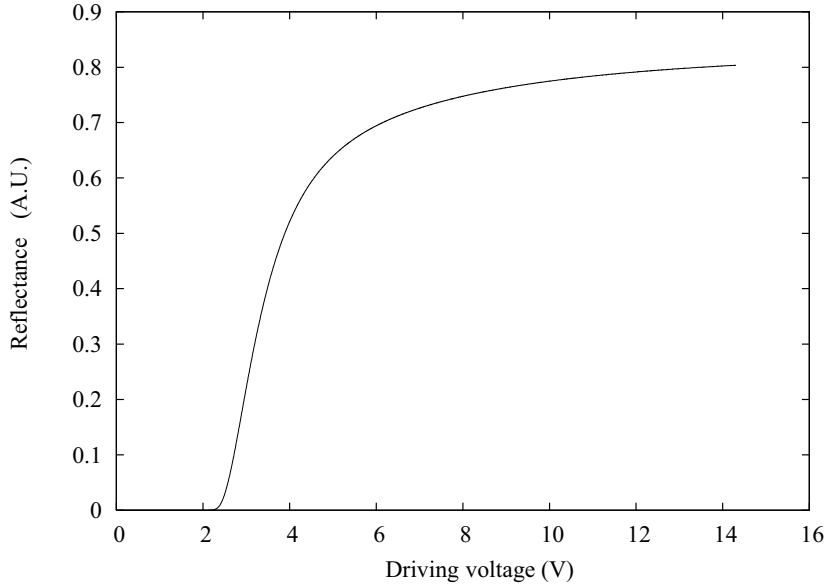

Figure 4.30: Simulated electro–optical response curve for a 1.380 μm thick MLC-6610 layer at 550 nm.

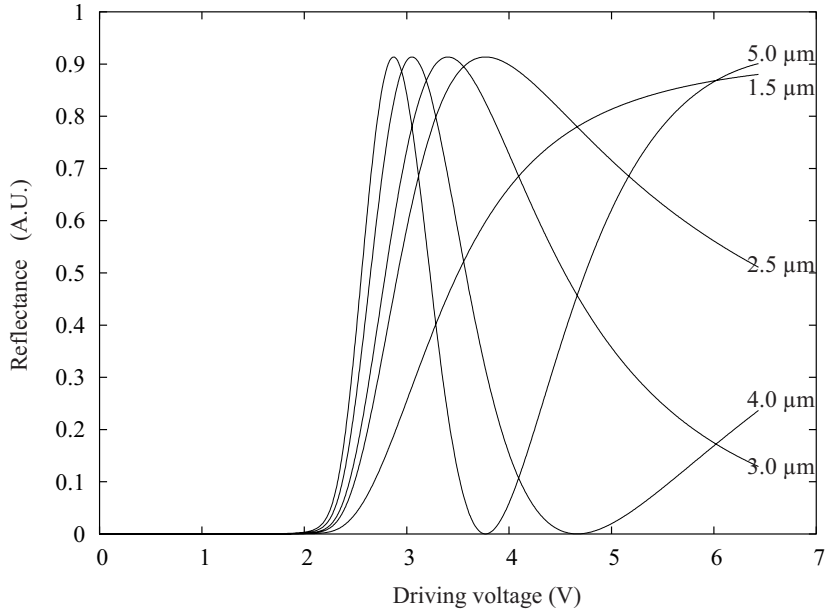

Figure 4.31: Simulated electro–optical response curves for different LC layer thicknesses.

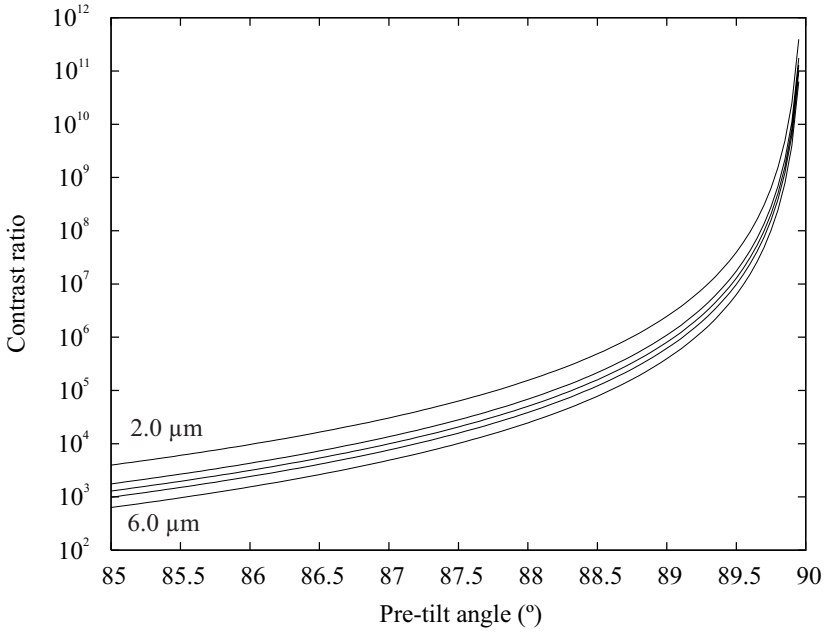

Figure 4.32: Calculated contrast ratio versus pre-tilt angle. Thickness of the LC layer ranges from 2 μm to 6 μm with 1 μm stepping. Calculation performed using the properties of MLC-6610, for perpendicular light incidence at 550 nm.

4.3.4 Contrast

The main strength of the vertically aligned mode is its achievement in contrast ratio. The virtual absence of residual birefringence in the black, un-driven state makes the contrast ratio for perpendicular light incidence almost only dependent on the quality of the polarisers. The only determining parameter here is the pre-tilt angle. Figure 4.32 shows how the contrast ratio for perpendicular incidence changes with pre-tilt angle, as calculated using (4.20).

Figure 4.33 shows basically the same information obtained from simulation. Because the simulation program takes the full stack (reflector - LC layer - glass) into account, the reflections at the glass interfaces are also considered and this explains the saturation of the contrast for pre-tilt angles larger than 89 °.

A good quality MacNeille PBS used in transmission can hardly achieve an extinction ratio of 5000:1 at perpendicular incidence [76], which means the VAN cell will most probably not be the limiting factor in on-axis contrast.

Changing the pre-tilt angle has some side effects. Figure 4.34 shows how the electro-optical response is influenced by a change in pre-tilt angle. The threshold voltage is reduced for lower pre-tilt angle values. Accordingly, the voltage for maximum brightness also shifts somewhat to the lower side. The

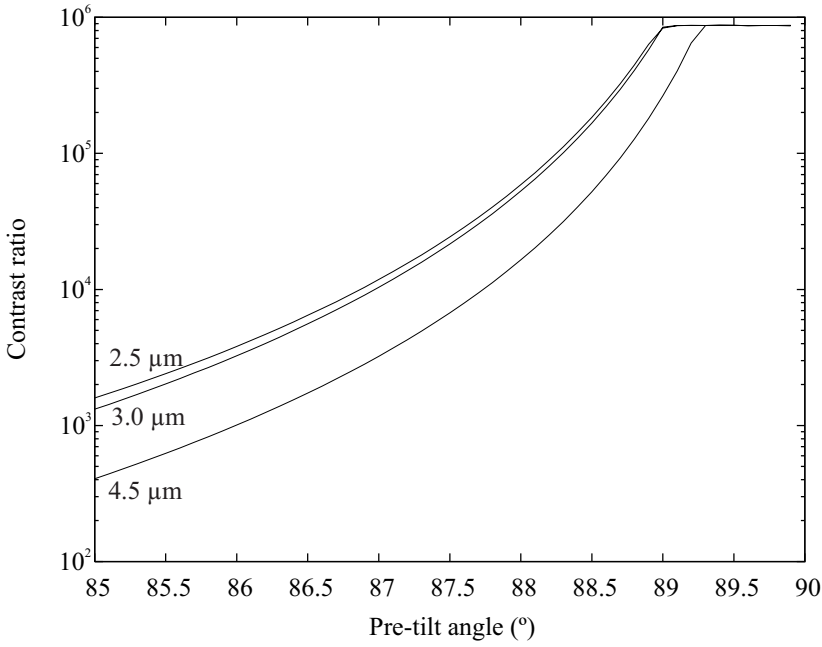

Figure 4.33: Simulated contrast ratio versus pre-tilt angle for a reflector - LC layer - glass stack. MLC-6610, perpendicular light incidence at 550 nm.

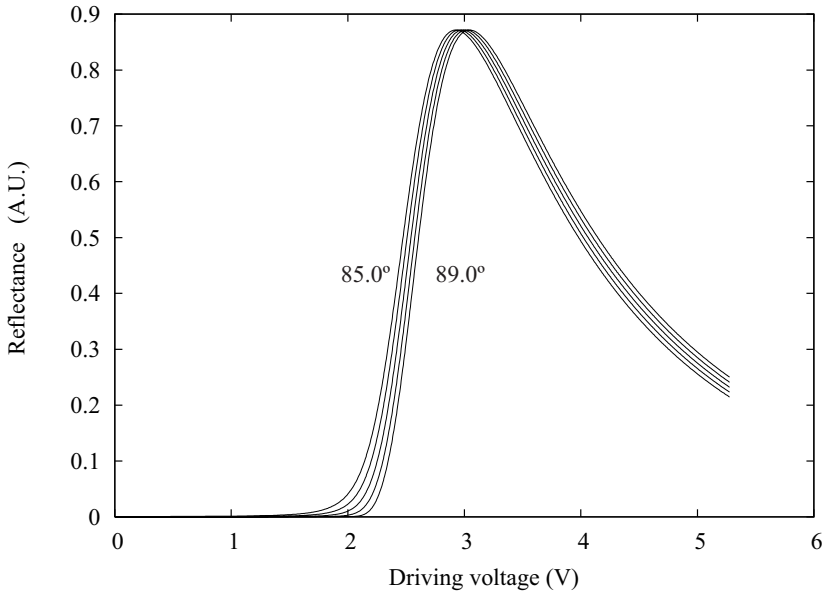

Figure 4.34: Simulated electro–optical response for pre-tilt angles varying from 85 ° to 89 ° with 1 ° stepping. MLC-6610, perpendicular light incidence at 550 nm.

response speed of the liquid crystal is also influenced by the pre-tilt angle (see further on). Lastly, the pre-tilt angle also plays a role in the occurrence of reverse tilt zones. This is also elaborated further on.

Realising a certain pre-tilt angle is the job of the alignment layer. These layers are treated in depth in a separate chapter.

Off-axis contrast Illumination with perfectly collimated light is the ideal case. In practice, high luminous flux over larger areas can only be achieved by allowing oblique rays. This will have its effect on the optical behaviour of the liquid crystal layer.

Some care must be taken when interpreting results from ray-tracing simulations involving oblique incidence and polarising components. Depending on the exact configuration of polarisers and analysers, some discrepancies between predictions can be encountered.

The configuration used in our simulation program is presented in figure 4.35. It basically assumes that the polariser and analyser are fixed to the light source and detector as they move around, which is a somewhat peculiar configuration for real projectors.

Furthermore, the intersection of the polarisation direction plane and the substrate plane is at a 45 ° angle. This represents the worst case scenario for the behaviour of the metal mirror with respect to polarisation preservation.

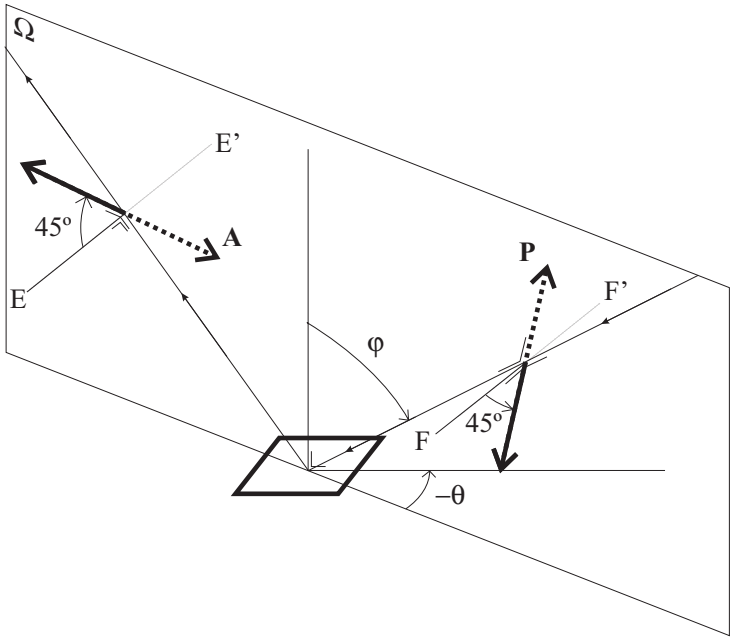

Figure 4.35: Arrangement of components used in the initial simulation of off-axis contrast. The incident light has azimuth angle θ and inclination angle φ. It is polarised by the polariser **P** which is oriented perpendicular to the propagation direction of the light and makes an angle of 45 ° with stretch FF', which itself is perpendicular to the plane of incidence Ω. The reflected light is analysed by the analyser **A**, which is oriented in a similar way, except that the 45 ° angle with stretch EE' is chosen such that the projection of **P** and **A** onto the base plane forms a cross.

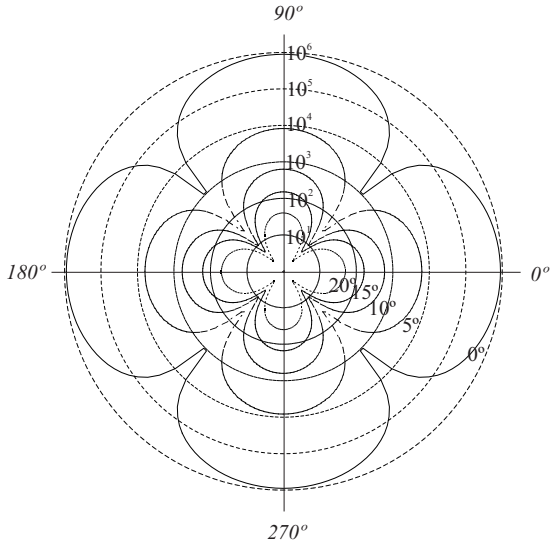

Figure 4.36: Polar contrast plot, showing contrast ratios for oblique incidence illumination. Contrast ratio is set out on the radial coordinate for varying azimuth angle as curves of equal inclination.

At this angle, even perfectly linearly polarised light will be reflected as slightly elliptically polarised. Consequently, if the incoming beam is already elliptically polarised, the ellipticity will be enlarged. Thus, this simulation setup does not represent very favourable conditions in this respect.

Figure 4.36 shows a simulation of how contrast changes with incidence direction. For a given inclination angle, the contrast value is set out on the radial coordinate while the azimuth angle varies.

It can be seen that contrast drops rapidly with inclination. Still, for an inclination of 15 °, the contrast ratio stays above 100:1 on average. The drop in contrast for odd multiples of 45 ° in azimuth angle at 0 ° inclination can be understood by looking at how the bright state is realised. In a vertically aligned cell, the bright state depends on the birefringence effect. When the polarisation of the incident light is parallel or perpendicular to the tilt plane of the liquid crystal molecules, the birefringence disappears and the bright state will be very dim. This is exactly what is happening in this configuration at 45 ° azimuth angle. The black state on the other hand is basically insensitive for azimuthal variations, so the contrast ratio inevitably decreases.

An alternative simulation configuration that mimics a projector environment a little better in some ways, is presented in figure 4.37. In all conventional optical engines one tries to keep the polarisation direction the same for all incidence angles, exactly what is done in this configuration. MacNeille polarising beamsplitters, the de facto standard components for polarisation management,

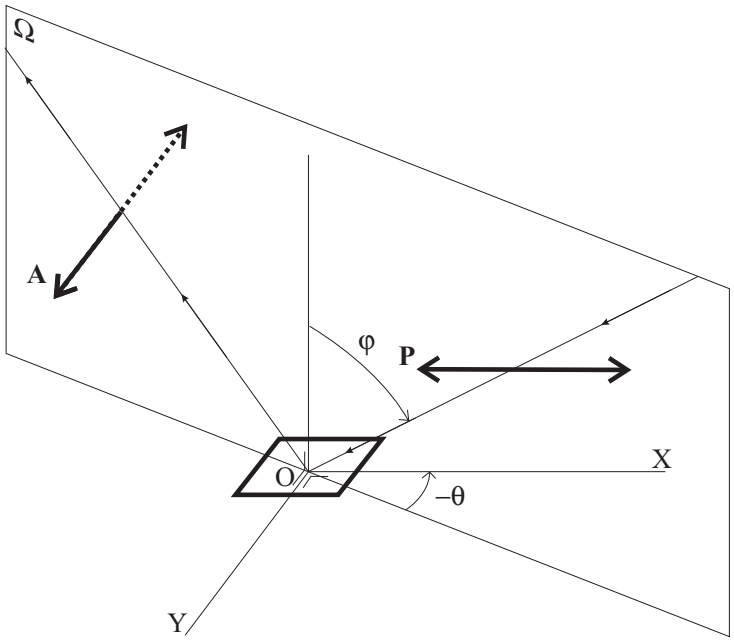

Figure 4.37: Alternative arrangement of components used for simulation of off-axis contrast. The incident light has azimuth angle θ and inclination angle φ. It is polarised by the polariser **P** which is parallel to the axis OX of the orthogonal reference axis pair OX,OY. The reflected light is analysed by the analyser **A** parallel to the axis OY.

are not perfect at this point [77], but are quite close to it. As an example, figure 4.38 shows the typical polarisation states produced by a McNeille polarising beamsplitter under oblique incidence. Very recently, an alternative PBS design even makes perfectly parallel polarisation directions for all incidence angles possible [78].

Calculations for the case of fixed polarisation direction using extended 2x2 Jones calculus have been presented by Armitage [79]. The result is shown in figure 4.39. The calculations assume that the bright state always has unity value.

Contrast still drops quite rapidly with inclination angle, but the geometry of the plot has changed somewhat. For an incidence angle of 15 °, which corresponds with an equivalent f/# number of 1.86, the contrast ratio now easily stays above 100:1.

Currently, an f/# number of 2.0 is about the lowest value considered for use in quality projectors. Knowing that the actual contrast measured on the screen is the integral over all possible incidence angles, it is clear that this value will be significantly higher than 100:1, probably close to 1000:1. For an f/# number of

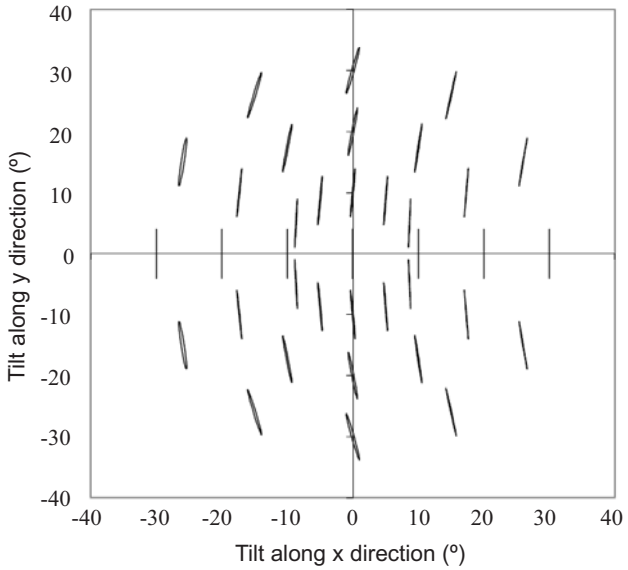

Figure 4.38: Polarisation states of the light for changing incidence angles after being reflected in a McNeille PBS. If the light is not perpendicular to the entrance face of the PBS, the polarisation state at the output is not perfectly linear anymore; it can become slightly elliptic and the polarisation direction can tilt somewhat. Picture courtesy of 3M Optical Systems.

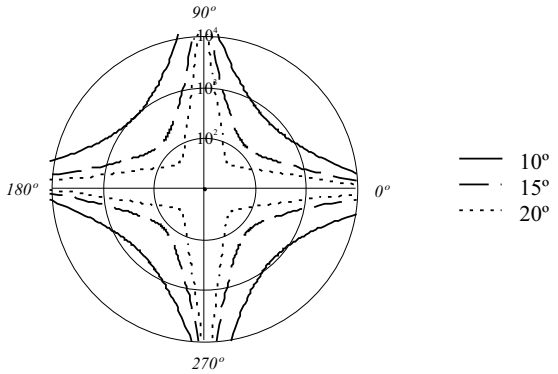

Figure 4.39: Polar contrast plot after Armitage, showing contrast ratios for oblique incidence illumination. Contrast ratio is set out on the radial coordinate for varying azimuth angle as curves of equal inclination..

3.0, the incidence angle is slightly less than 10° and the contrast almost always stays above 1000:1. Integrated contrast ratio would then probably be a few thousands, probably already beyond the limits if the optical system. If really needed, a compensation foil made of discotic crystals can further enhance the contrast ratio for oblique rays.

Other modes do not perform so well. The behaviour for oblique incidence is generally similar, and some wide viewing angle modes such as OCB or In Plane Switching even easily outperform VAN at this point, but the actual maximum (on-axis) contrast value that can be achieved is much lower. Reported contrast ratios for Mixed Twisted Nematic, the most obvious contender, are in the range of a few hundreds to one [80].

4.3.5 Voltage requirements

The voltage needed to drive the output intensity to its maximum is largely dependent on the liquid crystal layer thickness. In practice this thickness is set after outweighing the different factors involved: ease of manufacture, response speed and available driving voltage. Once this choice has been made, only the pre-tilt angle and the polar anchoring energy can still influence the voltage requirement. Both are a property of the alignment layer and are bound by the features of the alignment technique that will be employed. Especially the anchoring energy is not so easy to vary over a broad range.

In figure 4.34 the variation of the maximum voltage with the pre-tilt angle value was already shown. Figure 4.40 shows how the voltage changes with the anchoring energy. The covered range is broad, from truly rigid anchoring to low anchoring energies. From the two graphs, it can be concluded that the possible variations on the maximum voltage requirement will be relatively small.

The simulation of the electro–optical response takes only the liquid crystal layer itself into account. The actual voltage needed will be larger, since additional layers - such as alignment, reflection enhancement and transparent conductive layers - will cause additional capacitive and resistive voltage drops.

4.3.6 Response speed

Mathematical description

The reorientation speed of the liquid crystal molecules when an electrical field is applied depends on the elastic and viscous properties of the material. Due to the anisotropy, there are three elastic constants K_1, K_2, K_3, associated with the three basic forms of deformation in a uniaxial liquid crystal (splay, twist and bend). The viscous behaviour is usually described by a single parameter, the rotational viscosity. The differential equations describing the director motion in the one-dimensional case for a given dielectric displacement field are then as in (4.26) and (4.27) [81].

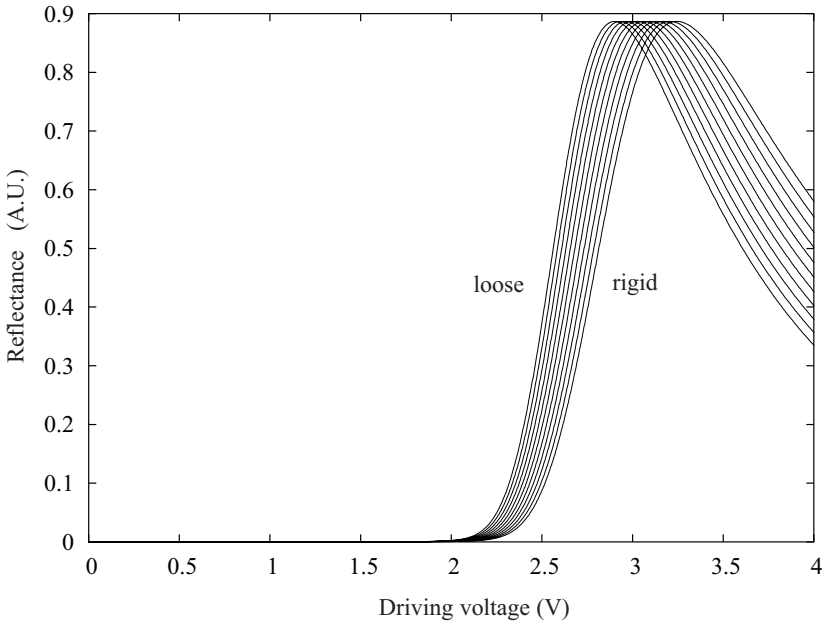

Figure 4.40: Electro–optical response curves for different anchoring energies. MLC-6610 with 88 ° pre-tilt angle. Energies vary from infinite (rigid anchoring) to 5×10^{-5}J/m

$$\begin{aligned}\gamma\frac{\partial\theta}{\partial t} &= \frac{1}{2}(K_3-K_1)\sin(2\theta)\left(\frac{\partial\theta}{\partial z}\right)^2 \\ &+\left((K_2-K_3)\cos^2(\theta)+\frac{K_3}{2}\right)\sin(2\theta)\left(\frac{\partial\phi}{\partial z}\right)^2 \\ &-K_2q_0\sin(2\theta)\frac{\partial\phi}{\partial z}+\left(K_1+(K_3-K_1)\sin^2(\theta)\right)\frac{\partial^2\theta}{\partial z^2} \\ &+\frac{D_z^2}{2\epsilon_0}\frac{\Delta\epsilon\sin(2\theta)}{\epsilon_\perp^2\left(1+\frac{\Delta\epsilon}{\epsilon_\perp}\sin^2(\theta)\right)^2}\end{aligned} \tag{4.26}$$

$$\begin{aligned}\gamma\frac{\partial\phi}{\partial t} &= (K_3-2K_2)\sin(2\theta)\frac{\partial\phi}{\partial z}\frac{\partial\theta}{\partial z} \\ &+\left(K_2+(K_3-K_2)\sin^2(\theta)\right)\frac{\partial^2\phi}{\partial z^2} \\ &+2\left(K_2q_0-K_3\sin^2(\theta)\frac{\partial\phi}{\partial z}\right)\tan(\theta)\frac{\partial\theta}{\partial z}\end{aligned} \tag{4.27}$$

K_i are the elastic constants, γ is the dynamic rotational viscosity, θ is the tilt and ϕ the twist angle, q_0 is the chiral pitch, D_z is the component of the dielectric displacement field along the cell normal, ϵ_0 is the dielectric permittivity in vacuum and z is the coordinate along the cell normal. Appropriate boundary conditions for the two substrate sides have to be added.

For a true vertical aligned cell there is no twist, so (4.27) is obsolete and (4.26) reduces to (4.28).

$$\begin{aligned}\gamma\frac{\partial\theta}{\partial t} &= \frac{1}{2}(K_3-K_1)\sin(2\theta)\left(\frac{\partial\theta}{\partial z}\right)^2 \\ &+\left(K_1+(K_3-K_1)\sin^2(\theta)\right)\frac{\partial^2\theta}{\partial z^2} \\ &+\frac{D_z^2}{2\epsilon_0}\frac{\Delta\epsilon\sin(2\theta)}{\epsilon_\perp^2\left(1+\frac{\Delta\epsilon}{\epsilon_\perp}\sin^2(\theta)\right)^2}\end{aligned} \tag{4.28}$$

A useful measure of comparison is the rise and fall time, usually defined as the time needed to switch from 10% to 90% of maximum brightness, or

the inverse. Derivation of expressions for a characteristic rise and fall time have been given in [82]. The resulting general expressions are very lengthy but for the vertically aligned mode they reduce to (4.29) and (4.30), with obvious notation.

$$T_r = \frac{\gamma d^2}{\pi^2 K_3} \frac{1}{\left(\frac{|\Delta\epsilon|}{\pi^2 K_3} V^2 - 1\right)} \qquad V > V_{th} = \pi \sqrt{\frac{K_3}{|\Delta\epsilon|}} \tag{4.29}$$

$$T_f = \frac{\gamma d^2}{\pi^2 K_3} \tag{4.30}$$

Since the restoring forces are strictly mechanical, the fall time is constant and is only determined by the elastic and viscous constants. The most important feature is the proportionality of the switching times to the square of the cell thickness d. Since material properties are generally not so easy to change, reduction of the cell-gap is the most straightforward way of obtaining faster cells. Of course, the minimum thickness is determined via Δn, which cannot be easily modified without in turn affecting the mechanical properties of the liquid crystal mixture.

Simulation

Simulations of the dynamical behaviour of liquid crystal are less accurate than the static ones. This is partly due to the fact that an accurate mathematical description of the fluid dynamics is very complicated, partly because even if the model is present, accurate data for the physical constants involved is not available. The discrepancy between simulation and measurements is therefore notorious. The simulations in this paragraph are thus only indicative.

Figure 4.41 shows the response of a standard cell to a voltage step at t = 10 ms as predicted by a model based on equation (4.28). The applied voltage corresponds to the one needed for maximum brightness. The apparent delay time reflects the time needed to get the molecules moving. If a logarithmic scale would be used on the Y-axis, the intensity change during this delay time would be obvious.

Advanced model

A more accurate model takes into account the flow effect that exists inside the cell when it is switched [83]. Such a model obviously includes a description of viscous flow; the anisotropy of the liquid crystal then implies that there exist several viscosity values, depending on the orientation of the molecule and the direction of flow. The model by Leslie and Ericksen [84, 85] provides such a description. For uniaxal liquid crystals it contains six so-called 'Leslie-viscosities' α_i that determine the behaviour of the fluid. Unfortunately, for

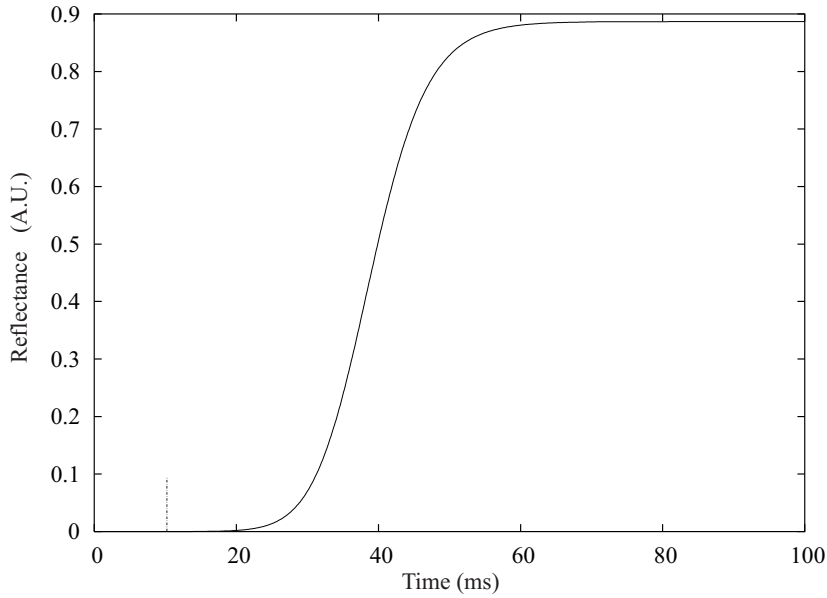

Figure 4.41: Optical response to a voltage step for maximum brightness at t = 10 ms. Simulated using a model based on rotational viscosity only. Pre-tilt angle 88 °.

most liquid crystals these coefficients are unknown and not easy to determine [86].

Some attempts to estimate these coefficients have been published in literature. The approximations proposed by Armitage and Larimer [87] allow to determine the most important of these shear viscosities. They use the Miesowicz viscosities [88], a more traditional but equivalent system. The Leslie coefficients and the Miesowicz viscosities are interrelated through the expressions in equation (4.31) [89]. Together with the Parodi relation [90] in (4.32), they allow to switch from one system to the other.

$$\begin{aligned} \eta_1 &= \frac{1}{2}(\alpha_4 + \alpha_5 - \alpha_2) \\ \eta_2 &= \frac{1}{2}(\alpha_4 + \alpha_6 + \alpha_3) \\ \eta_3 &= \frac{1}{2}\alpha_4 \\ \eta_{12} &= \alpha_1 \end{aligned} \tag{4.31}$$

$$\alpha_2 + \alpha_3 = \alpha_6 - \alpha_5 \tag{4.32}$$

Figure 4.42 shows a simulation of the response time using a model that

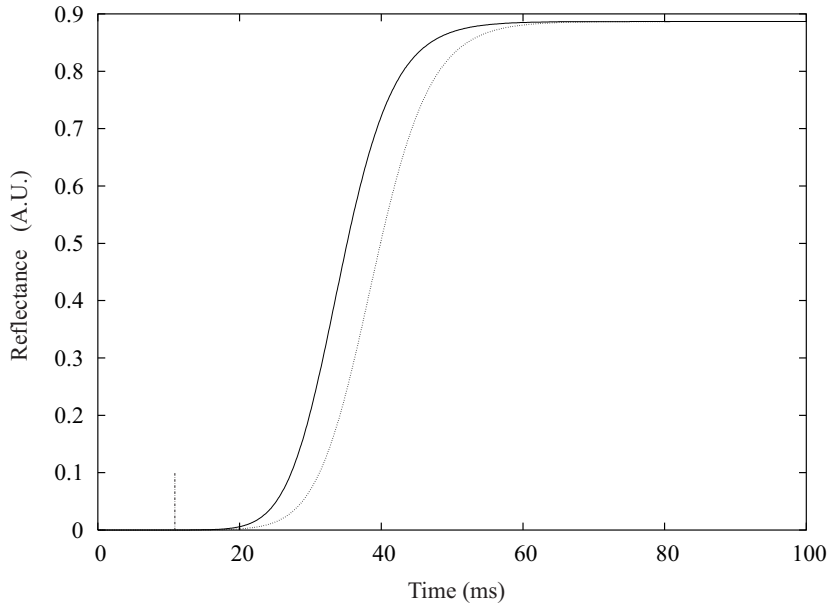

Figure 4.42: Optical response to a voltage step at t = 10 ms. Comparison between simulations using a model with viscous flow (solid line) and rotational viscosity only (dotted line). Pre-tilt angle 88 °.

incorporates shear viscosities. The dotted line is the original simulation, shown for comparison. The approximations are: $\eta_2 = \eta_{flow} = \nu_{flow} \cdot \rho = 20$ mPas, $\eta_1 = \gamma + \eta_2 = 168$ mPas, $\eta_3 = 2\eta_2 = 40$ mPas and $\eta_{12} = 0$. Here η_i are the shear viscosities, ν_{flow} is the kinematic flow viscosity and ρ is the density. Since the specific density of liquid crystals is very close to unity, the kinematic and dynamical viscosity are usually assumed identical. Numerical values are for MLC-6610.

The differences are significant. Using the 10 % to 90 % definition, a rise time of around 15 ms can be extracted. This of course disregards the delay time, which also accounts for 10 ms. The fall time can be extracted from figure 4.43. There is practically no delay in this case, and the fall time is around 6 ms.

An alternative approach to include flow effects in the dynamical model is to introduce a fictitious effective rotational viscosity that incorporates all effects. This makes it possible to keep the calculation one-dimensional, using the relatively simple equation (4.28). An expression for this effective viscosity is given in (4.33) [83].

$$\gamma_{eff} = \gamma - \frac{2\alpha_2^2}{\alpha_4 + \alpha_5 - \alpha_2} \tag{4.33}$$

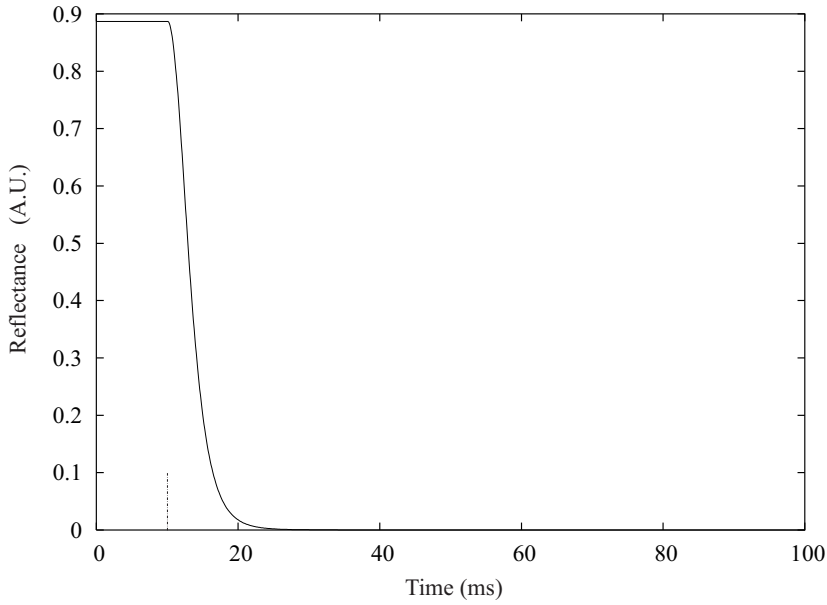

Figure 4.43: Optical response to a downward step at t = 10 ms. Simulation using the viscous flow model.

Application

Keeping in mind that the simulations are only indicative, it can still be concluded that the vertically aligned mode will be fast enough for displaying motion video. This assumes the panel is either operated in monochrome or the colour management system uses spatial separation instead of time separation techniques. Production of colour with the field or colour sequential technique is obviously next to impossible with the currently available liquid crystals, if the driving voltage is to be kept low. An advantageous factor in this issue is the fact that the temperature inside any commercial projector will always be higher than ambient, and the viscosities rapidly decrease with rising temperature (shear viscosities scale as $e^{\frac{E}{kT}}$, rotational viscosity as $Se^{\frac{E}{kT}}$ [91]).

Liquid crystals intended for the vertically aligned mode still have slightly higher rotational viscosity than conventional liquid crystals with the comparable dielectric and optical properties. This is due to the requirement of negative dielectric anisotropy, which is realised by putting a polar molecule group perpendicular to the molecular axis [92]. As this 'deforms' the molecule, making it less rod-like, the stability of the nematic phase is reduced and the protrusions increase the rotational viscosity. Research for better materials is in the hands of the few liquid crystal manufacturers. Recently, Merck announced some breakthroughs in their pursuit of fast negative anisotropy materials [93].

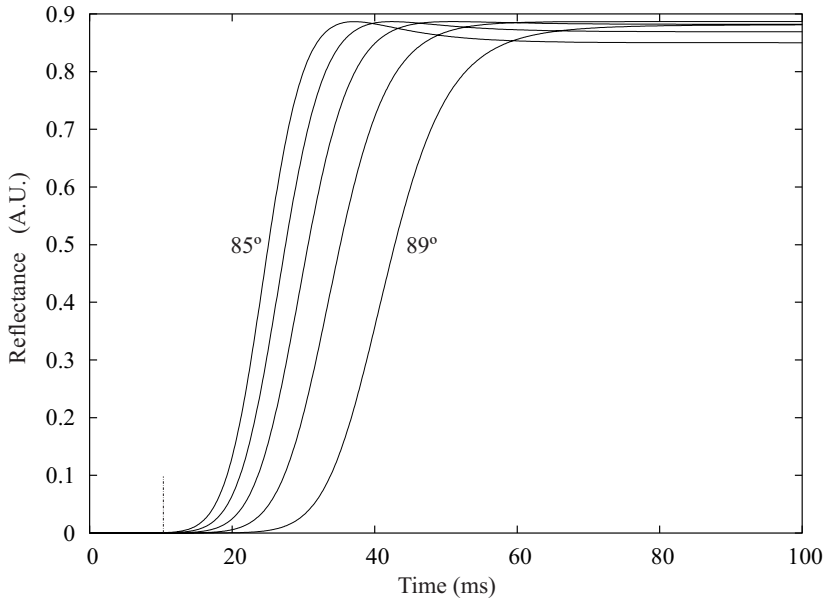

Figure 4.44: Influence of the pre-tilt angle on the response speed. The voltage step occurs at t = 10 ms and is identical for all curves. Simulation using the viscous flow model.

Of the materials available during this research, none actually allowed to have really thin cells while keeping the driving voltage low. Even the later introduced MLC-688X family is only slightly better, with rotational viscosity practically unchanged and birefringence only slightly higher.

Parameters

In the paragraph on contrast it was mentioned that the pre-tilt angle also has some influence on the response speed. Figure 4.44 shows how the response curves are altered if the pre-tilt angle changes. Lower values for the pre-tilt angle speed up the response. This is partly due to the steeper slope of the response curve, partly to the reduction of the initial delay time. Both result from the higher initial torque that is exerted on the molecules by the electrical field at lower pre-tilt angle values. A compromise between contrast and speed will thus have to be made.

As stated earlier, response speed is also highly dependent upon the cell thickness. Figure 4.45 shows the response speed of an MLC-6610 cell with the theoretical minimum thickness of 1.4 μm. To make a fair comparison, the same voltage step as for the 3.0 μm cell is applied. The rise time is greatly reduced, at the expense of a lower brightness. If the actually needed voltage step of

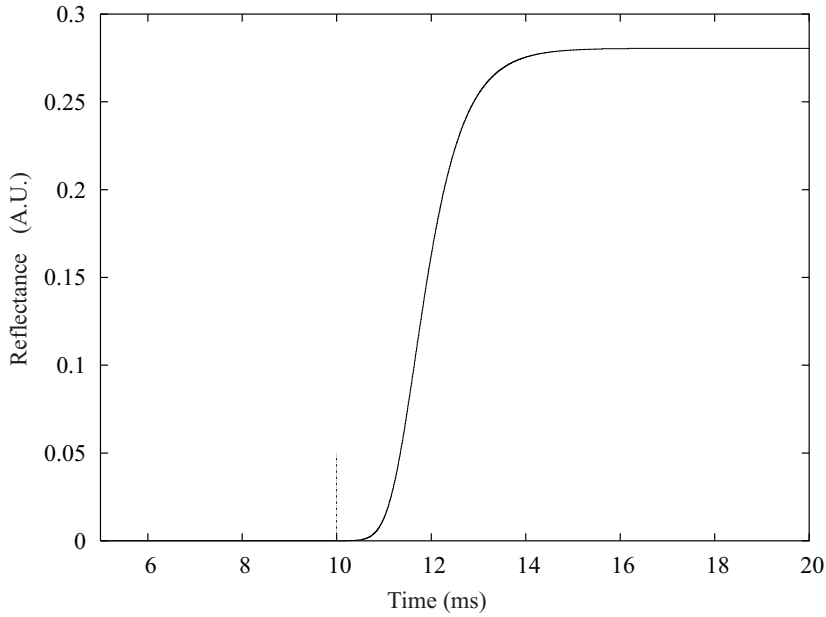

Figure 4.45: Optical response to a voltage step for a 1.4 μm MLC-6610 cell. Step magnitude (3.097 V) at 10 ms is for full brightness on a 3 μm cell. Pre-tilt angle 88 °.

around 12 V is applied, rise time becomes less than 1 ms.

Conclusion

Some modes are certainly faster than the vertically aligned nematic mode. Typical examples that are commonly used for projection include the MTN and HAN mode. Both are fast enough for field sequential addressing. Part of this faster reaction time is of course due to thinner cell-gaps, meaning the assembly is also somewhat more difficult for this modes. Nevertheless, speed is still one of the weaker points of VAN, although room for progress is available.

4.3.7 Wavelength dependence

The dependence of the output intensity upon wavelength is in fact the same as for the cell-gap thickness, as both magnitudes always show up in the combination $\frac{d\Delta n}{\lambda}$. The typical behaviour is depicted in figure 4.46: the electro–optical response curve corresponding with blue first reaches its maximum, then green, then red.

The birefringence itself also exhibits dispersion . Equation (4.34) shows a typical relation between Δn and λ using the single-band model [94]. Typical

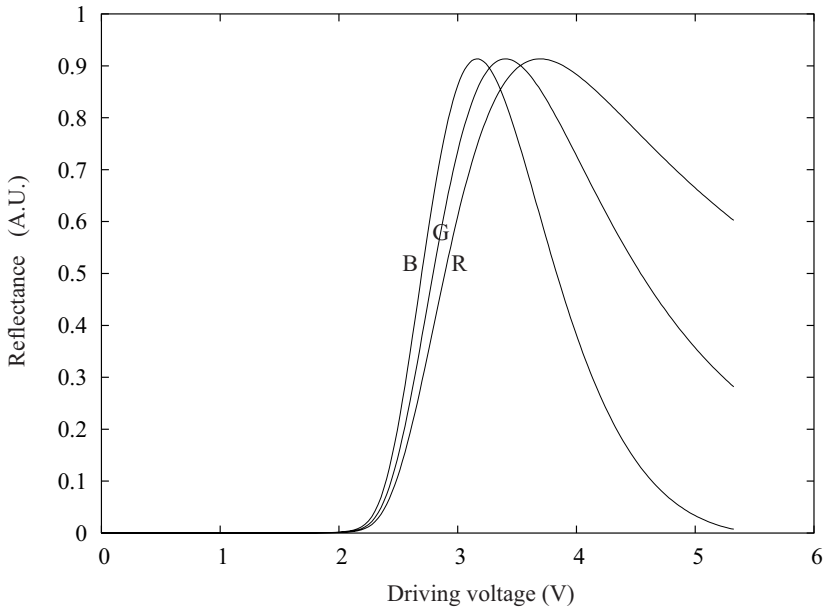

Figure 4.46: Optical response curves at 460, 550 and 640 nm.

values for the proportionality constant G and the electronic transition wavelength λ^* are 10^{-6} nm^{-2} and 250 nm, respectively.

$$\Delta n = G\frac{\lambda^2\lambda^{*2}}{\lambda^2 - \lambda^{*2}} \tag{4.34}$$

An interesting feature is the fact that the vertically aligned mode allows the use of one single cell-gap for all three colour channels. Adjusting the maximum driving voltage for each cell is enough to have full polarisation conversion efficiency for all three cells. For most other modes, like Mixed Twisted Nematic, this is not possible. Even if the cell-gap tolerance is large enough, a mismatch to the exact cell thickness always results in a drop in maximum polarisation conversion efficiency (see figure 4.52).

4.3.8 Tolerances

The assembly process of a liquid crystal cell limits the accuracy and repeatability of the mechanically determined parameters. This introduces deviations on the specified values. The broader the tolerances for these deviations are, the easier the manufacturing becomes for a fixed quality level. This section details on the tolerances of the crucial parameters.

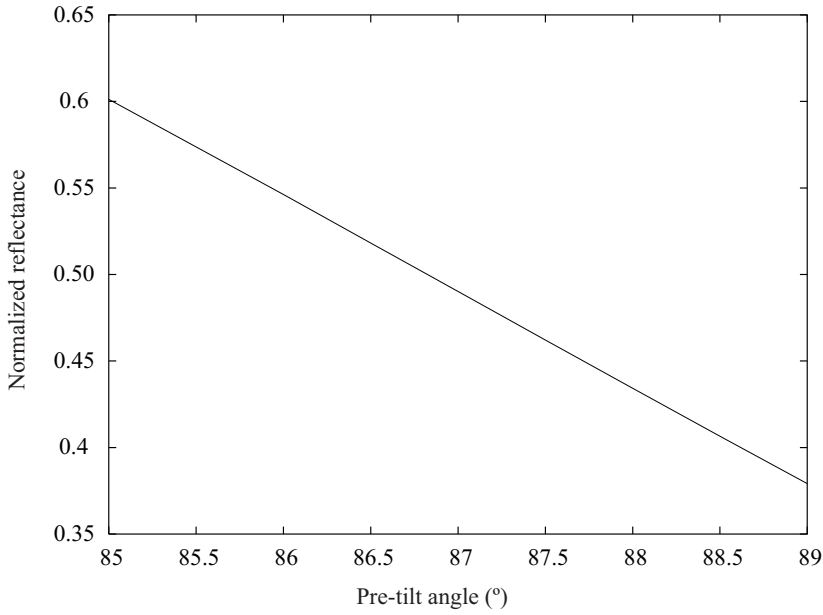

Figure 4.47: Output intensity versus initial pre-tilt angle for a vertically aligned cell. Driving voltage is chosen such that the output intensity for the 87 ° pre-tilt version is 0.5.

Pre-tilt angle

The changes in the electro-optical response curves have been depicted in figure 4.34. As already stated, the black state and thus the contrast is virtually not affected by a reasonable change in pre-tilt angle (figure 4.33). This is a unique feature of the vertically aligned mode. Other normally black modes like the HFE are also not very sensitive to pre-tilt variations, but the achieved contrast is much lower. Normally white modes like the MTN naturally have much more trouble in keeping a good dark state under pre-tilt angle variations since larger pre-tilt angle in this case means more residual birefringence near the substrates.

The largest intensity variations are to be expected when a grey value halfway the modulation curve is chosen. Figure 4.47 shows the intensity variation for several pre-tilt angle values around the 50 % brightness level for the vertically aligned mode. The variation is certainly not neglectable, but is not extraordinary compared to other modes. Figure 4.48 shows the same range of pre-tilt angle variations for a HFE cell. The output intensity variations are even larger. The MTN cell performs better, as shown in figure 4.49.

The influence of the pre-tilt angle on the speed characteristics was already visualised in figure 4.44.

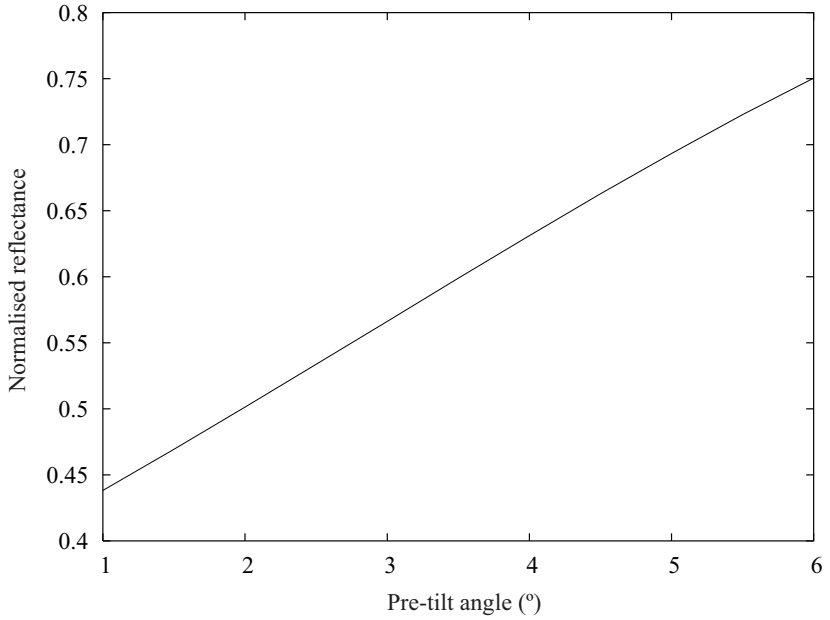

Figure 4.48: Output intensity versus initial pre-tilt angle for a HFE cell. Driving voltage is chosen such that the output intensity for the 2° pre-tilt version is 0.5.

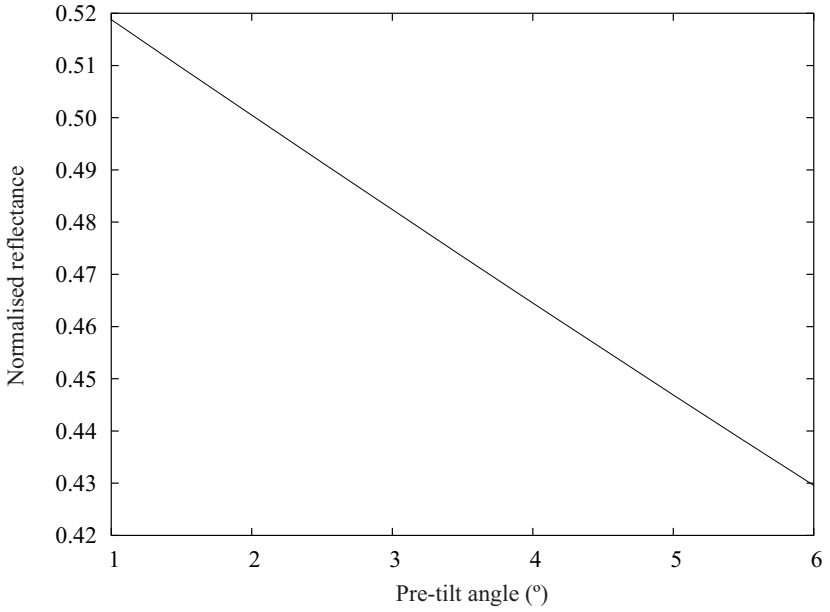

Figure 4.49: Output intensity versus initial pre-tilt angle for a MTN cell. Driving voltage is chosen such that the output intensity for the 2° pre-tilt version is 0.5.

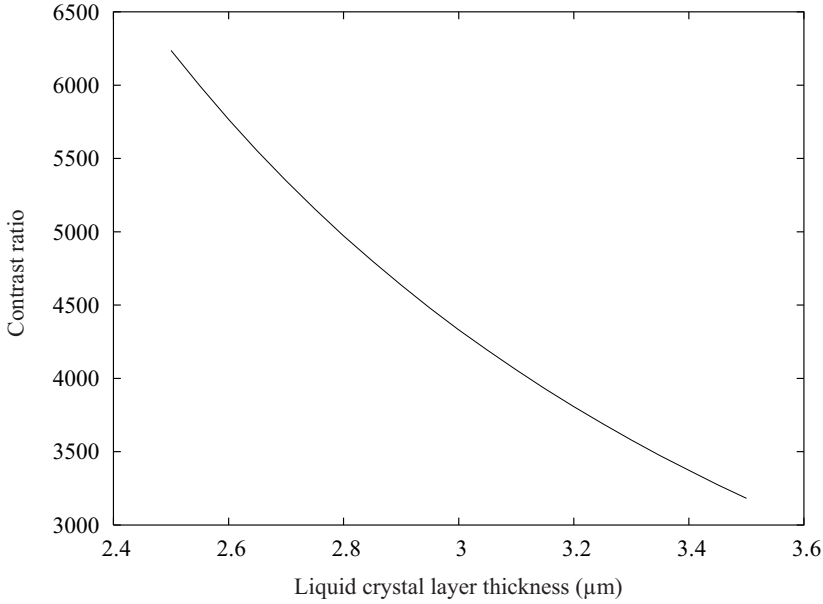

Figure 4.50: Calculated contrast ratio versus liquid crystal layer thickness at 86.0 ° pre-tilt angle for MLC-6610.

Cell-gap thickness

The uniformity of the cell-gap is probably the most challenging issue in the assembly process. A large cell-gap tolerance can therefore ease the manufacturing and suppress costs.

For the vertically aligned mode, the contrast ratio is again almost not affected by variations in cell-gap thickness. Figure 4.32 shows that theoretically the cell-gap can easily be doubled while contrast ratio is still exceptionally high, if the pre-tilt angle is large enough. If the pre-tilt angle is in the lower range, a cell-gap tolerance based on achieved contrast ratio may be defined. Figure 4.50 shows the evolution of contrast ratio with cell-gap thickness in the case of a pre-tilt angle of 86.0 °.

Of course, once a voltage is applied and the liquid crystal molecules are tilted, the situation changes. Figure 4.51 shows the electro-optical response curves for cells with gaps in a ± 10 % range around 3.0 μm.

Naturally, as the birefringence increases, so does the sensitivity for thickness variations. Modes that rely on the polarisation rotation effect are less prone to this phenomenon; the electro-optical curves would be closer to each other in the middle range.

For most modes, the maximum deviation that can be allowed is dictated by the contrast ratio that must be achieved. From equation 4.18 it can easily

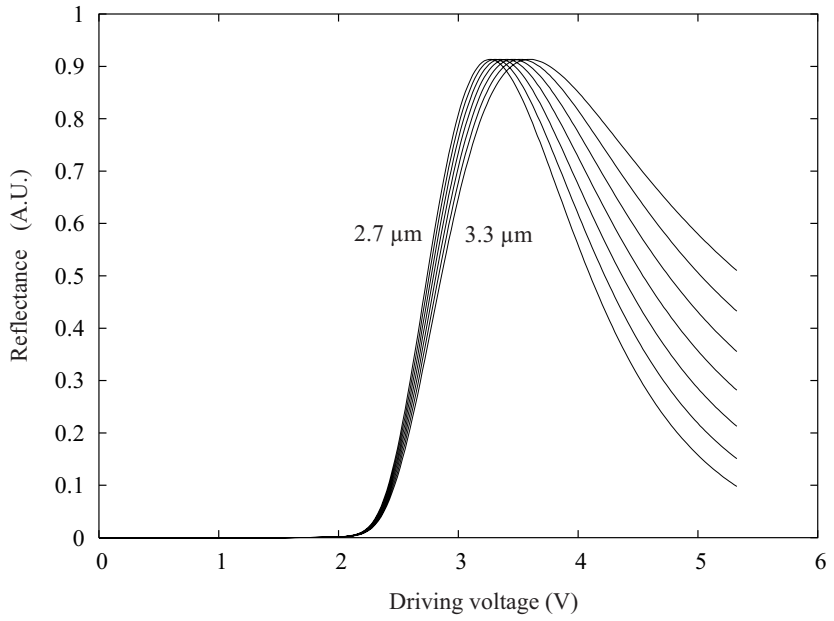

Figure 4.51: Response curves of a vertically aligned MLC-6610 cell for cell-gap values around 3.0 μm, step size 1.0 μm.

be derived that for the normally black homogeneous mode, for a contrast ratio of barely 100:1, the allowable change in cell-gap is less than a 0.032 fraction of the original thickness. To maintain the same contrast ratio on a Hybrid Field Effect cell, a variation of cell-gap of 0.15 times the original thickness is allowed. Normally White modes as the Mixed Twisted Nematic can achieve high contrast over a broad range of cell-gaps if only the driving voltage is taken large enough. Therefore, tolerances should be specified at a reference voltage. Figure 4.52 shows the electro-optical response of an MTN cell for a 10 % deviation in cell-gap. The overall tolerance is quite broad, except that the maximum brightness value inevitably drops.

As stated above, a cell-gap tolerance criterion based on contrast is not always very useful for the vertically aligned mode. It may make more sense to establish a criterion allowing for a certain amount of intensity variation at a certain brightness level. For example, from figure 4.51 the $\pm$ 10 % deviation in cell-gap causes approximately a $\pm$ 15 % change in output intensity around the 50 % brightness level. This is comparable to the performance of the Mixed Twisted Nematic mode (figure 4.52).

Cell-gap deviations of course influence the response speed, as evidenced by equations (4.29) and (4.30). This is however true for any liquid crystal mode, so this cannot be used as a criterion in favour or against a particular mode.

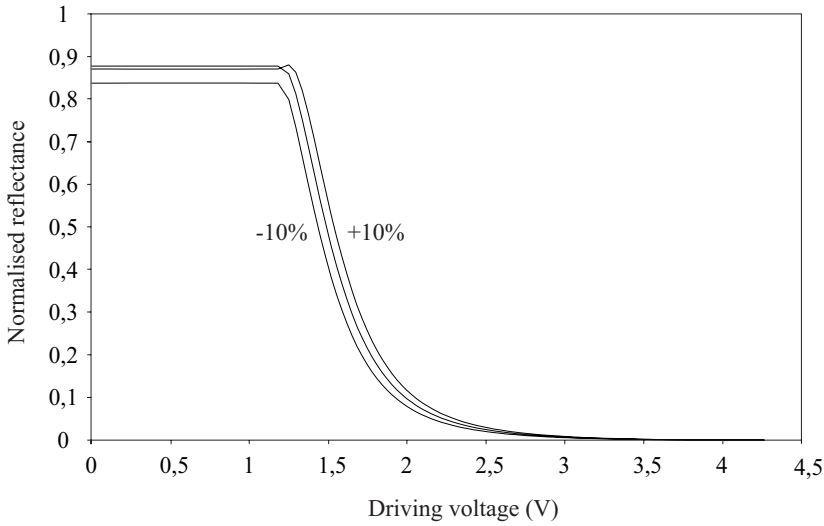

Figure 4.52: Response curves of a 1.814 μm Mixed Twisted Nematic cell for a cell-gap deviation of ± 10%.

Twist angle

Tolerances on the twist angle can be caused by the alignment layer (either inherently or due to mismatches when it is applied) or by registration errors when the substrates are joined. Quite obviously, the black state in a vertically aligned cell is not influenced by an additional twist. Also the grey levels and the full bright state are only very slightly affected by parasitic twist. Figures 4.53 and 4.54 show the intensity variation caused by a ± 10 ° deviation on the azimuthal orientation of the top substrate at 50 % and 100 % brightness level. Note that the introduction of twist can be done in two ways: symmetrically distributed around the polariser direction or one-sided. The graphs presented here are for one-sided twist.

Variations of the orientation of the bottom substrate give similar results. Combining both (thus symmetrically distributed twist) simply gives the sum of both separate effects.

Twisted modes are obviously much more prone to variations in the twist angle. Figure 4.55 shows the output intensity variation in a normally black Hybrid Field Effect cell around the 50 % brightness level for a ± 5 ° deviation on the bottom substrate azimuth angle. Figure 4.56 does the same for a normally white Mixed Twisted Nematic cell.

Normally White modes additionally show the largest sensitivity in the dark state, so that contrast ratio is then rapidly going down. This is illustrated in figure 4.57 for a normally white Mixed Twisted Nematic mode.

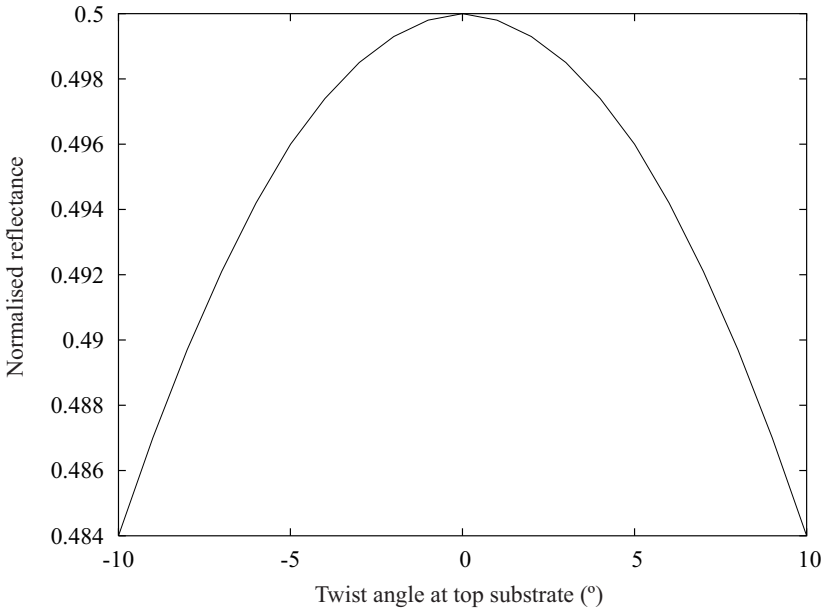

Figure 4.53: Intensity variation around the 50 % brightness level in function of the top substrate anchoring angle for a vertically aligned cell.

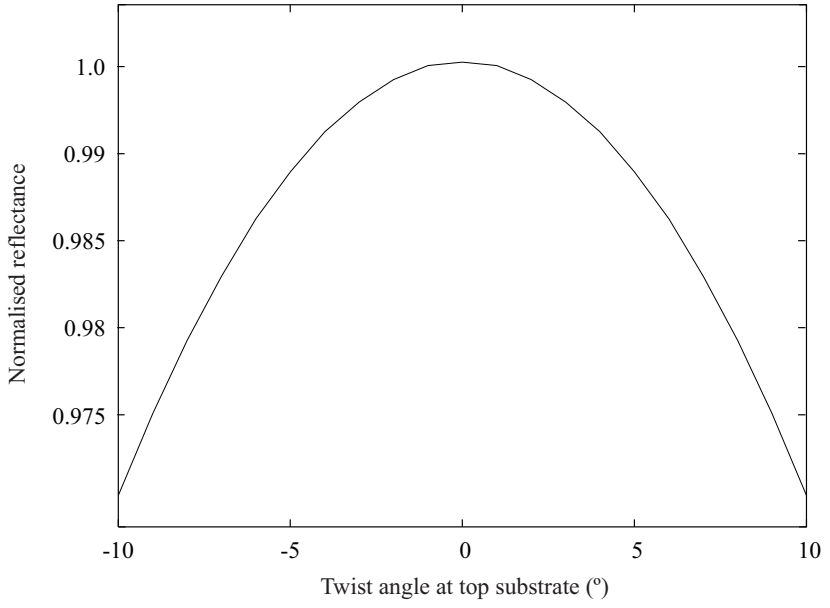

Figure 4.54: Intensity variation around the full brightness level in function of the top substrate anchoring angle for a vertically aligned cell.

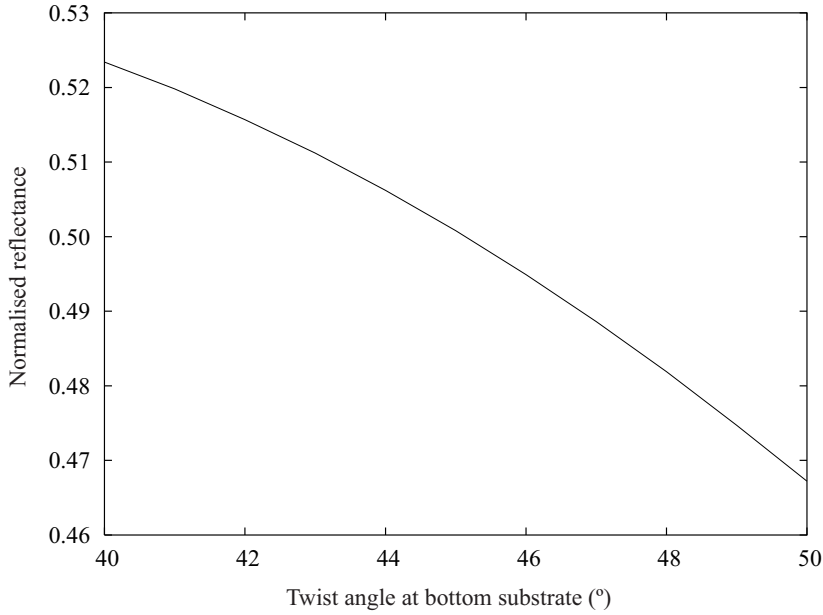

Figure 4.55: Intensity variation around the 50% brightness level in function of the bottom substrate anchoring angle for a 4 μm HFE cell, pre-tilt angle 2 °.

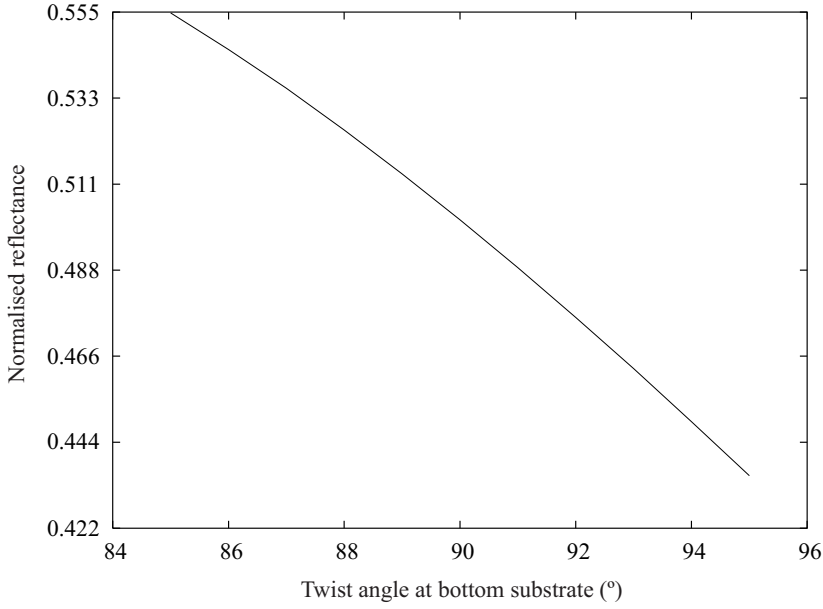

Figure 4.56: Intensity variation around the 50% brightness level in function of the bottom substrate anchoring angle for a 1.988 μm MTN cell.

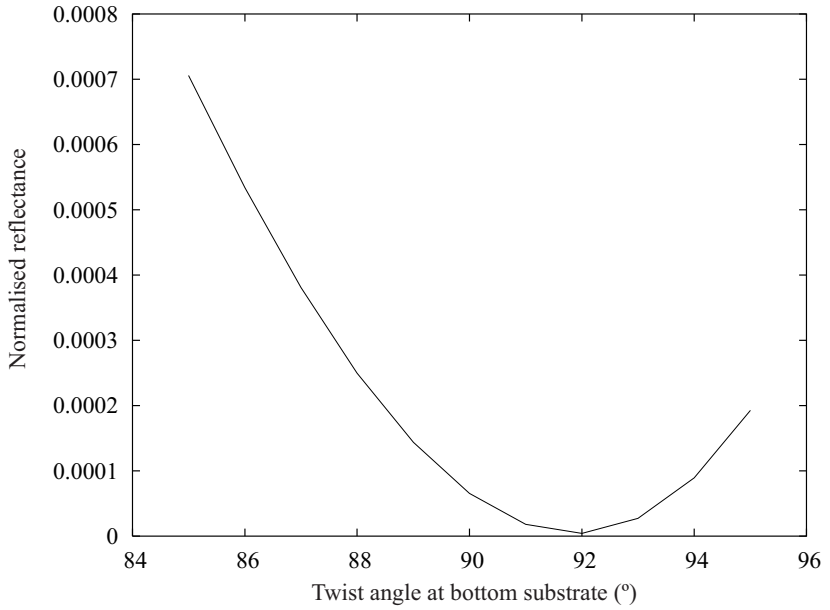

Figure 4.57: Intensity variation around the dark state (4 V) in function of the bottom substrate anchoring angle for a 1.988 μm MTN cell.

Chen et al. have reported an interesting relation between twist and response speed in homeotropically aligned cells [95, 96]. Based on numerical simulations of the hydro-dynamical flow equations, they state that even very small twist angle values (e.g. 0.1 °) substantially increase the response speed as compared to the absolutely non-twisted version. As such tight tolerances can never be achieved in the manufacturing, this is of little importance for real displays. Their simulations also predict an unneglectable increase of response speed for larger deviations on the twist angle.

In our experience, deviation in twist angle value contributes very little to response speed increase. Measured response speeds generally were in reasonable concordance with the values predicted by simulations using a simpler flow model. A possible explanation may be the comparatively lower voltages we use to drive the cells. As already indicated in [95], the influence of the twist angle seems to disappear at sufficiently low voltages, because the mechanism that causes the twist angle influence depends on the strength of the flow that is induced in the liquid crystal layer.

4.3.9 Conclusion

The vertically aligned nematic mode is a viable candidate for use in reflective projection applications. It features a combination of properties that make it

very attractive for the production of high quality reflective lightvalves in high volumes. High quality is achieved by the unprecedented contrast. High volume production is enabled by the large cell-gap tolerance, the insensitivity to most manufacturing tolerances and the possibility to have one cell-gap for the three colour channels. The driving voltage requirements are also modest, so the driving circuitry is not too complicated. The speed is sufficient for motion video, but does not allow field sequential addressing.

Chapter 5

Liquid crystal alignment

5.1 Introduction

The operation of virtually all nematic liquid crystal modes is based on the switching of the molecules between two states, usually defined by the presence or absence of an electrical field. In the absence of a field, another external force is needed to maintain a uniform and well-defined crystal texture. This force is exerted by the aligning layer, a thin layer of well chosen material that exhibits surface anchoring properties for the liquid crystal molecules that are in direct contact.

This chapter deals with the realisation of such alignment layers; of course, focus is put on the homeotropic alignment needed for vertically aligned devices.

During the development of liquid crystal devices, several types of alignment layers and aligning methods have been proposed and investigated. They can roughly be categorised by the nature of the material employed: organic or inorganic. A further classification is then made by means of the deposition and treatment of the layer.

It can already be noted that, at least up to very recently, from an industrial viewpoint, the organic alignment technique is by far dominant, being used in practically all LCD devices and in particular the massive amounts of AMLCD panels for notebooks and the like.

5.2 Alignment techniques

5.2.1 Organic materials

Buffed polyimide

The fact that liquid crystal molecules tend to align on certain organic materials when they have been rubbed was discovered pretty early on in the research of liquid crystals. Although it seems a rather awkward and unreliable technique at first, it has longtime been the only way to achieve alignment. Today, it still is the dominant technique for virtually all liquid crystal display applications and only relatively recent progress have made the alternatives viable for manufacturing.

In this technique, a thin layer (a few tens of nanometers) of polyimide material is spin-coated on the substrates. After polymerisation, the layer is rubbed with a cotton or rayon cloth mounted on a cylinder, using a special rubbing machine. Pressure, travelling speed, cylinder diameter and the like are all important process parameters defining the alignment properties. It has been demonstrated that the rubbing process creates tiny micro-grooves of high regularity and suitable interval (approximately 30 nm) in the alignment layer surface to which the liquid crystal molecules align and anchor themselves [97].

For homeotropic alignment, specific polyimides are available, e.g Nissan SE-1211. Without the rubbing process, perfect homeotropical alignment is obtained. A rubbing step allows to introduce a small pre-tilt angle. Alternatively, an underlayer of obliquely evaporated inorganic material can also serve as means of introducing a preferential tilting direction.

The main disadvantage of the buffed polyimide technique is the fact that it relies on mechanical contact to achieve its goal. Damage to the substrates may thus be caused by scratches, contamination with foreign substances and electrostatic discharges.

Photo-alignment

Because the rubbing process is in fact a rather harsh mechanical treatment of the underlying surface that can potentially damage the structures underneath and raises concerns about electro-static discharges, other, less rough methods to align liquids crystals have been searched for. Stretched polymers [98] and photo-lithography techniques [99] have been proposed, but the most promising non-contact method seems to be the photo-alignment technique, involving linearly polarised UV exposure of polymers.

In the original report by Gibbons [100], polyimide films doped with photosensitive azo-dye compounds are used. Later on mainly poly-vinyl-cinnamate and its derivatives have been used [101, 102, 103], but also polyimides [104]. Research is still active and new materials are still being proposed, e.g. hydroxy-

coumarin based polymers[105].

Alignment occurs perpendicular to the polarisation direction of a normally incident UV beam. To generate pre-tilt angles, double exposures, combined exposures or oblique irradiation are used.

Thermal stability can be a problem with some materials, as does the UV irradiation step itself. The organic molecules may suffer damage from the high energy photons and compromise the life-time of the devices [106]. The equipment needed for the exposures is also quite costly.

Langmuir-Blodgett films

Langmuir-Blodgett films are ultra-thin layers of organic material that have been deposited with a special technique. A Langmuir film [107] is a monolayer of organic molecules (generally amphiphilic) formed on the surface of a liquid. These Langmuir films can be transfered onto a solid carrier with the methods developed by K. Blodgett [108]. This way precisely controlled, highly uniform mono- or multilayers can be deposited on arbitrary substrates. Among the many uses for these films one also finds the alignment of liquid crystal phases. Quite some theoretical work has already been done, see e.g [109], but the application of this somewhat exotic technique is in practice restricted to laboratory spaces.

Surfactant dipping

Some surfactant molecules adhere well to electrode materials such as ITO and aluminium and align liquid crystal molecules. A simple dipping of the substrates is enough to apply the layer. Both homogeneous and homeotropic alignment can be obtained, depending on the surfactant type [110, 111]. The most used materials are trialkoxysilane, n,n-dimethyl n-octadecyl 3-aminopropyl trimethoxy sylil chloride (DMOAP) and n-methyl 3-aminopropyl trimethoxysilane. The major problem with this technique is the thermal stability, which basically does not exist. Pre-tilt angles are thus unpredictable and make this dipping technique unsuitable for practical purposes.

For homeotropic alignment, the treatment with DMOAP or, in general, silane based coupling agents and long-chain alcohols is often combined with an inorganic alignment layer [112]. The inorganic layer serves as an under-coat and is deposited first, using any of the oblique deposition techniques described next. The surface is then exposed to the coupling agent for a predetermined amount of time.

The long tail of the coupling agent's molecules orients the liquid crystal homeotropically, while the under-coat layer, where the polar head of the molecule is attached, ensures that there is a small pre-tilt angle in a known direction. The resulting orientations are however unreliable and hard to reproduce as they seem critically dependent on the exposure time and conditions to

the coupling agent.

5.2.2 Inorganic materials

In the 1970's, it was discovered that also inorganic materials can serve as alignment layers for liquid crystals. Certain oxides, especially the ones from silicon, tend to align liquid crystal molecules when deposited directionally as thin films.

Oblique evaporation

The most straightforward way to obtain the directionally deposited thin films required for the alignment layers is by using oblique evaporation.

In a conventional evaporator, the beam of material can be considered as emerging from a point source. At a reasonable distance, the material beam impinging on a comparably small substrate will thus be highly directional. By tilting the substrate relative to the incidence direction of this beam, oblique deposition at a certain angle is achieved, necessary for the aligning properties. To reduce the distance needed to obtain a directional beam, beam-shaping techniques (shielding off parts of the beam) are used.

A lot of research effort has been put into developing methods to get reliable, reproducible results with this technique. The great majority of this research concentrated on silicon-monoxide as evaporation material, and tried to achieve homeotropic alignment for liquid crystals with negative anisotropy, as this kind of alignment is difficult to achieve with the rubbing method.

Advantages of the oblique evaporation technique include the fact that it is a contact-less method, posing no risk of damaging the substrate either mechanically or by electrostatic discharge. The deposited layers are thinner than their organic equivalents, so less influence on the optical and dielectric behaviour of the device is to be expected. Further on, the superior stability of inorganic layers removes all concerns about life-time and reliability of the alignment system.

A considerable disadvantage may be the cost of the vacuum equipment. The needed directionality of the beam limits the size of the substrates or calls for large vacuum chambers, both considered unfavourable for high volume production. This can be circumvented with some engineering effort, e.g. the above mentioned beam-shaping or the use of linear evaporation sources. It is also fair to say that some deposition techniques that have been proposed are quite complex and do not always feature an equally high reproducibility.

Oblique sputtering

Because the oblique evaporation process was considered a not so efficient process, and the process equipment does not lend itself so easily to adoption in

a high volume production environment, attempts were made to introduce the sputter deposition technique, the workhorse of the semiconductor industry, for the deposition of the alignment layer.

It is obvious that the nature of the sputtering deposition method is not in good agreement with the need for a highly directional material beam. The bombardment of the target with heavy argon ions effectively results in target material atoms hitting the substrate at every possible angle, evidenced by the highly conformal nature of sputtered coatings.

One way to realise an oblique deposition system suitable for alignment layer coatings with a sputtering machine has been developed by the Bildschirminstitut of the Universität Stuttgart [113]. A vertical in-line sputtering machine is adapted to allow oblique deposition. The direction-less target material beam is transformed into a directional one by the use of sets of louvers. Oblique incidence is obtained by mounting the rectangular target on wedges, so that it is not parallel with the substrates anymore.

The produced alignment films are highly uniform, also on large substrates, but it is evident that the sputtering yield is drastically decreased by all the measures taken. It also remains to be seen if pre-tilt angles can be varied over some considerable range.

Ion beam writing

The most recent development in alignment technology was presented by IBM in 2001 [114]. Leaving behind all achievements with the existing technologies, a completely new system for aligning liquid crystal was devised. The technique is classified here under the heading of the inorganic materials, but as diamond-like carbon films are used it is of course debatable whether this is justified or not.

Starting from a rigorous study of the microscopic interactions between the liquid crystal molecules and the organic molecules of conventional alignment layers, the idea was to produce a layer with similar aligning characteristics but using a totally different process. Of course, this process had to be free of the disadvantages associated with the polymer rubbing technique and should not introduce any other serious drawbacks.

The proposed solution uses a diamond-like-carbon hard-coat, 3 to 15 nm thick deposited via chemical vapour deposition or sputtering. The alignment is obtained by bombarding the layer with ions. Scanning of the surface with an argon ion beam under an oblique incidence angle of 15 ° to 70 ° is able to introduce a pre-tilt angle of 0 to 10 ° with a uniform and strong anchoring. Homeotropic alignment has not been reported but should be equally possible.

The mechanism of alignment is explained by adopting a random network model of atomic arrangement in the film. Order is induced by exposure to the ion beam because unfavourably oriented rings of atoms are selectively de-

stroyed. The planes of the remaining rings are predominantly parallel to the direction of the ion beam [115].

The advantage of the ion-beam method over the classical polyimide solution is clear: it is a non-contact method with reliable results. The advantage over the other inorganic solutions is of a more subtle nature. Because the diamond-like-carbon layers are conductors, the liquid crystal layer is in contact with electrodes having equal work-functions, which is otherwise not the case for reflective devices [116]. Such symmetrical cells are preferable to obtain flicker-free displays, because the so-called Vcom is eliminated (see further on) [117]. To avoid charge leakage to neighbouring pixels, the resistance of the alignment film must of course be very high. This is achieved by controlling the hydrogen content of the deposited film.

The cost and relative complexity of the equipment needed for the deposition and treatment of these films clearly is the main drawback of the process.

5.3 Oblique evaporation technology

In the following section, a more detailed overview is given of the inorganic alignment technique, specifically the oblique evaporation method.

5.3.1 Principle

The fact that obliquely deposited films of certain materials can have different properties compared to regularly deposited ones has been known for quite some time. The first reports were made by Knorr and Hoffman [118] and Smith [119], both carrying out research in the area of thin magnetic films. Even before that, oblique deposition was employed in electron-microscopy to enhance contrast [120]. The research on the anisotropy introduced by oblique deposition in magnetic materials has been extensive; it finally led to the introduction of metal evaporated video tape, now an established technique [121, 122, 123]. The theories developed in this research give adequate insight in the deposition mechanism and the resulting films.

Although oblique deposition does introduce anisotropy in macroscopic properties such as electrical resistance and optical transmission, the special morphology of the layer is our main interest with regards to its use as alignment layer.

Layer morphology

Films deposited with an obliquely incident vapour stream will in general exhibit a columnar morphology. The axis of the columns will be inclined toward the impinging vapour stream, with the actual angle somewhere in-between the

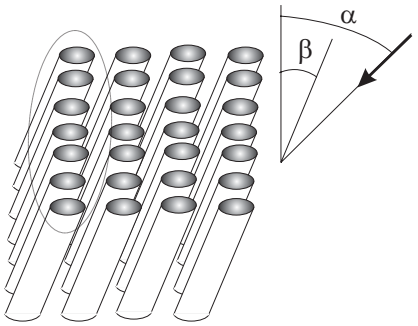

Figure 5.1: Schematic representation of the morphology of obliquely deposited films. The arrow indicates the direction of the impinging material stream (angle α with the substrate normal). The resulting columnar structures have an inclination angle β. They also tend to cluster together.

substrate normal and the incidence angle, depending on the deposition circumstances. The columns will also bundle themselves in rows, perpendicular to the plane of incidence, with the columnar separation being larger between the respective bundles than inside the bundles. The cross-section of the columns is generally elliptical. For crystalline materials, a specific texture is also observed, i.e. the orientation of the main axes of the crystal are dependent on the incidence angle and the deposition parameters [124]. Some elements are illustrated in figure 5.1.

Different theoretical models have been proposed to explain the observed features of obliquely deposited films. The inclination of the columns has been described with the discretised continuum model, self-shadowing, conservation of parallel momentum and angle dependent growth. Self-shadowing and conservation of parallel momentum can also be used for the bundling phenomenon. The shape of the cross-section of the columns can again be predicted by the conservation model, while the formation of texture is described by surface diffusion effects.

Discretised continuum model [125] Starting from the observation that a film grows in discrete steps, i.e. with at least the size of an atom for each step, it is stated that the edge of the layer cannot grow exactly towards the source, as it would in a continuum model.

Because of the finite atom size, a layer cannot terminate at any given position and thus the direction of growth deviates from the incidence angle. Instead, it is stated that the mean location where a layer terminates is that for which the continuum model thickness is one half (see figure 5.2). This then gives the so-called tangent rule (5.1), relating the incidence angle α to the column direction angle β, which seems to fit a great number of measurements.

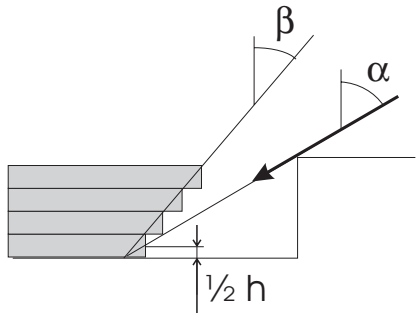

Figure 5.2: Illustration of the discretised continuum model. The arrow indicates the deposition direction (angle α), the growth direction is different (angle β.

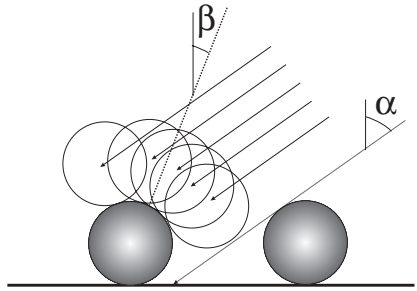

Figure 5.3: Illustration of the self-shadowing effect. The arrows indicate the direction of arriving particles. Although they make an angle α with the substrate normal, the average direction of growth will be along the angle β.

$$\tan(\alpha) = \frac{1}{2}\tan(\beta) \tag{5.1}$$

This model is now considered too simple, even by its authors; it is in fact only used for the now obviously empirical tangent rule.

Self-shadowing [125] A growth nucleus can experience shadowing effects from neighbouring nuclei. Looking at figure 5.3 it is clear that the nucleus to the right cuts off part of the impinging stream of atoms that would otherwise cluster around the left nucleus. The net result is a shift of the average position where atoms adhere to the growth nucleus. The growth direction is no longer along the incidence direction, but has moved towards the film normal.

The bundling effect is explained along the same line of reasoning [126, 127]. The initial growth nuclei cast their shadows on the areas right behind them and prevent both the formation of other nuclei and further growth in those places. This gives the columnar separation observed in the plane containing

the incidence direction and the film normal. Growth in the other direction is unrestricted, so the nuclei will eventually coalescence into chains of columns, the bundles.

Conservation of parallel momentum [128, 129] When atoms hit the substrate under some angle, the momentum parallel to the substrate will probably not be completely lost in the impact and the atom can still move a short distance in that direction. This causes the columns to grow in a direction more toward the substrate normal, provided the effect is not cancelled by random surface diffusion.

Bundling can also be explained with this model [130], although the self-shadowing model is sufficiently adequate and probably more convincing.

The (elliptical) shape of the column's cross-section is considered to be a result of the conservation of momentum combined with the presence of residual oxygen [131]. An atom hitting the column will travel for some short distance around it, due to the conservation of momentum. The position where it finally gets trapped is dependent on the local oxygen concentration, which varies around the column because of the continuous supply of new material at the front side of the column. The resulting distribution of the probability for atoms to adhere to the column is elliptical, hence the final shape of the column's cross-section.

Angle dependent growth [132] Because the columns are quite large compared to a single atom, a model that considers the film growth as a continuous process may also be successful. The substrate is assumed to have an initial roughness described by a function $r(x)$, while the growth rate is described by another function $G(\frac{dr}{dx})$, making it dependent on the slope of the underlying layer. This way columnar growth is obtained, but the results obviously vary strongly with the choice of the function G. A fully developed model, including all effects based on this approach also seems to be excessively complex [124].

Surface diffusion Surface diffusion plays an important role in any thin film deposition process. In the case of oblique deposition, it also plays a role in the crystal structure that is developed during the deposition, i.e. the direction of the crystal's main axes with respect to the substrate. This crystal orientation changes with the incidence angle of the deposition. Depending on the amount of surface diffusion, different relations between incidence angle and preferred growth orientation can be derived [133].

Conclusion In summary, it can be stated that the deposition process of obliquely deposited layers and the resulting layer morphology is well documented and that adequate models for the process are available.

Anchoring

The physics behind the anchoring of liquid crystal molecules to the obliquely deposited layers is far less well understood than the deposition itself. Up to now, no single satisfying theory has been presented that can adequately incorporate all experimental results.

The most recent attempt by Lu et al. [134] proposes the introduction of a Van der Waals potential in the surface anchoring energy; they see it as an extension to the classical theory of Barbero et al. [135] regarding surface orientation.

In the paper of Barbero, it is shown that in a nematic liquid crystal, a net polarisation can exist if a spatial gradient in the order parameter S is present while the director $\vec{n}$ remains constant. This polarisation is similar, in nature and magnitude, to the flexoelectric polarisation that occurs under the opposite conditions, a non-uniform director profile with constant order parameter [136].

This order polarisation term must be taken into account for the internal energy of the entire system, hence it influences the equilibrium configuration of that system.

The paper then covers in detail a particular case where the order polarisation plays a role: the director orientation at a so-called free surface. A typical example of such a free surface is the interface between the nematic and isotropic liquid crystal phase, stabilised by a temperature gradient. The predicted mean director orientation θ_0 is then extracted from equation (5.2), with L_2, r_1, r_2 and ϵ material parameters and θ_0 measured from the z-axis. For the few materials for which this data is available, the model is in agreement with measured data, proving its validity.

$$\left(\frac{3}{8} L_2 + \frac{2\pi}{\epsilon_\perp} (r_1 \cos^2\theta_0 + r_2) \frac{\left(\frac{\epsilon_\parallel}{\epsilon_\perp}\right) r_1 \cos^2\theta_0 + 2r_1 - \left(\frac{\epsilon_\parallel}{\epsilon_\perp}\right) r_2}{\left(1 + \left(\frac{\epsilon_\parallel}{\epsilon_\perp}\right) \cos^2\theta_0\right)^2} \right) \sin 2\theta_0 = 0 \tag{5.2}$$

Van der Waals forces Based on their observations that liquid crystals with positive anisotropy align homogeneously while negative anisotropy mixtures align homeotropically on identical surfaces and eliminating other possible causes, Lu et al. conclude that the anchoring force between LC and surface is caused by induced dipole to dipole interactions. This dipole interaction is based on Van der Waals forces and can be written in potential form as $-\frac{\lambda}{r^6}$. The constant λ is proportional to the product of the polarisabilities of the materials. The polarisability of the aligning layer is obviously constant, but the LC has two polarisabilities, corresponding with the anisotropy in dielectric permittivity. This is readily apparent from the Clausius-Mossotti equation (5.3), relating the molecular polarisability α of a non-polar medium to the dielectric

permittivity (N_V is the number density of the medium in molecules per cubic meter).

$$\frac{1}{3}N_V\alpha = \frac{\epsilon - 1}{\epsilon + 2} \tag{5.3}$$

This directly leads to the conclusion that materials with positive anisotropy will align homogeneously, while negative anisotropy means a preference for homeotropic alignment.

The dependence of the alignment upon the deposition parameters is attributed to the changing layer morphology. Extrapolating the aforementioned conclusions of Barbero to interfaces of liquid crystal with a solid alignment layer, it is argumented that order polarisation plays its role here as well. Using equation (5.2) for $L_2 = 0$ and $S \to 0$ a limit case for the director orientation at the interface can then be obtained. It follows that $\cos^2\theta_0 = \frac{1}{3}$ which means that for a liquid crystal with positive anisotropy the pre-tilt angle should always be less than 35.3°. For negative anisotropy, the complementary angle should be used, so pre-tilt is expected to be larger than 54.7°. Being a very coarse prediction, this is in agreement with most measurements.

5.3.2 Material choice

Possible materials

Materials suitable for use as an alignment layer are in principle abundant. Pure metals such as platinum, gold, tin, lead, aluminium, copper, silver, titanium and chromium, metal sulfides like cadmiumsulfide, leadsulfide, zincsulfide and antimonysulfide, halogenides and nitrides as calciumfluoride, magnesiumfluoride, lithiumfluoride, ceriumfluoride and boronnitride as well as oxides like siliconoxide, aluminiumoxide, titaniumoxide, indiumoxide, tinoxide, tungstenoxide and ceriumoxide have all been reported to work. For use in actual liquid crystal devices, considerations concerning material cost, ease of handling, availability, environmental compatibility and the like also play a crucial role.

Therefore, only a few materials have been thoroughly investigated. Metals are less appropriate because of their conductivity and the risk of ions released in the liquid crystal. Toxic and exotic compounds were also quickly abandoned. Most of the research effort has been focused on the oxides of silicon, SiO_x, with x frequently being 1 or at least less than 2. Occasionally some reports on aluminiumoxide can be found [137]. It is interesting to note that successful attempts to use ITO (indium-tinoxide) have never been reported, despite the attractiveness of the combined functionality of electrode and alignment layer.

The preference for SiO_x can be attributed to the initial good results that were obtained, together with the versatility of the material. The choice for SiO_x however has some drawbacks. First of all, neither SiO nor SiO_x is stoichiometrically stable. Every layer will have a certain tendency to further oxidise

towards SiO_2. For the same reason it can be difficult to obtain exactly the same material in-between different production batches. Sometimes the SiO_x is even produced inside the vacuum chamber by a controlled reaction of Si and oxygen, posing great problems regarding reproducibility.

Silicondioxide eliminates most of these problems. It is very stable, both stoichiometrically and in a more general chemical sense. It can be evaporated from quartz crystals of known quality, ensuring reproducibility between batches. Most importantly, we did not encounter any anomalies in the aligning properties of the material. Therefore, SiO_2 seems a more ideal choice.

Particularities

A point of concern may be the highly hydrophilic nature of the SiO_x / SiO_2. Moisture absorption is inherent to and practically inevitable for these layers. The presence of the water molecules can change the alignment behaviour, so a controlled humidity environment is recommended. For homeotropically aligned cells, the level of moisture saturation can cause a relatively small change in the obtained pre-tilt angle but it does not appear to actually break the intended alignment.

In unfavourable circumstances, the porous surface of the aligning layer might cause chromatic separation of the liquid crystal mixture into its constituting compounds.

SiO_2 surfaces also have a high tendency to adsorb carbon fractions. When this becomes excessive, the alignment properties will change or simply disappear. It is believed that this is the primary degradation mechanism for layers that are left exposed to air. The lifetime of freshly deposited layers is indeed limited; if the liquid crystal is not injected in the cell within a time window of some hours, the alignment properties are generally lost. Regeneration is generally possible by applying an appropriate bake-out step under vacuum, but high temperatures may be required.

5.3.3 Existing techniques

Several variants and adaptions of the original idea have been proposed throughout the years, trying to overcome the weak points and improve aspects such as manufacturability and reproducibility. A short overview covering the highlights is given below.

Static deposition

The original process [138] by Janning, also disclosed in a patent [139], covers the basic setup of an inclined substrate opposite to the evaporation source (see figure 5.4). The intended alignment is homogeneous, but the idea is easily

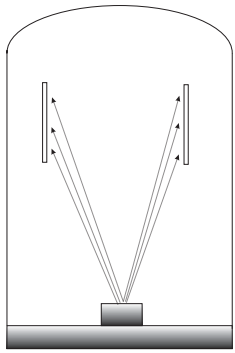

Figure 5.4: Arrangement for oblique evaporation according to Janning.

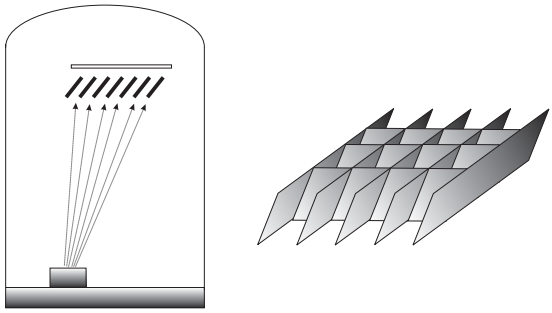

Figure 5.5: Arrangement for oblique evaporation with louvers in the material stream.

extended to homeotropic alignment. Near grazing incidence is preferred for good alignment and platinum is mentioned as the alignment material, along with other metals. A layer thickness of 20 Ångstrøms is set forth as optimal.

Several variants to this system have been proposed e.g. putting the substrate on the centreline of the evaporation source [140]. Even in more recent days, variants of this system are still devised, despite its drawbacks concerning incidence uniformity. In [141] for example, a practically identical approach is taken except for a layer thickness range that is shifted somewhat upward, in the range of tens to hundreds of nanometers. The alignment material is most often siliconmonoxide or SiO_x.

A more substantial alteration is the introduction of louvers in the evaporation path, allowing for a more stricter control of the oblique angle and making it possible to use larger substrates [142]. Figure 5.5 illustrates the principle. The louvers effectively block unwanted incidence angles and thus provide a rather uniform, well-defined range of incidence angles over the substrate area.

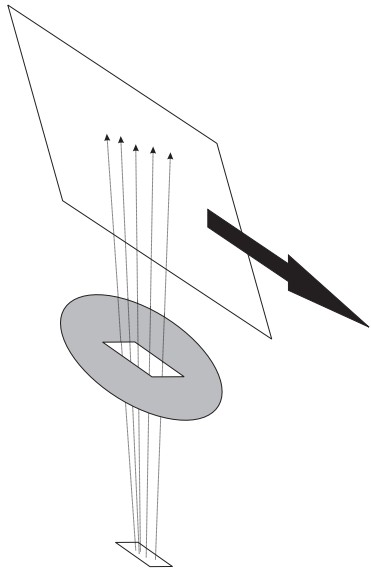

Figure 5.6: Oblique evaporation through an aperture with linearly moving substrate.

Linear sources and aperture limited deposition In order to overcome the limitations set on the dimensions of the substrate due to changing incidence angles, some other solutions have been suggested. The simplest way is of course to use a linear evaporation source instead of the conventional point source [143, 140]. The obtained layer uniformity depends largely on the attainable evaporation uniformity.

An alternative approach is to restrict the beam coming from the point source to a limited field of view by means of an aperture and let the substrate travel through the beam [144], see figure 5.6. The carrier system required for the linear motion of the substrates makes the apparatus rather complex, while the required space inside the vacuum chamber is also considerable.

Rotating deposition and double exposure

The techniques above have in common that the resulting pre-tilt angle is critically dependent on the incidence angle, making it rather difficult to obtain a good uniformity and reproducibility. To overcome this problem, yet some other variants of the oblique evaporation technique have been proposed.

Rotation oblique deposition The rotation oblique deposition by Hiroshima [145] allows a wide range of pre-tilt angles to be obtained. The substrate is mounted obliquely with respect to the evaporation source, but is mounted on a base that can rotate the substrate around its centre (figure 5.7).

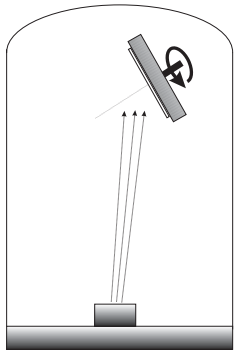

Figure 5.7: Rotation oblique evaporation method by Hiroshima.

The rotation speed can be varied continuously depending on the rotation position of the substrate. By choosing e.g. a sinusoidal relation between the angular speed and the position, the azimuthal distribution of the deposition can be changed. Depending on this distribution, a wide range of pre-tilt angles is obtained. Hiroshima reports pre-tilt angles for negative anisotropy liquid crystal ranging from 30° to 90°, linearly dependent on the distribution. Note that this is one case where the model of Lu discussed earlier does not hold.

The complexity of the equipment needed to provide the angular motion and the difficulty to coat several substrates at a time have prevented wide-spread use of this technique.

Double deposition Double evaporation techniques have also been employed in attempt to gain a greater controllability of the orientation layer. The substrate is thus coated obliquely from two distinctly different angles. The two depositions may occur simultaneously or subsequently. The different deposition angles are obtained in several ways. Impact plates splitting a single beam into two differently oriented ones have been used [146], as well as two separate sources at different heights [147] and shutter plates with windows that only allow some directions to pass [148]. Combinations of techniques, such as a rotating deposition followed by a short static one [149], can also be encountered.

Sputtering

Finally, some sputtering methods can be found in literature. Best-known is the system developed by Stuttgart University, commented on above. Some other variants can be found, e.g. one that does not use louvers or inclined targets but relies on changing incidence angles generated by a substrate passing under the target [150].

5.3.4 Proposed deposition technique

Setup

The oblique evaporation system we use tries to combine a number of advantages from the other techniques into a compact form. A standard bell-jar evaporator with a chamber diameter of 450 mm is used with only slight modifications applied. Figure 5.8 gives an overview of the arrangements inside the vacuum chamber.

The substrates are arranged on a carousel that can be mounted on a motor drive in the top of the chamber. The platters to which the substrates are fixed can be given a certain angle with respect to the rotation axis; this defines the incidence angle in a first reference plane. The carousel rotates so that each substrate passes briefly above the evaporation source. The vapour stream from the source is shielded by shutter plates so that only a narrow portion can pass, this restricts the possible incidence angles in a second reference plane, perpendicular to the first one. This way, the deposition geometry is fully determined.

The dimensions of the respective parts are as follows. The distance between the evaporation crucible and the centre-line of the substrates is 430 mm. The shutter plate is mounted just below the substrates, 400 mm above the crucible. A small sector is left out in the plate where the evaporated particles can pass. The sector width is 30 mm at the rim, while the diameter of the shutter is 420 mm. The sector is positioned right above the evaporation crucible. The substrates are mounted to the carousel with their centre-points on a circle with diameter 220 mm. The carousel has a rotational speed of half a revolution per second.

Figures 5.9 and 5.10 give an idea of the practical implementation of the system.

The orientation of the substrates with respect to the evaporation direction must be observed. The tilting direction of the liquid crystal molecules is determined by the plane of incidence of the evaporated material. For the homeotropical cell to work, this tilting direction needs to be at 45 ° with respect to the crossed polarisers. Generally these polarisers will have their axes aligned with the edge of the substrates; consequently the substrates must be mounted such that the plane of incidence makes an angle of 45 ° with the substrate edges (see figure 5.11.

Angular deviations Evaporation is carried out at a pressure around 3×10^{-6} mbar. The mean free path of the evaporated molecules can be calculated using equation (5.4), where T is the temperature, p the pressure, R Boltzmann's constant, N_A Avogadro's number and d the molecular diameter. With the above pressure and an approximate molecular diameter of 5 Ångstrøms or less, the mean free path is in the range of a few meters.

Figure 5.8: Arrangement inside the evaporator. Dimensions are as follows: source to substrates 430 mm, source to shutter 400 mm, diameter of clock 450 mm, diameter of substrate holder 220 mm, shutter opening at the rim 30 mm.

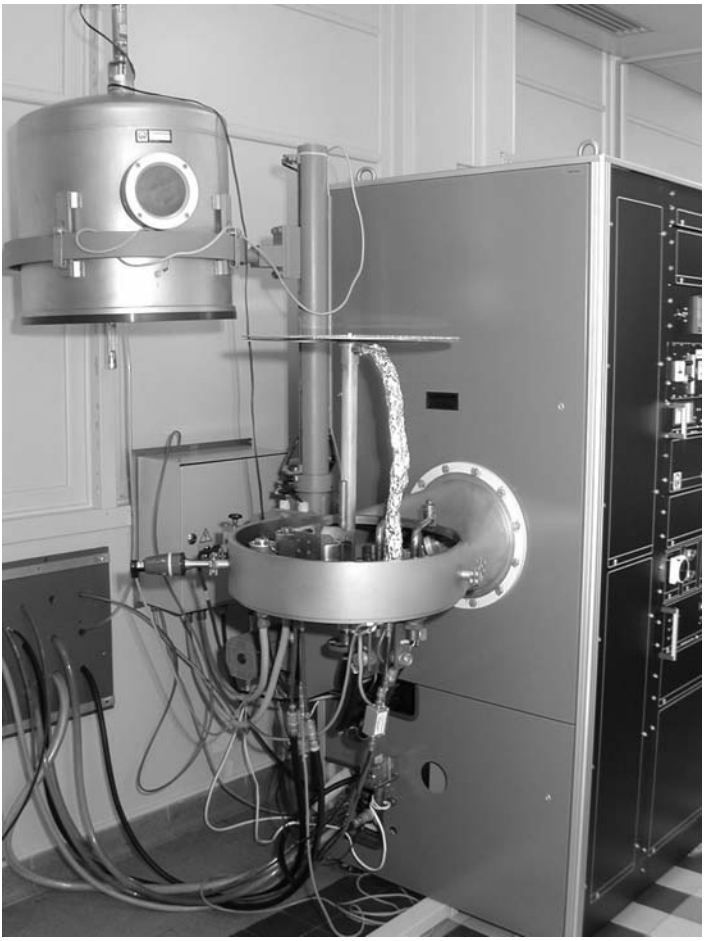

Figure 5.9: View on the evaporator clock of the Univex 450 system used for the deposition of alignment layers.

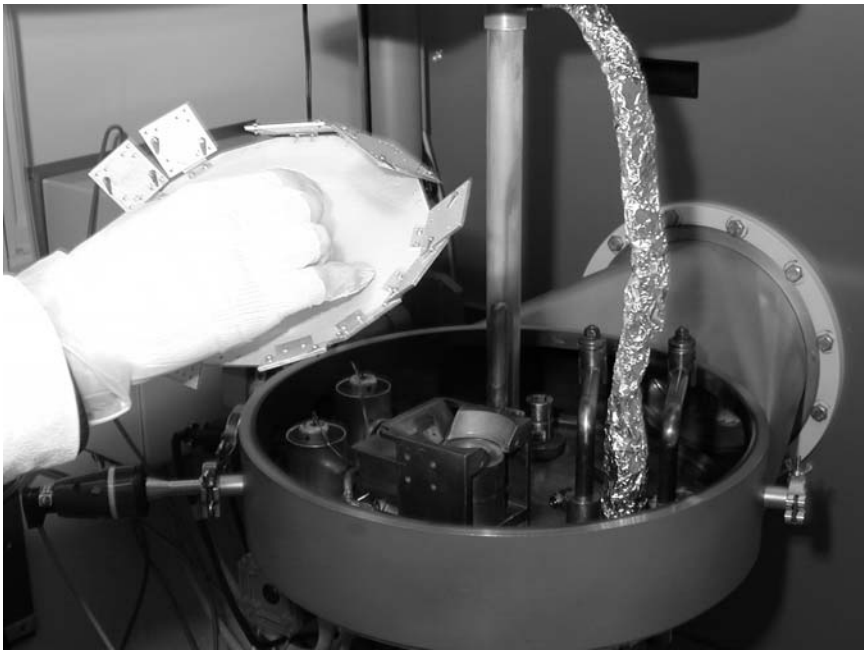

Figure 5.10: The carousel holder to mount the substrates for oblique evaporation. In the background the e-gun source in the clock is visible.

$$\mu = \frac{RT}{\sqrt{2}\pi d^2 p N_A} \tag{5.4}$$

This means the paths of the evaporated molecules can be considered straight lines coming from the source, there will be only limited scattering from source to substrate. With this assumption, the variation of incidence angles at the substrate can be calculated.

Looking at figure 5.11 and taking into account the dimensions given above, the worst case deviation can be determined. For the deviation in the first plane, coincident with the drawing plane, the deviation is limited by the opening in the shutter plates. An angular offset of only $\pm 2.0\,^\circ$ maximum is to be expected. Because of the rotation of the substrates, the incidence angles at every point of the substrate are averaged out, leading to a deposition under perfectly uniform conditions.

The deviation in the other reference plane actually depends on the size of the substrate. The largest substrates that have been coated were produced for the Mosarel project [14]; having a 50 mm diagonal they are by all standards huge microdisplays. For such substrates, the deviation is at most $\pm 3.2\,^\circ$. For more common devices having a diagonal of 18 mm (0.7 inch), the deviation is less than $\pm 2.4\,^\circ$. On neither of these cells, a pre-tilt variation over the substrate was detected. This is readily explained by the relatively flat slope of the relation pre-tilt angle to incidence angle at the considered interval. Another factor that helps uniformity is the pairing of top and bottom substrate, which can be done so that deviations at one side are cancelled out by an opposite deviation at the other side.

Problems will of course occur when very large substrates are to be coated, e.g. complete wafers. The dimensions of this type of evaporators are not suited for these sizes anyhow, so larger vacuum chambers must be used, which in turn will result in larger source to substrate distances and thus smaller deviations.

Resulting layers

The parameter space for the deposition process includes among others the incidence angle, layer thickness, evaporation speed, deposition temperature, evaporation pressure and so. All but two parameters were kept constant. Substrate heating was not used. Evaporation pressure is kept in the range 3×10^{-6} to 4×10^{-6} mbar. The effective deposition speed is 0.01 nm per second.

The incidence angle is varied in the range $40\,^\circ$ to $80\,^\circ$ (measured with respect to the substrate normal). The resulting pre-tilt angles are listed in table 5.1. Quasi-homeotropic alignment is obtained, and increasing incidence angles give higher pre-tilt angles. Above $50\,^\circ$ incidence angle, the orientation is very close to $90\,^\circ$. This seems consistent with the results published in [134]. The numbers are for 6 nm thick layers and MLC-6610 liquid crystal material. Other materials

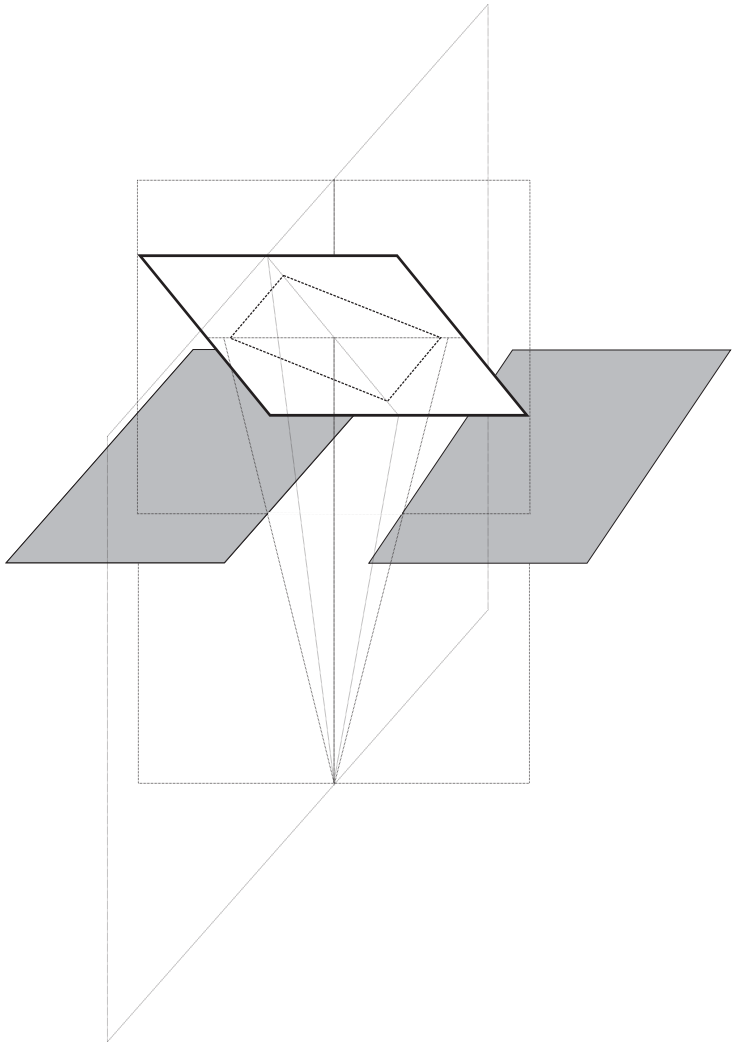

Figure 5.11: Detail of the evaporation geometry. The grey planes represent the shutter plates. The substrate holder is shown right above the opening, together with two orthogonal planes of reference intersecting the holder. The possible extent of the angular variation in these planes is also indicated. The contour in dashed lines shows how substrates are usually mounted.

Incidence angle	Pre-tilt angle
40 °	87.6 °
45 °	88.0 °
50 °	89.0 °
60 °	89.2 °
70 °	89.3 °
80 °	89.7 °

Table 5.1: Measured pre-tilt angles for different incidence angles using 6 nm SiO_2 layers and MLC-6610 liquid crystal

Liquid crystal mixture	Pre-tilt angle
MLC-6610	88.0 °
MLC-6609	88.6 °
MLC-6885	89.2 °
Mixture 1	89.3 °

Table 5.2: Measured pre-tilt angles for different liquid crystal mixtures using identical evaporation parameters for the alignment layer (6 nm SiO_2, 45 ° incidence angle). Mixture 1 is an experimental VAN mixture.

give slightly different numbers, but the general trendline is identical (see table 5.2.

Layer thickness was varied in the range of 5 to 10 nm. The layer thicknesses are monitored during deposition using the crystal oscillation method and verified afterwards with ellipsometry. All layers produce similar results with respect to the obtained pre-tilt angle (see figure 5.12). No trends could be detected, probably because the considered range is quite small. Thicker layers of 20 nm produced inconsistent results, with sometimes a broken alignment. Evaporation time also becomes uneconomically long for these thicknesses, so no further inquiries were made in this direction.

Anchoring Anchoring strength is most often described with the model put forth by Papoular [151]. The anchoring energy is split into contributions from a polar and an azimuthal component. It can be expressed as in (5.5), where θ and ϕ are the actual tilt and twist angles, respectively while θ_0 and ϕ_0 are the intended angles, K_1 the elastic constant and λ the respective coupling constants (in m) and W the anchoring energy in N/m. The coupling constants can be taken as a measure for the anchoring strength. For vertically aligned cells, only the tilt coupling is important.

$$W = \frac{\pi K_1}{2}\left(\frac{1}{\lambda_\theta}\sin^2(\theta-\theta_0) + \frac{1}{\lambda_\phi}\sin^2(\phi-\phi_0)\cos^2\theta\right) \tag{5.5}$$

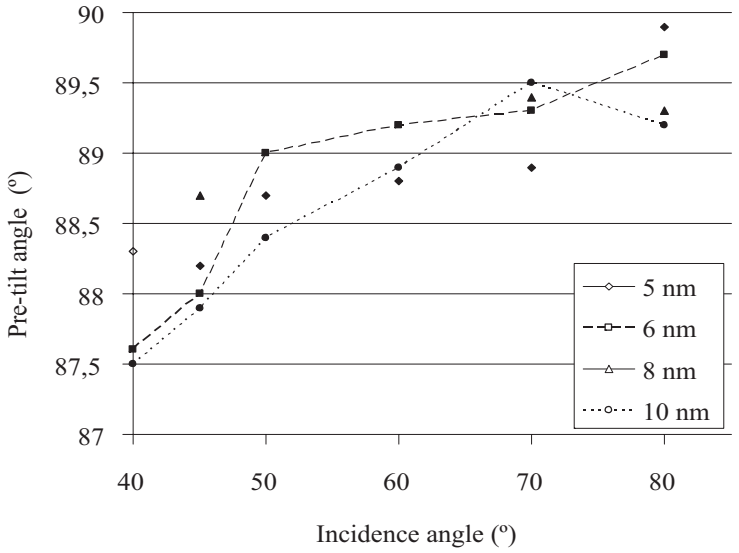

Figure 5.12: Measured pre-tilt angle versus evaporation incidence angle for some SiO_2 alignment layer thicknesses. Liquid crystal material is MLC-6610.

Extracted values for λ_θ are in the order of 10^{-5} m. This stands for only moderately strong anchoring, as polyimide layers, considered to exhibit strong anchoring show values in the range 10^{-6} to 10^{-8} m. It confirms the common knowledge that inorganic layers have inherently lower anchoring energies.

Anchoring strength varied only slightly with the thickness of the evaporated layer, and seemed to decrease with increasing layer thickness. The amount of variation is however small enough to be considered insignificant. Anchoring strength goes up for smaller incidence angles. The variation over the incidence angle range 40 ° to 80 ° is still less than 10 %. Figure 5.13 gives an overview of these trends.

Optimum settings From the above observations, optimum layer parameters were chosen as follows. The incidence angle is chosen in function of the desired pre-tilt angle; a value of 45 ° is used. This results in a pre-tilt angle of 88 °. The effective layer thickness is set at 6 nm. It provides a fair anchoring strength from what is available and avoids extreme values.

A key feature of the deposition technique and the chosen settings is the reliability and reproducibility of the produced alignment layers. The alignment properties are robust with respect to process condition variations and external factors during assembly.

Figure 5.14 attempts to quantify this reproducibility. Although a few hundred cells have been produced during this research, the amount of displays

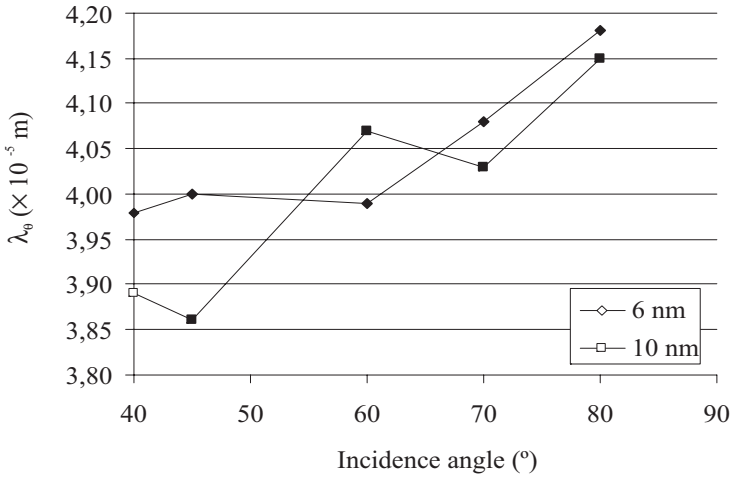

Figure 5.13: Measured anchoring energies versus evaporation incidence angle for 6 nm and 10 nm thick SiO_2 alignment layers. Liquid crystal material is MLC-6610.

with truly identical processing parameters is too low to perform a meaningful statistical analysis. From the data in figure 5.14, it is however fair to conclude that the variation on the resulting pre-tilt angle is well within $\pm 0.5\,^{\circ}$. The resulting change in contrast ratio may seem dramatic (e.g a measured on-axis contrast ratio ranging from 40000:1 to 120000:1) but has little impact on the overall performance because even at the lowest end of the range the contrast ratio of the cell is still not the limiting factor for the entire system.

Homogeneous alignment As a side project, homogeneously aligning layers have also been produced. Layer thicknesses between 10 and 20 nm indeed produce homogeneous alignment, while thicker layers tend to give homeotropic alignment. Best results are obtained with 20 nm layers and an incidence angle of $70\,^{\circ}$. Pre-tilt angle is around $1\,^{\circ}$.

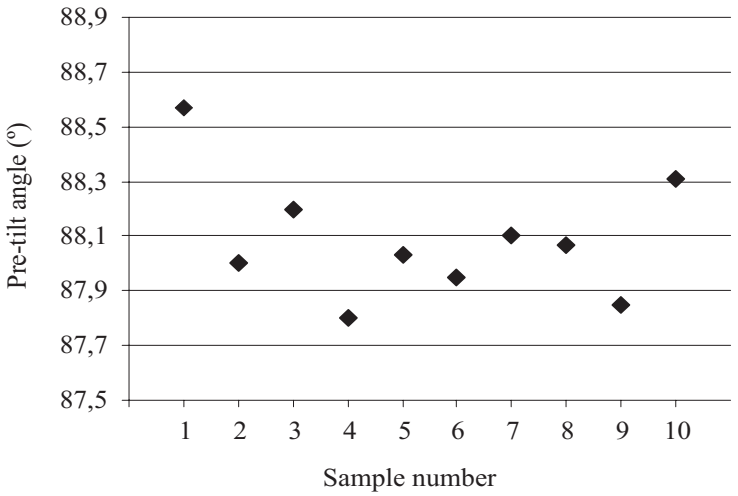

Figure 5.14: Measured pre-tilt angles on cells with identical evaporation parameter settings (6 nm SiO_2, 45 ° incidence angle). The samples include both cells that originate from the same evaporation cycle as well as completely unrelated evaporation batches.

Chapter 6

Cell assembly

6.1 Introduction

6.1.1 General

The cell assembly comprises the manufacturing of the actual cell, starting from the two substrates coated with an alignment layer. At first sight, this may seem a trivial or at the very least a well-known industrial practice, given the wealth of LC displays available in the stores. However, some serious pitfalls are present.

The nature of an LCOS microdisplay with respect to the manufacturing is somewhat different than closely related products such as AMLCD panels and poly-silicon lightvalves. In the active matrix panel business, the quest is now for ever larger screen sizes. In the LCOS microdisplay business, the trend obviously is in the opposite direction, bounded only by desired resolution and practical usefulness. Consequently, the size of a single LCOS display is usually still smaller than the tiniest direct-view screens.

Poly-silicon lightvalves do have approximately the same dimensions, but are manufactured entirely on glass substrates. The mismatch in materials for back and front substrate again sets the LCOS displays apart.

Finally, most of the traditional devices still employ transmissive LC modes. The switch from transmissive to reflective operation leads to a reduction of cell-gap width by one-half, further tightening assembly margins for the LCOS displays.

6.1.2 Wafer assembly versus cell assembly

Another issue that has to be dealt with is the distinction between cell based assembly and wafer based assembly. Unlike the flat-panel industry, which is

a completely integrated environment, the base substrate for LCOS displays is the wafer from the semiconductor fab. With microdisplays of 0.7 inch screen diagonal, an 8 inch wafer probably contains around 100 individual displays.

It is then tempting, and for volume production certainly preferable, to do the assembly on wafer scale, i.e perform as much assembly steps as possible on the entire wafer. In practice, this currently means the individual cells are cut out just before they have to be filled with liquid crystal. In future, the cut-out may even become the very last step if IBM's drop fill method [152] for ultra large panels can be adapted to very small liquid crystal amounts. A second advantage of this approach, next to the inherent high volume capability is the fact that the assembly machines developed for the manufacturing of larger TFT panels may be readily adopted for LCOS processing.

It should be noted however, that in the case of inorganic alignment layers the base substrate may not always be a wafer. If the constraints of the deposition equipment do not allow to coat an entire wafer within the specifications, there is no choice but to process individual dies. An industrial processing line might still be possible in this case, provided that the handling in subsequent steps can be fully automated. As will become clear further on, these steps are probably sufficiently basic to be performed by (dedicated) pick-and-place machines, so that high-volume production, comparable with the wafer-scale approach is within reach.

For the production of prototypes in a laboratory, a cell based approach is the recommended way. It obviously gives more freedom in the assembly process and controlling the parameters of each individual cell can lead to high quality devices. As a side note, since companies are generally not interested in this approach (a notable exception, using a proprietary cell based method, excluded), research in this area can still give some useful results.

In the remainder, a cell based approach is implicitly assumed. Most process steps are equal for both approaches. If needed, the wafer based variant will also be commented on.

6.2 Process Flow

The process flow given in table 6.1 is our standard assembly process for cell-based microdisplay manufacturing. It starts with a microdisplay die and a counter-glass sawn to the right dimensions. The actual assembly begins after the deposition of the alignment layer. For the wafer-based process, basically everything remains the same, except the starting substrates are now wafers and a 'singulate die' step has to be inserted before the filling step.

In the following paragraphs, some important aspects in the process flow will be commented on.

SILICON DIE	COUNTER-ELECTRODE
Clean	Clean
Deposit A.L.	Deposit A.L.
	Apply spacers by spin-coating
	Dispense sealing ring with UV-curable glue
Align and join die and counter-electrode	
Set cell-gap, fixation of the assembly	
Full cure of sealing ring	
Fill cell with liquid crystal	
Dispense end-seal cap	
Full cure of end-seal	

Table 6.1: Process flow for a cell based assembly

6.2.1 Glass material

Compatibility

First of all, the glass must of course be compatible with the liquid crystal. This comes down to the well-known requirement that it may not release ions (most notably potassium) during its lifetime. Consequently, if soda-lime glass is used, a diffusion barrier layer must be present. More expensive glass kinds who do not have this limitation, like borosilicate glass , may be strongly preferred. The additional cost will generally turn out to be negligible compared to the cost of the silicon substrate. Moreover, borosilicate glass is the proven substrate of the AMLCD industry and thus widely available and thoroughly studied.

As the two base substrates are made of different materials, it is advisable to choose the glass such as to minimise the mismatch in thermal expansion . This will facilitate the assembly procedure, especially regarding the uniformity of the cell gap. Again, borosilicate glass has excellent properties in this domain and can be manufactured to match the expansion coefficient of silicon as closely as possible [153].

In all our experiments, Corning 7059 or its successor Corning 1737F, both borosilicate glasses, have been used.

Mechanical properties

The elastic modulus of the glass substrate is generally somewhat lower than the one for silicon. The silicon die, which will inevitably exhibit some bow and warp, has to be laminated onto the glass while maintaining a good cell gap uniformity. It is therefore important that the glass substrate is thick enough to withstand the bending forces. On the other hand, too thick substrates will also make the assembly more difficult. The needed thickness naturally should depend on the silicon thickness, which varies with the wafer size. During this

research, silicon substrates coming from wafer sizes ranging from 4 to 8 inch have been used which translates to a silicon thickness of 650 to 850 μm. For all these sizes, good results have been obtained with 0.7 mm thick glass.

The flatness of the high quality float glass can safely be considered sufficient for our purpose, as it is the industry's standard substrate. If single dies are assembled, only the micro-roughness (originating from the variation in size of individual crystals) of the glass can play a role. On wafer scale, the so-called micro-corrugation (sub-micrometer variations with a period of several millimetres) will be dominant [81].

Lastly, it should be noted that glass also ages and becomes more brittle. This is usually termed atmospheric weathering. Borosilicate has excellent weathering resistance, but it may nevertheless be advisable not to use too old glass for the assemblies.

6.2.2 Cleaning

Since both substrate sides have to be coated with a very thin layer, the functionality of which the entire display depends on, the usual cleaning steps for thin-film coatings should be performed.

Silicon

The silicon part normally arrives directly from the cleanroom where it has been processed and should therefore be of high quality. The sawing step has however probably introduced some debris and the transport inevitably deteriorates the surface quality somewhat. Unless there are serious counter-indications, a soft clean step should suffice. This normally comprises an acetone, acetone / isopropanol / de-ionised water soak sequence.

Glass

For the glass substrates similar considerations apply. Care has to be taken for the edges of the glass, where tiny splinters, left over after the cutting, can still be covered with ITO and thus cause a short circuit between the counter electrode and the top metal surface. It depends on the design of the backplane whether this is harmful or not. Bevelled glass edges eliminate this problem, but are relatively expensive.

The sawing related problems are of course irrelevant in the wafer-based process, but there the debris problem will pop-up after the singulation, just before the filling. A clean cutting process is then mandatory, as the removal of particles at this stage is not evident.

6.2.3 Spacers

General

The spacers help maintain the distance between the two electrodes at the desired value. Usually, there are spacers at the sealing ring and in the active matrix. Spacers are available in two variants: so-called hard and soft spacers. The former are made of silica, mostly in the form of chopped fibre, have high compression strength but may pulverise if overloaded. They are mostly used in the sealing ring, because they may scratch the active matrix surface. The latter are made of organic materials, featuring a lower compression strength and larger elasticity but still high breaking strength. They are ideal for use in the active matrix.

In our technology, the Micropearl SP series round plastic spacers from Sekisui are used for both the sealing ring and the active matrix. The Micropearl spacers are made of divinylbenzene and are primarily intended as in-cell spacer. It is however perfectly possible to use them as an all-round spacer. From a mechanical viewpoint, the main difference with the conventional sealing spacers is the higher elasticity of the former. This is advantageous for an in-cell spacer: it allows it to adapt to the expansion and reduction of the liquid crystal layer due to temperature changes. If used as a sealing spacer, the elasticity will have to be taken into account while determining the initial cell gap.

Application

In-cell spacers Because of the acuity of the human eye for regular patterns, it is best that the spacers inside the active matrix be randomly distributed. For larger substrates, this is done by spraying the spacers over the substrate. For smaller substrates, reproducibility and uniformity of this procedure is hard to control and another method is preferred.

On the small glass substrates, spacers are applied using a spin-on technique. The spacers are dissolved in methanol and dispensed over the fast spinning substrate. Similar to the spin-coating technique, this results in a thin film of spacers and solvent. When the solvent has evaporated, the spacers adhere to the substrate. For small substrates (< 5 cm) that do not deviate too much from a square form this gives, somewhat counter-intuitively, uniform distributions.

Methanol was chosen as the solvent because of its high evaporation rate. It does not leave any residues and appears not to interfere with the action of the alignment layer. Other more common solvents like isopropanol do leave traces; water on the other hand is hard to remove and harmful for the alignment layer and the liquid crystal. To make sure all methanol is removed, the substrates are subjected to a short bake step on a hotplate afterwards.

Preparation Normally, spacers are delivered in dry form, as a powder. Adhesion between particles of this size can be quite strong and clustering is thus often observed. To avoid large conglomerates of spacers obscuring pixels, clusters can be removed just before dispensing by briefly submerging the solution in an ultrasonic agitation bath. Cylindrical spacers suffer less from clustering, but they can fall on top of each other and subsequently get crushed during lamination, causing equal damage.

Sealing ring spacers The spacers for the sealing ring are simply mixed into to glue. Clustering is not so important here, but a good mixing process is needed to ensure an even ratio of spacers and glue throughout the sealing ring.

Spacer distribution density in the sealing ring

The needed distribution density of spacers inside the sealing ring can at first be calculated based on the highest external load the display substrates are expected to withstand. If properly conceived, this peak load should occur in the assembly itself, during the lamination process.

To set up a calculation example, the dimensions of the XGA chip design can be used as a reference. The active matrix area measures 18.5 mm by 14.0 mm. In our process, the pressure during lamination is set at 3 bar. Supposing the sealing ring is placed exactly adjacent to the active matrix and further supposing it is by itself 1.0 mm wide, the pressure extends over an area of 20.5 mm $\times$ 16 mm = 328 mm^2. At 30 g/mm^2 this gives a total load of 9840 g or almost 10 kg.

A first obvious requirement is, of course, that the spacers may not be crushed, so the breaking strength is not exceeded. Using the empirical formula (6.1) provided by Sekisui [154], the approximate crushing strength of a single spacer can be calculated.

$$P = 38.4D^{1.75} \qquad P\text{: [kg]}, \; D\text{: [mm]} \tag{6.1}$$

For a 3.0 μm spacer this gives 1.47 g maximum load per spacer. Neglecting the possible presence of in-cell spacers, which have a much lower distribution density anyway, all spacers are to be located in the $2 \times (18.5 \text{ mm} + 14.0 \text{ mm}) \times 1.0 \text{ mm} = 65 \text{ mm}^2$ area of the sealing ring. To prevent crushing, a minimum density of (9840 g / 1.47 g/spacer) / 65 mm^2 = 103 spacers/mm^2 is needed. Obviously, this is a very low number. As could be expected, it also is not a very realistic number because only the integrity of the spacer is taken into account and dimensional stability is totally ignored.

Cell-gap considerations A better estimate is obtained by defining a desired minimum cell gap. If the plastic spacer is subjected to a compression force during the lamination, it will deform. The effective diameter will shrink, so in

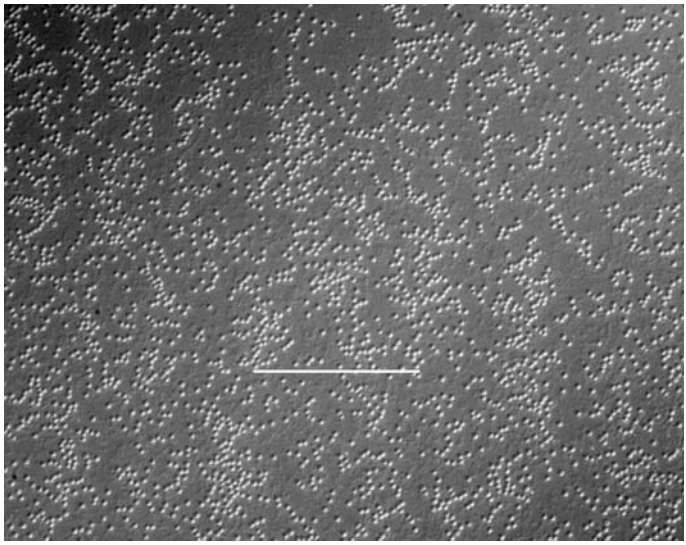

Figure 6.1: Micrograph of the spacer distribution inside the sealing material. The white bar is 100 μm long.

order to keep the cell gap at the desired value, the compression will have to be limited, as the curing of the sealing ring irreversibly fixes the cell-gap.

Setting forth a maximum diameter reduction of for example 5 %, the density calculation can be repeated to obtain a more realistic value. The actual cell-gap would then be 2.85 μm. The compression force corresponding with a 5 % diameter reduction for 3.0 μm spacers can be extrapolated from the data provided by Sekisui for larger diameters (see appendix). At 0.022 g per spacer, a 10 kg load then requires 454000 spacers or a distribution density of 7000 spacers/mm^2.

Figure 6.1 shows the resulting actual spacer distribution density used in the sealing ring. An average number of 20000 pcs/mm^2 is obtained. The initial cell-gap thickness will thus be only slightly lower than the 3.0 μm value.

Spacer distribution density in the active matrix

Just as for the sealing ring, the spacer distribution density in the active matrix cannot be set to an arbitrary value. There is a minimum density below which the spacers do not contribute anything to the mechanical stability. The upper bound is set by the fact that the spacers must remain invisible to the largest extent possible. Commonly encountered density values are in the range of 50 to 200 spacers/mm^2, with 100 as a fair average.

A calculation of the spacer distribution density can be based on the ability to prevent local deflections of the substrate.

Deformation of a sphere The compression behaviour of an elastic sphere on a rigid plate is governed by equation (6.2) [155]. F is the compressive force, r the radius of the sphere, s the effective diameter reduction, E the elastic modulus and ν the Poisson ratio.

$$s = 2F^{\frac{2}{3}} \sqrt[3]{\frac{9(1-\nu^2)^2}{16E^2 r}} \tag{6.2}$$

Usually a compressibility modulus K is defined as in (6.3), so that (6.2) can be transformed into (6.4).

$$K = \frac{E}{1-\nu^2} \tag{6.3}$$

$$F = \frac{\sqrt{2}}{3} s^{\frac{3}{2}} K \sqrt{r} \tag{6.4}$$

For a truly elastic material, the value K should be constant as it is fully determined by material constants. Measurements showed that for the Micropearl spacers, K depends both on the particle size and the compression rate [154]. Some K values can be found in the appendix.

Calculation example The starting situation now consists of 3.0 μm spacers which have been pre-compressed by the lamination process to 2.85 μm (5 % compression). Again as an example, an additional deviation of 5 % to this gap is allowed. This amounts to 142.0 nm and is a fair criterion in view of the cell gap tolerance of the vertically aligned mode. Using equation (6.4) the forces needed to compress the spacer to 2.85 μm and 2.7075 μm can be calculated. As a first approximation, the known K_{10} value for 5.0 μm spacers is used in both.

The difference between the two loads, $0.06367\ \mathrm{g} - 0.023385\ \mathrm{g} = 0.040285\ \mathrm{g}$ is the additional external load that can be allowed. With the spacer distribution density of 100 pcs/mm^2, this gives an additional allowable local pressure of 0.4 kg/cm^2, a very reasonable number in view of the tight requirements.

Figure 6.2 shows the spacer distribution density in the active matrix on a sample cell. The density amounts to approximately 100 spacers/mm^2.

Substrate influence In the preceding calculations, the influence of the substrates themselves has been totally neglected. In practice, the silicon substrate is usually glued onto a rigid carrier board (e.g steel) so the counterglass is the only part that can still deform.

The maximum deflection of a uniformly loaded rectangle, clamped at the sides, is given by formula (6.5). The pressure is denoted by p, L_x and L_y are

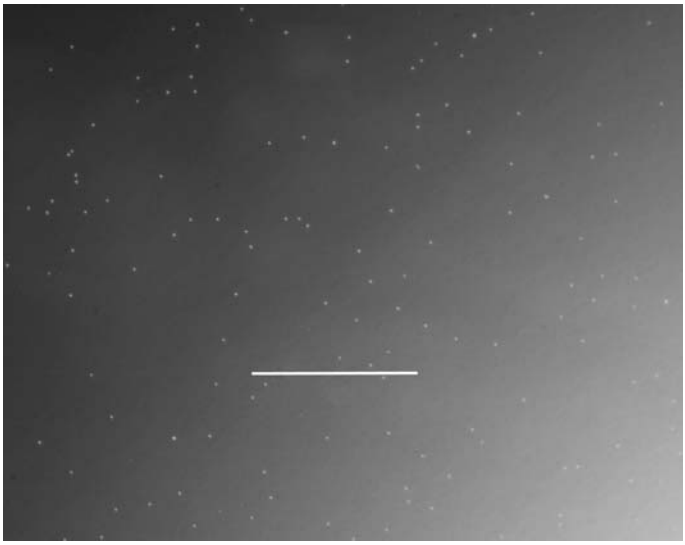

Figure 6.2: Micrograph of the spacer distribution inside the active matrix. The white bar is 200 μm long.

the length and width of the rectangle respectively, τ is the thickness and E the elastic modulus.

$$w_{max} = \kappa \frac{p \min(L_x, L_y)^4}{E\tau^3} \tag{6.5}$$

$\max(\frac{L_x}{L_y}, \frac{L_y}{L_x})$	1.0	1.2	1.4	1.6	1.8	2.0	∞
κ	0.0138	0.0188	0.0226	0.0251	0.0267	0.0277	0.0284

According to (6.5) and using the material constants for the Corning 1737F glass (see appendix), the same uniform load of 0.4 kg/cm^2 allowable for a 5 % deviation using spacers would give a peak deflection of 1.366 μm if no spacers where present, almost tenfold the allowed deflection that was set forth for the spacers. This illustrates both the validity of the approximation and the substantial contribution of spacers to the stability of the cell gap.

Precautions

It should be noted that all of the above calculations, both for the sealing and active matrix distribution density, should be treated as a very rough first approximation only. More refined calculations can be carried out, e.g by taking into account the statistical nature of the spacer particle size distribution, the

dependence of the compressibility value upon this distribution, temperature effects, creep, and so on.

In the case of the in-cell spacers, the liquid crystal layer itself has been totally ignored in the calculations. Being an almost incompressible liquid, it can contribute substantially to the cell-gap stability, provided the cell is properly filled.

In conclusion, it should be kept in mind that truly accurate and reliable predictions of resulting cell gaps are almost impossible and only experimental verification can determine the right parameters.

Alternatives

Two other approaches to the cell gap stability issue may be encountered.

Placed spacers The placed spacers technique uses an additional step at the semiconductor foundry to produce tiny studs of insulating material in the inter-pixel area intersections throughout the active matrix [156]. Polymer studs have also been reported [28, 157]. In the sealing ring, either densely packed studs are used as well, or conventional spacers are employed.

The placed spacers technique enables a very high accuracy for the height of the spacers. On the downside, mechanical strength usually requires higher densities than in the conventional approach. The studs should be small enough to remain invisible, which means that for current matrix designs the cell gap must be around 1 μm, otherwise the aspect ratio of the studs becomes too high to be stable.

The studs also disturb the alignment. Since they are present before the application of the alignment layer, they either prevent the rubbing in their vicinity or cast a shadow during the evaporation of an inorganic alignment layer. Both result in comet-shaped defects behind the placed spacers where no alignment can take place. For a great number of liquid crystal modes this is not really an issue, since the mere presence of a spacer already causes a larger halo-shaped defect to occur because the liquid crystal structure cannot adapt to the shape of the spacer. For some modes, like the vertically aligned, this is not true and the comet shaped defect can be annoying.

No spacers In the spacerless approach, no spacers at all are present in the active matrix. The uniformity of the cell gap is entirely dependent on the forces exerted at the edges of the substrates and the stability largely depends on the incompressibility of the liquid crystal fluid. A frequently used adaptation intended to ease the uniformity requirements in this case is a double sealing ring [14].

Having no spacers in the active matrix bans the possibility of having any artifacts showing up in the image due to disturbed alignment or scattered light.

6.2.4 Sealing ring

Purpose

The sealing ring has two functions: it must contain the liquid crystal and protect it from outside influences, and it must maintain the lamination of silicon and glass, taking special care of the cell gap uniformity.

The former function requires chemical inertness with respect to both the liquid crystal and the substances of the intended environment and also an impermeability for these substances. For normal environments, permeability of moisture is the main concern. The latter mainly requires good adhesion and bonding strength, together with evident requirements about reliability and aging.

Several types of glue are in use as sealing material. For an overview and selection criteria, see the section on material selection.

Application

In the flat-panel industry, the sealing ring is usually applied with a printing machine, through a stencil. This is a quick and efficient technique, but the smaller dimensions encountered in microdisplays make it quite difficult to merge it into the assembly process. In the particular case of inorganic alignment layers, the printing process can even be harmful to the proper functioning of that layer. Hence, for microdisplays, dispensing is the technique of choice.

Seal dimensions The final height of the sealing ring is set by the desired cell-gap, so in the current technology this will be very near 3.0 μm. The chosen width should be the result of a compromise. As the price of the silicon substrate is very high, there is a strong incentive to keep the area reserved for the sealing ring as small as possible, especially if it already exceeds the space needed for the peripheral integrated driving electronics. On the other hand, mechanical stability, impermeability and reliability all benefit from larger widths. A 300 μm sealing width has occasionally been reported [158], but mostly a width in the range of 650 to 1000 μm is encountered.

Setting forth a width of 750 μm, the cross-sectional area encompasses 2250 μm^2. At dispense time, this could for example be realised with a 60 μm wide and 40 μm high line, taking into account the cross section will be parabola-shaped. This kind of resolution is attainable with today's dispensing machines, provided some care is taken. For example, the glue viscosity should be well chosen. Watery fluids and high viscosity pastes are not very suited for high-precision dispensing. Ideal results are obtained if only moderate pressure has to be applied to the fluid. It is evident that smaller cell-gaps will quickly demand a more relaxed width specification.

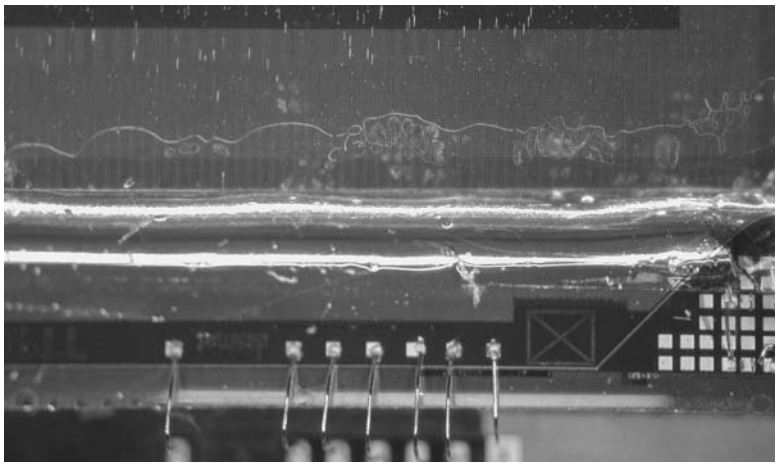

Figure 6.3: Micrograph of part of the sealing ring on a XGA cell.

Dispensing technique For laboratory research, semi-automatic or even manual dispensing is mostly used. Figure 6.3 shows a detail of a manually placed sealing ring on an XGA device. The maximum space foreseen for the ring between the active matrix and the bondpads is 1.4 mm, the actual width of the ring averages around 700 μm.

During this research, sometimes a different technique was used to circumvent the tight dispensing requirements.

A number of tiny drops of glue are dispensed at the border of the glass with a certain distance between them. The glass and the backplane are then pressed together and once the right cell gap is reached, this pre-assembly is fixed by curing the glue drops. The actual border seal can then be dispensed against the rim of the counter electrode with less worries about the exact amount of glue needed. Capillary forces will drag the glue inwards into the cell; when the desired seal width is reached, progression is stopped immediately by snap-curing the glue.

This two-step method enables the use of very thin seal borders together with small cell gaps but does not always give good uniformity, because the pre-assembly is not so strong.

6.2.5 Lamination

General

During the lamination step, the substrates are joined together while setting the cell gap value and its spatial uniformity.

The ease by which uniform cell gaps are obtained depends somewhat on the

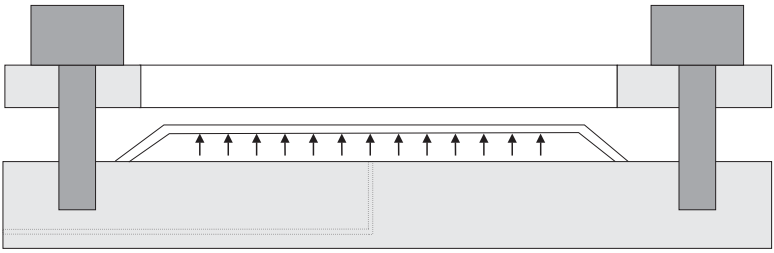

Figure 6.4: Sectional view of the press used for laminating the substrates. The top plate contains a glass window and is attached to the base with bolts. In the base a rubber cushion is mounted that can be inflated to provide an evenly distributed pressure.

bow of the substrates. Concave substrates, i.e. substrates where the centre-points for the radii of curvature are at the circuitry side, are the easiest to straighten out. Convex ones are more troublesome as most of the load needed to flatten out the bottom substrate has to be taken up by the in-cell spacers first. Bodammer [159] reported mostly convex silicon substrates for his FLC microdisplays. In our research, the silicon substrates turned out to be mostly concave.

Wafer-scale versus die-scale The above remark pertains to the die-scale approach. Obviously, lamination on wafer-scale and die-scale shows quite some differences. The bow of a single die is not the same as the bow of an entire wafer. Moreover, after singulating a wafer into individual cells, the stresses exerted on those cells are not the same as before the singulation, so their cell-gap may still change.

For wafer-scale assembly, the lamination usually takes place between two surfaces of proven flatness and parallelism which are actuated using some kind of servo-system. Both the long and short distance curvature must be removed in one step.

For the die-scale approach, several simple methods are in common use, ranging from pressing with weights [81] to vacuum compression. In this research, a press was used most of the time (see figure 6.4).

Press

The top part of the press consists of a removable window containing a thick sheet of glass with known flatness. The bottom side has a cushion of silicone rubber on which the assembly is placed, glass side upward. The window is put on top of the cell and screwed tightly to the base, after which the air pressure beneath the cushion is increased. This provides a very uniform compressive load over the whole cell area and forces the cell to adapt its form to the flat

window surface. Once a satisfying uniformity is reached, the UV-sensitive sealing material can be cured through the window.

The applied pressure must be adapted to the rigidity of both substrates. For the sizes and thicknesses of substrates used in this research, a value of 3 bar gave consistent good results. In the previous section on spacers, it was already demonstrated that the sealing ring spacer distribution density is adequate to take up this load. However, since the substrates are not infinitely rigid, they will bend under the load and the spacers inside the active matrix will also be compressed. It has to be verified whether this has no adverse effects either.

As already explained, the counter electrode plate is pressed against the window of the press, which can be considered as infinitely rigid, so only the silicon substrate will bend. Again using formula (6.5), we can calculate the maximum deflection of this backplate and end up with 5.7 μm. So in a first rough approximation, it can be stated that this substrate will have no significant influence and the compressive load will be entirely taken up by the spacers. At an in-cell spacer density of 100 pcs/mm^2 this gives 0.3 g per spacer, still conveniently far away from the breaking threshold of 1,47 g.

Lamination results

To judge the degree of uniformity of a cell, double-beam interferograms are used. The cell is illuminated with an extended quasi-monochromatic light-source, e.g. an optically extended laser-beam. The light reflected at the liquid crystal - glass interface and the light reflected at the pixel mirror interfere with each other and produce fringes of equal thickness. Each fringe then corresponds to a thickness variation of $\frac{\lambda}{4n}$.

Figure 6.5 shows some results of the lamination process. The cell pictured on the left was laminated with a simple weight, while for the right one the press was used. The numerous fringes in the former reveal a cell-gap variation that exceeds 1 μm, completely unacceptable for an originally intended cell-gap of 3 μm. In the latter, the cell-gap variation is barely enough to produce a single transition from maximum to minimum brightness, meaning the cell-gap variation is below 150 nm or less than 5 %.

An idea of how this translates into brightness variations on an uniform grey-level image is given by figures 6.6 and 6.7. For a number of driving voltages, the reflected light is calculated as function of the cell-gap value. In figure 6.6 this is done for a single wavelength of 550 nm. The graph represents a worst-case scenario, as it also takes into account interference phenomena. Actual light sources like arc-lamps emit only partially coherent light at best. Figure 6.7 shows the variation of the integrated reflectance over a number of wavelenghts. Only the wavelength band for green has been taken into account and a uniform lightsource spectrum (e.g. a xenon-lamp) was assumed.

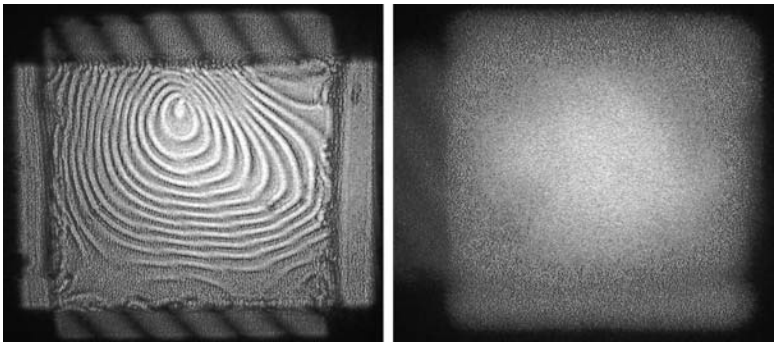

Figure 6.5: Uniformity of the cell-gap. Left a particularly bad example, right an excellent one. Monochromatic illumination at 645 nm. The cell is filled with liquid crystal, average refractive index 1.5.

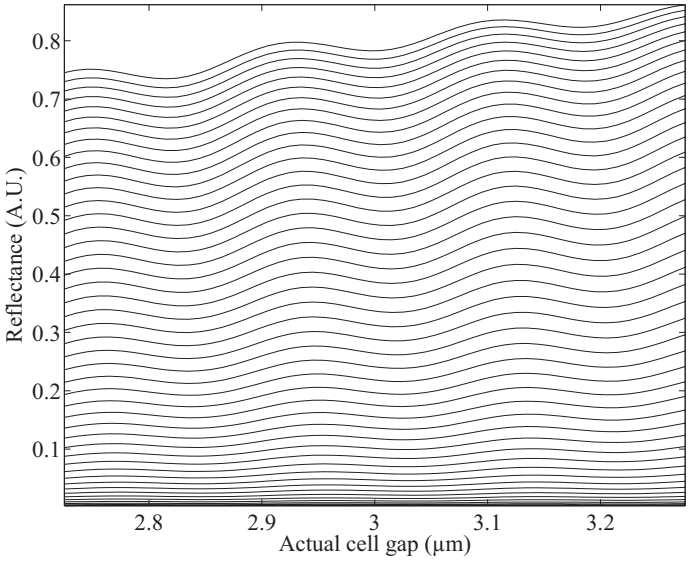

Figure 6.6: Reflectance versus cell-gap thickness for increasing driving voltages, calculated for a single wavelength at 550 nm.

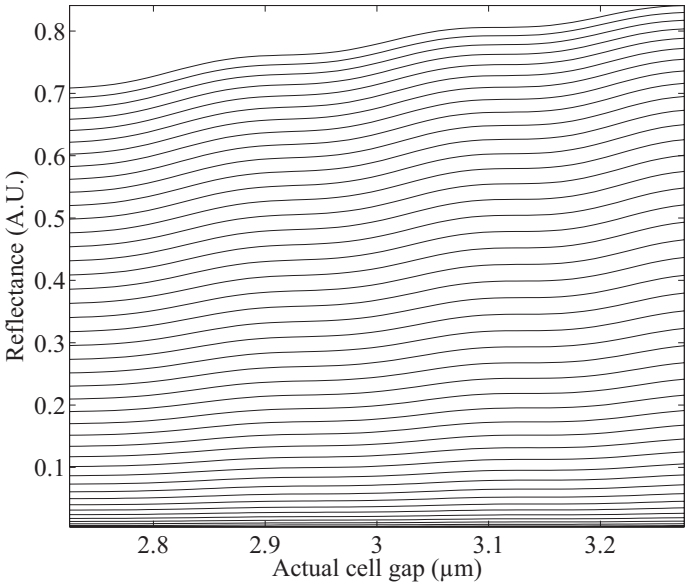

Figure 6.7: Wavelength-integrated reflectance versus cell-gap thickness for increasing driving voltages. Integration occurs over the wavelength band of the green channel (500 nm to 600 nm).

6.2.6 Filling

Industrial filling methods

Most liquid crystal devices are filled with the vacuum method.

During the dispensing of the sealing ring, an opening is left at one side of the cell. For the filling, the cell is put in a chamber which is pumped down to vacuum. Once the vacuum level is sufficient, the open side of the cell is brought into contact with liquid crystal in a small reservoir so that the inner part of the cell is sealed off. The pressure in the chamber is then gradually increased, so the liquid crystal is pushed further and further inside. When the pressure on the in- and outside of the cell is in balance again, the cell is completely filled and the sealing ring can be closed.

Normally a so-called liquid crystal filling tray is used to contain the liquid crystal. It consists of a long, shallow gutter, slightly wider than the filling opening made of metal or Teflon. When filled with liquid crystal, the surface tension of the latter causes the meniscus to protrude above the rim of the filling tray. The cell to be filled is gently lowered until the liquid crystal bridges the gap and the filling opening is immersed. The procedure is illustrated in figure 6.8.

This method is very well suited for industrial use, because it allows the

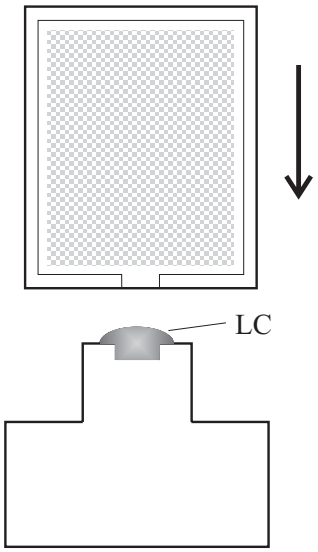

Figure 6.8: Illustration of the vacuum fill method with a filling tray.

filling of many identical cells at a time. Moreover, it does not need much excess liquid crystal to actually be able to fill something and the contact area between cells and liquid crystal is very limited, which keeps contamination low. The downside is the delicate contact between cells and liquid crystal while filling. Even small mechanical disturbances may break the continuous flow of liquid crystal, causing voids or even interrupting the filling process. It is therefore needed to have carefully designed dedicated holders for the cells, otherwise yield will be very low.

Drop-fill method Virtually all flat-panel AMLCDs are filled in the way described above, from tiny poly-silicon lightvalves to LCD TV panels. Only recently, with the advent of very large panels (Generation 5 to 7), this method is abandoned [160]. Because the filling time is proportional to the panel area, the waiting time needed for the filling to complete becomes uneconomical. For these panel sizes, nowadays IBM's drop-fill method [161, 152] is used. In this approach, the exact amount of liquid crystal is dispensed beforehand on one of the panels. There is no filling opening anymore, so when the panels are laminated onto each other, the entire assembly is finished in this one step. It speaks for itself that this requires accurate tooling of the process and in fact shifts difficulties to the interaction between liquid crystal and the uncured sealing material.

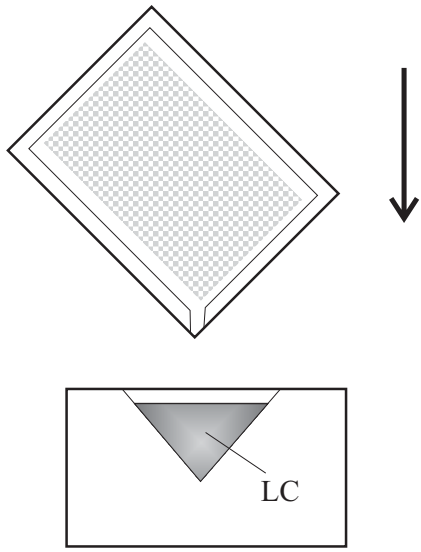

Figure 6.9: Illustration of the submersion fill method.

Filling methods for research

In research, many different cell sizes and formats may have to be filled, so the filling tray is not the most adequate tool for the job. During our research, a submersion method, being a variation on the traditional vacuum method, was used.

The recipient for the liquid crystal is made large enough so the part of the cell with the filling opening can be submerged. This is mostly efficiently done when the filling opening is placed in a corner (figure 6.9). Now any reasonable size of substrates can be filled, and the sealing of the vacuum inside the cell is much more robust. The disadvantages are of course the larger amount of excess liquid crystal that is needed and the fact that the cell is actually washed in the liquid crystal, which contributes significantly to the contamination of the mixture. Figure 6.10 shows the filling equipment used during this research: the vacuum clock with a built-in actuated cantilever to move the cell up and down above the liquid crystal reservoir.

Capillary filling Another method that is sometimes used is capillary filling [74]. Here two, preferably wide openings are left at opposite sides in the sealing. A drop of liquid crystal is put at one opening, and capillary forces will drag the fluid further inside the cell-gap until it is completely filled. This method is relatively simple, but it has some drawbacks. Air can quite easily get trapped during the filling process, resulting in incomplete filling. There is also more risk of contamination, the filling speed depends on the cell gap but is generally

Figure 6.10: Vacuum clock with actuator for the submersion fill method.

quite low and the end seal area is much larger. For all these reasons, this method has not been used in our research.

Single drop method At the beginning of our experiments, a filling method very similar to the drop fill method was used.

On one substrate a preliminary sealing ring was dispensed in the form of dots. The number of dots is not enough to make a closed sealing ring after lamination but the adhesion strength is already high enough to fixate the assembly. On the same substrate a drop of liquid crystal is dispensed which should be large enough to cover the whole area. The top substrate is then laminated onto the other one, spreading out the liquid crystal. Because the sealing ring is not closed, the excess liquid crystal can escape in-between the glue drops. Curing the glue fixates this pre-assembly. Excess liquid crystal is cleaned off and the final sealing ring can be dispensed against the edge of the substrates.

The main problem with this method is of course the possible interaction of the liquid crystal and the wet sealing glue. Although certainly suitable for certain devices, as was later proved by IBM, in the specific case of inorganic alignment layers this approach posed to much problems in an early stage and was therefore abandoned. It remains however a very interesting route, as it could enable a wafer-scale assembly up to the final step.

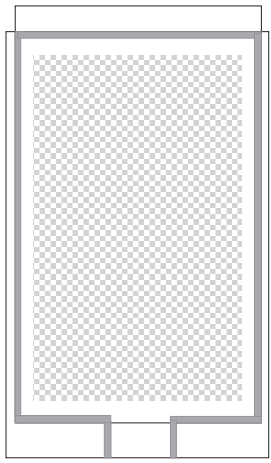

Figure 6.11: Entrance zone at the filling opening.

6.2.7 End seal

Application

As a last step, the cell has to be closed after the filling. This is a more delicate step than the main seal, as the wet glue now comes into contact with the liquid crystal.

Choosing the right glue minimises the interaction but there will always be an interface zone where the alignment of the liquid crystal will be disturbed. It is evident that this zone should not get into the active matrix area. Keeping the filling opening small is one option but is limited by the fact that the filling speed and reliability cannot be jeopardised. A trick that is often used is to provide an entrance zone (fig 6.11). This localises potential problems outside the active matrix and even makes the filling easier but wastes some additional silicon.

For mechanical strength and reliability, the glue of the end seal should enter the gap between the substrates for at least a few hundred micrometer. This is mostly achieved by applying a tightly controlled pressure on the cell beforehand, expelling a fraction of the liquid crystal. After the end seal is dispensed, the pressure is released, so the glue is dragged inside. Figure 6.12 shows the resulting end seal using this procedure. A possible complication with this method is that it may disturb the carefully obtained cell gap uniformity.

Calculation

To get an idea of the pressure needed, the following rough approximation procedure can be used. If in the centre of the display a localised, as yet unknown

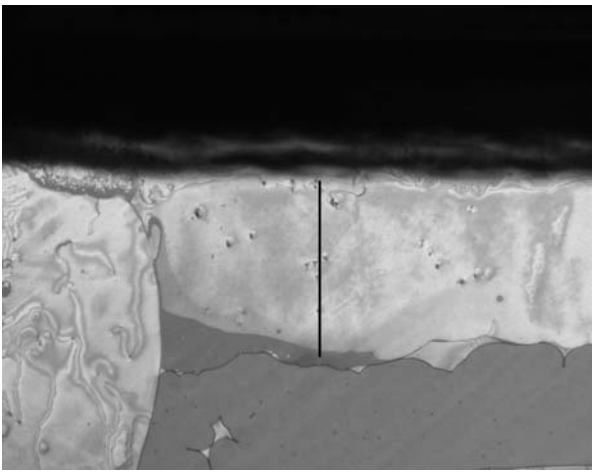

Figure 6.12: End seal glue dragged in between the substrates at the filling opening. Left is a part of the main seal, the horizontal stretch belongs to the end seal. The reference bar is 500 μm high.

pressure is applied, the counter glass will deform. This deformation can be idealised as a linear one, going from the its maximum value in the centre to zero at the borders. The amount of liquid crystal expelled is then the volume of a cone, having the maximum deformation as height and a circular base surface with a radius being the average of the rectangular sides. This volume will be replaced with glue once the pressure is released.

If the glue should enter the display about 500 μm and the filling opening is 3 mm wide, 500 μm $\times$ 3000 μm $\times$ 2.85 μm $= 4.27 \times 10^6$ μm^3 are needed. The height of the cone and thus the maximum deformation then comes down to $4.27 \times 10^6/(\pi \times 8000^2/3) = 0.0637$ μm. Using formula (6.4) and a spacer density of 100 pcs/mm^2 this gives 0.053 kg/cm^2 for the local pressure. Again, this is only a rough approximation. In practice a uniform pressure will be applied, often through a rubber cushion, instead of a point load.

6.3 Material selection

6.3.1 General considerations

The adhesive used for the sealing ring is of crucial importance to the functioning and reliability of the device. Ideally, it should have good mechanical properties such as high adhesion strength, high breaking strength and high ductility combined with chemical characteristics such as inertness to other substances (especially the liquid crystal) and impermeability to water. Of course, these characteristics should not deteriorate with time. Additionally, for productiv-

ity's sake it would be advantageous if the material is easily handled and applied and poses no environmental problems.

In practice, the adhesive will always be a polymer. Moreover, thermosetting polymers are preferred over thermoplastics in view of the mechanical and chemical stability that is required.

Polymer adhesives are among others differentiated by the way the polymerisation is started. Commonly encountered systems include the addition of thermal energy (heat curing), mixing with a second component like a hardener, a co-polymer or a primer (two-component systems), the presence of a substance like water vapour or oxygen and the irradiation with UV-rays. The polymerisation type affects mainly the ease of handling of the material. In principle, the kind of curing mechanism can be chosen freely, but from a production point of view, it is beneficial to keep cycle times short so rapidly curing adhesives will prevail.

The base molecule of the polymer is of course another main characteristic. Classical adhesives comprise silicones, polyesters, polyimides, cyanoacrylates, mercaptoesters, poly-urethanes, and epoxies. Most of them are available both as two-component or thermal curing and as UV-curable.

6.3.2 Polymer adhesives

Silicones

Silicones have excellent sealing properties and are often used as encapsulation materials. They feature a high chemical resistance against many aggressive substances, are highly impenetrable for moisture, have good adhesion on many materials and keep these characteristics over a very wide temperature range. They would be ideally suited, except that silicones are also highly elastic materials and thus unsuited to maintain the cell-gap.

Polyimides

Polyimides can withstand high temperatures, but their very smooth and inert surface results in low peeling strength, a rather disadvantageous characteristic. Additionally, resistance to alkaline substances and especially moisture is rather low.

Cyano-acrylates

Cyano-acrylates, well known as superglue, have good bonding strength to many materials and cure very rapidly. On the downside, the rapid curing results in high shrinkage during the process. The cured material is rather brittle and quite sensitive to shock. Moreover, although the curing mechanism uses the water

molecules present on surfaces or in the air, prolonged exposure to moisture strongly degrades the bonding strength.

Poly-urethanes

Poly-urethanes have excellent mechanical properties, but the temperature range in which they are usable is somewhat limited. Chemical sensitivity is not so good either. Nonetheless, poly-urethanes are frequently used as encapsulation material for packaging of (cheap) electronics.

Poly-urethanes that are polymerised by irradiation with UV are also commonly used as cure-on-demand adhesive in the electronics and optics industry [162]. This variant is mostly based on urethane acrylates and uses a free radical based polymerisation. The photo-initiator decomposes into free radicals which can open π-bonds on the monomer, making it suitable for polymerisation. Unfortunately, the free radicals can also react with oxygen, preventing the real polymerisation taking place. This is the so-called oxygen inhibition. The free radical polymerisation also causes a relatively large amount of shrinkage during the curing.

Mercaptoesters

Mercaptoesters, which are based on thiolene monomers, have long been the standard UV-curing adhesive. Despite this, the time needed to thoroughly cure these materials can easily extend over several (tens of) hours. Mercaptoesters nowadays are outperformed by the urethane acrylate based adhesives [162].

Epoxies

Epoxies feature excellent mechanical characteristics like toughness, low shrinkage, rigidity and high creep resistance. This is combined with chemical inertness to many aggressors.

The polymerisation of an epoxy takes place by opening the epoxide ring, which results in a shrinkage during curing that is only one tenth of the shrinkage related to a free radical polymerisation. Classic epoxies use hardeners to start the crosslinking. In two-component systems epoxy and hardener have to be mixed together, in one-component systems the hardener is already present and is activated by adding thermal energy. Typical hardeners include polyamides, amido-amines and aromatic amines. As they are built into the polymer network, the type of hardener influences the properties of the resulting epoxy.

UV-curing epoxies are crosslinked by cationic polymerisation. The photo-initiator decomposes into an acid - conjugate base pair and the cation starts the crosslinking by breaking open the epoxide ring. As a side effect, the polymerisation does not immediately stop when the illumination is stopped. A so-called dark cure can occur. This can be exploited for curing areas that cannot be

adequately illuminated. Curing with visible light is sometimes also available. It circumvents the difficulty of curing thicker sections of UV-curing adhesives, resulting from the fact that most plastics, including the adhesives itself, absorb a significant portion of UV light.

6.3.3 Initial selection

Based on the characteristics in the list above, epoxies or urethane acrylates seem the obvious choices, considering their combined mechanical and chemical properties. Epoxies may have some higher preference, because of their low shrinkage and higher chemical resistance.

As for the type of polymerisation, UV-curing probably offers the best combination of features. It allows high cycle times and precise assemblies. For the main seal, rapid curing two-component epoxies can also be considered, at the expense of some additional mixing work. For the end seal, on-demand curing is virtually a prerequisite.

Assemblies have been made with both urethane acrylates and epoxies, with good results.

Degree of curing

It is important that the degree of crosslinking of the polymer is as high as possible. Not only does this increase the mechanical properties (higher glass transition temperature) and the overall performance (higher chemical resistance), it is also mandatory to avoid subsequent interaction with the liquid crystal.

Frequently the curing schedule provided by the manufacturer must be exceeded to achieve this chemically full cure. Figure 6.13 shows the result of an incomplete cure. Although the seal is mechanically indistinguishable from a totally full cure, when the cell is filled, a thin interaction zone is present at the liquid crystal interface where the alignment deviates from the homeotropic. Proper curing conditions (other than the manufacturer's specifications) result in a clear, abrupt interface at the sealing ring.

6.3.4 Influence of inorganic alignment layers

Besides this normal chemical inertness requirement, it turned out that the use of inorganic alignment layers imposes additional, more strict demands on the type of glue used. In the course of this research, it became apparent that, although functional displays can be obtained with most of the commonly used seal materials if properly processed, the realisation of a reliable main seal that lasts with time is not easily obtained.

A sometimes rapid degradation of the initial alignment occurred in the

Figure 6.13: Misalignment zone at the interface between the sealing ring and the liquid crystal due to insufficient curing. Left is seal material, right liquid crystal. Photographed through crossed polarisers.

majority of our tests, quickly disqualifying the devices for use. The displays exhibit a zone of interaction at the seal where the vertical alignment is broken and converted into a more or less planar one, with preservation of the preferential direction. This misalignment zone starts at the seal borders and grows inwards with time until the complete display is affected and rendered useless.

Figure 6.14 shows the interaction at the seal in a relatively early stage, while figure 6.15 shows the device when the misalignment has completely covered the entire cell. The time needed to affect a complete cell varies from a few days to several weeks.

6.3.5 Selection for inorganic alignment layers

Procedure

In order to solve the problem outlined above, a survey of seal materials was carried out, regardless of the mechanical considerations outlined above. Preliminary experiments already ruled out external factors and showed that the choice of glue is indeed the crucial parameter. A selection of the glue types that were tested is shown in table 6.2. Different basic chemical formulations were chosen and different brands were included to avoid brand-specific particularities.

As stated before, it is important to be certain that the interaction is not due to incompletely cured seal material. This was assured by using various curing

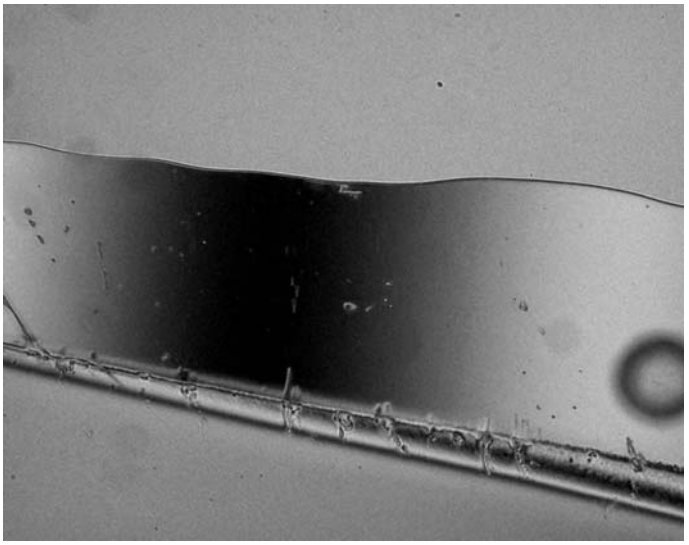

Figure 6.14: Micrograph of the liquid crystal – glue interface in the beginning of the contamination process. Top area is the glue, bottom area liquid crystal. The interface area features randomly changing bright colours due to the gradually shifting tilt angle. This greyscale image was produced by extracting the green colour information.

Figure 6.15: Photograph of a XGA cell where the contamination process has progressed so far as to affect the complete cell. Colour information is directly translated into greyscale.

Norland NOA-68	mercaptoester
Norland electronic adhesive range	mercaptoester
Mitsui Struct Bond XN-5A	
Threebond 3026B (series 3000)	
Sekisui Photolec series	
Dymax OP Series	urethane acrylate
Grace Amicon	underfill material
Nammix XS8436-79	thermal epoxy
Loctite series 3000 and 300	epoxy
Epotek UVS-91	
Epotek OG series	bisphenol epoxy
Emerson & Cumming Ecobond UV9502	
Ablestik Luxtrak series	

Table 6.2: A selection of tested adhesive materials

schemes, some of which largely exceeded the manufacturer's specifications.

From these tests, the OG series from Epotek were the only ones that could produce a completely perfect seal. Next to that, only the UVS-91 glue performs well enough to be a good second choice.

We were not able to extract a trend as to which glues do or do not work based on their material composition. This is largely due to the lack of information about the precise composition of the glues. Besides the base materials (oligomers and monomers), which are generally identifiable via the Material Safety Data Sheets, the glue may contain hardeners, accelerators, photoinitiators, diluents, fillers and other additives that make up a manufacturer's proprietary formulation, the details of which are not disclosed.

Chemical analysis can shed some light on the adhesive composition, but it generally results in a myriad of detected hydrocarbon fractions, making it impossible to identify a single offending substance.

Failure mechanism

A hypothesis about the mechanism at work can however be set forth.

Hydrocarbon fractions released from the sealing material are adsorbed at the silica surface of the alignment layer. As the adsorption energies can be quite high (cf. the use of silica in chromatography applications), these fractions may even replace the liquid crystal molecules and thus alter the Van der Waals interactions between the liquid crystal and the alignment layer. The hydrocarbons may further diffuse into the cell and thus gradually break the alignment of the complete cell. This is similar to the explanation proposed to elucidate the limited lifetime of an alignment layer in open air.

Evidence This hypothesis is supported by some additional observations. First, the misalignment is not complete but seems to affect only the amount tilt, not the tilt direction, indicating the properties of the alignment layer are modified, not destroyed. It is also well known that the anchoring energy of inorganic layers tends to be already somewhat lower, making them more prone to foreign contaminants, as misalignment can more quickly become the lowest energy configuration of the system. Thirdly, the phenomenon is strictly confined to the use of inorganic layers. If homeotropic aligning polyimides are used, such as Nissan SE-1211, none of the degradation phenomena are observed and all glues that can be fully cured yield good results.

End seal particularities

For the end seal, an additional difficulty lies in the fact that the uncured glue has to be directly in contact with the liquid crystal. This cannot be avoided, so the influence on each other should be as small as possible. The constituents of the glue may not poison the liquid crystal and the liquid crystal should not disrupt the curing of the glue.

The compatibility of liquid crystal and glue is sometimes monitored with Differential Scanning Calorimetry [163]. In this method, contamination of a liquid crystal is detected as a shift in the position of the isotropic temperature of the liquid crystal.

Test method Initially, a somewhat simpler method was used to get an idea of compatibility. For each glue type a known amount of uncured glue is dispensed and then brought into contact with the liquid crystal for a fixed amount of time. After that, the curing starts according to a preset scheme. The liquid crystal is then carefully removed and the residual amount of cured glue is determined.

Interactions between glue and liquid crystal can thus be observed: glue dissolved in the liquid crystal is removed together with the liquid crystal and will cause a weight reduction, while liquid crystal dissolved in the glue gets trapped and increases the apparent weight. It is implicitly assumed that a possible weight change inherent to the curing process is minimal. This is true for all glues considered here.

Results The results are summarised in table 6.3. All of the glues that show significant weight changes indeed perform bad as an end seal. On the other hand, a small weight change does not imply a certain success, some glues like Norland 68 and Threebond do not work at all as an end seal.

Also over here, the OG series and UVS-91 turned out to be the best performing.

Glue	before (g)	after (g)	diff. (g)	diff. (%)
Norland 68	0,0313	0,0313	0	0
OG116-31	0,0429	0,0438	0,0009	2,1
OP-21	0,0153	0,0223	0,007	45,7
OP-29	0,0107	0,0143	0,0036	33,6
OP-61	0,0117	0,0138	0,0021	17,9
Threebond	0,0349	0,0345	-0,0004	-1,1
GY + HY	0,0456	0,0451	-0,0005	-1,1
Lx0301	0,0428	0,0539	0,0111	25,9
Loctite 352	0,0264	0,0309	0,0045	17,0
UVS-91	0,0942	0,0962	0,002	2,1
OG142	0,0484	0,0497	0,0013	2,7
OP54	0,0159	0,0236	0,0077	48,4
OP30	0,0092	0,0107	0,0015	16,3
OP29V	0,0219	0,0291	0,0072	32,9

Table 6.3: Glue and liquid crystal mixability test results. First column is the weight of the uncured glue sample, second column the weight after exposure to liquid crystal and curing. Third and fourth column show the absolute and relative weight changes, respectively.

6.3.6 Conclusion

The introduction of an inorganic alignment layer has consequences for the entire display assembly process and is not limited to the deposition technique of the layer itself. The sealing materials used in the assembly require special attention and must be carefully selected to be compatible with the presence of the inorganic layer.

6.4 Curing conditions

As stated earlier, the curing conditions that deliver optimal results can deviate from the recommendations of the manufacturer. The curing schedules given below are for the OG116-31 epoxy material from Epotek, which has become the standard sealant in our technology. The presented values are safe choices, it may be possible to get shorter cycle times and a still reasonable yield by reducing some process times.

The OG adhesive material is a single component epoxy resin that must be cured through UV irradiation. It also offers the possibility to enhance the curing by supplying some additional heat during the process.

The UV radiation is delivered by a high intensity xenon-mercury arc lamp and uniformly distributed over a 5 cm diameter circular area with beam-expanding optics. The radiation from the lamp is also filtered with a cut-off

filter at 365 nm to prevent damage to molecular bonds by too energetic photons.

For the main seal a two stage cure is used. During the lamination, when the display is still in the press, an irradiation intensity of 200 mW/cm^2 is used for 10 minutes. The thick glass window of the press absorbs about 40 % of the intensity, so the effective intensity is 120 mW/cm^2. This matches the manufacturers recommended schedule and effectively does provide a very reliable lamination of the substrates. To obtain the required non-interaction with the liquid crystal, a second curing stage is added. The intensity is reduced to 60 mW/cm^2 to avoid unnecessary damage to the material, but the time window is extended to one hour. Additionally, the complete assembly is heated up to 86 °C to intensify the crosslinking process. The temperature is chosen just below the glass transition temperature of the sealing material, so that a maximum effect is achieved without the risk for dimensional changes to the lamination.

As for the end seal, some additional precautions are needed. The liquid crystal, that is now in the assembly must be shielded from the UV radiation to the largest extent possible. It is also advisable to keep the assembly at room temperature to avoid the occurrence of voids when cooling down. On the other hand, the crosslinking should start as fast as possible to minimise interaction with the liquid crystal.

Inhibition of the sealant - liquid crystal interaction is achieved with an initial cure intensity of 250 mW/cm^2 during five minutes. The assembly is in contact with a large heat sink to avoid temperature rises. Thorough crosslinking inside the difficult to reach cell-gap is ensured by a second illumination at 100 mW/cm^2 for one hour.

Chapter 7

Evaluation

7.1 Introduction

The four preceding chapters explored the different aspects of the manufacturing of microdisplays. In this chapter, the functional performance of the devices is investigated.

A first evaluation happens at the level of the cell itself, trying to measure the intrinsic qualities of the lightvalve. Imaging optics is excluded as much as possible here. It comprises characteristics such as contrast ratio, driving voltage and response speed.

The second, and probably the most important evaluation is the perceived quality of still images and moving imagery. Additional projection optics are needed here, and the resulting quality judgements therefore depend in part on these optics.

7.2 Measurement method for cell parameters

7.2.1 General

For transmissive devices, especially the ones employing twisted liquid crystal configurations, display metrology methods are thoroughly investigated and standardised [164, 165, 166, 167, 168]. Publications concerning measurements for reflective devices are far less common and most are aimed at liquid crystal modes employing twist [169]. To be able to measure the characteristics of the produced devices, a dedicated measuring method was constructed.

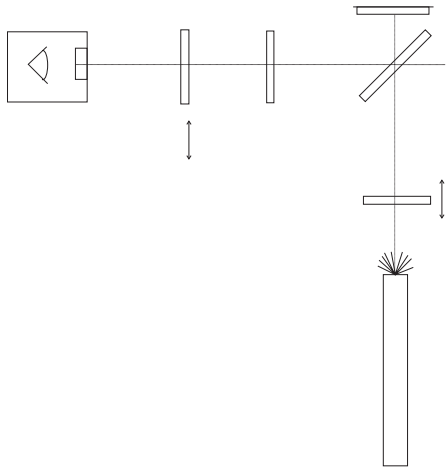

Figure 7.1: Schematic overview of the optical measuring set-up. The light emitted by the laser passes a polariser and a beamsplitter and hits the display. The reflected light again hits the beamsplitter and goes on through a quarter-wave plate and analyser to reach the detector.

Measurement set-up

Due to the size of a typical LCOS device, illumination with a laser spot is most convenient if one wants to scan the active area to detect non-uniformities. The laser is also the ideal source of light to measure the inherent contrast ratio of the cell. The set-up is an on-axis configuration. Figure 7.1 schematically shows the arrangement of the optical elements in the measuring device.

The laser source is a HeNe-laser emitting virtually non-polarised light at 543 nm. The beam is first linearly polarised by a Glan-Thompson polariser. These polarisers offer high extinction ratios in the crossed configuration (a ratio of more than 10^5 is easily achieved), which will be needed in view of the expected high contrast of the cell itself. The light is then sent through a broadband dielectric beamsplitter and projected onto the display under test. The reflected beam again encounters the beamsplitter, where a part of the light is sent back to the source, the other part travels towards the quarter-wave plate. The quarter-wave plate is mounted such that its optical axis can be rotated and the angle precisely read. A second Glan-Thompson polariser, with its polarisation direction perpendicular to the first one, serves as analyser before the light is collected by a high-speed, high sensitivity avalanche photo-detector.

7.2.2 Contrast

If the quarter-wave plate is left out of the optical path, the contrast ratio obtainable with the cell can be measured directly. From this value, an estimate (value is no larger than) for the pre-tilt angle can already be obtained using formulas 7.1 and 7.2, knowing the physical properties of the liquid crystal.

$$CR = \frac{1}{\sin^2\left(\frac{2\pi d}{\lambda}(n_{eff} - n_o)\right)} \tag{7.1}$$

$$n_{eff} = \frac{n_e n_o}{\sqrt{n_0^2 + (n_e^2 - n_o^2)\cos^2(\alpha)}} \tag{7.2}$$

The equation for the contrast ratio also contains the cell gap as a parameter; its influence is however modest enough to justify the use of an initial guess. Figure 7.2 illustrates this, showing the theoretical contrast versus pre-tilt angle for different cell thickness using the properties of MLC-6610.

7.2.3 Cell-gap

To determine the cell gap, the quarter-wave plate is used. In a VAN cell the molecules are uniformly tilted to change the actual birefringence of the layer. Considering the most ideal case, in the non-driven state the molecules are perfectly vertical and there is no birefringence. When a large enough voltage is applied, the molecules are switched form vertical to fully horizontal and when using a properly polarised light beam as input, the reflected beam can be decomposed into two orthogonal components having a phase difference of exactly

$$\sigma = \frac{4\pi d \Delta n}{\lambda} \tag{7.3}$$

where d stands for cell gap and Δn and λ have their usual meaning.

Knowing this phase difference, the cell gap value can be calculated as:

$$d = \sigma \frac{\lambda}{4\pi\Delta n} + k\frac{\lambda}{2\Delta n} \qquad k = 0, 1, 2, 3, \ldots \tag{7.4}$$

Phase retardation

To determine the phase retardation, the output intensity curve obtained by varying the direction of the quarter-wave plate's optical axis is used.

For the calculations, some reference axes must be defined as in figure 7.3. The X- and Y-axis coincide with the p- and s-polarisation at the beamsplitter mirror, respectively. The light emerging from the polariser and entering the display is linearly polarised along the Y-axis. The X'Y'-axes are a second set

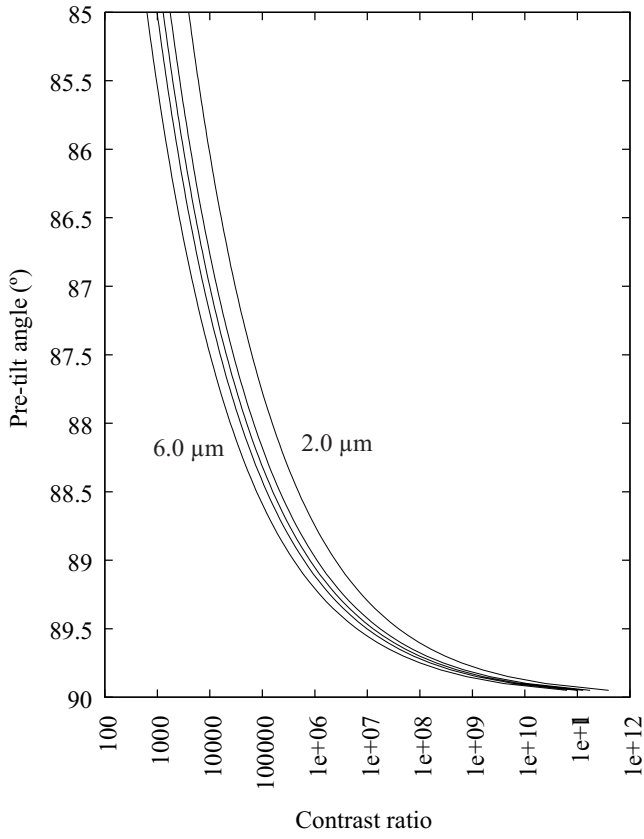

Figure 7.2: Predicted contrast ratio versus pre-tilt angle for cell gaps ranging between 2 and 6 μm. Calculated using the properties of MLC-6610.

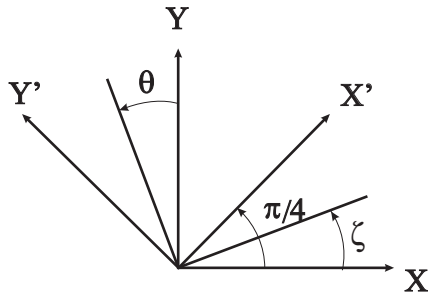

Figure 7.3: Reference axes used in the calculations.

turned 45 ° counterclockwise from the XY-pair. They should coincide with the ordinary and extraordinary axes of birefringence of the display.

The rotation of the optical axis of the quarter-wave plate is denoted θ and measured counterclockwise starting from the Y-axis. The direction of the analyser is normally oriented along the X-axis, but may be varied in a more general approach. The angle is denoted ζ and is measured counterclockwise from X, so ζ equals 0 ° in the case of crossed polarisers.

The display transforms the linearly polarised light into elliptically polarised light which can be represented either with the ellipticity parameters β and χ or the magnitudes of two orthogonal linearly polarised waves $E_{X'}$ and $E_{Y'}$ and their phase difference δ.

The light first encounters the beamsplitter mirror were it may undergo a first transformation due to the fact that the coefficient of reflection can depend on the polarisation state. Even a non-polarising beamsplitter will generally not split the beam evenly with respect to the polarisation; typically the s-component will be nicely split into a 50/50 ratio but the p-component will have a 30/70 ratio. The reflection coefficient for p-polarised light will be denoted C_x here, for s-polarised light it will be C_y.

Depending on the rotation angle θ, the polarisation state of the beam is further modified by the quarter-wave plate before being sent through the analyser. The intensity of the latter beam is measured by the photo-detector.

Calculations After the mirror, the components along X' and Y' have amplitudes respectively:

$$E_{X'}^{mirror} = \tag{7.5}$$

$$\frac{1}{2}\sqrt{\left(E_{X'}(C_x+C_y)+E_{Y'}(C_y-C_x)\cos(\delta)\right)^2+\left(E_{Y'}(C_y-C_x)\sin(\delta)\right)^2}$$

$$E_{Y'}^{mirror} = \tag{7.6}$$

$$\frac{1}{2}\sqrt{(E_{X'}(C_x-C_y)+E_{Y'}(C_x+C_y)\cos(\delta))^2+(E_{Y'}(C_x+C_y)\sin(\delta))^2}$$

and phase retardations:

$$\rho_{X'}^{mirror} = \arctan\left(\frac{E_{Y'}(C_y-C_x)\sin(\delta)}{E_{X'}(C_x+C_y)+E_{Y'}(C_y-C_x)\cos(\delta)}\right) \tag{7.7}$$

$$\rho_{Y'}^{mirror} = \arctan\left(\frac{E_{Y'}(C_x+C_y)\sin(\delta)}{E_{X'}(C_y-C_x)+E_{Y'}(C_x+C_y)\cos(\delta)}\right) \tag{7.8}$$

The quarter-wave plate further transforms these components into:

$$\begin{aligned} E_{X'}^{quart} &= \sqrt{\Big(\big(A_{X'Y'}E_{X'}^{mirror}\cos(\alpha_{X'Y'}+\rho_{X'}^{mirror})+\dots \\ &\quad +A_{Y'Y'}E_{Y'}^{mirror}\cos(\alpha_{Y'Y'}+\rho_{Y'}^{mirror})\big)^2+\dots \\ &\quad +\big(A_{X'Y'}E_{X'}^{mirror}\sin(\alpha_{X'Y'}+\rho_{X'}^{mirror})+\dots \\ &\quad +A_{Y'Y'}E_{Y'}^{mirror}\sin(\alpha_{Y'Y'}+\rho_{Y'}^{mirror})\big)^2\Big) \end{aligned} \tag{7.9}$$

$$\begin{aligned} E_{Y'}^{quart} &= \sqrt{\Big(\big(A_{X'X'}E_{X'}^{mirror}\cos(\alpha_{X'X'}+\rho_{X'}^{mirror})+\dots \\ &\quad +A_{Y'X'}E_{Y'}^{mirror}\cos(\alpha_{Y'X'}+\rho_{Y'}^{mirror})\big)^2+\dots \\ &\quad +\big(A_{X'X'}E_{X'}^{mirror}\sin(\alpha_{X'X'}+\rho_{X'}^{mirror})+\dots \\ &\quad +A_{Y'X'}E_{Y'}^{mirror}\sin(\alpha_{Y'X'}+\rho_{Y'}^{mirror})\big)^2\Big) \end{aligned} \tag{7.10}$$

$$\begin{aligned} \rho_{X'}^{quart} &= \arctan\left(\frac{A_{X'X'}E_{X'}^{mirror}\sin(\alpha_{X'X'}+\rho_{X'}^{mirror})+}{A_{X'X'}E_{X'}^{mirror}\cos(\alpha_{X'X'}+\rho_{X'}^{mirror})+}\quad\dots\right. \\ &\quad \left.\dots\quad\frac{A_{Y'X'}E_{Y'}^{mirror}\sin(\alpha_{Y'X'}+\rho_{Y'}^{mirror}}{A_{Y'X'}E_{Y'}^{mirror}\cos(\alpha_{Y'X'}+\rho_{Y'}^{mirror})}\right) \end{aligned} \tag{7.11}$$

$$\rho_{Y'}^{quart} = \arctan\left(\frac{A_{X'Y'}E_{X'}^{mirror}\sin(\alpha_{X'Y'}+\rho_{X'}^{mirror})+}{A_{X'Y'}E_{X'}^{mirror}\cos(\alpha_{X'Y'}+\rho_{X'}^{mirror})+} \quad \cdots \right.$$
$$\left. \cdots \quad \frac{A_{Y'Y'}E_{Y'}^{mirror}\sin(\alpha_{Y'Y'}+\rho_{Y'}^{mirror}}{A_{Y'Y'}E_{Y'}^{mirror}\cos(\alpha_{Y'Y'}+\rho_{Y'}^{mirror})}\right) \tag{7.12}$$

The pairs $(E_{X'}^{quart}, \rho_{X'}^{quart})$ and $(E_{Y'}^{quart}, \rho_{Y'}^{quart})$ again denote the amplitude and phase of the components along the X' and Y' axes, respectively. The expressions for $A_\star$ and $\alpha_\star$ are defined as:

$$A_{X'Y'} = A_{Y'X'} = \sin(\theta)\cos(\theta)\sqrt{2} \tag{7.13}$$

$$\alpha_{X'X'} = \arctan\left(\frac{1}{\tan^2(\theta)}\right) \tag{7.14}$$

$$A_{X'X'} = \frac{1}{\sin(\alpha_{X'X'}) + \cos(\alpha_{X'X'})} \tag{7.15}$$

$$\alpha_{Y'Y'} = \arctan\left(\tan^2(\theta)\right) \tag{7.16}$$

$$A_{Y'Y'} = \frac{1}{\sin(\alpha_{Y'Y'}) + \cos(\alpha_{Y'Y'})} \tag{7.17}$$

Finally, the intensity picked up by the detector is given by:

$$I = \left(E_{X'}^{quart}\cos(\zeta) + E_{Y'}^{quart}\sin(\zeta)\cos(\rho_{Y'}^{quart} - \rho_{Y'}^{quart})\right)^2 + \left(E_{Y'}^{quart}\sin(\rho_{Y'}^{quart} - \rho_{Y'}^{quart})\right)^2 \tag{7.18}$$

The resulting graphs of intensity versus quarter-wave plate rotation angle, as shown in figure 7.4, can be used to identify the original set of parameters $E_{X'}$, $E_{Y'}$ that created them.

Extraction In a fully automated system, measuring the intensity for a large number of different θ's and then using curve-fitting software to extract the initial parameters may be the best approach. The position and relative magnitude of the maxima and minima in the curves are however also enough to uniquely identify the parameters. Thus, the number of measurements can be reduced by searching for maxima and minima only. The extraction of the parameters then requires the creation of a cost function and a search algorithm to find the minimum thereof. The cost function of course penalises deviations between the

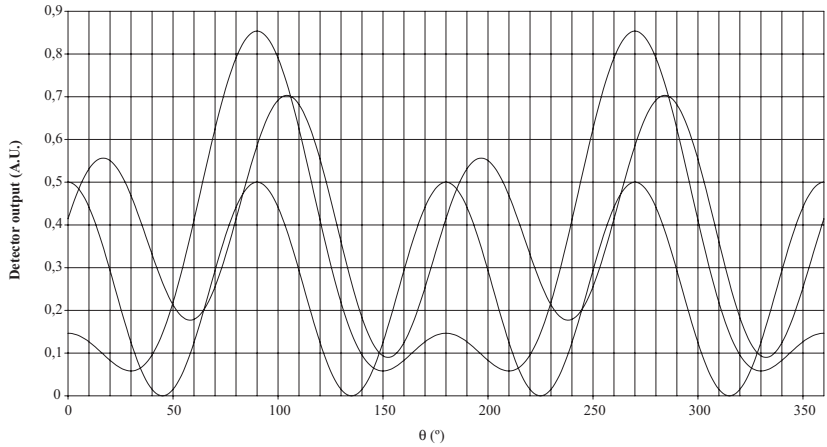

Figure 7.4: Calculated detector output versus rotation angle of the quarter-wave plate for three different settings ($\delta = 0$, E_x/E_y=1; $\delta = 45\,^\circ$, $E_x/E_y = 1$; $\delta = 20\,^\circ$, $E_x/E_y = 0.2679$). Output is in arbitrary units.

intensity measured in the extrema and the intensity calculated for the same. To make sure the measured extrema do actually correspond with calculated extrema, it may be useful to add a penalty in case the tangent line should not be horizontal in the supposed extrema. A typical cost function then might take the form:

$$
\begin{aligned}
F(\delta, E_{X'}, E_{Y'}) = & \qquad (7.19)\\
& W_1 \left(I_1^{meas} - I(\theta_1^{meas}, \delta, E_{X'}, E_{Y'})\right)^2 \\
& + W_2 \left(\frac{I(\theta_1^{meas} + \tau, \delta, E_{X'}, E_{Y'}) - I(\theta_1^{meas} - \tau, \delta, E_{X'}, E_{Y'})}{2\tau} \right)^2 \\
& + W_3 \left(I_2^{meas} - I(\theta_2^{meas}, \delta, E_{X'}, E_{Y'})\right)^2 \\
& + W_4 \left(\frac{I(\theta_2^{meas} + \tau, \delta, E_{X'}, E_{Y'}) - I(\theta_2^{meas} - \tau, \delta, E_{X'}, E_{Y'})}{2\tau} \right)^2 + \ldots
\end{aligned}
$$

In the above expression, W_i are positive weighing factors and τ should be a very small number, representing an infinitesimal step. In the general case, there will be four minima and four maxima over the range $\theta = 0\,^\circ$ - $360\,^\circ$, but as the quarter-wave plate has an axis of symmetry, only two consecutive pairs are really needed. Including all four pairs is anyhow a useful check for the validity of the measurements.

Although the cost function is quite complicated, no special requirements are imposed on the search algorithm; the Generalised Reduced Gradient method, a pretty standard algorithm for non-linear but smooth multi-variate problems

performs excellent.

Cell-gap In this ideal case, the cell-gap is found by substituting σ with δ in equation (7.4). The right value for k is usually quite obvious, when in doubt, comparing a measured electro-optical characteristic to a simulated one for the assumed cell gap quickly yields the right number.

7.2.4 Non-ideal conditions

Pre-tilt

A first, small enhancement to the ideal case reckons with the fact that the molecules are not perfectly vertical in the non-driven state but have a small pre-tilt. The procedure outlined above can be used to obtain the phase retardation δ_0 in the non-driven state, obviously a very small number. From the value of δ_0, an accurate estimate for the pre-tilt angle can be calculated.

For the cell gap determination, σ in equation (7.4) should then be replaced by $\delta - \delta_0$.

Director profile

The assumption that the molecules are aligned fully horizontal when measuring the actual phase retardation imposes a condition on the measurement that will almost never be met. The surface anchoring energy at the alignment layer always induces a zone near the electrodes where the orientation gradually shifts from vertical to horizontal.

Moreover, the voltages required to fully switch the molecules can be quite large compared to the ones needed to drive the display in the regular way. Many backplanes may not be able to deliver these voltages, so the condition is a priori not met. It is therefore most useful to accommodate for this in the measurement method itself.

Profile simulation The Franck-Oseen theory permits to calculate the director configuration of liquid crystal layers subjected to electrical fields. Knowing the director configuration across the liquid crystal layer, the actual birefringence value can be calculated. Substituting the nominal value $\Delta n = n_e - n_o$ in equation (7.3) and (7.4) with this value corrects for the error made.

The correct simulation of the director profile needs input values for the pre-tilt angle, the anchoring energy at the alignment surfaces and the applied voltage. Fortunately, the director configuration does not depend upon the actual cell thickness, at least not in a first order approximation.

The anchoring energy introduces a new degree of freedom for which an additional constraint is needed. This constraint can be found in the requirement

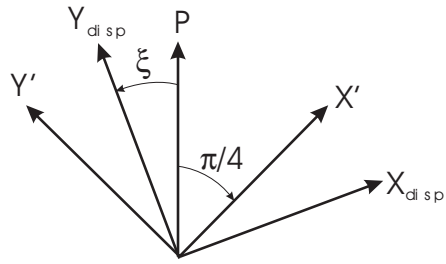

Figure 7.5: Orientation of axes for the calculation of the display rotation.

that the simulated electro-optical response and the measured one should fit as close as possible. Indeed, the anchoring energy completes the set of parameters needed for a full description of the liquid crystal layer, so a correct value should also give the optimal match between model and reality. It should be noted that the one-dimensional simulation models for static director configurations are mature enough to give reliable predictions.

Display rotation

The measurement accuracy can still be influenced by external factors. In the previous discussion, it was assumed that the axes of birefringence of the display exactly coincide with the X'Y' axes pair.

In practice, it will be very difficult to realise the mounting of the panels in such a way that there will never be a deviation of a few degrees. We can take this into account by exploiting the fact that when properly mounted, the display can only produce polarised light with varying ellipticity χ, but fixed ellipse rotation angle β (it should be either 45 ° or 135 ° when measured in the X'Y' reference). If the extraction procedure outlined above yields slightly deviant results, this must be caused by a rotation of the entire display.

The situation is depicted in figure 7.5. Linearly polarised light along the direction of P enters the display; after passing through it, a phase retardation difference of δ_{true} exists between the components along X_{disp} and Y_{disp}. As the rotation ξ of the display with respect to P is not exactly $\frac{\pi}{4}$ anymore, these components must be transformed into the X'Y' reference to be used in the previous model.

Their amplitudes and phase differences are then given by:

$$E_{X'} = \sqrt{\left(\left(\cos(\xi)\cos\left(\frac{\pi}{4}-\xi\right) - \sin(\xi)\sin\left(\frac{\pi}{4}-\xi\right)\cos(\delta_{true})\right)^2 + \ldots + \left(-\sin(\xi)\sin\left(\frac{\pi}{4}-\xi\right)\sin(\delta_{true})\right)^2\right)} \tag{7.20}$$

$$E_{Y'} = \sqrt{\left(\left(\cos(\xi)\sin\left(\frac{\pi}{4}-\xi\right) + \sin(\xi)\cos\left(\frac{\pi}{4}-\xi\right)\cos(\delta_{true})\right)^2 + \ldots + \left(\sin(\xi)\cos\left(\frac{\pi}{4}-\xi\right)\sin(\delta_{true})\right)^2\right)} \tag{7.21}$$

$$\upsilon_{X'} = \arctan\left(\frac{-\sin(\xi)\sin\left(\frac{\pi}{4}-\xi\right)\sin(\xi)}{\cos(\xi)\cos\left(\frac{\pi}{4}-\xi\right) - \sin(\xi)\sin\left(\frac{\pi}{4}-\xi\right)\cos(\delta_{true})}\right) \tag{7.22}$$

$$\upsilon_{Y'} = \arctan\left(\frac{\sin(\xi)\cos\left(\frac{\pi}{4}-\xi\right)\sin(\xi)}{\cos(\xi)\sin\left(\frac{\pi}{4}-\xi\right) + \sin(\xi)\cos\left(\frac{\pi}{4}-\xi\right)\cos(\delta_{true})}\right) \tag{7.23}$$

$$\delta = \upsilon_{Y'} - \upsilon_{X'} \tag{7.24}$$

Optimising the values of ξ and δ_{true} to match $E_{X'}$, $E_{Y'}$ and δ gives both the rotation angle ξ, which is as yet of no further use and the actual value of δ_{true}, to be used in equation (7.4) as $\sigma = \delta_{true} - \delta_0$.

Residual twist

Lastly, it is possible that the alignment of the top and bottom substrates is not perfectly concurrent, thus introducing some twist. Figure 7.6 shows the influence of twist on the polarisation state of the light coming out of the display.

In the non-driven state, the twist has very little influence, as could be expected. Even for a total twist angle of 10 °, which is quite large given the manufacturing capabilities, its influence on the polarisation state is at least an order of magnitude lower than the above described display rotation. Thus, we can still use the procedure above in the non-driven state.

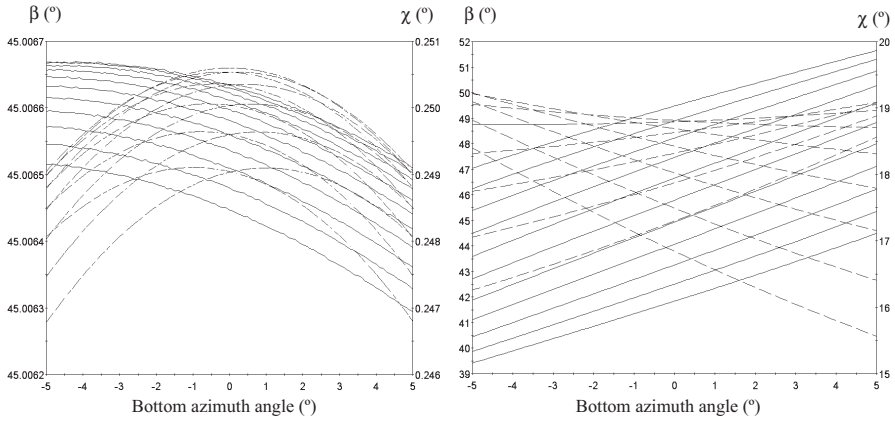

Figure 7.6: Influence of twist upon the polarisation state of the light emerging from the display. Left shows the non-driven state (88 ° pre-tilt angle), right the switched state (1 ° tilt angle). The horizontal axis gives the orientation imposed by the bottom substrate; the orientation imposed by the top substrate, also ranging from −5 ° to 5 °, yields the bundle of curves. Full line is β, dotted line χ. Simulated using the properties of MLC-6610.

When the molecules tilt toward the horizontal, the influence of the twist, if present, cannot be discarded anymore. If the polarisation state still contains an ellipse rotation angle not equal to 45 ° or 135 ° after correcting the values for the display rotation ξ, the entire model for the display rotation will have to be replaced with one that includes twist. As this increases complexity substantially and the introduced error is relatively small, it may be more interesting to use graphs such as figure 7.6 to estimate the twist and apply an approximate correction to δ .

7.3 Electro-optical characterisation

7.3.1 Electro-optical response curve

A typical electro-optical response curve is shown in figure 7.7. The threshold voltage is slightly higher than 2 Volts, while maximum brightness is attained at 3.4 Volts. This makes the actual modulation range less than 1.5 Volts. For 8 bit grey levels and assuming even spacing, this comes down to 5 millivolts per level.

Using the measurement procedure outlined above, some cell parameters can be extracted. The final step comprises the fitting of the simulated response curve to the measured one. Figure 7.7 also shows the results of the fitting procedure. The extraction procedure then gives a pre-tilt angle of 88 °, an

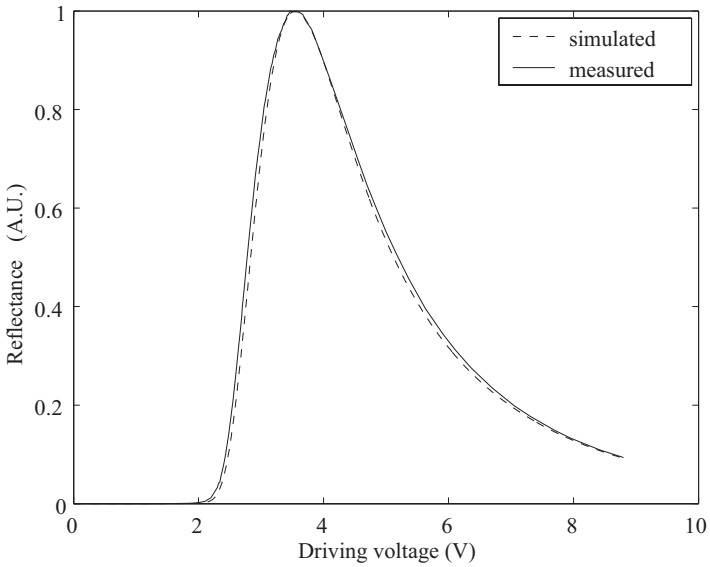

Figure 7.7: Measured electro–optical response of a typical cell. Dashed line shows the characteristic obtained by simulation after fitting the cell parameters to the measurement.

actual cell-gap thickness of 2.865 μm and a moderate anchoring energy. The measured on-axis contrast amounts to 80000:1, in line with what is expected based on the pre-tilt angle value.

7.3.2 Switching speed

The switching speed of the liquid crystal is characterised by its response to a voltage step, normally from black to full brightness and vice versa. The response consists of a delay time and the actual transition time, usually taken between the 10 % en 90 % levels as explained earlier.

Figures 7.8 and 7.9 show a typical response to an upward and downward step, respectively. The voltage step starts at 2.5 ms for figure 7.8 and at 4 ms for figure 7.9.

Rise and fall times are thus below 10 ms. The total time, including the delay time which is somewhat larger for the upward step, stays below 15 ms. This is largely sufficient for displaying blur-free video images in a non-colour-sequential approach.

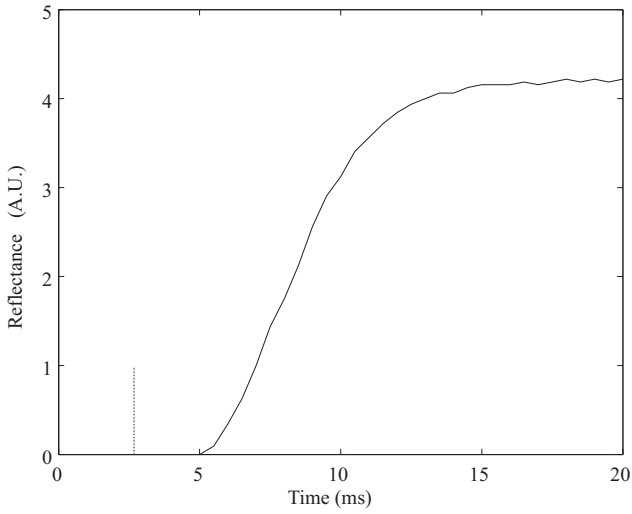

Figure 7.8: Measured response of a typical cell to a voltage step at 2.5 ms (black to full brightness).

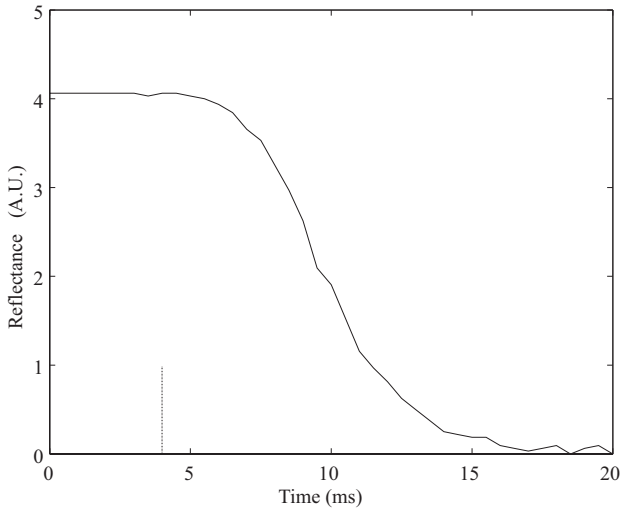

Figure 7.9: Measured response of a typical cell to a downward voltage step at 4 ms (full brightness to black).

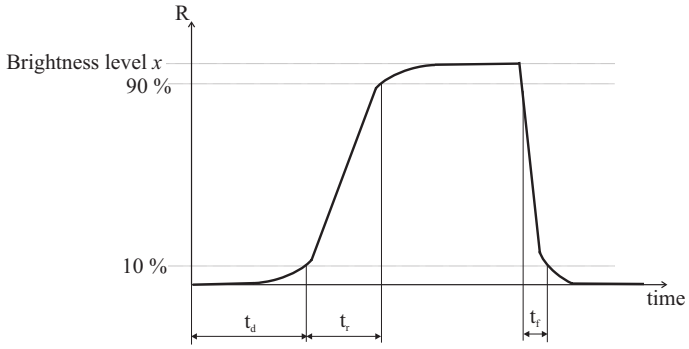

Figure 7.10: Definition of the transition times (rise and fall time) and the delay time. The delay time starts when the electrical pulse is applied.

brightness level	delay time (ms)	rise time (ms)	fall time (ms)
100 %	4.32	3.52	3.60
90 %	7.28	8.00	3.20
80 %	8.28	9.80	3.16
70 %	9.12	11.4	3.16
60 %	10.42	12.92	2.84
50 %	11.26	14.12	2.80
40 %	12.50	17.40	2.60
30 %	13.30	21.10	2.60
20 %	15.00	25.00	2.56
10 %	17.60	31.50	2.45

Table 7.1: Measured transition times to various brightness levels starting from black. 100 % means maximum brightness

Intermediate grey levels

Although the rise and fall times as given above are often the only numbers cited, response times to and from intermediate grey levels also contain useful and sometimes revealing information.

Transition times to neighbouring grey levels can be a multiple of the normal rise time, as can the delay time. This is important to consider when a switch to colour-sequential architectures is envisaged.

Table 7.1 gives an overview of switching times measured on a cell for the transition black → brightness level x and back. The definition of the different times is shown in figure 7.10.

It is clear that the electrically driven transition is slowed down severely when the step height becomes small. On top of that, the delay time increases at the same pace. The mechanically driven transition on the other hand can

ms	0	10	20	30	40	50	60	70	80	90	100
0		26,5	21,4	19,0	16,0	14,2	12,7	11,2	9,7	8,1	5,2
10	1,5		21,1	16,5	14,3	12,8	11,5	10,3	9,0	7,4	4,7
20	3,7	12,4		17,9	14,5	12,9	11,2	9,9	8,49	7,1	4,4
30	3,5	11,4	10,4		15,8	13,6	11,5	9,5	8,30	6,9	4,2
40	3,5	10,5	10,4	10,4		14,4	11,6	9,8	8,23	6,7	4,0
50	3,4	10,0	10,0	9,7	9,3		13,8	10,0	8,6	6,8	3,9
60	3,5	9,8	9,8	9,8	9,8	10,0		12,4	8,7	7,0	3,8
70	3,5	9,5	10,0	9,5	9,3	8,9	8,5		10,2	7,4	3,8
80	3,5	9,0	9,7	10,0	9,6	9,4	8,9	8,3		8,6	3,9
90	3,6	9,0	9,4	9,6	9,8	9,3	8,9	9,0	8,6		4,2
100	4,0	9,2	10,0	9,9	9,8	9,7	9,3	9,1	8,7	8,0	

Table 7.2: Matrix of transition times between arbitrary brightness levels. Starting level is found in the leftmost column, end level in the topmost row. Values obtained by calibrated simulation.

be considered unaffected by the step magnitude. This is exploited in some variants of the so-called 'overdrive schemes', where one tries to limit transition times by 'resetting' the pixel in-between every frame and then let it relax to the desired state. To be effective, the reset operation must consist of an electrical pulse with a largely exaggerated amplitude, in order for this transition to occur very fast. The following mechanical relaxation also has a limited and known transition time, so that the combination of both can be advantageous. For a normally black mode like VAN, however, the reset-state coincides with full brightness, so the panel may not be illuminated when the reset is performed. This may cause additional difficulties.

A complete matrix with transition times to and from arbitrary brightness levels is given in table 7.2 and figure 7.11. Values are obtained by simulation using calibrated parameters and verified with measurements by random checks.

A notable characteristic is the fact that the fall times remain fairly constant throughout, even between neighbouring and/or midway levels. This is generally not the case for twisted modes.

7.3.3 Vcom

A particularity of LCOS devices is the fact that the electrodes that switch the liquid crystal are made of different materials, usually aluminium and indium-tinoxide. This results in the presence of an internal voltage in the cell that can disturb its operation.

If frame inversion is used, the internal voltage turns a symmetrical driving voltage into a slightly asymmetrical one, resulting in uneven brightness levels between frames. This flicker has a frequency of half the frame refresh frequency and can thus be very annoying in the case of conventional frame rates (60 Hz

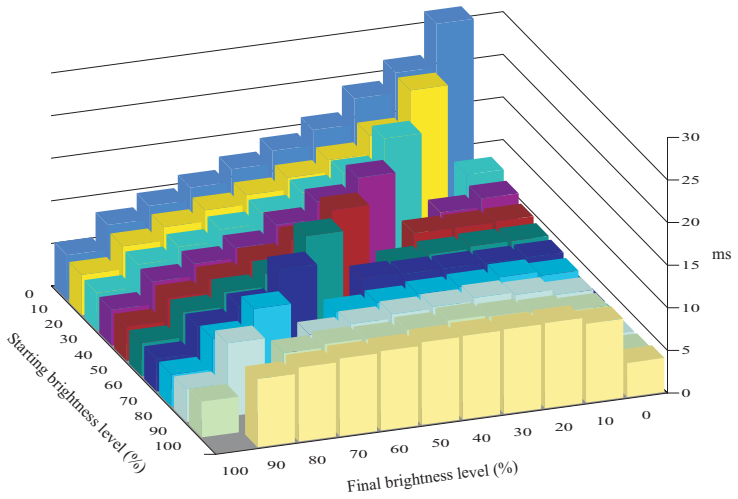

Figure 7.11: Graphical representation of transition times between arbitrary brightness levels. Starting level is set out on the left axis, end level on the right axis. Times are in milliseconds, values obtained by calibrated simulation.

to 75 Hz) (figure 7.12).

Besides the quick and dirty remedy of substantially increasing the frame rate, it is also possible to add an external DC voltage to the driving signals that compensates for the internal voltage, so that the flicker disappears. This offset voltage is generally termed Vcom and it is in fact the only measure for the internal voltage.

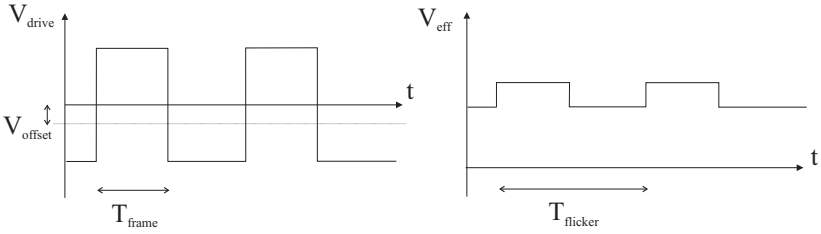

Figure 7.12: Origin of flicker in LCOS cells. Although the supplied driving voltage is symmetrical (e.g. referenced to the counter-electrode), the internal offset voltage makes it asymmetrical. The resulting effective driving voltage to which the liquid crystal reacts is shown on the right.

Work-function

The obvious source of the internal voltage is of course the difference in work-function of the two electrode materials. For a conductor, the work-function is easily obtained via the Fermi-level energy, defined by equation (7.25). Here $\frac{N}{V}$ is the number density of electrons , m is the mass of the electron and $\hbar$ the Bohr magneton. The work-function of aluminium amounts from 4.06 eV to 4.41 eV while values for ITO range from 4.5 eV up to 5.15 eV, depending on the composition [170], giving energy differences of 90 meV to 1090 meV.

$$E_f = \left(\frac{\hbar^2}{2m}\right)\left(\frac{3N\pi^2}{V}\right)^{\frac{2}{3}} \tag{7.25}$$

Drift

There are however strong indications that a difference in work-function alone cannot be the entire explanation. First, the range of measured Vcom values is rather broad and varies from 100 mV to 1100 mV, with no apparent correlation to cell gap thickness, liquid crystal type or other material properties. This already seems incompatible with a potential difference caused exclusively by work-function differences. Next, the observed Vcom value usually differs from one place to another within a single lightvalve. Lastly, and maybe most importantly, the Vcom value tends to drift with time. Figure 7.13 illustrates both phenomena. A cell is driven continuously with a symmetrical waveform at half maximum brightness and the Vcom is measured periodically by determining the offset voltage needed to eliminate wobbling in the optical intensity.

Note that in the graph only the incremental drift is shown, the starting value of zero is not the actual Vcom value. The initial condition of the cell is 'pristine', i.e. it has not been operated for at least 24 hours. Both measurements seem to evolve to a regime value if sufficient time has passed but there is a large discrepancy between the actual figures.

In literature, the so-called battery effect is often cited as an explanation for the shift with time. A stack of aluminium, polyimide and liquid crystal material behaves like a battery and may cause the drift of the Vcom [116, 171]. Unfortunately, the alignment polyimide, crucial in this theory, is not at all present in our devices, yet we still observe the drift with time.

For devices with inorganic alignment layers, a drift model based on charges trapped at the surface of the SiO_2 insulator layer seems more promising. It coincides with the observation that the drift at the border of the cell, where contamination of the materials with glue fragments is more likely, is significantly larger. Such a model can also fit the observed increase of Vcom with temperature, shown in figure 7.14.

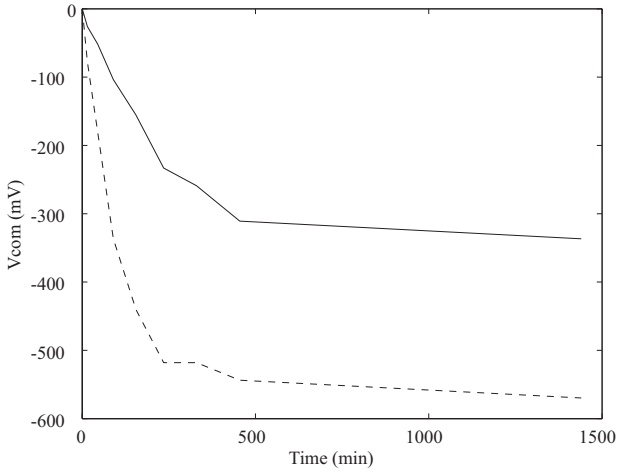

Figure 7.13: Incremental evolution of Vcom with time. Solid line shows the measurements in the middle of the cell, dashed line near the borders.

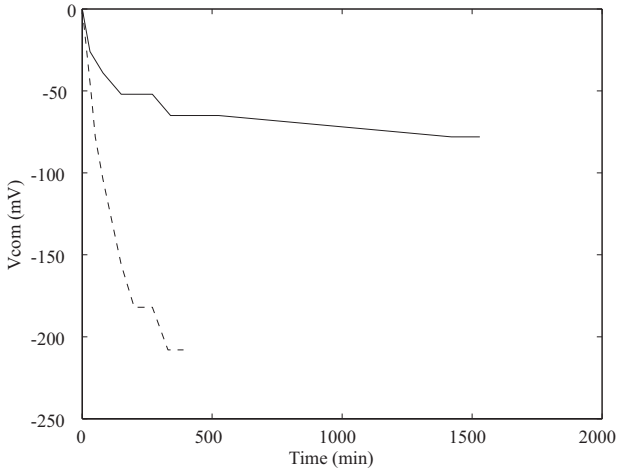

Figure 7.14: Evolution of the Vcom shift for a cell at room temperature (solid line) and at 50 °C (dashed line).

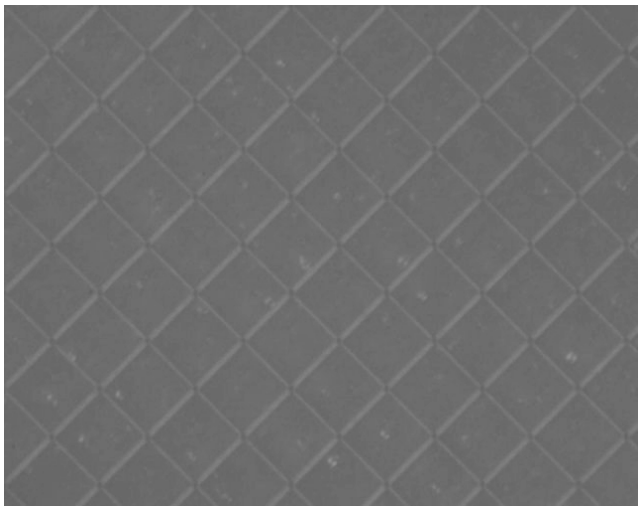

Figure 7.15: Micrograph of some pixels with spacers for a vertically aligned cell in the black state. Contrast and brightness of the image are digitally enhanced to actually show some features.

7.3.4 Spacer visibility

One of the nice features of the vertically aligned mode is that it is very forgiving to the presence of spacers inside the active area, eliminating the need to develop spacerless assembly techniques.

The vertical orientation of the liquid crystal is hardly affected by the spacers, so the black state and thus the contrast is preserved. Also when tilting the molecules, the rotation is hardly obstructed. This is quite different for the twisted modes, where the helix is invariably destroyed in the neighbourhood of a spacer.

Figure 7.15 illustrates the invisibility of spacers in the VAN cell. Although the picture has been digitally enhanced, spacers are hardly distinguishable.

7.4 Fringe field effects

7.4.1 Disclinations

Up to now the liquid crystal layer has been treated as a one-dimensional entity. All calculations assumed a slab of liquid crystal with a certain thickness, but laterally extending to infinity. In some cases, this simplification is not correct anymore. The ratio of the width of a single pixel to the liquid crystal thickness can be such that the electrical field cannot be considered uniform over the pixel

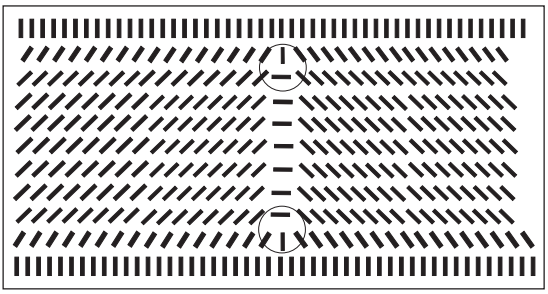

Figure 7.16: Disclinations in a vertically oriented liquid crystal. The two disclinations, indicated by the circles are connected with a horizontally oriented area. The zones to the left and right of them have inverted tilt angles.

width anymore. The fringe fields at the borders must be taken into account if the correct director configuration must be obtained.

The inhomogeneous field and director configuration will have repercussions on the optical behaviour. In general, the resolution associated with a pixel width will be reduced because at the borders of the pixel the director configuration is not the expected one.

Ultimately, fringe fields can introduce disclinations in the director configuration. Disclinations are linear or point-like defects in the continuously varying director orientation. They are very similar to the dislocations encountered in crystallography. A typical disclination in a vertically oriented liquid crystal is shown in figure 7.16.

The molecule layers close to the borders are anchored by the alignment layer and are oriented upright. If the bulk molecules have a rather large opposite tilt, an incompatibility is introduced. The lowest energy configuration for the area connecting the two zones with opposite tilt is obviously a homogeneous orientation, but this can only be achieved by allowing two spots where continuity is broken (marked by the circles). These are the disclinations. Both disclinations and the homogeneous boundary layer connecting them separate two topologically incompatible areas; for this configuration to exist, the total energy of it should be lower than the total energy of the highly deformed director profile that is needed if continuity is to be preserved.

As stated before, the initial opposite tilt areas in the director alignment are caused by electrical fringe fields to neighbouring pixels at different voltages, illustrated by figure 7.17. As pixel sizes shrink, the fringe fields become more and more dominant with respect to the main field; consequently its effects also become more pronounced.

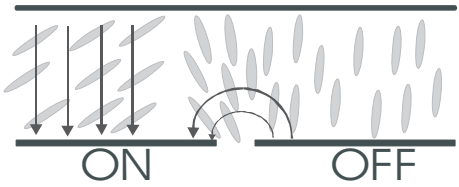

Figure 7.17: Reverse tilt due to fringe fields.

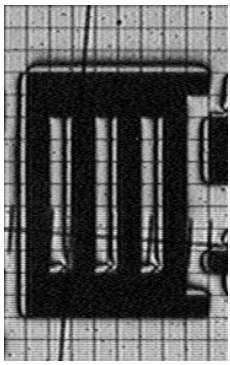

Figure 7.18: Optical effects of disclination lines. Pixels are 11.4 μm wide.

7.4.2 Optical consequences

Static effects

The optical repercussions of the presence of disclination are serious. The disclinations and the area connecting them have completely wrong director orientations. In the case of the vertically aligned mode, this results in a dark line inside a white (switched on) pixel. This reduces the perceived brightness of this pixel and gives the pixel edges a fuzzy, unsharp aspect. Black pixels luckily remain unaffected, so contrast is not jeopardised. The disclinations and the wall can take up a considerable portion of the pixel as shown in figure 7.18.

Apart from the disclinations itself, the two zones with inverted tilt do not behave the same for obliquely incident light rays. The effective retardation can be totally different for the two pixel parts, resulting in different perceived grey levels.

Dynamic effects

Besides this static effect, a dynamic effect also exists, manifesting itself as trailing edges around moving objects on the screen. Figure 7.19 shows what can happen. A white block moves across a black background. Depending

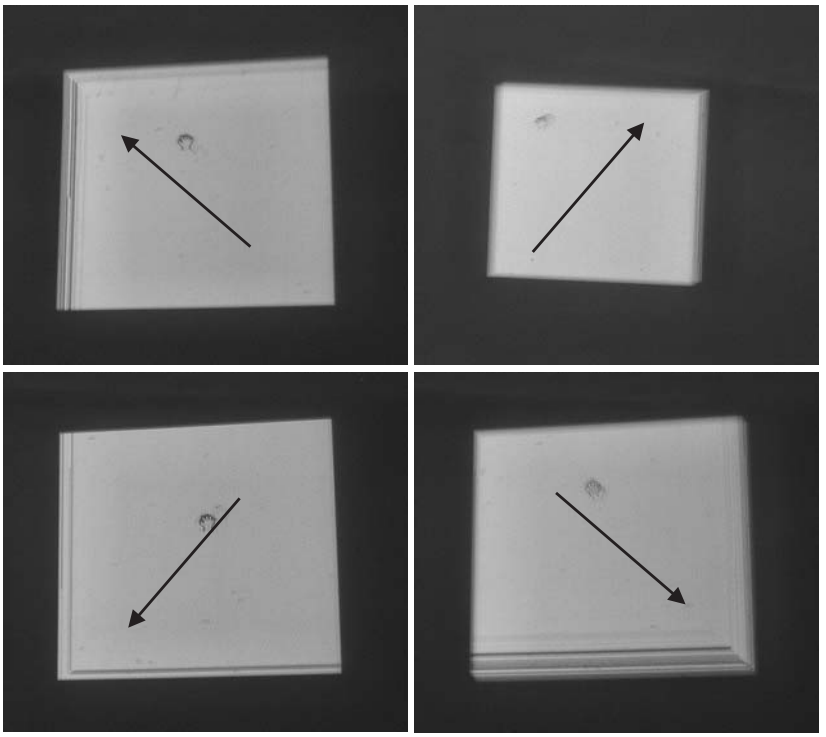

Figure 7.19: Dynamic effects related to the presence of disclinations. The white block is slowly moved along the screen diagonals.

on the direction, more or less pronounced 'lingering lines' are noted in the neighbourhood of the block's borders.

One explanation states that the lines are caused by the fact that even when a fringe field at the block's borders disappears due to the movement of the block, the disclinations themselves can take considerable more time to annihilate. The disclinations do represent a state of higher energy and should therefore disappear, but some additional energy is required for the rearrangement, hence the possible delay time. The dependence on the motion direction is explained by the pre-tilt angle, which determines the position of the disclination (see below). Similar observations are presented in [171].

Further on, it will become clear that the driving voltages used in our devices are actually low enough to prevent the occurrence of 'real' disclinations. Reverse tilt domains are still present, but they are separated by an inversion wall, which is simply an area with vertical alignment. In this situation, the above explanation does not hold anymore.

It is however still possible to create a plausible explanation. The existence of the reverse tilt zones is actually enough to create a delay. Pixels near the

reverse tilt zone will, when switched on, at first take over the reverse tilt because of the elastic coupling between the liquid crystal molecules. Contrary to the original situation, the fringe field that stabilised the reverse tilt zone is now gone, so this zone must disappear. Obviously, this rearrangement will again cost energy, which can account for the observed delay.

7.4.3 Remedies

It will be clear from the preceding paragraphs that the optical effects of fringe fields can be serious enough to call for measures that preserve image quality.

Of course, the fringe fields themselves cannot readily be altered, but it may be possible to reduce the optical repercussions by carefully tuning the liquid crystal mode parameters. For VAN, the main parameters are obviously the pre-tilt angle and the anchoring energy. To reveal the mechanisms in play, simulation tools to predict the director configuration under various circumstances are needed. In the following section, a method for simulating two-dimensional director profiles is developed.

It is possible to get rid of the dynamic effect by introducing column or pixel inversion mode driving [116]. This creates more or less permanent fringe fields between pixels, eliminating the need for any rearrangement of molecules. Of course, this makes things worse in the static case, since the fringe fields are then effectively stronger.

7.5 Two-dimensional simulation of director configurations

7.5.1 General

Various mathematical approaches exist for the simulation of liquid crystal director orientations. In the simplest form, each discretised director orientation is represented by an inclination and azimuth angle pair (θ, ϕ). This representation has the advantage that it provides easy insight in the physics of the problem, but it has the inconvenience that the azimuth becomes undefined for vertical orientation. It is therefore not frequently used.

Most commonly, the discretised directors are represented by the triple of direction cosines (n_x, n_y, n_z). The discretised director field is thus modelled as a set of unity vectors, pointing along the local director.

The equilibrium configuration is then the set of directors $\vec{n}(\vec{r})$ and voltage distribution $V(\vec{r})$ that satisfies equation (7.26) over the considered space and meets the boundary conditions.

$$\delta\mathcal{F} = 0, \qquad \mathcal{F} = \int_v f dv, \qquad f = f_d - f_e \tag{7.26}$$

$$f_d = \frac{1}{2}K_1(\nabla\vec{n})^2 + \frac{1}{2}K_2(\vec{n}.\nabla\vec{n})^2 + \frac{1}{2}K_3(\vec{n}\times\nabla\times\vec{n})^2 + pK_2(\vec{n}.\nabla\vec{n}) \tag{7.27}$$

$$f_e = \frac{1}{2}\vec{E}\vec{D} = \frac{1}{2}\vec{E}\epsilon_0\widetilde{\epsilon}\vec{E} \tag{7.28}$$

$$\vec{E} = -\vec{\nabla}V \tag{7.29}$$

Equation (7.26) states that for a solution of the static problem, the Gibbs free energy should be stationary. The Gibbs free energy of a liquid crystal within a fixed potential configuration consists of the elastic deformation energy, which is given by the Frank-Oseen equation (7.27) [172, 173] and the energy of the electric field (7.28), (7.29). The Franck-Oseen equation is given here in the common vector representation. The constants K_i are the elastic deformation constants and refer to the three possible 'pure' states of deformation in a uniaxial liquid crystal: splay, twist and bend respectively. For non-chiral liquid crystals, the pitch value p of the chirality is zero and the last term in the equation vanishes.

For a uniaxial liquid crystal, the relation between the director orientation and the dielectric permittivity tensor is given by equation (7.30).

$$\epsilon_{ij} = \epsilon_\perp\delta_{ij} + \Delta\epsilon n_i n_j \tag{7.30}$$

Elaboration of equation (7.26) will lead to a set of non-linear, scalar partial differential equations with five unknowns. Although such problems can be handled by today's computational techniques, it remains a rather complicated and cumbersome problem. Solving the dynamical equations, which give the time dependent evolution and iterating until the steady state is achieved, is then often a more preferred approach.

Before embarking on the derivation of the dynamical equations, it is worthwhile to first consider in more detail the vector representation of the director field. After all, the vector model for the director field of nematic liquid crystals appears to be the natural choice, but there is one pitfall. In the model, a director represented by $\vec{n}$ is completely different and fully incompatible with the director represented by $-\vec{n}$. In reality, a director has no 'pointing direction' and the above mentioned fields are identical. This can lead to completely wrong predictions of the director configuration if the above situation occurs during the simulation. To avoid this, some effort has been spent in developing a calculation method that takes the nematic symmetry into account [174, 175, 176]. To achieve this, the alignment tensor $\overline{Q}$ is introduced, defined as in equation

(7.31), with S being the scalar order parameter and δ_{ij} the Kronecker delta symbol. This traceless tensor has the correct symmetry properties.

$$Q_{ij} = S(n_i n_j - \frac{\delta_{ij}}{3}) \tag{7.31}$$

Next, equation (7.27), expressing the elastic energy, has to be rewritten in terms of the alignment tensor. This is done via a Ginzburg-Landau expansion, i.e. it is assumed that the free energy can be written as a power series in terms of $\overline{Q}$ and its spatial derivatives. Identifying the multiplying constants in this power series is a tedious job. Up to now, a third order expansion has been completed [177, 176]. The resulting mathematical description has the correct symmetry properties, at the expense of a more complex formalism and hence longer computation times.

More recently, it has been shown that the tensor method is not always superior to the vector model. Because of the discrete nature of the simulation, initial topologically inequivalent states can slip through grid points and disappear in the tensor model, whereas they do not in the vector model [178]. Generally, neither the tensor nor the vector model will give correct results in these cases, but the output of the vector approach tends to be closer to the physical reality.

As will become clear later on, the vector model turned out to be adequate enough to simulate the behaviour of the vertically aligned mode in the configurations of interest .

7.5.2 Director dynamics

The equations governing the dynamics of the liquid crystal can be obtained using the principle of virtual work, stating that the work performed by external forces during a virtual displacement must be converted into Joule heat or added to the internal energy of the considered system. Treating the liquid crystal layer as a non permanently polarised, non-conducting medium, ignoring all additional dielectric layers, discarding any flow phenomena and further assuming the system is electrically insulated from the outside, the energy balance can be written as in (7.32).

$$\int_V \overline{M} \cdot \delta\vec{n}\,\mathrm{d}v + \int_S \overline{M^S} \cdot \delta\vec{n}\,\mathrm{d}s = \int_V \delta f_d\,\mathrm{d}v + \int_S \delta f_s\,\mathrm{d}s + \int_V \delta f_e\,\mathrm{d}v \tag{7.32}$$

This states that the work performed by the external torque $\vec{M}$ must increase either the elastic energy density f_d or electrical energy density f_e. Furthermore, a distinction has already been made between the bulk and the borders. Alignment of the liquid crystal layer is imposed only via the edges, so its contribution

to the energy will be comparatively large. It thus makes sense to treat the edges as a singularity and introduce the surface integrals to treat them separately.

The external torques $\vec{M}$ and $\vec{M^S}$ at the border can be inertial forces and viscous forces. In liquid crystals, the inertial forces can practically always be ignored [179]. The viscous torque can be written as (7.33) [180] where γ is the rotational viscosity.

$$\overline{M} = -\gamma \frac{\partial \vec{n}}{\partial t} \tag{7.33}$$

The elastic energy density is given by the Oseen-Franck equation (7.27) and reduces for a non-chiral liquid crystal to (7.34).

$$f_d = \frac{1}{2} K_1 (\nabla \vec{n})^2 + \frac{1}{2} K_2 (\vec{n}.\nabla \vec{n})^2 + \frac{1}{2} K_3 (\vec{n} \times \nabla \times \vec{n})^2 \tag{7.34}$$

The anchoring energy density at the borders is introduced as a kind of penalty function as in (7.35). The constant β modulates the anchoring strength and is somewhat similar to the dimensionless coupling constant χ in the better known one-dimensional version of the Rapini-Papoular theory [151]. The vector $\vec{n_0}$ contains the imposed direction at the alignment layer.

$$f_s = \beta (1 - (\vec{n} \cdot \vec{n_0})^2) \tag{7.35}$$

Up to now, the equations still apply to the general case. Before proceeding, we will restrict ourselves to a two-dimensional approach. Figure 7.20 depicts the situation. Only the cross-section Ω is considered instead of the three-dimensional volume of liquid crystal. The situation in all other cross-sections Ω', Ω'', ... is identical to the one in Ω, so all derivatives with respect to z must be zero. This also implies that the electrical E-field cannot have a component along the z-axis.

In equation (7.32), the volume integrals then become surface integrals over Ω and the surface integrals reduce to line integrals along the contour of Ω.

The integral containing the elastic energy f_d is by far the most complicated term and requires some transformation. Being a function of both the director components (n_x, n_y, n_z) and their derivatives with respect to x and y, (see(7.36)), the variation of f_d can be written as in (7.37).

$$\int_\Omega \delta f_d \, \mathrm{d}\Omega = \iint \delta f_d \left(n_x, n_y, n_z, \frac{\partial n_x}{\partial x}, \frac{\partial n_y}{\partial x}, \frac{\partial n_z}{\partial x}, \frac{\partial n_x}{\partial y}, \frac{\partial n_y}{\partial y}, \frac{\partial n_z}{\partial y} \right) \mathrm{d}x\mathrm{d}y \tag{7.36}$$

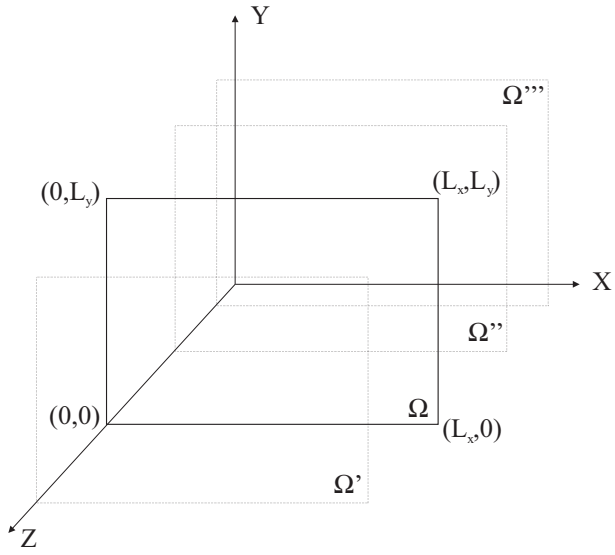

Figure 7.20: Reference axes for the derivation of the equations in the two-dimensional case.

$$\iint \frac{\partial f_d}{\partial n_x}\delta n_x + \frac{\partial f_d}{\partial n_y}\delta n_y + \frac{\partial f_d}{\partial n_z}\delta n_z + \frac{\partial f_d}{\partial(\frac{\partial n_x}{\partial x})}\delta(\frac{\partial n_x}{\partial x}) + \frac{\partial f_d}{\partial(\frac{\partial n_y}{\partial x})}\delta(\frac{\partial n_y}{\partial x}) + \frac{\partial f_d}{\partial(\frac{\partial n_z}{\partial x})}\delta(\frac{\partial n_z}{\partial x}) + \frac{\partial f_d}{\partial(\frac{\partial n_x}{\partial y})}\delta(\frac{\partial n_x}{\partial y}) + \frac{\partial f_d}{\partial(\frac{\partial n_y}{\partial y})}\delta(\frac{\partial n_y}{\partial y}) + \frac{\partial f_d}{\partial(\frac{\partial n_z}{\partial y})}\delta(\frac{\partial n_z}{\partial y})\,\mathrm{d}x\mathrm{d}y \tag{7.37}$$

The terms with the spatial derivatives can be transformed using two successive partial integrations. As an example, the terms containing n_x are transformed as in (7.38).

$$\iint \frac{\partial f_d}{\partial(\frac{\partial n_x}{\partial x})}\delta(\frac{\partial n_x}{\partial x}) + \frac{\partial f_d}{\partial(\frac{\partial n_x}{\partial y})}\delta(\frac{\partial n_x}{\partial y})\,\mathrm{d}x\mathrm{d}y =$$
$$\int_0^{L_y}\left\{\left|\frac{\partial f_d}{\partial(\frac{\partial n_x}{\partial x})}\delta n_x\right|_{x=0}^{x=L_x} - \int_0^{L_x}\frac{\partial}{\partial x}\left(\frac{\partial f_d}{\partial\left(\frac{\partial n_x}{\partial x}\right)}\right)\delta n_x\,\mathrm{d}x\right\}\mathrm{d}y$$
$$+\int_0^{L_x}\left\{\left|\frac{\partial f_d}{\partial(\frac{\partial n_x}{\partial x})}\delta n_x\right|_{y=0}^{y=L_y} - \int_0^{L_y}\frac{\partial}{\partial y}\left(\frac{\partial f_d}{\partial\left(\frac{\partial n_x}{\partial y}\right)}\right)\delta n_x\,\mathrm{d}y\right\}\mathrm{d}x \tag{7.38}$$

The variation of the electric energy density δf_e is obtained starting from equation (7.39).

$$\frac{\partial f_e}{\partial t} = \frac{1}{2}\frac{\partial(\vec{E}\vec{D})}{\partial t} = \frac{1}{2}\epsilon_0\left(\frac{\partial\vec{E}}{\partial t}\widetilde{\epsilon}\vec{E} + \vec{E}\frac{\partial\widetilde{\epsilon}}{\partial t}\vec{E} + \vec{E}\widetilde{\epsilon}\frac{\partial\vec{E}}{\partial t}\right) \tag{7.39}$$

Due to the symmetry of the tensor $\widetilde{\epsilon}$, the first and last term in the sum are identical. Introducing now the partial time derivative of the displacement field $\vec{D}$, (7.39) can be rewritten as in (7.40).

$$\frac{\partial f_e}{\partial t} = \vec{E}\frac{\partial\vec{D}}{\partial t} - \frac{1}{2}\epsilon_0\vec{E}\frac{\partial\widetilde{\epsilon}}{\partial t}\vec{E} \tag{7.40}$$

From Maxwell's law $\vec{\nabla}\vec{D} = \rho$ and the principle of conservation of charge in an isolated system $\vec{\nabla}\vec{J} + \frac{\partial\rho}{\partial t} = 0$, an expression for $\frac{\partial\vec{D}}{\partial t}$ can be obtained: (7.41).

$$\frac{\partial\vec{D}}{\partial t} = -\vec{J} \tag{7.41}$$

The liquid crystal is assumed to be non-conducting, hence $\vec{J} = 0$ and the first term in (7.40) also vanishes.

Combining all this, the variation δf_e can be written as in (7.42).

$$\delta f_e = -\frac{1}{2}\epsilon_0\left(\vec{E}\frac{\partial\widetilde{\epsilon}}{\partial n_x}\frac{\partial n_x}{\partial t}\vec{E} + \vec{E}\frac{\partial\widetilde{\epsilon}}{\partial n_y}\frac{\partial n_y}{\partial t}\vec{E}\right)dt \tag{7.42}$$

Or simply

$$\delta f_e = -\frac{1}{2}\epsilon_0\left(\vec{E}\frac{\partial\widetilde{\epsilon}}{\partial n_x}\vec{E}\,\delta n_x + \vec{E}\frac{\partial\widetilde{\epsilon}}{\partial n_y}\vec{E}\,\delta n_y\right) \tag{7.43}$$

At last, one can remark that (7.43) is formally equivalent to (7.44), a more compact notation.

$$\delta f_e = -\frac{\partial f_e}{\partial n_x}\delta n_x - \frac{\partial f_e}{\partial n_y}\delta n_y \tag{7.44}$$

Substituting (7.38) and equivalents together with (7.44) back in (7.32), we obtain (7.45).

$$\begin{aligned}
&\iint -\gamma \left(\frac{\partial n_x}{\partial t}\delta n_x + \frac{\partial n_y}{\partial t}\delta n_y + \frac{\partial n_z}{\partial t}\delta n_z \right) \mathrm{d}y\mathrm{d}x \\
&+ \int_0^{L_x} -\gamma^S \left(\frac{\partial n_x}{\partial t}(x,0)\delta n_x(x,0) \dots \right. \\
&\qquad \left. \dots + \frac{\partial n_y}{\partial t}(x,0)\delta n_y(x,0) + \frac{\partial n_z}{\partial t}(x,0)\delta n_z(x,0) \right) \mathrm{d}x \\
&+ \int_0^{L_x} -\gamma^S \left(\frac{\partial n_x}{\partial t}(x,L_y)\delta n_x(x,L_y) \dots \right. \\
&\qquad \left. \dots + \frac{\partial n_y}{\partial t}(x,L_y)\delta n_y(x,L_y) + \frac{\partial n_z}{\partial t}(x,L_y)\delta n_z(x,L_y) \right) \mathrm{d}x \\
&+ \int_0^{L_y} -\gamma^S \left(\frac{\partial n_x}{\partial t}(0,y)\delta n_x(0,y) \dots \right. \\
&\qquad \left. \dots + \frac{\partial n_y}{\partial t}(0,y)\delta n_y(0,y) + \frac{\partial n_z}{\partial t}(0,y)\delta n_z(0,y) \right) \mathrm{d}y \\
&+ \int_0^{L_y} -\gamma^S \left(\frac{\partial n_x}{\partial t}(L_x,y)\delta n_x(L_x,y) \dots \right. \\
&\qquad \left. \dots + \frac{\partial n_y}{\partial t}(L_x,y)\delta n_y(L_x,y) + \frac{\partial n_z}{\partial t}(L_x,y)\delta n_z(L_x,y) \right) \mathrm{d}y \\
&= \iint \left(A_1\delta n_x + A_2\delta n_y + A_3\delta n_z \right) \mathrm{d}y\mathrm{d}x \\
&+ \int_0^{L_x} \left(B_1\delta n_x(x,0) + B_2\delta n_y(x,0) + B_3\delta n_z(x,0) \right) \mathrm{d}x \\
&+ \int_0^{L_x} \left(B_4\delta n_x(x,L_y) + B_5\delta n_y(x,L_y) + B_6\delta n_z(x,L_y) \right) \mathrm{d}x \\
&+ \int_0^{L_y} \left(B_7\delta n_x(0,y) + B_8\delta n_y(0,y) + B_9\delta n_z(0,y) \right) \mathrm{d}y \\
&+ \int_0^{L_y} \left(B_{10}\delta n_x(L_x,y) + B_{11}\delta n_y(L_x,y) + B_{12}\delta n_z(L_x,y) \right) \mathrm{d}y \\
&+ \iint \left(C_1\delta n_x + C_2\delta n_y \right) \mathrm{d}y\mathrm{d}x
\end{aligned} \tag{7.45}$$

With

$$
\begin{aligned}
A_1 &= \frac{\partial f_d}{\partial n_x} - \frac{\partial}{\partial x}\left(\frac{\partial f_d}{\partial\left(\frac{\partial n_x}{\partial x}\right)}\right) - \frac{\partial}{\partial y}\left(\frac{\partial f_d}{\partial\left(\frac{\partial n_x}{\partial y}\right)}\right) \\
A_2 &= \frac{\partial f_d}{\partial n_y} - \frac{\partial}{\partial x}\left(\frac{\partial f_d}{\partial\left(\frac{\partial n_y}{\partial x}\right)}\right) - \frac{\partial}{\partial y}\left(\frac{\partial f_d}{\partial\left(\frac{\partial n_y}{\partial y}\right)}\right) \\
A_3 &= \frac{\partial f_d}{\partial n_z} - \frac{\partial}{\partial x}\left(\frac{\partial f_d}{\partial\left(\frac{\partial n_z}{\partial x}\right)}\right) - \frac{\partial}{\partial y}\left(\frac{\partial f_d}{\partial\left(\frac{\partial n_z}{\partial y}\right)}\right)
\end{aligned}
\tag{7.46}
$$

$$
\begin{aligned}
B_1 &= \frac{\partial f_s}{\partial n_x(0)} - \frac{\partial f_d}{\partial\left(\frac{\partial n_x}{\partial y}\right)}(x,0) \\
B_2 &= \frac{\partial f_s}{\partial n_y(0)} - \frac{\partial f_d}{\partial\left(\frac{\partial n_y}{\partial y}\right)}(x,0) \\
B_3 &= \frac{\partial f_s}{\partial n_z(0)} - \frac{\partial f_d}{\partial\left(\frac{\partial n_z}{\partial y}\right)}(x,0)
\end{aligned}
\tag{7.47}
$$

$$
\begin{aligned}
B_4 &= \frac{\partial f_s}{\partial n_x(L_y)} + \frac{\partial f_d}{\partial\left(\frac{\partial n_x}{\partial y}\right)}(x,L_y) \\
B_5 &= \frac{\partial f_s}{\partial n_y(L_y)} + \frac{\partial f_d}{\partial\left(\frac{\partial n_y}{\partial y}\right)}(x,L_y) \\
B_6 &= \frac{\partial f_s}{\partial n_z(L_y)} + \frac{\partial f_d}{\partial\left(\frac{\partial n_z}{\partial y}\right)}(x,L_y)
\end{aligned}
\tag{7.48}
$$

$$
\begin{aligned}
B_7 &= \frac{\partial f_s}{\partial n_x(0)} - \frac{\partial f_d}{\partial\left(\frac{\partial n_x}{\partial x}\right)}(0,y) \\
B_8 &= \frac{\partial f_s}{\partial n_y(0)} - \frac{\partial f_d}{\partial\left(\frac{\partial n_y}{\partial x}\right)}(0,y) \\
B_9 &= \frac{\partial f_s}{\partial n_z(0)} - \frac{\partial f_d}{\partial\left(\frac{\partial n_z}{\partial x}\right)}(0,y)
\end{aligned}
\tag{7.49}
$$

$$
\begin{aligned}
B_{10} &= \frac{\partial f_s}{\partial n_x(L_x)} + \frac{\partial f_d}{\partial\left(\frac{\partial n_x}{\partial x}\right)}(L_x, y) \\
B_{11} &= \frac{\partial f_s}{\partial n_y(L_x)} + \frac{\partial f_d}{\partial\left(\frac{\partial n_y}{\partial x}\right)}(L_x, y) \\
B_{12} &= \frac{\partial f_s}{\partial n_z(L_x)} + \frac{\partial f_d}{\partial\left(\frac{\partial n_z}{\partial x}\right)}(L_x, y)
\end{aligned} \tag{7.50}
$$

$$
C_1 = -\frac{\partial f_e}{\partial n_x} \qquad C_2 = -\frac{\partial f_e}{\partial n_y} \tag{7.51}
$$

Equation (7.45) should be valid for random virtual displacements, so it is equivalent to the following set of equations (7.52):

$$
\begin{aligned}
-\gamma\frac{\partial n_x}{\partial t} &= \frac{\partial f_d}{\partial n_x} - \frac{\partial}{\partial x}\left(\frac{\partial f_d}{\partial\left(\frac{\partial n_x}{\partial x}\right)}\right) - \frac{\partial}{\partial y}\left(\frac{\partial f_d}{\partial\left(\frac{\partial n_x}{\partial y}\right)}\right) - \frac{\partial f_e}{\partial n_x} \\
-\gamma\frac{\partial n_y}{\partial t} &= \frac{\partial f_d}{\partial n_y} - \frac{\partial}{\partial x}\left(\frac{\partial f_d}{\partial\left(\frac{\partial n_y}{\partial x}\right)}\right) - \frac{\partial}{\partial y}\left(\frac{\partial f_d}{\partial\left(\frac{\partial n_y}{\partial y}\right)}\right) - \frac{\partial f_e}{\partial n_y} \\
-\gamma\frac{\partial n_z}{\partial t} &= \frac{\partial f_d}{\partial n_z} - \frac{\partial}{\partial x}\left(\frac{\partial f_d}{\partial\left(\frac{\partial n_z}{\partial x}\right)}\right) - \frac{\partial}{\partial y}\left(\frac{\partial f_d}{\partial\left(\frac{\partial n_z}{\partial y}\right)}\right)
\end{aligned} \tag{7.52}
$$

These are the Euler-Lagrange equations governing the director motion. Equation (7.45) should also hold for displacements at the borders, so similarly we obtain :

$$
\begin{aligned}
-\gamma^S \frac{\partial n_x}{\partial t}(x,0) &= \frac{\partial f_s}{\partial n_x(0)} - \frac{\partial f_d}{\partial\left(\frac{\partial n_x}{\partial y}\right)}(x,0) \\
-\gamma^S (\frac{\partial n_x}{\partial t}(x,L_y) &= \frac{\partial f_s}{\partial n_x(L_y)} + \frac{\partial f_d}{\partial\left(\frac{\partial n_x}{\partial y}\right)}(x,L_y) \\
-\gamma^S \frac{\partial n_x}{\partial t}(0,y) &= \frac{\partial f_s}{\partial n_x(0)} - \frac{\partial f_d}{\partial\left(\frac{\partial n_x}{\partial x}\right)}(0,y) \\
-\gamma^S \frac{\partial n_x}{\partial t}(L_x,y) &= \frac{\partial f_s}{\partial n_x(L_x)} + \frac{\partial f_d}{\partial\left(\frac{\partial n_x}{\partial x}\right)}(L_x,y) \\
-\gamma^S \frac{\partial n_y}{\partial t}(x,0) &= \frac{\partial f_s}{\partial n_y(0)} - \frac{\partial f_d}{\partial\left(\frac{\partial n_y}{\partial y}\right)}(x,0) \\
-\gamma^S \frac{\partial n_y}{\partial t}(x,L_y) &= \frac{\partial f_s}{\partial n_y(L_y)} + \frac{\partial f_d}{\partial\left(\frac{\partial n_y}{\partial y}\right)}(x,L_y) \\
-\gamma^S \frac{\partial n_y}{\partial t}(0,y) &= \frac{\partial f_s}{\partial n_y(0)} - \frac{\partial f_d}{\partial\left(\frac{\partial n_y}{\partial x}\right)}(0,y) \\
-\gamma^S \frac{\partial n_y}{\partial t}(L_x,y) &= \frac{\partial f_s}{\partial n_y(L_x)} + \frac{\partial f_d}{\partial\left(\frac{\partial n_y}{\partial x}\right)}(L_x,y) \\
-\gamma^S \frac{\partial n_z}{\partial t}(x,0) &= \frac{\partial f_s}{\partial n_z(0)} - \frac{\partial f_d}{\partial\left(\frac{\partial n_z}{\partial y}\right)}(x,0) \\
-\gamma^S \frac{\partial n_z}{\partial t}(x,L_y) &= \frac{\partial f_s}{\partial n_z(L_y)} + \frac{\partial f_d}{\partial\left(\frac{\partial n_z}{\partial y}\right)}(x,L_y) \\
-\gamma^S \frac{\partial n_z}{\partial t}(0,y) &= \frac{\partial f_s}{\partial n_z(0)} - \frac{\partial f_d}{\partial\left(\frac{\partial n_z}{\partial x}\right)}(0,y) \\
-\gamma^S \frac{\partial n_z}{\partial t}(L_x,y) &= \frac{\partial f_s}{\partial n_z(L_x)} + \frac{\partial f_d}{\partial\left(\frac{\partial n_z}{\partial x}\right)}(L_x,y)
\end{aligned}
\tag{7.53}
$$

The rotational viscosity at the borders, γ_S, is in fact part of an already very advanced modelling. Practically no data exists as to what value it should be given. Usually, it is simply set to zero, meaning the rotational viscosity at the borders is assumed to be identical to the one in the bulk.

To obtain the actual equations for the model, we still have to fill in the expressions for f_d, f_e and f_s in (7.52) and (7.53). From (7.34), (7.28) and (7.35) and applying the two-dimensional restriction we first obtain :

$$f_d = \frac{1}{2}\left(K_1\left(\frac{\partial n_x}{\partial x}+\frac{\partial n_y}{\partial y}\right)^2 + K_2\left(n_x\frac{\partial n_z}{\partial y}+n_y\frac{\partial n_z}{\partial x}\dots\right.\right.$$
$$\dots + n_z\left(\frac{\partial n_y}{\partial x}-\frac{\partial n_x}{\partial y}\right)\Bigg)^2 + K_3\left(\left(n_y\left(\frac{\partial n_y}{\partial x}-\frac{\partial n_x}{\partial y}\right)+n_z\frac{\partial n_z}{\partial x}\right)^2\right.$$
$$\left.\left.\dots+\left(n_x\left(\frac{\partial n_y}{\partial x}-\frac{\partial n_x}{\partial y}\right)-n_z\frac{\partial n_z}{\partial y}\right)^2+\left(n_x\frac{\partial n_z}{\partial x}+n_y\frac{\partial n_z}{\partial y}\right)^2\right)\right) \tag{7.54}$$

$$f_e = \frac{1}{2}\epsilon_0\left(\left(\epsilon_\perp+\Delta\epsilon\, n_x^2\right)E_x^2 + 2\Delta\epsilon\, n_x n_y E_x E_y + \left(\epsilon_\perp+\Delta\epsilon\, n_y^2\right)E_y^2\right) \tag{7.55}$$

$$f_s = \beta\left(1-\left(n_x n_{x0}+n_y n_{y0}+n_z n_{z0}\right)^2\right) \tag{7.56}$$

Substitution then finally gives :

$$\begin{aligned}
-\gamma\frac{\partial n_x}{\partial t} \;=\;& (2K_2-K_3)n_x\left(\frac{\partial n_z}{\partial y}\right)^2 + 2(K_2+K_3)n_y\frac{\partial n_z}{\partial x}\frac{\partial n_z}{\partial y}\\
&+(3K_2-K_3)n_z\frac{\partial n_y}{\partial x}\frac{\partial n_z}{\partial y} - 2K_2 n_z\frac{\partial n_x}{\partial y}\frac{\partial n_z}{\partial y} + K_3 n_x\left(\frac{\partial n_y}{\partial x}\right)^2\\
&-K_3 n_x\left(\frac{\partial n_x}{\partial y}\right)^2 + K_3 n_x\left(\frac{\partial n_z}{\partial x}\right)^2 - K_1\frac{\partial^2 n_z}{\partial x^2}\\
&+\left(K_2 n_z^2 + K_3(n_x^2+n_y^2) - K_1\right)\frac{\partial^2 n_y}{\partial x\partial y} + (K_2-K_3)n_x n_y\frac{\partial^2 n_z}{\partial y^2}\\
&+(K_2+K_3)\left(n_z\frac{\partial n_y}{\partial y}\frac{\partial n_z}{\partial x}+n_y n_z\frac{\partial^2 n_z}{\partial x\partial y}\right) - 2K_3 n_y\frac{\partial n_y}{\partial y}\frac{\partial n_x}{\partial y}\\
&-\left(K_2 n_z^2 + K_3(n_x^2+n_y^2)\right)\frac{\partial^2 n_x}{\partial y^2} + 2K_3 n_y\frac{\partial n_y}{\partial y}\frac{\partial n_y}{\partial x}\\
&-\epsilon_0\Delta\epsilon E_x(E_x n_x + E_y n_y)
\end{aligned} \tag{7.57}$$

$$
\begin{aligned}
-\gamma\frac{\partial n_y}{\partial t} &= -K_3 n_y\left(\frac{\partial n_z}{\partial x}\right)^2 + 2K_3 n_x\frac{\partial n_z}{\partial x}\frac{\partial n_z}{\partial y} - 2K_2 n_z\frac{\partial n_z}{\partial x}\frac{\partial n_y}{\partial x} \\
&\quad +(K_2-K_3)n_z\frac{\partial n_x}{\partial y}\frac{\partial n_z}{\partial x} - K_3 n_y\left(\frac{\partial n_y}{\partial x}\right)^2 + K_3 n_y\left(\frac{\partial n_x}{\partial y}\right)^2 \\
&\quad +K_3 n_y\left(\frac{\partial n_z}{\partial y}\right)^2 - (K_2-K_3)\left(n_z\frac{\partial n_x}{\partial x}\frac{\partial n_z}{\partial y} + n_x n_z\frac{\partial^2 n_z}{\partial x\partial y}\right) \\
&\quad -(K_2+K_3)n_y n_z\frac{\partial^2 n_z}{\partial x^2} + 2K_3 n_x\frac{\partial n_x}{\partial x}\frac{\partial n_x}{\partial y} \\
&\quad +\left(K_2 n_z^2 + K_3(n_x^2+n_y^2) - K_1\right)\frac{\partial^2 n_x}{\partial x\partial y} - 2K_3 n_x\frac{\partial n_x}{\partial x}\frac{\partial n_y}{\partial x} \\
&\quad -\left(K_2 n_z^2 + K_3(n_x^2+n_y^2)\right)\frac{\partial^2 n_y}{\partial x^2} - K_1\frac{\partial^2 n_y}{\partial y^2} \\
&\quad -\epsilon_0\Delta\epsilon E_y(E_x n_x + E_y n_y)
\end{aligned}
\tag{7.58}
$$

$$
\begin{aligned}
-\gamma\frac{\partial n_z}{\partial t} &= -2K_3 n_x\frac{\partial n_y}{\partial x}\frac{\partial n_z}{\partial y} - 2K_2 n_y\frac{\partial n_z}{\partial x}\frac{\partial n_y}{\partial x} - K_3 n_z\left(\frac{\partial n_y}{\partial x}\right)^2 \\
&\quad +2(K_3-K_2)n_z\frac{\partial n_x}{\partial y}\frac{\partial n_y}{\partial x} + (2K_3-4K_2)n_x\frac{\partial n_x}{\partial y}\frac{\partial n_z}{\partial y} \\
&\quad -2(K_2+K_3)n_y\frac{\partial n_x}{\partial y}\frac{\partial n_z}{\partial x} + K_3 n_z\left(\frac{\partial n_x}{\partial y}\right)^2 - K_3 n_z\left(\frac{\partial n_z}{\partial x}\right)^2 \\
&\quad -K_3 n_z\left(\frac{\partial n_z}{\partial y}\right)^2 - 2(K_2+K_3)n_x n_y\frac{\partial^2 n_z}{\partial x\partial y} - 2K_3 n_x\frac{\partial n_x}{\partial x}\frac{\partial n_z}{\partial x} \\
&\quad -\left(K_2 n_y^2 + K_3(n_x^2+n_z^2)\right)\frac{\partial^2 n_z}{\partial x^2} \\
&\quad -(K_2+K_3)\left(n_y\frac{\partial n_x}{\partial x}\frac{\partial n_z}{\partial y} + n_y n_z\frac{\partial^2 n_y}{\partial x^2}\ \ldots\right. \\
&\qquad\qquad \left.\ldots - n_y\frac{\partial n_z}{\partial x}\frac{\partial n_x}{\partial y} - n_y n_z\frac{\partial^2 n_x}{\partial x\partial y}\right) \\
&\quad -2K_3 n_y\frac{\partial n_y}{\partial y}\frac{\partial n_z}{\partial y} - \left(K_2 n_x^2 + K_3(n_y^2+n_z^2)\right)\frac{\partial^2 n_z}{\partial y^2} \\
&\quad -(K_2+K_3)n_x\frac{\partial n_y}{\partial y}\frac{\partial n_z}{\partial x} \\
&\quad -(K_2-K_3)\left(n_x\frac{\partial n_z}{\partial y}\frac{\partial n_y}{\partial x} + n_x n_z\frac{\partial^2 n_y}{\partial x\partial y} - n_x n_z\frac{\partial^2 n_x}{\partial y^2}\right)
\end{aligned}
\tag{7.59}
$$

Using the assumption that $\gamma^S = 0$ as previously indicated and further

assuming that only the top and bottom plates impose an alignment on the sample as in an actual LC stack, so that $f_s \equiv 0$ at $x = 0$ and $x = L_x$, the equations at the borders become as in (7.60) and (7.61), respectively for the horizontal and the vertical boundaries.

$$\begin{aligned}
&(K_3 - K_2)n_x n_z \frac{\partial n_z}{\partial y} - (K_2 + K_3)n_y n_z \frac{\partial n_z}{\partial x} \\
&\qquad + \left(K_2 n_z^2 + K_3(n_x^2 + n_y^2)\right)\left(\frac{\partial n_x}{\partial y} - \frac{\partial n_y}{\partial x}\right) \\
&\qquad\qquad +2\beta\left(n_x n_{x0} + n_y n_{y0} + n_z n_{z0}\right) = 0 \\
&K_1\left(\frac{\partial n_x}{\partial x} + \frac{\partial n_y}{\partial y}\right) + 2\beta\left(n_x n_{x0} + n_y n_{y0} + n_z n_{z0}\right) = 0 \\
&\left(K_2 n_x^2 + K_3(n_y^2 + n_z^2)\right)\frac{\partial n_z}{\partial y} + (K_2 + K_3)n_x n_y \frac{\partial n_z}{\partial x} + (K_2 - K_3)n_x n_z \frac{\partial n_y}{\partial x} \\
&\qquad +(K_3 - K_2)n_x n_z \frac{\partial n_x}{\partial y} + 2\beta\left(n_x n_{x0} + n_y n_{y0} + n_z n_{z0}\right) = 0
\end{aligned} \tag{7.60}$$

$$\begin{aligned}
&\left(K_2 n_x^2 + K_3(n_y^2 + n_z^2)\right)\frac{\partial n_z}{\partial y} + (K_2 + K_3)n_x n_y \frac{\partial n_z}{\partial x} \\
&\qquad +(K_2 - K_3)n_x n_z \frac{\partial n_y}{\partial x} + (K_3 - K_2)n_x n_z \frac{\partial n_x}{\partial y} = 0 \\
&(K_3 - K_2)n_x n_z \frac{\partial n_z}{\partial y} - (K_2 + K_3)n_y n_z \frac{\partial n_z}{\partial x} \\
&\qquad + \left(K_2 n_z^2 + K_3(n_x^2 + n_y^2)\right)\left(\frac{\partial n_x}{\partial y} - \frac{\partial n_y}{\partial x}\right) = 0 \\
&K_1\left(\frac{\partial n_x}{\partial x} + \frac{\partial n_y}{\partial y}\right) = 0
\end{aligned} \tag{7.61}$$

7.5.3 Numerical solution

To numerically solve the equations, they have to be discretised, both in the space and time domain. For the spatial discretisation, a rectangular grid is put over the considered area. The spatial derivatives at node i are then approximated with their finite difference version, as in (7.62).

$$\begin{aligned}
\left(\frac{\partial f}{\partial x}\right)_i &= \frac{f_{i+1} - f_{i-1}}{2\Delta x} \\
\left(\frac{\partial^2 f}{\partial x^2}\right)_i &= \frac{f_{i+1} - 2f_i + f_{i-1}}{(2\Delta x)^2} \\
\left(\frac{\partial^2 f}{\partial x \partial y}\right)_{i,j} &= \frac{f_{i+1,j+1} - f_{i-1,j+1} - f_{i+1,j-1} + f_{i-1,j-1}}{4\Delta x \Delta y}
\end{aligned} \tag{7.62}$$

Non-evenly spaced grids can be advantageous for the simulation of larger topologies containing areas where the spatial variation of the director orientation is a priori suspected to be much lower than in others. The finite difference formulas of (7.62) then take the form of (7.63) and (7.64).

$$\begin{aligned}
\left(\frac{\partial f}{\partial x}\right)_i &= \frac{{\Delta x_-}^2 f_{i+1} + ({\Delta x_+}^2 - {\Delta x_-}^2) f_i - {\Delta x_+}^2 f_{i-1}}{2\Delta x} \\
\left(\frac{\partial^2 f}{\partial x^2}\right)_i &= 2\frac{\Delta x_- f_{i+1} - (\Delta x_- + \Delta x_+) f_i + \Delta x_+ f_{i-1}}{\Delta x_+ \Delta x_- (\Delta x_- + \Delta x_+)}
\end{aligned} \tag{7.63}$$

$$
\begin{aligned}
\left(\frac{\partial^2 f}{\partial x \partial y}\right)_{i,j} &= \frac{(\Delta x_+ - \Delta x_-)(\Delta y_+ - \Delta y_-)}{\Delta x_- \Delta x_+ \Delta y_- \Delta y_+} f_{i,j} \\
&+ \frac{\Delta x_- \Delta y_-}{\Delta x_+ \Delta y_+ (\Delta x_- + \Delta x_+)(\Delta y_- + \Delta y_+)} f_{i+1,j+1} \\
&+ \frac{\Delta y_- (\Delta x_+ - \Delta x_-)}{\Delta x_- \Delta x_+ \Delta y_+ (\Delta y_- + \Delta y_+)} f_{i,j+1} \\
&- \frac{\Delta x_+ \Delta y_-}{\Delta x_- \Delta y_+ (\Delta x_- + \Delta x_+)(\Delta y_- + \Delta y_+)} f_{i-1,j-1} \\
&- \frac{\Delta x_+ (\Delta y_+ - \Delta y_-)}{\Delta x_- \Delta y_+ \Delta y_- (\Delta x_- + \Delta x_+)} f_{i-1,j} \\
&+ \frac{\Delta x_- (\Delta y_+ - \Delta y_-)}{\Delta x_+ \Delta y_+ \Delta y_- (\Delta x_- + \Delta x_+)} f_{i+1,j} \\
&- \frac{\Delta x_- \Delta y_+}{\Delta x_+ \Delta y_- (\Delta x_+ + \Delta x_-)(\Delta y_- + \Delta y_+)} f_{i+1,j-1} \\
&- \frac{\Delta y_+ (\Delta x_+ - \Delta x_-)}{\Delta x_+ \Delta x_- \Delta y_- (\Delta y_- + \Delta y_+)} f_{i,j-1} \\
&+ \frac{\Delta x_+ \Delta y_+}{\Delta x_- \Delta y_- (\Delta x_- + \Delta x_+)(\Delta y_- + \Delta y_+)} f_{i-1,j-1}
\end{aligned}
\tag{7.64}
$$

At the boundaries, (7.62) cannot be used anymore and has to be replaced with (7.65), which approximates the derivative using a second order Lagrange polynomial. For non-evenly spaced grids, (7.65) must be altered accordingly.

$$
\begin{aligned}
\left(\frac{\partial f}{\partial x}\right)_0 &= \frac{-3f_0 + 4f_1 - f_2}{2\Delta x} \\
\left(\frac{\partial f}{\partial x}\right)_N &= \frac{f_{N-2} - 4f_{N-1} + 3f_N}{2\Delta x}
\end{aligned}
\tag{7.65}
$$

For the iteration in time, three schemes are commonly used: the Euler forward method, Euler backward and the Chrank-Nicholson method. The latter are implicit methods and in this case require the additional solving of a rather large set of equations at each time step in order to obtain the next iteration value. Additionally, the implementation of these methods is rather involved. The benefit is that the algorithm is unconditionally stable.

Presently, only the Euler forward method has been used in the simulation code. The time derivative is then, obviously, approximated by (7.66).

$$\left(\frac{\partial f}{\partial t}\right)_i = \frac{f_{i+1} - f_i}{\Delta t} \tag{7.66}$$

Being an explicit method, it is very easy to implement. At the downside, the timestep has to be chosen sufficiently small to ensure stability and accuracy. In part, this can be enforced during the simulation by monitoring the computed solution at each timestep and comparing it to the previous one. If the discrepancy between two consecutive solutions is perceived as too big, the calculation step is redone using a smaller timestep. This helps stability somewhat, but the timestep must still be chosen small enough to keep the accuracy high.

Boundary conditions

The equations describing the behaviour at the boundaries still require some attention. If γ^S is set to zero as suggested, the time derivative vanishes and an updated value cannot be computed in a straightforward way.

A way around this is to interpret equations (7.60) and (7.61) as boundary conditions imposed on the spatial derivatives. Thus, (7.60) is transformed into a set of equations with unknowns $(\frac{\partial n_x}{\partial y}, \frac{\partial n_y}{\partial y}, \frac{\partial n_z}{\partial y})$. The other derivatives can be computed the usual way and the set is easily solved.

If it is further assumed that $(\frac{\partial n_x}{\partial y}, \frac{\partial n_y}{\partial y}, \frac{\partial n_z}{\partial y})$ are only slowly varying, the just computed values can also be used for the next timestep. Using (7.60) the new value for the director components at the horizontal boundaries is obtained by substituting the just computed spatial derivative and the already updated director components in the bulk. The same procedure is used for the vertical boundaries, using (7.61) with unknowns $(\frac{\partial n_x}{\partial x}, \frac{\partial n_y}{\partial x}, \frac{\partial n_z}{\partial x})$.

This completes the numerical solution of the director dynamics.

Procedure

The algorithm then looks as follows: Starting from an initial director distribution and the electrical boundary conditions, the electrical potential distribution is computed with the Poisson equation: $\vec{\nabla}(\vec{\nabla}V) = 0$. Several fine pieces of simulation code for this are readily available and can be used as such. Knowing the electrical field, the director configuration can be updated using the Euler-Lagrange equations. This will slightly change the dielectric anisotropy of the stack, so a new iteration is started by recomputing the electrical potential distribution. This repeats until a steady state is obtained.

7.5.4 Optics

The resulting optical behaviour of the stack for normally incident light with a given director configuration is most easily calculated using Jones matrices. Each node in the grid is considered as the middle point of an LC slab with otherwise uniform properties. Optically this slab behaves like a retardation plate and its Jones matrix is represented by (7.67), assuming the polarisation state of the incoming light is referenced to the optical axes of the slab.

$$\mathbf{J_i} = \begin{pmatrix} \exp\left(-in_{eff}\frac{2\pi}{\lambda}d_i\right) & 0 \\ 0 & \exp\left(-in_o\frac{2\pi}{\lambda}d_i\right) \end{pmatrix} \tag{7.67}$$

The Jones representation of the entire stack is obtained by simple matrix multiplication as in (7.68), where $\mathbf{R}$ is the rotation matrix as defined in (4.11), ψ_i is the angle between the X-axis and the projection of the local director onto the X-Z plane and superscript Tr denotes the transposed matrix.

$$\mathbf{J_{stack}} = \prod_{i}^{N} \mathbf{R}^{Tr}(\psi_i)\mathbf{J_i}\mathbf{R}(\psi_i) \tag{7.68}$$

$$\psi_i = \arccos\left(\frac{n_{x,i}}{\sqrt{n_{x,i}^2 + n_{z,i}^2}}\right) \tag{7.69}$$

For a reflective device, the light has to pass twice through the stack, so the resulting intensity of the reflected light is given by (7.70). The vectors $\mathbf{P}$ and $\mathbf{A}$ contain the polarisation states of the polariser and the analyser, respectively.

$$I_{refl} = \left(\text{magnitude}(\mathbf{A}^{Tr}\mathbf{J_{stack}}^{Tr}\mathbf{J_{stack}}\mathbf{P})\right)^2 \tag{7.70}$$

7.6 Simulation results

7.6.1 Preliminary

Pixel model

To minimise computation times and ease the interpretation of the results, all simulations are confined to a single pixel and its environment. The boundary conditions of the pixel surroundings are chosen to mimic an active matrix.

Figure 7.21 depicts the considered situation. The pixel has a pitch L and is attributed a fixed voltage U. To the left and to the right are half pixels at voltage 0. The pixels are separated by inter-pixel gaps of fixed width (0.5 μm), as they are determined by the chosen semiconductor technology. Opposite of the pixel, at a distance d is the unpatterned counterelectrode, also at 0 Volts.

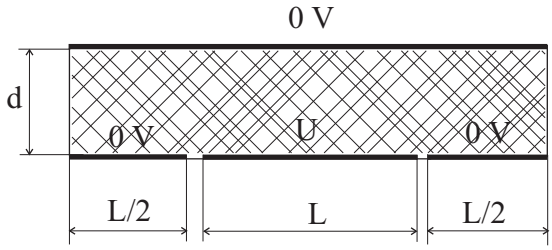

Figure 7.21: Layout model of a pixel used in the simulations.

The remaining areas that have no potential assigned yet (inter-pixel gaps, side walls) are attributed Neumann boundary conditions of the form $\partial V/\partial \vec{r} = 0$, $\vec{r}$ being either the x or y coordinate.

Two instances of pixel geometry are considered: a rather relaxed L/d = 8 ratio and the more challenging L/d = 3.8, corresponding with the current WXGA device. As the cell-gap is fixed at 3 μm, the former is thus obtained for L = 24 μm, while the latter needs L = 11.4 μm.

Alignment of the liquid crystal is imposed on the top and bottom substrates in a uniform way (no pixelation). At the side walls there is no alignment.

Simulation parameter settings

All material parameters are given the values for the actual liquid crystal (MLC-6610 in this case).

The timestep for the iteration should be small enough to maintain numerical stability. Inspection of the equations (7.57), (7.58) and (7.59 in their discrete form shows that the magnitude $\frac{\gamma \Delta h^2}{\Delta t}$ (Δh a characteristic grid distance) can be considered as a time-grid constant governing the reaction speed. If it becomes too large, updated values may deviate too much from the previous ones and the iteration becomes unstable. Consequently, both the rotational viscosity and the grid spacing must be taken into account when determining the timestep. The value for the rotational viscosity is taken from the manufacturer's data, the grid spacing must be chosen for accuracy. The algorithm is somewhat flexible in that it automatically reduces the timestep (within specified limits) if it judges that updated values vary too rapidly.

As said, the number of grid points determines the accuracy of the solution. Figure 7.22 illustrates how for example the resulting reflectance profile can change as the grid becomes finer. Too few grid points can filter out rapid variations.

For all simulations, we used $\gamma = 0.148$ Pas and 160 horizontal gridpoints for the entire pixel model (either 18 μm or 36 μm wide). Vertically 40 gridpoints are used. The initial timestep is then 100 microseconds, possibly reduced to 1

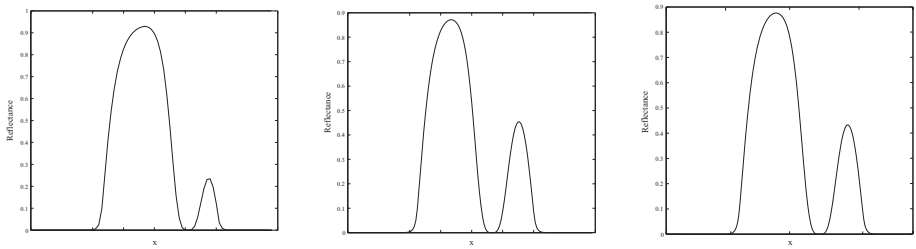

(a) 80 points (b) 160 points (c) 320 points

Figure 7.22: Comparison of simulation results obtained with an increasing number of grid points on the horizontal axis. Shown is the resulting reflectance profile of an arbitrary configuration.

microsecond.

The explicit iteration scheme also results in a not very accurate time behaviour. Equilibrium conditions are almost invariably attained after much longer transition times than in reality.

Anchoring energies are modelled with the parameter β. Values ranged from 0.001 (rigid) to 0.00001 (extremely loose anchoring).

Lastly, it can be noted that a disclination is a discontinuity, while the Oseen-Franck equation used for the free energy stems from a continuity model. The free energy of a disclination is then indeed infinite. The discretisation however makes the use of the Oseen-Franck equation still possible: the energy attributed to a disclination is determined by the grid distance.

7.6.2 Inversion wall versus real disclination

The occurrence of a disclination requires a certain field strength. For a given geometry, a critical voltage exists above which the disclination comes into being. Below that voltage, only an inversion wall is present. Figure 7.23 shows the director field in the latter case.

Because of the moderate voltage, the tilt in both zones of the pixels is still relatively small. The inversion of tilt angle can still be matched for without breaking continuity through the introduction of a so-called inversion wall, which is basically a homeotropically oriented area through which the tilt can be inverted.

As the electrical field is increased, the directors at both sides of the wall tilt more and more to the horizontal. It is clear that this configuration will become unstable above a certain threshold, as a slight bend deformation between the two nearly horizontal directors together with two disclinations (see figure 7.16) will be energetically more favourable than the strong splay deformation [181].

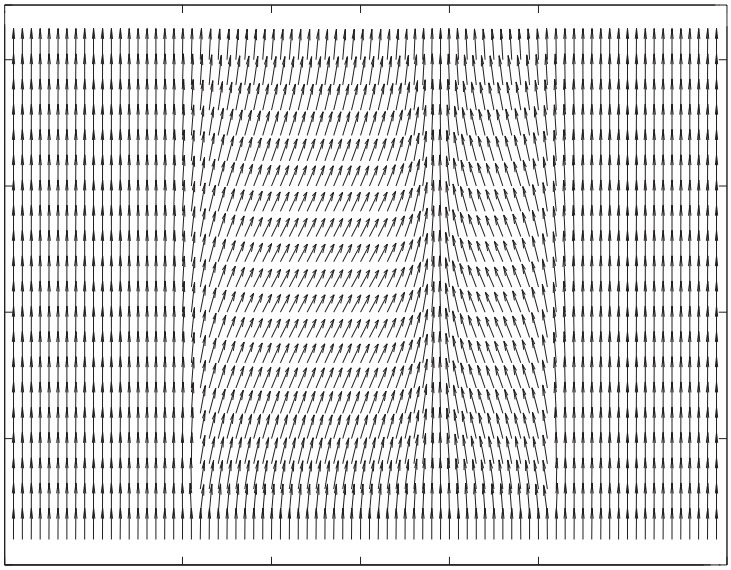

Figure 7.23: Director field with the middle pixel at 3 V. L/d = 8, pre-tilt angle 89.5 °, rigid anchoring. The distance between the outer tick marks indicates the extent of the middle pixel.

Unfortunately, this is one of the cases where the vector approach will go wrong. Because the vectors representing the directors at both sides of the wall point towards each other, the simulator considers them incompatible. Hence, the bend state always has higher energy than the splay state and the switch-over will never occur. This is illustrated by figure 7.24.

At the upside, for the pixel geometries considered here, the needed switching voltages are still conveniently far away from the critical voltage, so that the vector model can still be used.

Looking at the reflectance profiles (figure 7.25), two things can be noted. First of all, although the director profile in the supercritical case is physically meaningless, the predicted reflectance profile is still remarkably close to reality (see [181]). Second, the optical effects of the inversion wall are not necessarily more advantageous than the ones coming from a full disclination.

7.6.3 Pixel width to cell-gap ratio

The ratio pixel width / cell-gap certainly does have an influence on the form of the optical reflectance profile. Figure 7.26 shows the profiles for a L/d value of 8 and 3.8. Both are driven with the same voltage, required to full brightness in a non-pixelated environment.

There is a small shift in the position of the inversion wall: the lower the

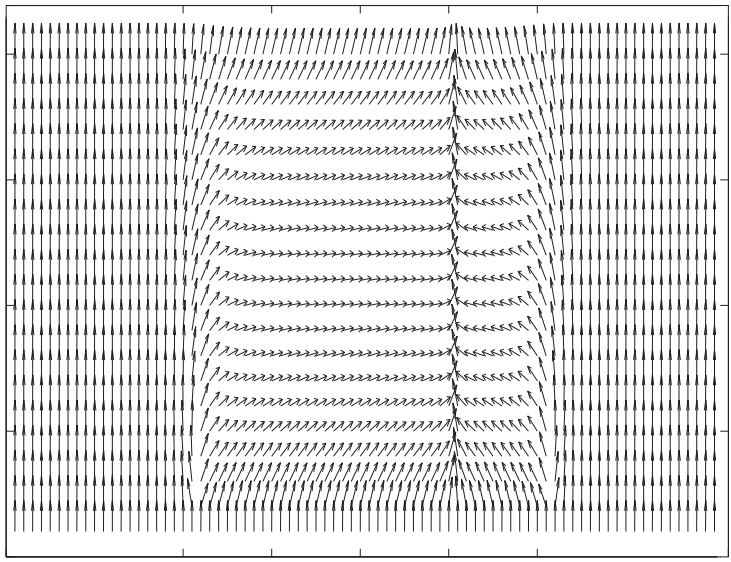

Figure 7.24: Director field with the middle pixel at 6 V. L/d = 8, pre-tilt angle 89.5 °, rigid anchoring. The distance between the outer tick marks indicates the extent of the middle pixel.

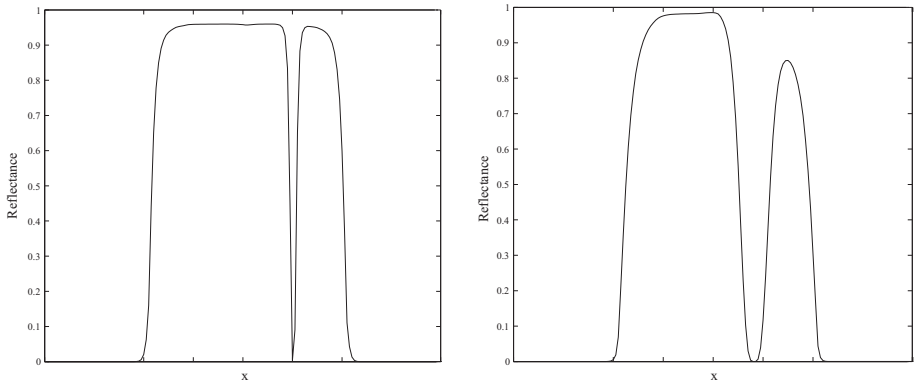

(a) Driving voltage 6 V (b) Driving voltage 3 V

Figure 7.25: Reflectance profiles in the super- and subcritical case (left and right resp.). L/d = 8, pre-tilt angle 89.5 °, rigid anchoring.

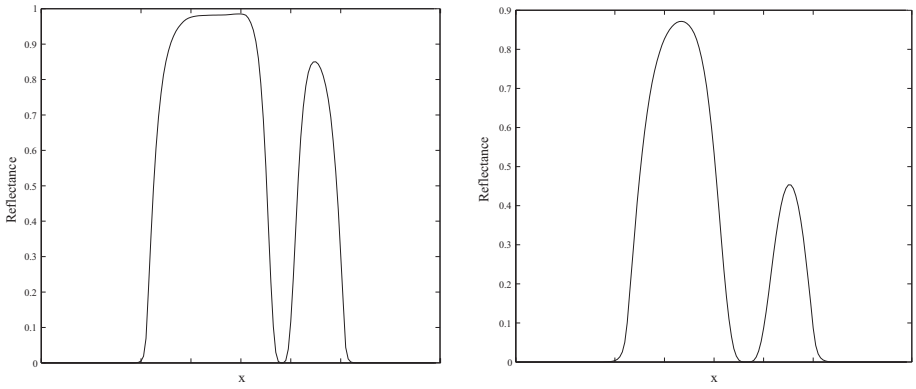

(a) L/d = 8 (b) L/d = 3.8

Figure 7.26: Reflectance profiles for different pixel width to cell-gap ratios. Pre-tilt angle 89.5 °, rigid anchoring, middle pixel at 3 Volts.

ratio, the more the wall shifts towards the centre of the pixel. More important is the fact that for the smaller ratio, the director profile is influenced enough to prevent the reflectance in the main area from reaching 100 %. The reflectance profile of the pixel also moves more and more away from the rectangular form. This can be counterbalanced somewhat by increasing the driving voltage, but only at the price of strengthening the fringe fields.

7.6.4 Influence of pre-tilt angle

The value of the pre-tilt angle can have quite some influence on how the inversion wall manifests itself in the reflectance profile. Figure 7.27 illustrates this for two rather extreme cases : 89.5 ° and 85 ° pre-tilt angle. In the latter case, the wall has shifted towards the edge of the pixel, while the secondary bump is reduced dramatically.

The director field for the 85 ° pre-tilt angle configuration is shown in figure 7.28. Compared to the profile in figure 7.23, it is clear that the lower pre-tilt angle causes the homeotropically oriented zone to move away from the centre, where it can now blend in more easily with the undisturbed areas.

A similar behaviour is observed in the case of lower L/d ratios, figures 7.29 and 7.30. The secondary bump gradually shrinks, while the position of the black line shifts towards the pixel edge. It can also be seen that the extreme case of 85 ° pre-tilt angle, which is unacceptable in terms of contrast ratio, is not needed to reduce the secondary bump significantly. A pre-tilt angle value around 88.5 ° represents a good compromise between contrast and reflectance profile distortion.

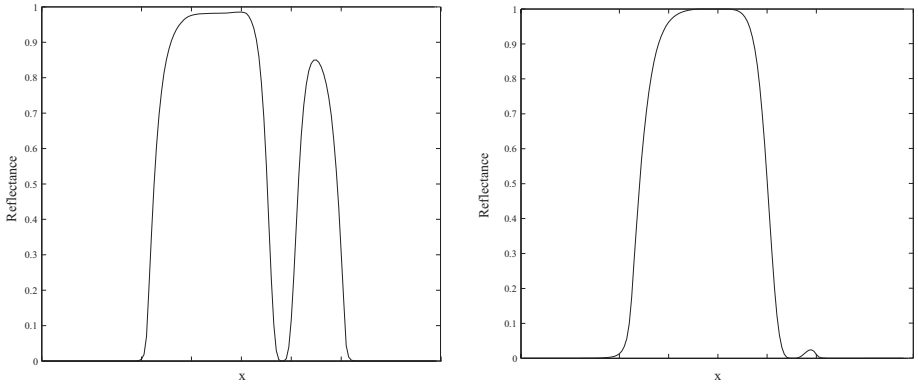

(a) 89.5 ° (b) 85 °

Figure 7.27: Reflectance profiles for different pre-tilt angles at L/d = 8 and for rigid anchoring. Middle pixel at 3 Volts.

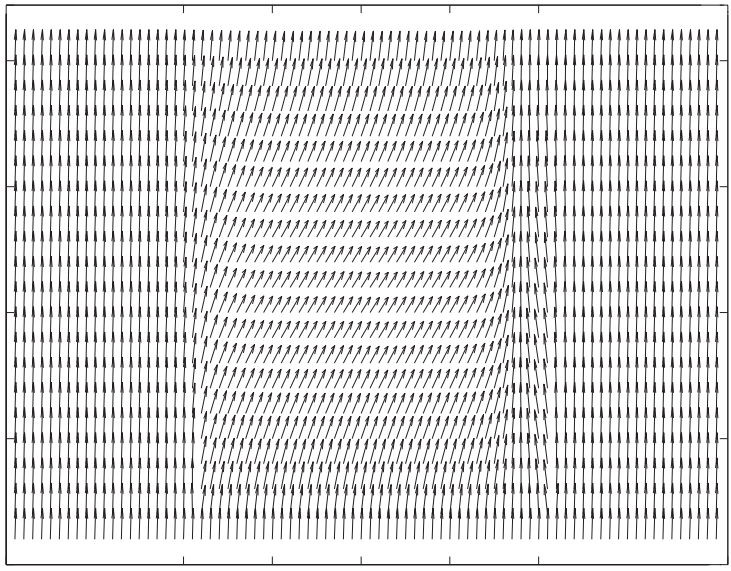

Figure 7.28: Director field at 85 ° pre-tilt angle. Middle pixel at 3 V, rigid anchoring, L/d = 8.

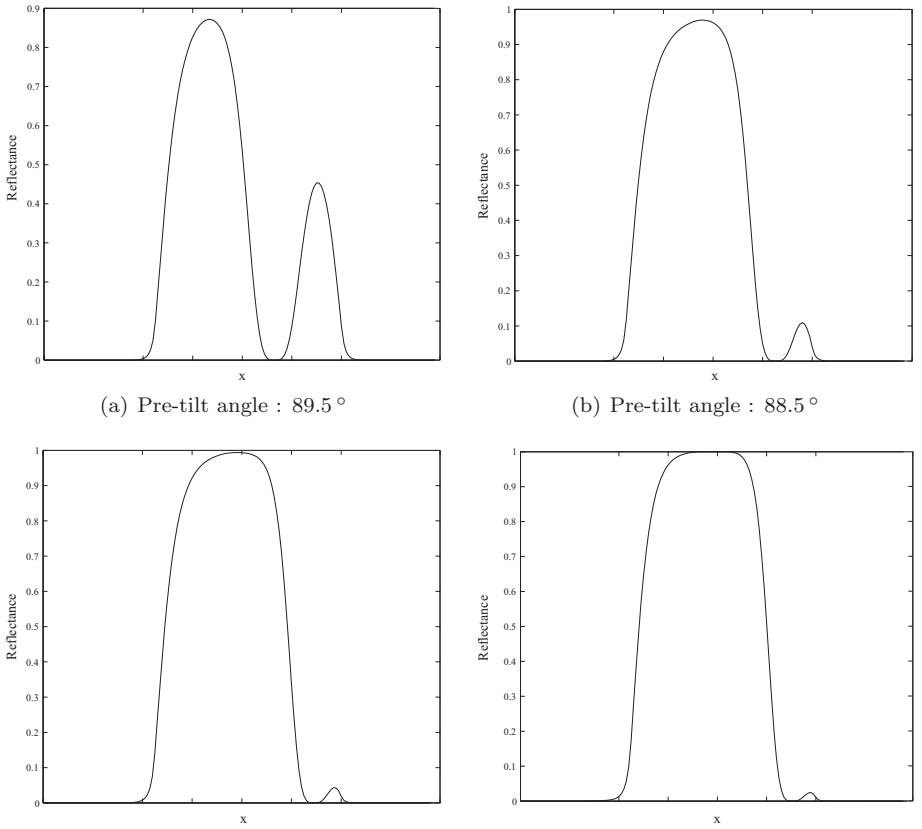

(a) Pre-tilt angle : 89.5 °

(b) Pre-tilt angle : 88.5 °

(c) Pre-tilt angle : 87 °

(d) Pre-tilt angle : 85 °

Figure 7.29: Reflectance profiles for changing pre-tilt angles at L/d = 3.8 with rigid anchoring. Middle pixel at 3 Volts.

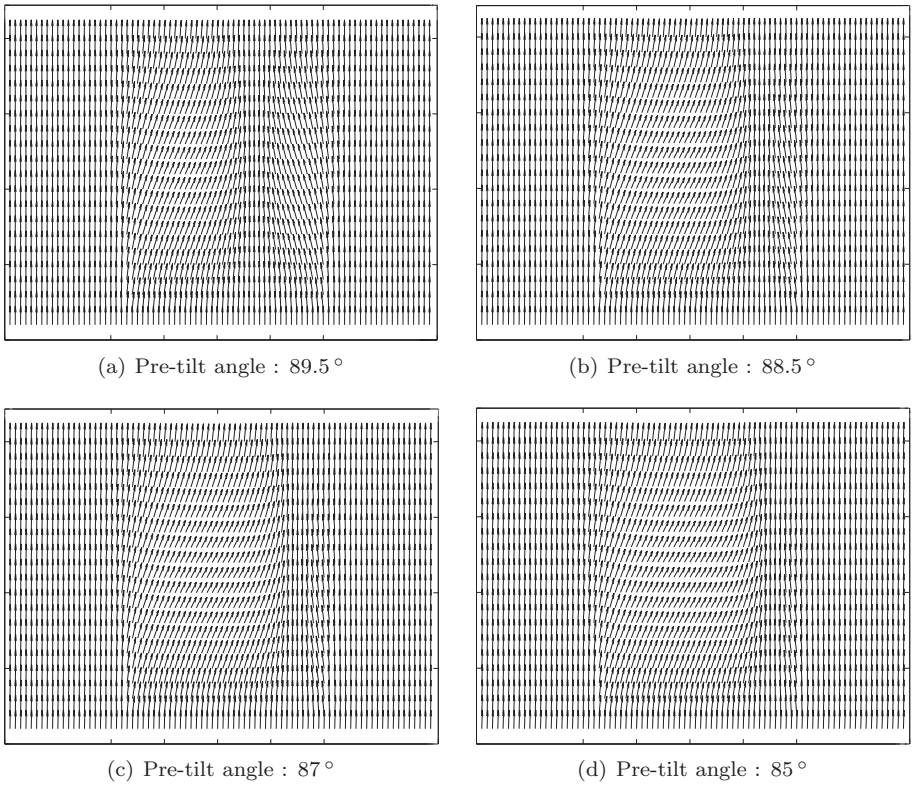

(a) Pre-tilt angle : 89.5 °

(b) Pre-tilt angle : 88.5 °

(c) Pre-tilt angle : 87 °

(d) Pre-tilt angle : 85 °

Figure 7.30: Director fields for changing pre-tilt angles at L/d = 3.8 with rigid anchoring. Middle pixel at 3 Volts.

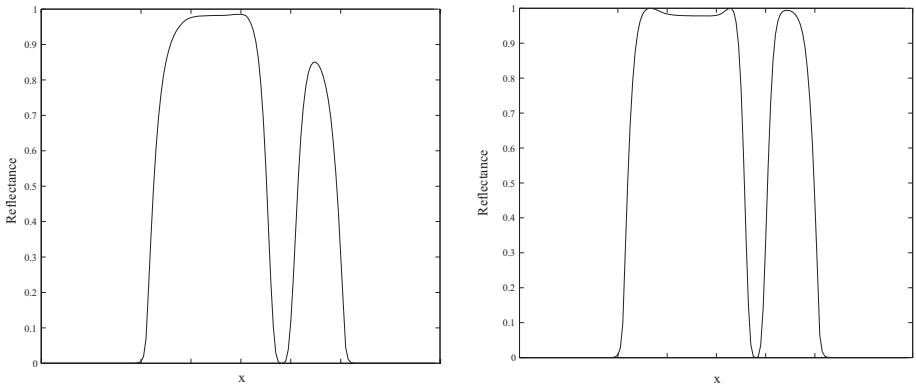

(a) $\beta = 0.001$ (b) $\beta = 0.0001$

Figure 7.31: Reflectance profiles for different anchoring strengths. Pre-tilt angle is 89.5 °, L/d = 8. A value of $\beta = 0.001$ is equivalent to rigid anchoring. Middle pixel at 3 Volts.

7.6.5 Influence of anchoring strength

A second parameter that can have some influence on the two-dimensional director arrangement is the anchoring strength of the molecules at the cell borders.

Figure 7.31 compares the reflectance profiles for systems with rigidly anchored border layers and more loosely anchored ones. Maybe somewhat surprisingly, the looser anchored system has a more prominent secondary bump than the rigid one.

The main bump however has a dimple. This indicates that in this region the reflectance value on the electro-optical response curve is to be found in the second part of the curve, past the top value. Otherwise said, the looser anchoring strength modified the electro-optical response curve so that the driving voltage is somewhat too high. If the voltage is adjusted, a different picture is obtained. Figure 7.32 gives the reflectance profiles for lower anchoring energies with matched driving voltages. As with the pre-tilt angle change, the secondary bump gradually shrinks in height for lower anchoring energies, although far less dramatically. The position of the inversion wall, on the contrary, does not change.

Looking at the director profile, one can only observe that it looks very similar to the profile of the rigidly anchored case (figure 7.33). It may thus be concluded that the improvement in reflectance profile is simply due to a reduction of the (fringe) field strength.

Also over here, the same behaviour is encountered for the L/d = 3.8 case. Figure 7.34 shows the evolution in the reflectance profile for ever lower anchoring strengths and adjusted voltages.

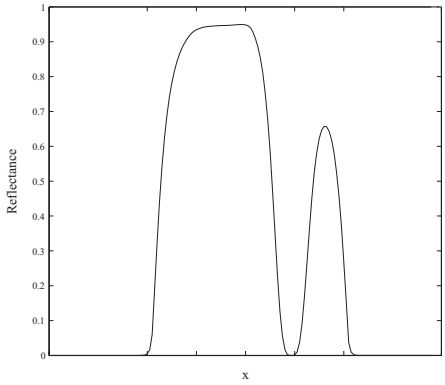

(a) $\beta = 0.0001$, U = 2.75 V

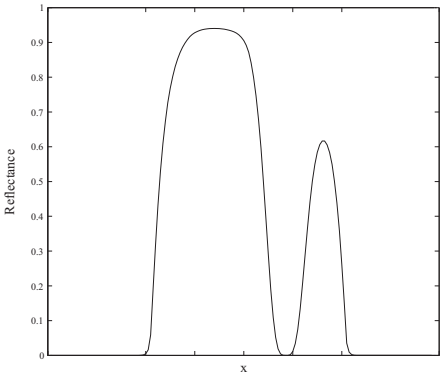

(b) $\beta = 0.00004$, U = 2.5 V

Figure 7.32: Reflectance profiles for different anchoring strengths width adjusted driving voltages. Pre-tilt angle is 89.5 °, L/d = 8.

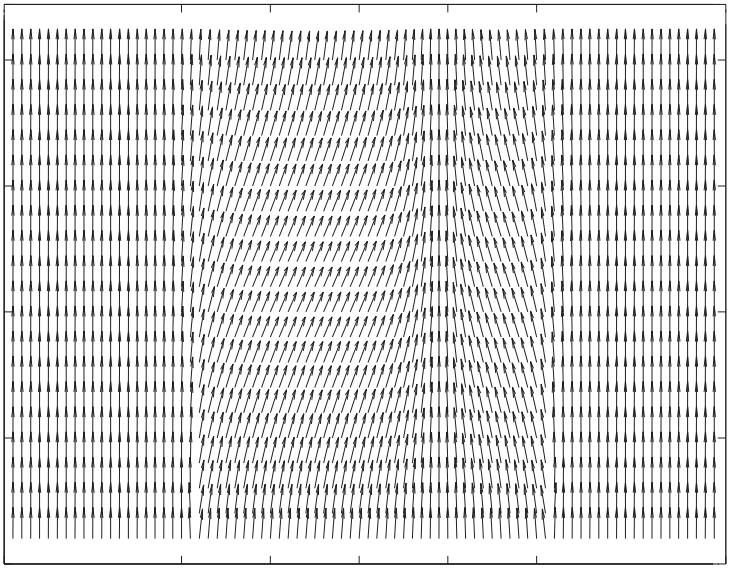

Figure 7.33: Director field in the case of a loose anchoring. $\beta = 0.00004$, U = 2.5 V, pre-tilt angle is 89.5 °, L/d = 8.

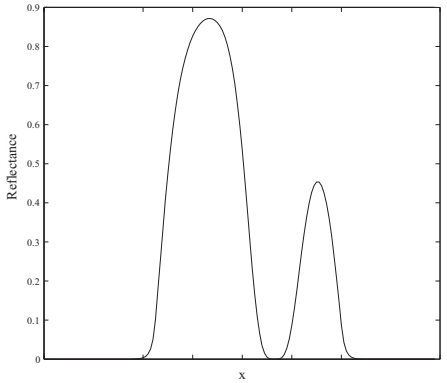

(a) $\beta = 0.001$, U = 3 V

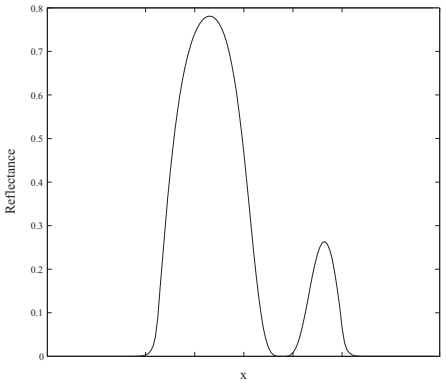

(b) $\beta = 0.0001$, U = 2.75 V

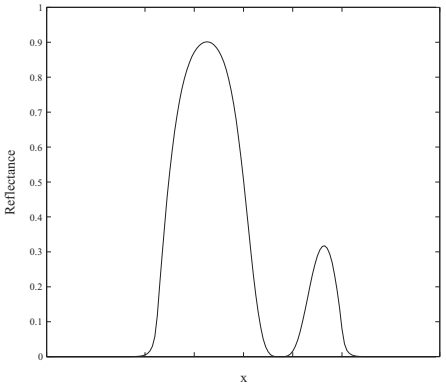

(c) $\beta = 0.00003$, U = 2.5 V

Figure 7.34: Reflectance profiles for changing anchoring strengths at L/d = 3.8. Pre-tilt angle is 89.5 °.

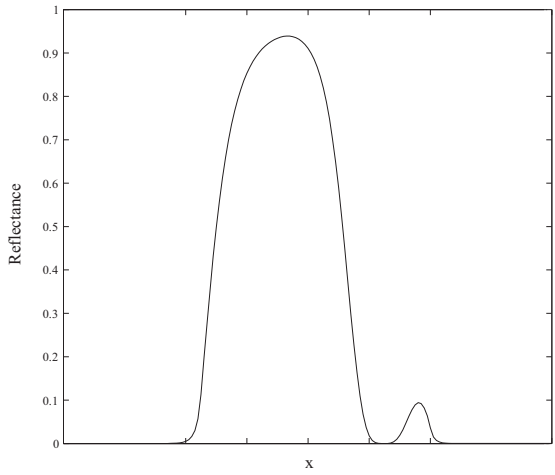

Figure 7.35: Reflectance profile obtained with optimised settings. Pre-tilt angle is 88.5 °, $\beta = 0.000085$, U = 2.75 V.

7.6.6 Combined effects

A combination of both systems can give optimal results. As an example, figure 7.35 shows the obtained reflectance profile for the following settings: pre-tilt angle 88.5 °, $\beta = 0.000085$, driving voltage U = 2.75 V.

The insights obtained with the simulations are of course to be used for the improvement of real displays. The oblique evaporation alignment technique is conveniently used to implement the alignment parameter settings. Figure 7.36 shows a detail of the pixel matrix of such a display.

7.7 Projector

7.7.1 General

As always in the display world, the perceived quality of a device is ultimately determined by the subjective appreciation of the shown images, regardless of any measurements that may tell a different story. As the developed devices are primarily intended to be used for projection, the final step evidently is getting them mounted in a projector. To achieve good quality however, the projector optics must be matched to the projection source in a way that does not permit large deviations. Combined with the fact that, at the time the first devices were produced microdisplays of this size and nature were rather rare, the best way to achieve a convincing demonstration of the device was building a dedicated prototype projector.

In this section the design and practical construction of a 'discrete compo-

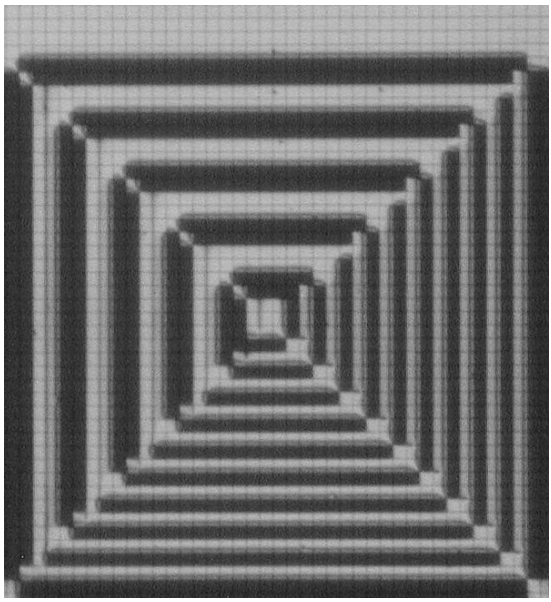

Figure 7.36: Micrograph of a display manufactured with optimised settings to reduce fringe field effects.

nents' projector is briefly discussed. Although during the course of research a number of versions were built, adapting the system to the different panel sizes, lamp powers and optical components that became available, only the latest version is treated here. It uses the WXGA lightvalves and was designed for an f/# number of 3.0.

7.7.2 Projector configuration

The design of a full-colour projection system requires some initial choices.

An obvious first decision that has to be taken is the number of light-valves that will be used. Based on the current response speed achieved with the VAN devices, a one-cell solution (time-sequential colour separation) is not really an option. Apart from that, there are several other reasons why a three valve system (spatial colour separation) will always be superior for larger light fluxes [182].

Any even marginally efficient projection system needs an integrator component to collect the light from the illumination source and transform it into a suitable format with uniform intensity. Two systems are in use: integrator pipes and lens arrays. The choice of the integrator system is linked with the reflector type of the lamp: integrator pipes need elliptical reflectors, lens arrays are used with parabolic reflectors. Both systems perform equally well so that a

preference for either is usually based on manufacturing considerations. In this design an integrator pipe is used.

Etendue

The concept of preservation of etendue governs to a large part the design of the illumination system. The etendue of a macroscopic beam of light rays at a certain position is formally defined by (7.71). Integration occurs over both the considered surface A and the considered solid angle Ω. The angle θ is measured between $d\Omega$ and the surface normal of dA and n is of course the index of refraction.

$$E = \int\int n^2 \cos\theta dA d\Omega \tag{7.71}$$

For all 'normal' optical systems it can be demonstrated that the etendue of a beam travelling through the system is either preserved or increased but cannot decrease. On the other hand, an optical system will always have a single component that puts a maximum value on the etendue of the beam that can still pass through it. Consequently, if the etendue of the beam before that component is larger, part of the generated light in that beam is inevitably wasted.

In a projection system, the lightvalve will always be the etendue limiting factor, due to the dimensions of the microdisplay and the limited acceptance angle (to preserve contrast). To maximise efficiency, the light collection optics must thus be designed to gather as much light as possible from the lightsource without exceeding the system etendue set by the lightvalve.

Design procedure

The design procedure for the projector starts with the lightvalve. As this is a rectangular plane with a known fixed acceptance angle, formula (7.71) is easily evaluated and the etendue of the lightvalve can be calculated with (7.72).

$$E_{LCOS} \approx \frac{\pi A_{LCOS}}{4(f/\#)^2} \tag{7.72}$$

For the WXGA lightvalve, with an active area of 15 mm $\times$ 9.5 mm and an f/# number of 3.0, this gives 12.4 mm^{2}sr.

With this system etendue, the maximum light throughput can already be found by looking at the collection efficiency versus etendue graph of the particular lamp that was selected for the system. If all technical details of the lamp are known, this graph can be obtained from simulation; alternatively, an analytical expression can be found in [183].

Simply matching the etendue is not enough, the lightvalve also determines what the acceptance angle should be. The maximum incidence angle of a light ray emerging from the lamp is determined by the the type (ellipticity) and size of the reflector. Due to construction limits, only a relatively small selection is actually available. Currently, maximum angles vary from 35 ° to 15 °, considerably larger than what the lightvalves can accept. Hence the beam will have to be transformed. This is done by the lens system and sometimes also partly by the integrator pipe.

Ray-tracing optical simulation software is used to evaluate different lens configurations and optimise the design so that all boundary conditions are met.

Light source

The common types of high luminous flux lamps used in projection are all arc lamps: xenon lamps, metal halide lamps and high pressure mercury lamps.

Of these, the mercury lamps offer the smallest arc gaps today. The etendue of a beam produced by an arc lamp is approximately proportional to the square of the arc gap [184]. Consequently, the mercury lamps are best suited to provide an etendue matched to microdisplays. On the downside, mercury lamps are only available at lower power ranges - less than 500 W. In this projector, a 150 W UHP lamp from Philips with a 76 mm elliptical reflector is used.

The collection efficiency can be obtained with ray tracing, as illustrated in figure 7.37, or measured directly through an aperture that matches the system etendue. For the considered lamp and lightvalve, the collection efficiency is about 0.35.

Integrator

The integrator pipe captures the light from the lightsource, which is circularly symmetric and transforms it into a uniform rectangular illumination field. This is achieved by the multiple reflections inside the pipe. As a rule of thumb, the length of the pipe should be at least five times the characteristic opening size.

The format of the output window of the pipe should match the LCOS cell. The shape of the pipe can either be straight or tapered, depending on whether a reduction in maximum incidence angle is wanted or not.

In high performance systems the integrator pipe is a solid block of fused silica glass and total internal reflection is used to contain the light flux. To lower manufacturing costs, a hollow pipe made of mirror glass is often used for prototypes, as is the case here.

The entrance of the integrator pipe is positioned at the second focal point of the elliptical lamp reflector.

The pipe used in this projector is hollow, constructed with glass plates

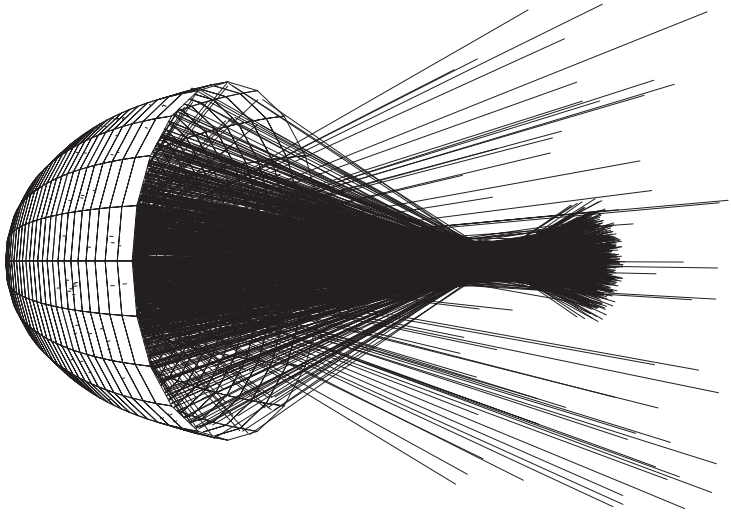

Figure 7.37: Ray-tracing simulation of the reflector - arc system to determine the collection efficiency versus etendue curve. The reliability of the results greatly depends on the modelling of the arc.

coated with bare aluminium. The pipe is straight, has a rectangular opening of 10 mm $\times$ 6 mm and is 120 mm long.

Relay optics

The lenses between the integrator pipe and the colour management unit image the output of the integrator pipe onto the LCOS panels with as less loss as possible. Most often the lens system introduces a magnification from the integrator output to the lightvalve. This reduces the maximum incidence angle at the lightvalve, beneficial for the contrast.

The lens system is preferably telecentric at the lightvalve side. This ensures that all lightcones have identical angular distributions. The benefit of this is the preservation of uniformity of the illumination throughout the colour management system, which consists of many angle dependent optical coatings.

A four lens system was adopted here. Only standard lenses were used and the design is the result of a trade-off between simplicity and performance.

The rectangular illumination field at the integrator pipe is magnified by 1.5 to match the lightvalve dimensions. Figures 7.38 and 7.39 show the predicted uniformity of illumination at the lightvalve's position. Close to the edges, the uniformity is not so good anymore. This is due to the fact that no 'overfill' was taken into account (meaning the area to illuminate is taken slightly larger than the actual lightvalve area to provide some margin). This was done deliberately to keep the light flux on the valve itself as high as possible.

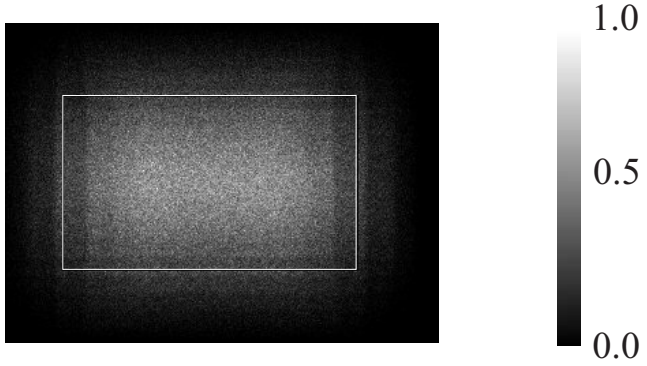

Figure 7.38: Ray-tracing simulation result of the uniformity of illumination at the lightvalve's position. The white rectangle indicates the outer dimensions of the lightvalve.

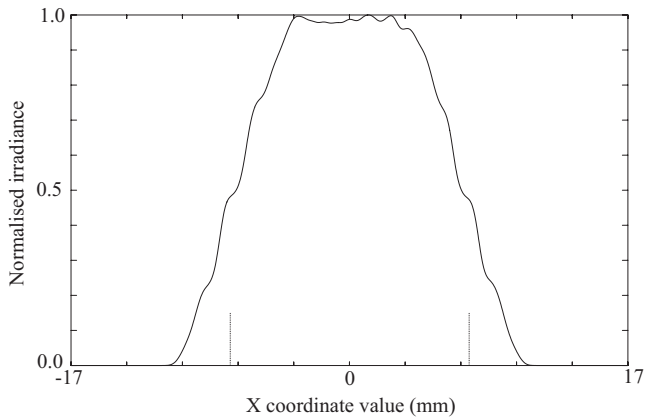

Figure 7.39: Detail of a ray-tracing simulation result of the uniformity of illumination at the lightvalve's position. Shown is the illumination profile through the centre of the lightvalve along the long axis. The bars indicate the extent of the lightvalve.

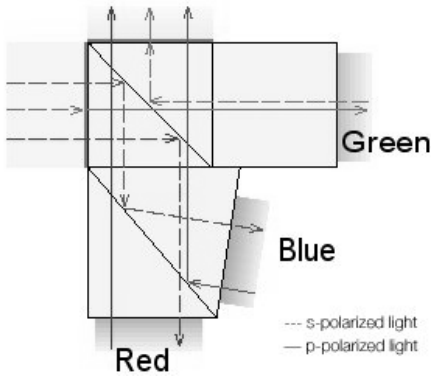

Figure 7.40: Working principle of the ColorCorner. S-polarised light enters the topmost glass cube from the left. A wavelength dependent polarisation sensitive coating immediately turns this into p-polarised light for the green wavelength band. This means it can pass the beamsplitting coating and goes straight on to the green panel. The red and blue wavelength band is reflected at the beamsplitting coating and sent downward, where a dichroic coating splits them up and sends them to the respective panels. If the polarisation remains unchanged at the panels, the light simply travels back to the source. If the polarisation is turned, the beamsplitting coating will now let the blue and red part pass through, while the green is reflected, so all the light exits via the top. To have all p-polarised light going to the projection lens, the s-polarised green wavelength band is again transformed with a special coating.

Colour management

The classic and best-performing colour management architecture is the X-cube with 3 polarising beamsplitters configuration [185, 186]. It is however quite complex and bulky and thus not so suited for the rapid development of a prototype intended as a feasibility demonstrator.

Instead, a compact and integrated colour management block is used : the ColorCorner from Unaxis. Its working principle is illustrated in figure 7.40. Its compactness and ease of handling come at a price; the design of the ColorCorner has several flaws. Among others, the colour balance is far from optimal (a tremendous amount of light in the red colour band is wasted) and the contrast is very moderate. On the other hand, it can simply be inserted in the light path without any further hassle.

To enhance contrast, a pre-polariser at the entry of the ColorCorner and a clean-up polariser at the exit are added. Wire-grid polarisers (e.g. the Proflux from Moxtek) are very convenient for this purpose: they do not need cooling and are very stable under high light fluxes.

At every colour channel a quarter-wave plate is inserted between the LCOS cell and the ColorCorner. The optical axis of the quarter-wave plate must be aligned with the expected polarisation. With this additional measure, the 'skew

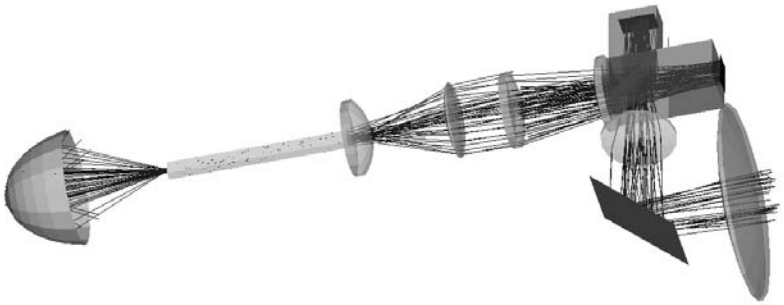

Figure 7.41: Shaded element view of the projector design. The projection lens at the bottom right is simplified to two lenses and a mirror.

ray depolarisation' effect, meaning that light rays hitting the splitter coating under an oblique angle have a deviant polarisation and are thus not entirely blocked, is greatly reduced [187]. This enhances the contrast significantly, but only works for mirror-like surfaces like a homeotropical lightvalve in the dark state.

Projection lens

The projection lens can be chosen more or less independently from the illumination optics. Important features are the back-focal distance (because of the bulky colour management block that must be accommodated for) and the throw-ratio. For this projector, a projection lens designed for a different system was reused.

7.7.3 Implementation

Figure 7.41 shows a somewhat simplified layout of the projector design as produced by the ray-tracing simulation program. Figures 7.42a and b give an impression of the realisation of the projector. Finally, figure 7.43 shows the projector at work.

With the design data, an estimate of the expected light output can be made. The efficiency of an UHP arc-lamp is about 65 lm/W, the 150 W lamp will thus output 9750 lumens. For the chosen f/# number, the collection efficiency is 0.35, so only 3410 lumens will enter the colour management system. Since no polarisation recuperation is foreseen and the colour management unit can only accept one polarisation direction, again half of the light is wasted, leaving 1705 lumens. The combined efficiency of the colour management, panel and projection lens is again hardly 0.5 (see table 3.1), so finally around 850

Position	0	0.1	0.2	0.3	0.4	0.5
Illuminance (lux)	430	583	664	831	827	830
Position	0.5	0.6	0.7	0.8	0.9	1.0
Illuminance (lux)	830	832	829	670	585	435

Table 7.3: Measured illuminance along a horizontal line through the centre of the screen. Position is in fractions of screen width.

lumens is actually expected on the screen. This is nicely in agreement with the measurements, which indicate around 800 lumen on screen. This is the maximum output of the system, producing the so-called 'projector-white'.

If adjustments for colour balancing are done to achieve the standard D65 white, the output drops to around 500 lumen. This is common for all high-pressure mercury lamp systems, because their spectral intensity curves drop towards the red (see figure 3.8), but the problem is still aggravated by the ColorCorner's characteristics.

The above figures give a luminous efficiency of about 12 % (9750 lumens to 800 lumens) and an overall luminous efficacy of 5 lumens per Watt. As a comparison, today's top-notch projectors (that do use polarisation recuperation) end up in the range of 10 to 12 lm/W.

The uniformity of illumination is given in table 7.3. It is in good agreement with the predictions from the ray-tracing simulations.

A sequential contrast ratio of 300:1 can be attained. This may seem (and effectively is) a disappointingly low value in view of the expectations that may have come up during the selection of the liquid crystal mode. As was already suggested before, the reason for this low value is entirely to be sought in the design of the ColorCorner. This can be illustrated by the fact that if the liquid crystal panels are replaced with mirrors and quarter-wave plates, the contrast ratio hardly improves ($\simeq$ 350:1). Evaluation of the panels in projection engines of third parties confirmed that the panels do live up to the expectations.

In view of the above, it will not be surprising that the ANSI contrast ratio is a mere 30:1 as well. The ANSI contrast value is anyhow in the foremost place a measure for the quality of the projection lens, which obviously has a flaw.

Apart from the low contrast, which by the way is not really noticeable in 'normal' viewing conditions (slightly dimmed ambient light), it can be stated that the projector served its purpose well, both as an evaluation tool throughout the research, as well as a convincing technology demonstrator.

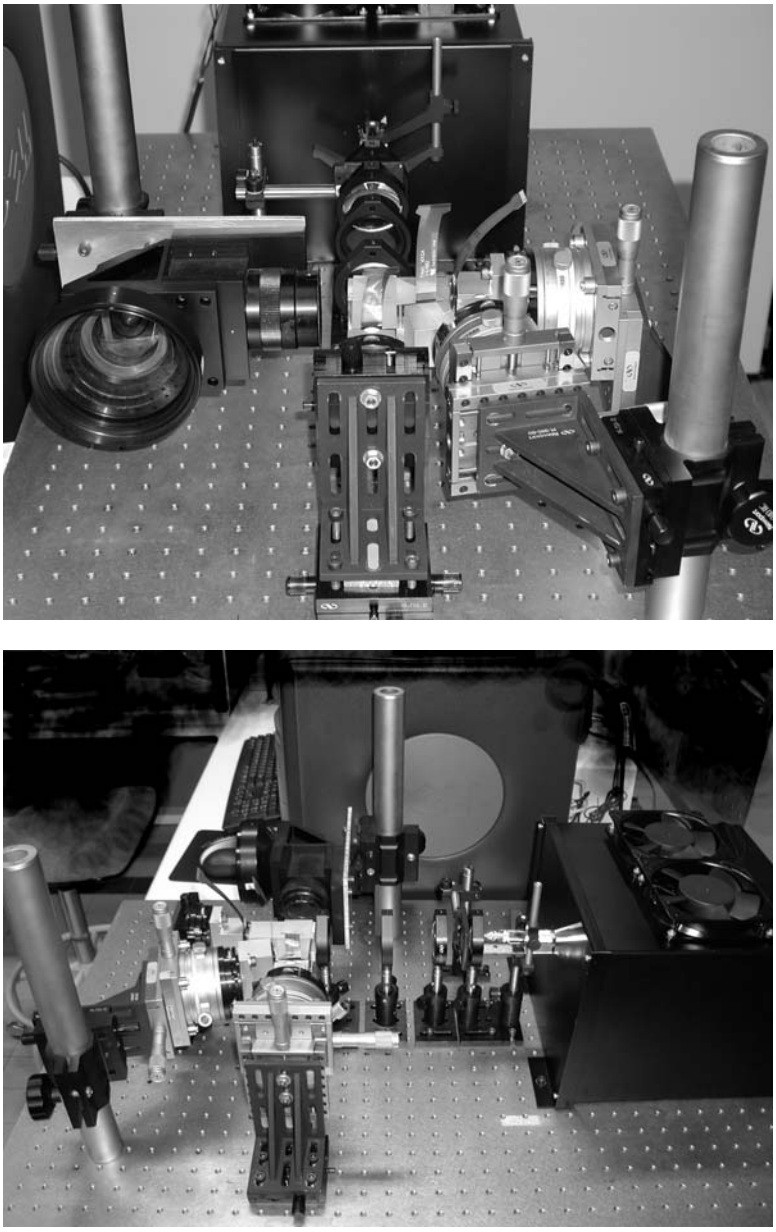

Figure 7.42: Breadboard implementation of the projector; top: front view, bottom: side view. The black box with the fans contains the lamp. Protruding from the box is the integrator; next to it the relay lenses. The most bulky part comprises the three positioning devices holding the panels in their exact relative position around the ColorCorner. Each provides 6 degrees of freedom with micrometer positioning resolution. The projection lens is prominently visible on the left of the top picture.

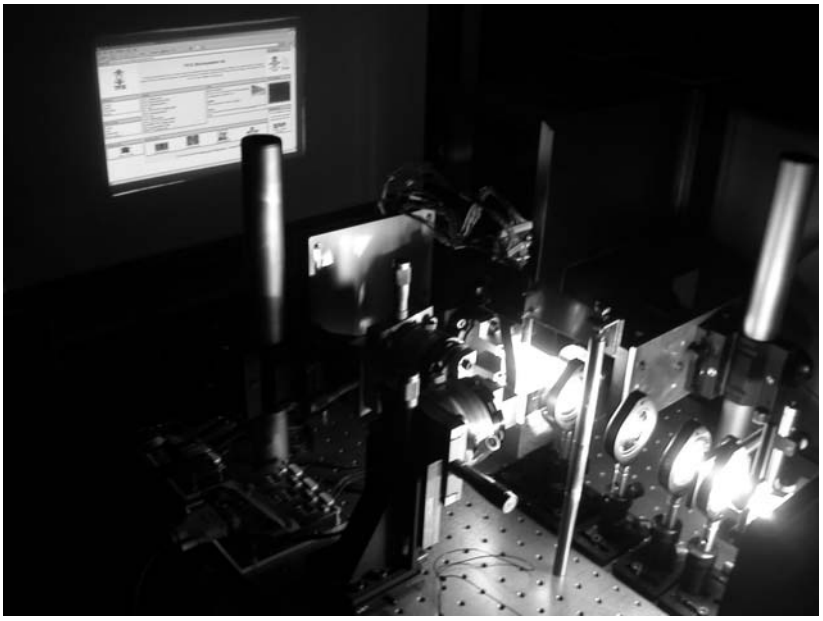

Figure 7.43: Projector at work.

Chapter 8

Conclusion and outlook

8.1 Concluding summary

In the previous text, the different stages in the concept, fabrication and evaluation of a liquid crystal on silicon based microdisplay projection system have been traversed and thoroughly discussed.

The first stage comprises the preparation of the silicon backplane, to make it suitable for the task of light-modulating device. Two key issues must be taken care of: adequate lightshielding of the circuitry and planarisation of the IC topography to enable the production of mirrors on top of the device. A CMOS technology independent approach and a foundry integrated one to achieve this are presented. The former makes extensive use of specialised polyimides both for the planarisation and the lightshielding. The latter relies on the anti-reflection coatings present in the metallisation stack to obtain lightshielding and uses polishing steps for the planarisation. It is demonstrated that both systems are viable and perform well in their intended application. The ease of an integrated system makes it the preferred solution nowadays but the polyimide solution can provide superior lightblocking if well implemented.

After the preparation of the backplane, the liquid crystal mode has to be chosen. This is done based on criteria of contrast ratio, voltage requirements, response speed and efficiency. An overview of liquid crystal modes suitable for projection is given and out of these the vertically aligned nematic mode is selected. This is then further accounted for through the characterisation of the features of this mode and a comparison to the rivalling modes, most notably the mixed twisted nematic. The vertically aligned mode performs equal to or better than these systems, except for the response speed.

The choice for the vertically aligned mode has consequences for the implementation of the alignment layer. Homeotropic alignment is far less common than homogeneous alignment and thus not straightforward to achieve. Af-

ter a weighing of advantages and disadvantages, an aligning system based on obliquely evaporated inorganic layers is chosen. The existing multitude of techniques is considered, thereafter an adapted proprietary version is proposed. Its main feature is the robustness of the process in terms of reproducibility, a frequent shortcoming of the existing techniques.

The next stage is the assembly of the biplane. A detailed process flow, based on a cell-per-cell assembly process is given. Focus is on issues such as uniformity and stability which are influenced by the presence of two different base materials. The sealing of the devices turns out to require special attention, as the presence of the inorganic alignment layer gives rise to unexpected interactions. A careful selection of the glue system is required to obtain a reliable process, resulting in stable displays.

Finally, some opto-electronic evaluations must be carried out. A measurement method for cell parameters such as cell-gap and pre-tilt angle, specifically aimed at vertically aligned devices is developed. Characterisation of some cells is carried out, resulting in a confirmation of the predicted performance. The possible image deterioration related to the presence of fringe fields is addressed. To this extent, simulation code is developed; the results lead to optimised values for the cell parameters. Lastly, a projector system using a three-panel architecture based on a commercial colour management solution is designed and implemented.

8.2 Future

Display technology evolves quite fast. LCOS microdisplays were quite an obscure topic when this research started, as was the use of inorganic alignment layers. Today, the first TV-sets based on LCOS microdisplays are on the market, and a limited number of companies actually use inorganic alignment layers for some of their devices.

Nevertheless, there is always room for further research. As already indicated in the text, there is still a large opportunity for fundamental research into the nature of the aligning mechanism of inorganic layers. The current knowledge about this subject is quite scattered and mostly descriptive. A unifying model that encompasses all previous findings is probably not within reach, but certainly a great challenge.

Somewhat less fundamental research can also be performed on the subject of the interaction between the sealing material and the alignment layer.

From a more practical viewpoint, some applied research or product development is of course also possible (and probably more likely to be pursued). The current trends in the LCOS world are for faster panels and a higher pixel-count. The former is driven by the search for single panel solutions, which itself stems from the belief that this will be the cheaper solution. The latter is a more general trend, fuelled by high-definition applications that become common and

the quest for digital cinema.

The search for faster switching cells is primarily a search for new liquid crystal materials. Some incremental improvements can however also be expected from clever driving techniques.

A higher pixel-count will result in larger devices or smaller pixels and most probably both. The former requires deep insight in the assembly process, especially if spacerless cells at thin cell-gaps are desired. Smaller pixels will worsen the influence of fringe fields, so further development of the simulation of the director behaviour in two and possibly three dimensions may also be worthwhile.

Appendix A

List of publications

1. A reflective polymer dispersed information display made on CMOS. G. Van Doorselaer, N. Carchon, J. Van den Steen, D. Cuypers, J. Vanfleteren, H. De Smet, and A. Van Calster. In *Proceedings of the ICPS*, pages 222–225, Antwerpen, Belgium, September 1998.

2. Characterization of a paper-white reflective PDLC microdisplay for portable IT applications. G. Van Doorselaer, N. Carchon, J. Van den Steen, J. Vanfleteren, H. De Smet, D. Cuypers, and A. Van Calster. In *Proceedings of the 1998 International Display Research Conference (AsiaDisplay98)*, pages 55–58, Seoul, Korea, September 1998.

3. A paper-white chip-based display MCM package for portable IT products. G. Van Doorselaer, B. Dobbelaere, M. Vrana, X. Xie, N. Carchon, J. Van den Steen, J. Vanfleteren, H. De Smet, D. Cuypers, and A. Van Calster. In *Proceedings of IMAPS'98*, pages 543–547, San Diego, California, November 1998.

4. A silicon based reflective polymer dispersed LC display for portable low power applications. G. Van Doorselaer, N. Carchon, J. Van den Steen, J. Vanfleteren, H. De Smet, D. Cuypers, and A. Van Calster. In *Proceedings of the 11th International Symposium on Electronic Imaging*, pages 95–102, San Jose, California, January 1999.

5. The design and fabrication of a 2560x2048 pixel microdisplay chip. H. De Smet, J. Van den Steen, N. Carchon, D. Cuypers, C. De Backere, M. Vermandel, A. Van Calster, A. De Caussemaeker, A. Witvrouw, H. Ziad, K. Baert, P. Colson, G. Schols, and M. Tack. In *Proceedings of the 19th International Display Research Conference (EuroDisplay99)*, pages 493–496, Berlin, Germany, September 1999.

6. Reflective vertically aligned nematic liquid crystal microdisplays for projection applications (invited paper). A. Van Calster and D. Cuypers. In

Proceedings of the International Conference on Electronic Imaging, Projection Displays 2000, Vol. 3954, pages 112–119, San Jose, California, January 2000.

7. Vertically aligned nematic liquid crystal displays for projection purposes. D. Cuypers. In *Proceedings of the Spring '00 SID-ME-Chapter meeting*, Balzers, Liechtenstein, March 2000.

8. Flicker reduction in AMLC displays by individual pixel voltage correction. G. Van Doorselaer, J. Van den Steen, H. De Smet, D. Cuypers, and A. Van Calster. In *Proceedings of the 20th International Display Research Conference (IDRC)*, pages 447–450, Palm Beach, Florida, September 2000.

9. Miniature reflective displays. A. Van Calster, F. Bruyneel, D. Cuypers, N. Carchon, G. Van Doorselaer, J. Van den Steen, and H. De Smet. In *Proceedings of the 7th International Display Workshops (IDW00)*, pages 179–182, Kobe, Japan, December 2000.

10. Microdisplays: A cost-effective technology for high-resolution displays. A. Van Calster, D. Cuypers, F. Bruyneel, N. Carchon, G. Van Doorselaer, J. Van den Steen, and H. De Smet. In *Proceedings of Displays and Vacuum Electronics*, Information Technology Society of VDE, pages 115–119, Germany, May 2001.

11. A 0.9" XGA LCOS backplane for projection applications. J. Van den Steen, G. Van Doorselaer, D. Cuypers, H. De Smet, A. Van Calster, F. Chu, and L.Y. Tseng. In *Proceedings of the Microdisplay Conference*, pages 87–90, Westminster, Colorado, August 2001.

12. Monocrystalline silicon active matrix reflective light valve (invited paper). H. De Smet, J. Van den Steen, D. Cuypers, N. Carchon, and A. Van Calster. In *Proceedings of Cupid Microdisplays*, pages –, Edinburg, Scotland, September 2001.

13. Design, fabrication and evaluation of a high-performance XGA VAN-LCOS microdisplay. H. De Smet, D. Cuypers, A. Van Calster, J. Van den Steen, and G. Van Doorselaer. *Displays*, 23(3):89–98, 2002.

14. Reflective color PDLC displays using color filters. F. Bruyneel, D. Cuypers, H. De Smet, and A. Van Calster. In *SID International Symposium Digest of Technical Papers, Vol. XXXIII*, pages 534–537, Boston, Massachusetts, May 2002.

15. A XGA VAN-LCOS projector. G. Van Doorselaer, D. Cuypers, H. De Smet, J. Van den Steen, A. Van Calster, K.S. Ten, and L.Y. Tseng. In *Proceedings of the 22nd International Display Research Conference (EuroDisplay02)*, pages 205–208, Nice, France, October 2002.

16. Assembly of an XGA 0.9" LCOS display using inorganic alignment layers for VAN LC. D. Cuypers, G. Van Doorselaer, J. Van den Steen, H. De Smet, and A. Van Calster. In *Proceedings of the 22nd International Display Research Conference (EuroDisplay02)*, pages 551–554, Nice, France, October 2002.

17. A projection system using vertically aligned nematic liquid crystal on silicon panels. D. Cuypers, G. Van Doorselaer, J. Van den Steen, H. De Smet, and A. Van Calster. In *Proceedings of the 9th International Display Workshops (IDW02)*, pages 45–48, Hiroshima, Japan, December 2002.

18. Measurement methodology for vertically aligned nematic reflective displays. D. Cuypers, H. De Smet, G. Van Doorselaer, J. Van den Steen, and A. Van Calster. In *Proceedings of the International Conference on Electronic Imaging, Projection Displays IX, Vol. 5002*, pages 62–72, Santa Clara, California, January 2003.

19. On the development of VAN LCOS microdisplays (invited). H. De Smet, J. Van den Steen, G. Van Doorselaer, D. Cuypers, N. Carchon, and A. Van Calster. In *Proceedings of the IEEE LEOS Annual Meeting Conference*, pages 814–815, Tucson, Arizona, October 2003.

20. Spice model for a dynamic liquid crystal pixel capacitance. H. De Smet, J. Van den Steen, and D. Cuypers. In *Proceedings of the 10th International Display Workshops (IDW03)*, pages 53–56, Fukuoka, Japan, December 2003.

21. WXGA LCOS projection panel with vertically aligned nematic LC. D. Cuypers, J. Van den Steen, G. Van Doorselaer, H. De Smet, and A. Van Calster. In *Proceedings of the 10th International Display Workshops (IDW03)*, pages 1541–1544, Fukuoka, Japan, December 2003.

22. Electrical model of a liquid crystal pixel with dynamic, voltage history-dependent capacitance value. H. De Smet, J. Van den Steen, and D. Cuypers. *Liquid Crystals*, 31(5):705–711, 2004.

23. Fringe-field induced disclinations in van LCOS panels. D. Cuypers, H. De Smet, and A. Van Calster. In *Proceedings of 11th International Display Workshops (IDW04)*, pages 1679–1682, Niigata, Japan, December 2004.

24. Increased lumens per etendue by combining pulsed LEDs. H. Murat, H. De Smet, D. Cuypers, Y. Meuret, H. Thienpont, M. Vervaeke, and L. Desmet. In *Proceedings of the International Conference on Electronic Imaging, Projection Displays XI, Vol. 5740*, pages 1–12, San Jose, California, January 2005.

25. Time sharing of pulsed LEDs increases lumen output within the same etendue. H. Murat, H. De Smet, and D. Cuypers. In *Proceedings of the joint SID meeting (SID-ME/Le Club Visu)*, only on CDROM, Ghent, Belgium, March 2005.

26. Fringe field effects in microdisplays. D. Cuypers, H. De Smet, and A. Van Calster. In *SID International Symposium Digest of Technical Papers, Vol. XXXVI*, pages 1298–1301, Boston, Massachusetts, May 2005.

Appendix B

Properties of liquid crystals

B.1 MLC-6608

Physical properties of MLC-6608 as provided by Merck KGaA. Measured at 20 °C. Refractive indices at 589.3 nm wavelength. Dielectric permittivity at 1.0 kHz.

T_{iso}	90.0 °C
$T_{smectic-nematic}$	< -30.0 °C
n_e	1.5578
n_o	1.4748
Δn	0.0830
$\epsilon_\perp$	7.8
$\epsilon_\parallel$	3.6
$\Delta\epsilon$	-4.2
K_1	16.7 pN
K_2	?
K_3	18.1 pN
γ	186 mPas

Additional physical properties estimated according to Armitage and Larimer [87].

ν_{flow}	$\sim$ 20 mPas
η_1	$\sim$ 206 mPas
η_2	$\sim$ 20 mPas
η_3	$\sim$ 40 mPas

B.2 MLC-6609

Physical properties of MLC-6609 as provided by Merck KGaA. Measured at 20 °C. Refractive indices at 589.3 nm wavelength. Dielectric permittivity at 1.0 kHz.

T_{iso}	91.5 °C
$T_{smectic-nematic}$	< -30.0 °C
n_e	1.5514
n_o	1.4737
Δn	0.0777
$\epsilon_\perp$	7.1
$\epsilon_\parallel$	3.4
$\Delta\epsilon$	-3.7
K_1	17.2 pN
K_2	?
K_3	17.9 pN
γ	162 mPas

Additional physical properties estimated according to Armitage and Larimer [87].

ν_{flow}	$\sim$ 20 mPas
η_1	$\sim$ 182 mPas
η_2	$\sim$ 20 mPas
η_3	$\sim$ 40 mPas

B.3 MLC-6610

Physical properties of MLC-6610 as provided by Merck KGaA. Measured at 20 °C. Refractive indices at 589.3 nm wavelength. Dielectric permittivity at 1.0 kHz.

T_{iso}	79.5 °C
$T_{smectic-nematic}$	< -30.0 °C
n_e	1.5824
n_o	1.4828
Δn	0.0996
$\epsilon_\perp$	6.6
$\epsilon_\parallel$	3.5
$\Delta\epsilon$	-3.1
K_1	14.6 pN
K_2	?
K_3	16.5 pN
γ	148 mPas
ν_{flow}	20 mPas

Additional physical properties estimated according to Armitage and Larimer [87].

η_1	$\sim$ 168 mPas
η_2	$\sim$ 20 mPas
η_3	$\sim$ 40 mPas

B.4 MLC-6885

Physical properties of MLC-6885 as provided by Merck KGaA. Measured at 20 °C. Refractive indices at 589.3 nm wavelength. Dielectric permittivity at 1.0 kHz.

T_{iso}	74.5 °C
n_e	1.5820
n_o	1.4821
Δn	0.0999
$\epsilon_\perp$	7.6
$\epsilon_\parallel$	3.8
$\Delta\epsilon$	-3.8
K_1	13.2 pN
K_2	?
K_3	14.8 pN
γ	152 mPas

Additional physical properties estimated according to Armitage and Larimer [87].

ν_{flow}	$\sim$ 20 mPas
η_1	$\sim$ 172 mPas
η_2	$\sim$ 20 mPas
η_3	$\sim$ 40 mPas

B.5 MLC-6882

Physical properties of MLC-6882 as provided by Merck KGaA. Measured at 20 °C. Refractive indices at 589.3 nm wavelength. Dielectric permittivity at 1.0 kHz.

T_{iso}	69.0 °C
Δn	0.0978
$\Delta\epsilon$	-3.0
K_1	13.1 pN
K_3	12.8 pN
γ	108 mPas

B.6 MLC-6883

Physical properties of MLC-6883 as provided by Merck KGaA. Measured at 20 °C. Refractive indices at 589.3 nm wavelength. Dielectric permittivity at 1.0 kHz.

T_{iso}	73.0 °C
Δn	0.1086
$\Delta\epsilon$	-3.4
K_1	13.1 pN
K_3	13.5 pN
γ	133 mPas

B.7 MLC-6884

Physical properties of MLC-6884 as provided by Merck KGaA. Measured at 20 °C. Refractive indices at 589.3 nm wavelength. Dielectric permittivity at 1.0 kHz.

T_{iso}	74.5 °C
Δn	0.0970
$\Delta\epsilon$	-5.0
K_1	13.3 pN
K_3	14.8 pN
γ	209 mPas

B.8 MLC-6886

Physical properties of MLC-6886 as provided by Merck KGaA. Measured at 20 °C. Refractive indices at 589.3 nm wavelength. Dielectric permittivity at 1.0 kHz.

T_{iso}	75.0 °C
Δn	0.0899
$\Delta\epsilon$	-3.8
K_1	13.8 pN
K_3	14.8 pN
γ	146 mPas

Appendix C

Properties of Selectilux HTR3-200

Material properties issued by OCG Microelectronic Materials Inc., the original manufacturer of this type of polyimide material. The material was afterwards marketed and produced by several other companies under different names.

C.1 Physical properties

Viscosity at 25°C	2350 mPas
Solids content	51 %
Density	1.135 kg/m^3
Flash point	95°C
Solvent	N-methylpyrrolidone
Main component	poly-[N,N'-(4,4'-oxidiphenylene)-pyromellitimide
Exposure dose	15 - 25 mJ/cm^2 per μm thickness
Curing temperature	400°C
Total weight loss after curing	55 %

C.2 Electrical properties

Dissipation factor at 1 kHz	0.004
Dielectric strength	10^6 V/cm
Dielectric constant at 1 kHz	3.5
Volume resistivity	$10^{16}\,\Omega$cm

Appendix D

Properties of DARC300

DARC 300 black polyimide is a non-conducting pigmented polymer that produces a film with very high absorption. The data below is extracted from application notes issued by Brewer Science Specialty Materials Division.

D.1 Process flow

Coat & bake APX-K1 adhesion promoter
Softbake DARC300 on a hot plate
Spin Coat DARC300 for 90 s
β-bake DARC300 in convection oven
Coat & bake positive photoresist
Expose photoresist
Develop for 20 s using TMAH developer
Rinse for 30 s in de-ionized water
Strip photoresist using Safestrip
Final cure at 230°C for 60 minutes in oven

Nominal film thickness 1.0 μm when spun at 1000 rpm for 90 seconds.

D.2 Physical properties

Brookfield viscosity at 37.8°C	65 - 75 cp
Optical density of a film with nominal thickness at 540 nm	2.3
Surface roughness of a thickness nominal film (ANSI B46.1-1978)	80 Ångstrøm

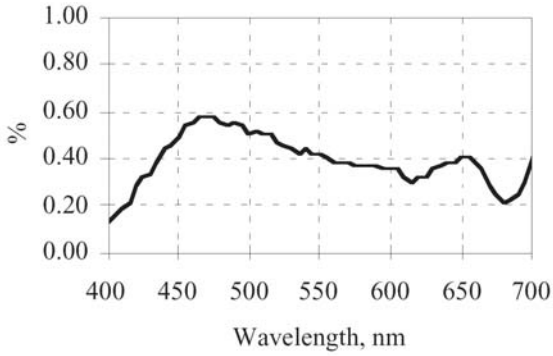

Figure D.1: Transmittance profile of a nominal thickness DARC300 film.

Appendix E

Properties of EXP99019V

General properties an provisional properties of the experimental photosensitive black polyimide material EXP99019V by Brewer Science.

Brookfield viscosity at 37.8°C	4.3 cPs
Nominal film thickness	1.02 μm
Particle count 1 μm at 500X visual	0
Optical density at 540 nm	2.8 /μm
Surface roughness of a nominal film (ANSI B46.1-1978)	$<$ 1 nm

Appendix F

Properties of Sekisui Micropearl SP

General properties of the material Micropearl SP spacers are made of. Measurements carried out on dedicated samples. Data taken from [154].

compressive breaking strength	11 kg/mm^2
compressive elastic modulus	480 kg/mm^2
specific density	1.19
thermal expansion coefficient	9.8×10^{-5}/°C
thermal decomposition temperature	330°C
volume resistivity	$3.6 \times 10^{14}\Omega$cm
dielectric constant	2.9
dielectric loss tangent	0.02
total light transmittance	86.0 %
haziness	3.5 %
refractive index	1.57
volatile component	0.6 %

Compression hardness measurements on actual spacers. Data taken from [154].

∅ (μm)	Compression load (g)		K (kg/mm^2)		Breaking strength	
	10 %	20 %	10 %	20 %	Load (g)	strain (%)
5.00	0.13	0.26	493	349	3.52	59.2
	0.14	0.31	531	416		
6.00	0.18	0.38	474	354	4.65	56.0
	0.17	0.38	448	354		
7.00	0.22	0.49	426	335	6.56	58.5
	0.22	0.48	426	329		
8.00	0.26	0.60	385	314	8.5	59.0
	0.28	0.64	415	335		
9.00	0.30	0.73	351	302	10.10	55.3
	0.35	0.85	410	352		
10.00	0.39	0.98	370	329	12.19	56.3
	0.41	0.98	389	329		

From the above data compression strengths for smaller diameter spacers can be extracted via extrapolation. From theory, the relation between the compression force and the diameter at constant strain ratio, should be quadratic. A second order polynomial fit on the averaged data for 10 % strain yields equation F.1.

$$y = 0.0026x^2 + 0.0132x \qquad R^2 = 0.998 \qquad y\text{: [g]}, \; x\text{: [}\mu\text{m]} \qquad \text{(F.1)}$$

Compression force values for different strain rates can be estimated from the given ones, keeping in mind that according to theory the compression force scales as $s^{3/2}$, s being the strain ratio.

Appendix G

Properties of silicon

Being the base material for the enormous semiconductor industry, silicon as a material has been extensively studied. Published data can vary depending on doping concentration, measurement method and other parameters. As small overview of relevant material data is given below.

G.1 Mechanical properties

Density [188]	2330kg/m^3

G.1.1 Linear coefficient of thermal expansion.

T (K)	CTE (10^{-6}/K)
100	-0.5
200	1.1
400	2.7
1000	4.7

G.1.2 Linear elastic modulus (GPa).

Si substrate, isotropic, linearly thermoelastic. [189]	165
Si<100>, single crystal, undoped, value obtained by nano indentation at a load of 0.2mN with indentation depth at peak load 24nm. [190]	179
Si<100>, single crystal, undoped, value obtained by nano indentation at a load of 15 mN with indentation depth at peak load 267 nm.	202
Si<100>, single crystal, P+ type (boron doped), value obtained by nano indentation at a load of 0.2 mN with indentation depth at peak load 44 nm.	62
Si<100>, single crystal, P+ type (boron doped), value obtained by nano indentation at a load of 15 mN with indentation depth at peak load 318 nm.	125
Si<111>, wafer, value obtained by using micro-indentation test. [191]	163 – 188
Si<111>, crystalline, undoped, polished, obtained by SAW technique. [192]	160
Material property used in the finite element computations of ultra microhardness indentation of thin films. [193]	127

G.1.3 Poisson's Ratio.

Si substrate, isotropic, linearly thermoelastic.[189]	0.22
Si<111>, crystalline, undoped, polished, obtained by SAW technique. [192]	0.27
Material property used in the finite element computations of ultra microhardness indentation of thin films. [193]	0.278

For the mechanical calculations, the elastic modulus was taken to be an average value of 150 GPa while Poisson's ratio was assumed to be 0.3.

Appendix H

Properties of Corning 1737F

Corning 1737F is an alkaline earth boro-aluminosilicate glass sold as fusion drawn sheets and primarily used as substrates for the active matrix flat panel industry. Properties listed below are extracted from the material information sheets issued by Corning Inc, version 2002.

H.1 Mechanical and electrical properties.

Density [188]	2540kg/m^3
Elastic modulus	70.9 GPa
Poisson's ratio	0.23
Shear modulus	28.9 GPa
Vickers hardness	633
CTE (0 – 300°C)	37.6×10^{-7}/K
CTE (room temp.)	42.0×10^{-7}/K
Volume resistivity	($\log_{10}$) 13.5
Dielectric permittivity (1 kHz)	5.7
Dielectric loss tangent (1 kHz)	0.10 %

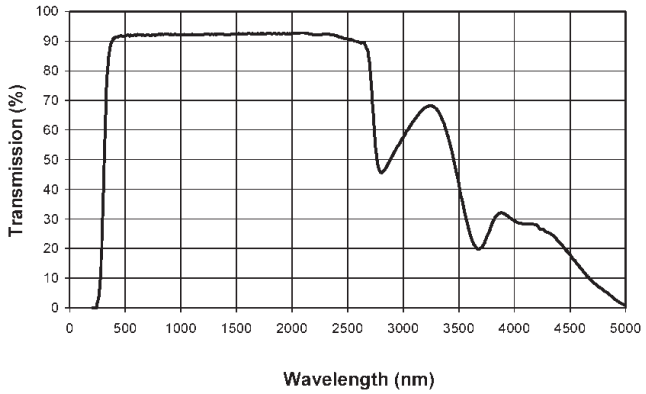

Figure H.1: Optical transmission of a 0.7 mm Corning 1737F sheet.

H.2 Optical properties.

H.2.1 Refractive index.

λ (nm)	n
435.8	1.5247
480	1.5247
486.1	1.5244
546.1	1.5203
589.3	1.5183
643.8	1.5161
656.3	1.5160
1300	1.5051
1541	1.5023

Birefringence constant : 333 (nm/cm)/(kg/mm^2)

H.2.2 Transmission and absorption.

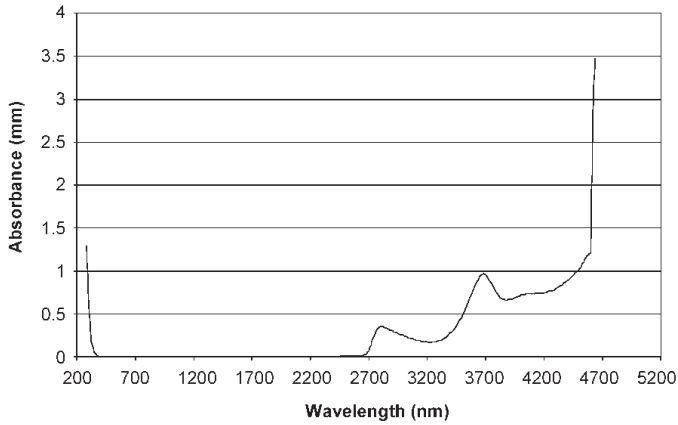

Figure H.2: Optical absorption of a 0.7 mm Corning 1737F sheet.

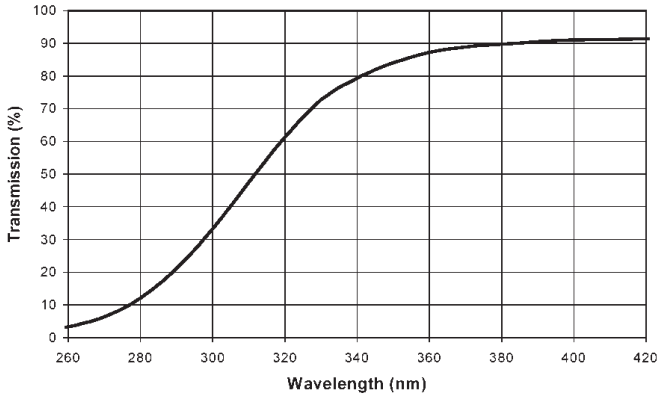

Figure H.3: Ultraviolet transmission of a 0.7 mm Corning 1737F sheet.

Appendix I

Properties of OG116-31

OG116-31 is a single component UV curable epoxy resin designed for general adhesive bonding, sealing and encapsulation. The properties listed below are extracted from the material datasheets provided by Epoxy Technology Inc. (Epotek).

I.1 Physical properties

colour before cure	off-white
colour after cure	clear / colourless
viscosity (23°C, 10 rpm)	25000 cPs
thixotropic index	1.15
specific gravity	1.2
Shore D hardness	82
glass transition temperature (Tg)	90°C
CTE (below Tg)	68×10^{-6}/K
CTE (above Tg)	223×10^{-6}/K
outgassing to 200°C	0.5 %
degradation temperature	390°C

I.2 Optical properties

refractive index	1.5684
transmission (450 nm to 900 nm)	> 98 %

I.3 Recommended cure

Minimum advised cure schedule : 100 mW/cm^2 for 1 to 2 minutes at 300 to 400 nm wavelength.

Appendix J

ColorCorner

J.1 Optical properties

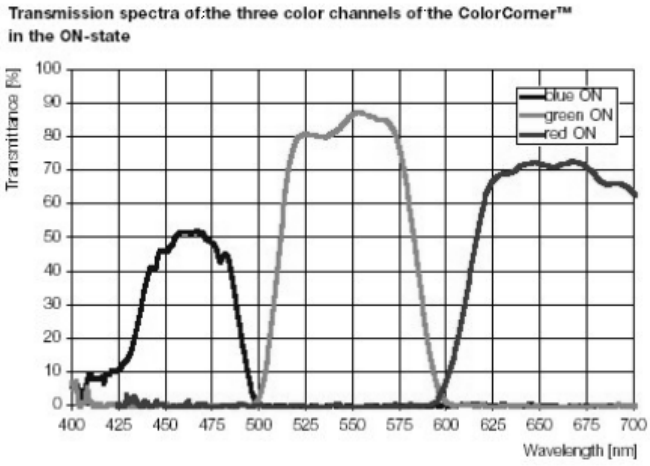

Figure J.1: Transmission spectra of the ColorCorner.

Bibliografie - Bibliography

[1] E. Baumann. The Fischer large screen projection system. *Journal of the SMPTE*, 60:344, 1953.

[2] T.P. Brody, J.A. Asars, and G.D. Dixon. A 6x6 inch 20 lines-per-inch liquid crystal display panel. *IEEE Transactions on Electronic Devices*, ED-20:995, 1973.

[3] Seiko Epson Corporation. Product information of the L3D13U HTPS LCD panel in their 3LCD range. Product brochure, 2004.

[4] R.D. Sterling and W.P. Bleha. Electronic cinema using ILA projector technology. In *SID International Symposium Digest of Technical Papers*, Vol XXX, San Jose, California, USA, May 1999. SID.

[5] Y. Nagae, K. Ando, A. Asano, L. Takemoto, J. Havens, P. Jones, D. Reddy, and A. Tomita. Compact liquid-crystal projectors with high optical efficiency. In *SID International Symposium Digest of Technical Papers*, Vol XXVI, pages 223–226, Orlando, Florida, USA, May 1995. SID.

[6] T. Nagata, I. Takemoto, T. Miyazawa, A. Asano, K. Yanagawa, S. Nakamura, H. Nakagawa, K. Saitou, N. Okabe, K. Matsumoto, and A. Iguchi. Silicon chip based reflective PDLC light valve for projection display. In *SID International Symposium Digest of Technical Papers*, Vol XXIX, Anaheim, California, USA, May 1998. SID.

[7] P. Cacharelis, U.S. Kim, J. Frazee, P. Moore, K. Brown, R. Luttrell, P. Rentein, and R. Flack. An 0.8-μm EEPROM technology modified for a reflective PDLC light-valve application. In *SID International Symposium Digest of Technical Papers*, Vol XXVIII, pages 289 – 292, Boston, Massachusetts, USA, May 1997. SID.

[8] E.G. Colgan and M. Uda. On-chip metallization layers for reflective light valves. *IBM Journal of Research and Development*, (42):339–345, 1998.

[9] R.L. Melcher et al. Design and fabrication of a prototype projection data monitor with high information content. *IBM Journal of Research and Development*, (42):321–336, 1998.

[10] F. Sato and Y. Yagi. High resolution and bright LCD projector with reflective LCD panels. In *SID International Symposium Digest of Technical Papers*, Vol XXVIII, pages 997 – 1000, Boston, Massachusetts, USA, May 1997. SID.

[11] H. Kurogane, K. Doi, T. Nishihata, A. Honma, M. Furuya, S. Nakagaki, and I. Takanashi. Reflective AMLCD for projection displays: D-ILA. In *SID International Symposium Digest of Technical Papers*, Vol XXIX, Anaheim, California, USA, May 1998. SID.

[12] C. De Backere, M. Vermandel, and A. Van Calster. Light shielding with liquid crystal on silicon displays. In *Proceedings of the 1998 International Display Research Conference*, Seoul, Korea, September 1998. SID.

[13] H. C. Huang, Y. T. Wong, C. T. Nguyen, and H. S. Kwok. Planarization of liquid -crystal-on-silicon projection display with multilevel metallization and chemical-mechanical polishing. In *SID International Symposium Digest of Technical Papers*, Vol XXVII, pages 685–688, San Diego, California, USA, May 1996. SID.

[14] Mosarel Consortium. Mosarel final report (public version). European Commission DGXXII, March 2000. Esprit Project 25340.

[15] Max Born and Emil Wolf. *Principles of Optics*, section XI, pages 633–671. Cambridge University Press, The Pitt Building, Trumpington Street, Cambridge, United Kingdom, seventh (expanded) edition, 1999.

[16] Z. Oyama, H. Ohsaki, X. Hayashi, and K. Tachibana. A new layer system for wideband anti-reflection coatings designed for CRTs. In *SID International Symposium Digest of Technical Papers*, Vol XXIX, Anaheim, California, USA, May 1998. SID.

[17] N.Y. Kim, Y.B. Son, J.H. Oh, C.K. Hwangbo, and M.C. Park. TiN_x layer as an antireflection and antistatic coating for display. *Surface and Coatings Technology*, (128):156–160, 2000.

[18] Hiro Ishikawa, Yoshiharu Honjo, and Kazuo Watanabe. Three-layer broad-band antireflective coating on web. *Thin Solid Films*, (351):212–215, 1999.

[19] Patrick Candry, K. Henry, B. Verniest, and W. Schorpion. A high light-output active matrix TN liquid crystal projector for video and datagraphics applications. In *SID International Symposium Digest of Technical Papers*, Vol XXIV, pages 291–294, Seattle, Washington, USA, May 1993. SID.

[20] I. Wegrzecka, M. Wegrzecki, M. Grynglas, J. Bar, A. Uszynski, R. Grodecki, P. Grabiec, S. Krzeminski, and T. Budzynski. Design and properties of silicon avalanche photodiodes. *Opto-electronics Review*, 12(1):95 – 104, 2004.

[21] Peter A. Keller. *Electronic display measurement : concepts, techniques and instrumentation*, chapter 1.5, page 16. Display Technology. John Wiley & Sons, Inc., New York, 1997.

[22] N. Carchon, G. Van Doorselaer, A. M. De Cubber, J. De Baets, A. Van Calster, P. Candry, and J. Bruggeman. A poly-CdSe active matrix for PNLC projection displays. In Y. Kuo, editor, *Proceedings of the 3rd symposium on thin film transistor technologies*, number 96-2 in Electrochemical Publications, pages 366–374, Pennington, New Jersey, October 1996. The Electrochemical Society.

[23] J. Van den Steen, N. Carchon, G. Van Doorselaer, C. De Backere, J. De Baets, H. De Smet, J. De Vos, J. Lernout, J. Vanfleteren, and A. Van Calster. Technology and circuit aspects of reflective PNLC microdisplays. In *Proceedings of the 1997 International Display Research Conference*, pages 195–198, Toronto, Canada, September 1997. SID.

[24] G. Van Doorselaer, N. Carchon, J. Van den Steen, D. Cuypers, J. Vanfleteren, H. De Smet, and A. Van Calster. A reflective polymer dispersed information display made on CMOS. In *Proceedings of the ICPS*, pages 222–225, Antwerpen, Belgium, September 1998.

[25] G. Van Doorselaer, N. Carchon, J. Van den Steen, J. Vanfleteren, H. De Smet, D. Cuypers, and A. Van Calster. Characterization of a paper-white reflective PDLC microdisplay for portable IT applications. In *Proceedings of the 1998 International Display Research Conference*, pages 55–58, Seoul, Korea, September 1998. SID.

[26] G. Van Doorselaer, N. Carchon, J. Van den Steen, J. Vanfleteren, H. De Smet, D. Cuypers, and A. Van Calster. A silicon based reflective polymer dispersed LC display for portable low power applications. In *Proceedings of the 11th international symposium on Electronic Imaging*, pages 95–102, San Jose, California, USA, January 1999. SPIE.

[27] K. Kasahara, T. Yanagisawa, K. Kasai, and T. Adachi. In *Biennial Display Research Conference*, Conference Record of the IEEE, pages 96–101. IEEE, 1980.

[28] Miler Schuck, Peter Kazlas, Michael Radler, Douglas McKnight, and Kristina Johnson. Post-processing and assembly of reflective microdisplays. *Journal of the SID*, 7(2):93–100, 1999.

[29] A. Hermanns, L.M. Shirey, R.E. Geer, M.J. Radler, Z. Bian, and B.R. Ratna. A post-processing sequence for liquid-crystal-on-silicon microdisplays. In Ranganathan Shashidhar, editor, *Liquid Crystal Materials, Devices and Applications VII*, Vol 3635, pages 103–111, San Jose, California, USA, January 1999. IS&T.

[30] J. Z. Z. Zhong, A. Abileah, S. V. Thomsen, and H. Amari. A TFT-LCD fabricated with ultra-low reflectance organic black matrix. In *Proceedings of the 5th International Display Workshops*, pages 307–310, Kobe, Japan, December 1998. ITE, SID.

[31] C. W. Kim, S. G. Rho, D. K. Jung, E. J. Jeong, S. Y. Kim, and H. G. Yang. Development of organic photoresist for color filter black matrix. In *Materials Research Society Symposium Proceedings*, volume 424, page 329, 1997.

[32] M. Tani, T. Sugimura, M. Sakagawa, S. Ito, and T. Okano. A novel black matrix with high optical density and low reflection. In *Proceedings of the 5th International Display Workshops*, pages 321–324, Japan, December 1996. ITE, SID.

[33] S. Sega, T. Yoshihara, H. Yamagata, A. Inoue, and T. Kageyama. Pigment-dispersed organic black-matrix photoresists with high optical density. In *Proceedings of the 5th International Display Workshops*, pages 387–390, Japan, December 1997. ITE, SID.

[34] G. de Keyzer, A. Schaffner, V. Hall-Goulle, B. Wagner, Z. Hao, N. Reichlin, and M.-C. Morandi. Novel black photoresists with high photospeed and high optical density based on latent pigments. In *Proceedings of the 5th International Display Workshops*, pages 291–294, Kobe, Japan, December 1998. ITE, SID.

[35] D. Burdeaux, P. Townsend, and J. Carr. *Journal for Electronic Materials*, (19):1366, 1990.

[36] A. O'Hara, J. R. Hannah, and I. Underwood. *Applied Optics*, (32):5556, 1993.

[37] M. H. Schuck, D.J. Mc Knight, and K. M. Johnson. Spin-cast planarisation of liquid-crystal-on-silicon microdisplays. *Optics Letters*, (22):1114, 1997.

[38] B. Merriman, J. Craig, and A. Nader. In *Proceedings of the 39th ECC*, 5, 1990.

[39] B. Verweire and R. Defever. Limitation of resolution of LCOS-based projection displays by diffraction effects. In *Proceedings of the 19nd International Display Research Conference*, pages 489–492, 1998.

[40] R.B. Meyer. In *Vth International Liquid Crystal Conference*, June 1974.

[41] N. A. Clark and S. T. Lagerwall. Submicrosecond bistable electro-optic switching in liquid crystals. *Applied Physics Letters*, 36, 1980.

[42] K. Miyachi and A. Fukuda. *Antiferroelectric liquid crystals*, volume 2B of *Handbook of Liquid Crystals*. Wiley - VCH, 1998.

[43] W. Haase, S. A. Pikin, F. V. Podgornov, E.P. Pozhidaev, H. Moritake, and A. D. L. Chandani Perera. Thresholdless hysteresis-free switchable FLC materials. In L.-C. Chien, editor, *Liquid Crystal Materials, Devices, and Applications IX*, Vol 5003, pages 51–62, Santa Clara, California, USA, January 2003. IS&T.

[44] R. C. Jones. New calculus for the treatment of optical systems. *Journal of the Optical Society of America*, 31:488, 1941.

[45] A. Lien. Extended Jones matrix representation for the twisted nematic liquid-crystal display at oblique incidence. *Applied Physics Letters*, 57:2767 – 2769, 1990.

[46] A. Lien and C.-J. Chen. A new 2x2 matrix representation for twisted nematic liquid crystal displays at oblique incidence. *Japanese Journal of Applied Physics*, 35:1200 – 1203, 1996.

[47] D.W. Berreman. Optics in stratified and anisotropic media: 4x4 matrix formulation. *Journal of the Optical Society of America*, 62, 1972.

[48] G.H. Heilmeier, J.A. Catellano, and L.A. Zanoni. Guest-host interactions in nematic liquid crystals. *Molecular Crystals and Liquid Crystals*, 8:293–304, 1969.

[49] K.H. Yang and Minhua Lu. Nematic liquid crystal modes for Si wafer-based reflective spatial light modulators. *Displays*, 20:211–219, 1999.

[50] V. Freedericksz and V. Zolina. Forces causing the orientation of an anisotropic liquid. *Transactions of the Faraday Society*, 29, 1933.

[51] J. Patel and G.B. Cohen. Inverse twisted nematic liquid crystal device. *Applied Physics Letters*, 68(25):3564, 1996.

[52] J. O. Kwag, K. C. Shin, J. S. Kim, S. G. Kim, and S. S. Kim. Implementation of a new wide-viewing-angle mode. In *SID International Symposium Digest of Technical Papers*, Vol XXXI, pages 256–259, Long Beach, California, USA, May 2000. SID.

[53] A. Takeda, S. Kataoka, T. Sasaki, H. Chida, H. Tsuda, K. Ohmuro, T. Sasabayashi, Y. Koike, and K. Okamoto. Super-high image quality multi-domain vertical alignment LCD by new rubbing-less technology. In *SID International Symposium Digest of Technical Papers*, Vol XXIX, pages 1077–1080, Anaheim, California, USA, May 1998. SID.

[54] P.J. Bos and K.R. Koehler/Beran. The pi-cell: A fast liquid crystal optical switching device. *Molecular Crystals and Liquid Crystals*, 113:329, 1984.

[55] P.L. Bos and J.A. Rahman. An optically 'self-compensating' electro-optical effect with wide angle of view. In *SID International Symposium Digest of Technical Papers*, Vol XXIV, pages 273–276, Seattle, Washington, USA, May 1993. SID.

[56] Y. Yamaguchi, T. Miyashita, and T. Uchida. Wide viewing angle display mode for the active matrix LCD using bend-alignment liquid crystal cell. In *SID International Symposium Digest of Technical Papers*, Vol XXIV, pages 277–280, Seattle, Washington, USA, May 1993. SID.

[57] M. Xu, D. Yang, J. Bos, X. Jin, F. Harris, and S. Cheng. Very high pretilt alignment and its application in Pi-cell LCDs. In *SID International Symposium Digest of Technical Papers*, Vol XXIX, pages 139 – 142, Anaheim, California, USA, May 1998. SID.

[58] S. Matsuo et al. Field-induced deformation of hybrid-aligned nematic liquid crystals: New multicolor liquid crystal display. *Journal of Applied Physics*, 47(9), 1976.

[59] T. Uchida, T. Ishinabe, and M. Suzuki. A bright reflective LCD using optically compensated bend cell with gray-scale capability and fast response. In *SID International Symposium Digest of Technical Papers*, Vol XXVII, pages 618–621, San Diego, California, USA, May 1996. SID.

[60] J. Glueck, E. Lueder, T. Kalfass, and H.-U. Lauer. Color-TV projection with fast-switching reflective HAN-mode light valves. In *SID International Symposium Digest of Technical Papers*, Vol XXIII, pages 277–280, Boston, Massachusetts, USA, May 1992. SID.

[61] C. Gooch and H. Tarry. The optical properties of twisted nematic liquid crystal structures with twist angles ≤ 90. *Journal of Physics D: Applied Physics*, 8:1575–1584, 1975.

[62] C. Gooch and H. Tarry. Optical charcteristics of twisted nematic liquid crystal films. *Electronics Letters*, 10(1):2–4, 1974.

[63] M. Schadt and W. Helfrich. Voltage dependant optical activity of a twisted nematic liquid crystal. *Applied Physics Letters*, 18, 1971.

[64] T.J. Scheffer and J. Nehring. Supertwisted nematic LCDs. In *SID Lecture notes for Seminar M-6*, Vol 1, Anaheim, California, USA, May 1998. SID.

[65] Shin-Tson Wu, Chiung-Sheng Wu, and Chen-Lung Kuo. Comparative studies of single-polarizer reflective liquid-crystal displays. *Journal of the SID*, 7(2):119–125, 1999.

[66] Y. Saitoh, Y. Yoshida, and H. Kamiya. Reflective twisted-nematic-mode color TFT-LCD panel. In *SID International Symposium Digest of Technical Papers*, Vol XXVIII, pages 651–654, Boston, Masachusetts, USA, May 1997. SID.

[67] J. Chen, F. H. Yu, S. Tang, H. Huang, and H. Kwok. New optimized reflective LCD modes for direct-view and projection displays. In *SID International Symposium Digest of Technical Papers*, Vol XXVIII, pages 639–642, Boston, Masachusetts, USA, May 1997. SID.

[68] K.H. Yang. In *Conference Proceedings EuroDisplay 96*. SID, 1996.

[69] Philip J. Bos et al. Optically active diffractive device. United States Patent, 1997. Patent Nr. 5,638,201.

[70] Philip J. Bos et al. Reflective optically active diffractive device. United States Patent, 1998. Patent Nr. 5,825,448.

[71] P.G. De Gennes and J. Prost. *The Physics of Liquid Crystals*. Clarendon, second edition, 1993.

[72] J.W. Doane et al. Front lit flat panel displays from polymer stabilized cholesteric textures. In *Japan Display*, 1992.

[73] Y.M. Zhu and D.-K. Yang. High speed dynamic drive scheme for bistable reflective cholesteric displays. In *SID International Symposium Digest of Technical Papers*, Vol XXVIII, Boston, Masachusetts, May 1997. SID.

[74] F. Bruyneel. *Introductie van kleur in reflectieve PDLC en PNLC microdisplays*. PhD Dissertation, Universiteit Gent, Faculteit Toegepaste Wetenschappen, Vakgroep Elektronica en Informatiesystemen, March 2002. Contains text in English.

[75] Van Calster et al. Bucket brigade. Internal document, 2002. Not published.

[76] Unaxis Optics. HELF-polarizing beamsplitter. Electronically published datasheet, 2000. UBO 106 RE (0501-1).

[77] Alan E. Rosenbluth, Minhua Lu, K.-H. Yang, Kenneth Ho, Rama N. Singh, and Teruhiro Nakasogi. Correction of contrast in projection systems by means of phase-controlled prism coatings and band-shifted twist compensators. In Ming H. Wu, editor, *Projection Displays 2000: Sixth in a Series*, Vol 3954, pages 63–90, San Jose, California, USA, January 2000. IS&T.

[78] Stephen Eckhardt, Charles Bruzzone, David Austen, and James Ma. 3M PBS for high performance LCOS optical engine. In Ming H. Wu, editor, *Projection Displays IX*, Vol 5002, pages 106–110, Santa Clara, California, USA, January 2003. IS&T.

[79] David Armitage. Contrast ratio of vertically aligned cell. In M.H. Wu, editor, *Projection Displays 2000: Sixth in a Series*, Vol 3954, pages 197–205, San Jose, California, USA, January 2000. IS&T.

[80] Shin-Tson Wu and Chiung Sheng Wu. Mixed-mode twisted nematic liquid crystal cells for reflective displays. *Applied Physics Letters*, 68(11):1455, 1996.

[81] P. Vetter. *Vloeibare kristallen in kleurenbeeldschermen met aktieve matrix*. PhD Dissertation, Rijksuniversiteit Gent, Faculteit Toegepaste Wetenschappen, Laboratorium voor Elektronica en Meettechniek, June 1991.

[82] S. Saito and H. Yamamoto. Transient behaviours of field-induced reorientation in variously oriented nematic liquid crystals. *Japanese Journal of Applied Physics*, 17(2), 1978.

[83] Jack Kelly and Syed Jamal. Modeling the dynamics of TN devices with flow. pages 5–12.

[84] F.M. Leslie. Some constitutive equations for anisotropic fluids. *Quarterly Journal for Mechanics and Applied Mathematics*, 19:357, 1966.

[85] J.L. Ericksen. Anisotropic fluids. *Arch. Rational Mech. Anal.*, 4:231, 1960.

[86] O. Cossalter and D.A. Mlynski. Determination of Leslie's viscosities with high accuracy directly from the electro-optic response of a LCD. *Liquid Crystals*, 19(4):545 – 547, 1995.

[87] D. Armitage and J. Larimer. Nematic liquid-crystal viscosity and response time. In *SID International Symposium Digest of Technical Papers*, Vol XXVII, pages 584–587, San Diego, California, USA, May 1996. SID.

[88] M. Miesowicz. *Nature*, 136:261, 1935.

[89] H. Ehrentraut and S. Hess. Viscosity coefficients of partially aligned nematic and nematic discotic liquid crystals. *Physical Review E*, 51(3):2203–2212, 1995.

[90] O. Parodi. Stress tensor for a nematic liquid crystal. *Journal de Physique*, 31:581, 1970.

[91] David Armitage and James Larimer. Liquid crystal response time. In Ming H. Wu, editor, *Projection Displays IV*, Vol 3296, pages 19–29, San Jose, California, USA, January 1998. IS&T.

[92] Michael Hird, John W. Goodby, and Kenneth J. Toyne. Nematic materials with negative dielectric anisotropy for display applications. In Ranganathan Shashidhar, editor, *Liquid Crystal Materials, Devices, and Flat Panel Displays*, Vol 3955, pages 15–23, San Jose, California, USA, January 2000. IS&T.

[93] Melanie Klasen-Memmer, Matthias Bremer, and Kazuaki Tarumi. Advanced liquid crystal materials with negative dielectric anisotropy for monitor and TV applications. In *Proceedings of the 9th International Display Workshops*, Vol XXVII, pages 93–95, Hiroshima, Japan, December 2002. ITE, SID.

[94] F. Guerin, J.M. Chappe, P. Joffre, and D. Dolfi. Modelling, synthesis and characterization of a millimeter-wave multilayer microstrip liquid crystal phase shifter. *Japanese Journal of Applied Physics*, (36):4409, 1997.

[95] Li Yi Chen. The influence of the flow effect on the dynamics of liquid-crystal displays. Master's thesis, National Chiao Tung University, Institute of Electro-Optical Engineering, 2000.

[96] Shu-Hsia Chen and Li-Yi Chen. Flow effect in the chiral-homeotropic liquid-crystal cell. *Applied Physics Letters*, 75(22):3491, 1999.

[97] T. Ito and K. Nakanishi. Regularity and narrowness of the intervals of the microgrooves on the rubbed polymer surfaces for LC alignment. In *SID International Symposium Digest of Technical Papers*, Vol XXIII, pages 393–396, Boston, Massachusetts, USA, May 1992. SID.

[98] H. Aoyama, Y. Yamazaki, N. Matsuura, H. Mada, and S. Kobayashi. Alignment of liquid crystals on the stretched polymer films. *Molecular Crystals and Liquid Crystals*, 72:127, 1981.

[99] Y. Kawata, K. Takatoh, M. Hasegawa, and M. Sakamoto. The alignment of nematic liquid crystals on photolithographic micro-groove patterns. *Liquid Crystals*, 16:1027, 1994.

[100] W.M. Gibbons, P.J. Shannon, S.T. Sun, and B.J. Swetlin. Surface-mediated alignment of nematic liquid crystal with polarized laser light. *Nature*, 351:49, 1991.

[101] M. Schadt, M. Schmitt, V. Kizinkov, and V. Chigrinov. Surface-induced parallel alignment of liquid crystals by linearly polymerized photopolymers. *Japanese Journal of Apllied Physics Part 1*, 31:2155, 1992.

[102] Y. Iimura, T. Saitoh, S. Kobayashi, and T. Hashimoto. *Journal of Photopolymerization Science and Technology*, 8:258, 1995.

[103] Y. Iimura, H. Akiyama, , X.T. Li, and S. Kobayashi. Photo-alignment control of LC and its applications to LCD fabrication. In Ranganathan Shashidhar, editor, *Liquid Crystal Materials, Devices and Apllications VI*, Vol 3297, pages 8–17, San Jose, California, USA, January 1998. IS&T.

[104] J.L. West, M. Nishikawa, and Y. Reznikov. Generation of high pretilt in photo-aligned polyimides. In Ranganathan Shashidhar, editor, *Liquid Crystal Materials, Devices and Apllications VII*, Vol 3635, pages 16–22, San Jose, California, USA, January 1999. IS&T.

[105] P.O. Jackson, R. Karapinar, M.O. Neill, P. Hindmarsh, G.J Owen, and S.M Kelly. Alignment models for coumarin-containing polymers for liquid crystal displays. In Ranganathan Shashidhar, editor, *Liquid Crystal Materials, Devices and Applications VII*, Vol 3635, pages 38–47, San Jose, California, USA, January 1999. IS&T.

[106] K.H. Yang, K. Tajima, A. Takenaka, and H. Takano. Charge trapping properties of UV-exposed polyimide films for the alignment of liquid crystals. *Japanese Journal of Apllied Physics Part 2*, 35:L561, 1996.

[107] I. Langmuir. *Journal of the American Chemical Society*, 39:1848, 1917.

[108] K. Blodgett. *Journal of the American Chemical Society*, 57:1007, 1935.

[109] G. Barbero and A.G. Petrov. Nematic liquid crystal anchoring on Langmuir-Blodgett films: Steric, biphilic, dielectric and flexoelectric aspects and instablities. *Journal of Physics: Condensed Matter*, 6:2291–2306, 1994.

[110] F.J. Kahn. Orientation of liquid crystals by surface coupling agents. *Applied Physics Letters*, 22:386, 1973.

[111] S. Matsumoto, K. Kawamoto, and N. Kaneko. Surface-induced molecular orientation of liquid crystals by carboxylatochromium complexes. *Applied Physics Letters*, 27:268, 1975.

[112] A. Masano, K. Toshio, S. Shigeo, N. Hiroyuki, S. Masanobu, and S. Tadayuki. Liquid crystal display device and method of producing the same. European Patent, 1991. Patent Nr 0541388, Victor Company of Japan.

[113] R. Bürkle and T. Kallfass. Process and apparatus for applying orienting layers to a substrate for alignment of liquid crystal molecules. United States Patent, 1995. Patent Nr 5,658,439.

[114] Yoshiki Nakagawa, Yoshimine Kato, Yukito Saitoh, Kazumi Sakai, Hiroyuki Satoh, Kazuhiro Wako, and Shuichi Odahara. Novel LC alignment method using diamond like carbon film and ion beam alignment. In *SID International Symposium Digest of Technical Papers*, Vol XXXII, San Jose, California, USA, June 2001. SID.

[115] P. Chaudhari, J. Lacey, J. Doyle, E. Galligan, A. Lien, A. Callegari, G. Hougham, N. Lang, P. S. Andry, R. John, K.-H. Yang, M. Lu, C. Cai, J. Speidell, S. Purushothaman, J. Ritsko, M. Samant, J. Sthr, Y. Nakagawa, Y. Katoh, Y. Saitoh, K. Sakai, H. Satoh, S. Odahara, H. Nakano, J. Nakagaki, and Y. Shiota. Atomic-beam alignment of inorganic materials for liquid-crystal displays. *Nature*, 411:56 – 59, 2001.

[116] Minhua Lu and K.H. Yang. Reflective nematic LC devices for LCOS applications. In *SID International Symposium Digest of Technical Papers*, Vol XXXI, Long Beach, California, USA, May 2000. SID.

[117] M. Lu and K.H. Yang. Flicker-free reflective liquid crystal cell. United States Patent, 1997. Patent Nr 5,764,324, International Business Machines Corporation.

[118] T.G. Knorr and R.W. Hoffman. *Physical Review*, 113:1039–1046, 1959.

[119] D.O Smith. Anisotropy in permalloy films. *Journal of Applied Physics*, 30(5):264S–265S, 1959.

[120] H. Konig and G. Helwig. Über die struktur schräg aufgedampfter schichten und ihr einfluβ auf die entwicklung submikroskopischer oberflächenrauhigkeiten. *Optik*, 6(2):111–125, 1950.

[121] L. Abelmann, P. ten Berge, J.C. Lodder, and Th.J.A Popma. Oblique evaporation of $Co_{80}Ni_{20}$ part I: Fixed angle of vapour incidence. *Journal of the Magnetic Society of Japan*, 18:291–294, 1994.

[122] P. ten Berge, L. Abelmann, J.C. Lodder, A. Schrader, and S. Luitjens. Oblique evaporation of $Co_{80}Ni_{20}$ part II: Continously varying angle of vapour incidence. *Journal of the Magnetic Society of Japan*, 18:295–298, 1994.

[123] L. Abelmann. *Oblique evaporation of $Co_{80}Ni_{20}$ films for magnetic recording.* PhD Dissertation, Universiteit Twente, 1994.

[124] L. Abelmann and C. Lodder. Oblique evaporation and surface diffusion. *Thin Solid Films*, 305:1–21, 1994.

[125] A.G. Dirks and H.J. Leamy. Columnar microstructure in vapour-deposited films. *Thin Solid Films*, 47:219–233, 1977.

[126] H.J. Leamy, G.H. Gilmer, and A.G. Dirks. *The microstructure of vapour deposited thin films*, volume 6 of *Current topics in materials science*, pages 309–344. North-Holland, 1980.

[127] H.J. Leamy and A.G. Dirks. The microstructure of amorphous rare earth / transition-metal thin films. *Journal of Physics*, D10:L95–L98, 1977.

[128] K. Hara. Anomalous magnetic anisotropy of thin films evaporated at oblique incidence. *Journal of Science Hiroshima University*, (34):139–163, 1970.

[129] K. Hara, M. Kamiya, T. Hashimoto, K. Okamoto, and H. Fujiwara. Oblique incidence anisotropy of the iron films evaporated at low substrate temperature. *Journal of Magnetism and Magnetic Materials*, 73:161–166, 1988.

[130] H. Fujiwara, K. Hara, M. Kamiya, T. Hashimoto, and K. Okamoto. Columnar growth in evaporated iron films. *Journal of Magnetism and Magnetic Materials*, 35:296–298, 1983.

[131] J.G.W. van de Waterbeemd and G.W. Oosterhout. Effect of the mobility of metal atoms on the structure of thin films deposited at oblique incidence. *Philips Research Report*, 22:375–387, 1967.

[132] S. Lichter and J. Chen. Model for columnar microstructure of thin solid films. *Physical Review Letters*, 56(13):1396–1399, 1986.

[133] A. van der Drift. Evolutionary selection, a principle governing growth orientation in vapour-deposited layers. *Philips Research Report*, 22:267–288, 1967.

[134] M. Lu, K.H. Yang, and J.S. Chey. Homeotropic alignment of liuid crystals by single evaporation of SiO_2. In *Proceedings of the 6th International Display Workshops*, pages 121–124, Sendai, Japan, December 1999. ITE, SID.

[135] G. Barbero, I. Dozov, J.F. Palierne, and G. Durand. Order electricity and surface orientation in nematic liquid crystals. *Physical Review Letters*, 56(19):2056–2059, 1986.

[136] R.B. Meyer. *Physical Review Letters*, 22:319, 1969.

[137] G. Hauck. Liquid crystal alignment on obliquely deposited Al_2O_3 surfaces. *Physica Status Solidi*, 70(1):K43 – K46, 1982.

[138] J.L. Janning. Thin film surface orientation for liquid crystals. *Applied Physics Letters*, 21(4):173, 1972.

[139] John L. Janning. Alignment film for a liquid crystal display cell. United States Patent, 1973. Patent Nr 3,834,792, The National Cash Register Company.

[140] T. Toru, A. Kazuo, A. Kazuo, and N. Shinichi. Method for manufacturing the substrate for liquid crystal display. United States Patent, 1990. Patent Nr 4,897,290, Konishiroku Photo Industries.

[141] N. Kato, R. Sekura, and T. Iwaki. Method of introducing slightly titlting homeotropic orientation into liquid crystal, liquid crystal electro-optical device and liquid crystal light valve. United States Patent, 1995. Patent Nr 4,897,290, Seiko Instruments Inc.

[142] M. Oue, O. Asai, K. Iwasaki, and H. Kawakami. Method of forming alignment film for liquid crystal display cell. United States Patent, 1976. Patent Nr 4,897,290, Hitachi Ltd.

[143] K. Nobuyoshi. Manufacture of liquid crystal display element. Japan Patent, 1982. Patent Nr 57084428, Nissan Motor Company Ltd.

[144] H. Amstutz, M. Kaufmann, J. Nehring, and T.J. Scheffer. Process and apparatus for the production of an orientation layer on a plane surface of a plate, and a liquid crystal substrate plate produced thereby. United States Patent, 1985. Patent Nr 4,705,359, BBC Brown, Boveri & Company, Ltd.

[145] K. Hiroshima. Controlled high-tilt-angle nematic alignment compatible with glass frit sealing. *Japanese Journal of Applied Physics*, 21(12):L761 – L763, 1982.

[146] A. Sawada. Orientation treatment of liquid crystal cell substrate. Japan Patent, 1981. Patent Nr 56099318, Citizen Watch Company Ltd.

[147] Alignment control of liquid crystal molecules. Patent of the United Kingdom of Great Britain, 1981. Patent Nr 1603905, Citizen Watch Company Ltd.

[148] K. Suganuma. Orientation treatment method of liquid crystal cell substrate. Japan Patent, 1980. Patent Nr 55006306, Citizen Watch Company Ltd.

[149] H. Vithana, Y.K. Yung, S.H. Jamal, R. Herke, P.J. Bos, and D.L. Johnson. A well-controlled tilted-homeotropic alignment method and a vertically aligned four-domain LCD fabricated by this technique. In *SID International Symposium Digest of Technical Papers*, Vol XXVI, pages 873–875, Orlando, Florida, USA, May 1995. SID.

[150] J. Duchene. Device for depositing an orientation layer of a liquid crystal cell. European Patent, 1986. Patent Nr 0184487, Commissariat Energie Atomique.

[151] A. Rapini and M. Papoular. Distortion d'une lamelle nématique sous champs magnétiques; conditions d'ancrage aux parois. *Journal de Physique*, 30(4):C4.54–C4.56, 1969.

[152] Hiroyuki Kamiya, Ken Tajima, Kohichi Toriumi, Kazuo Terada, Hiroshi Inoue, Toshinubo Yokoue, Nobuo Shimizu, Takeshi Kobayashi, Shuichi Odahara, Gareth Hougham, Chen Cai, James H. Glownia, Robert J.

von Gutfeld, Richard John, and Shui-Chih Alan Lien. Development of one drop fill technology for AM-LCDs. In *SID International Symposium Digest of Technical Papers*, Vol XXXII, San Jose, California, USA, June 2001. SID.

[153] J.C. Lapp. Glass substrates for AMLCD applications: properties and implications. San Jose, California, USA, February 1997. IS&T.

[154] Ltd. Sekisui Chemical Co. LCD & Packaging use products. Sent on request, 1999. Sekisui product information.

[155] Landau and Lifschutz. *Theory of Elasticity*, pages 37 – 42. Tokyo Tosho.

[156] Philips Components LCOS Group. Engaze: A singular new approach to LCOS display technology. White paper, June 2001.

[157] H. Yamashita, Y. Saitoh, S. Matsumoto, and M. Kodate. Precise cell-thickness control by spacer-ball-free structure and its application to large-size TFT-LCDs. In *SID International Symposium Digest of Technical Papers*, Vol XXVII, pages 600–604, San Diego, California, USA, May 1996. SID.

[158] Paul R. Brown Jr. HANA Microdisplay Technologies Inc. Oral communication, 2003.

[159] Georg Bodammer, David W. Calton, and Ian Underwood. Investigation of the bow of silicon backplanes for microdisplay applications. In *SID International Symposium Digest of Technical Papers*, Vol XXXII, San Jose, California, USA, June 2001. SID.

[160] Jun H. Souk. AMLCD manufacturing technology. SID2001 Technical Seminar Notes, June 2001.

[161] S. Yamada, S. Kimura, N. Sakai, Y. Yamada, H. Matsukawa, and S. Hisamitsu. A new production of the large size TFT-panel by LC-dropping method. In *SID International Symposium Digest of Technical Papers*, Vol XXXII, San Jose, California, USA, June 2001. SID.

[162] K. Rhodes. A new high performance bonding option for optical assembly. In *Integrated Optics Devices IV*, Vol 3936, San Jose, California, USA, January 2000. SPIE.

[163] K. Horie, H. Miura, and T. Takeoka. Study of a UV-curing sealing resin for LCDs. In *SID International Symposium Digest of Technical Papers*, Vol XXVII, pages 534–538, San Diego, California, USA, May 1996. SID.

[164] A. Lien and H. Tanako. Cell gap measurements of filled twisted nematic liquid crystal displays by a phase compensation method. *Journal of Applied Physics*, (69):1304, 1991.

[165] A. Lien. The general and simplified Jones matrix represantations for the high pretilt twisted nematic cell. *Journal of Applied Physics*, (67):2853, 1990.

[166] K.H. Yang and H. Tanako. Measurements of twisted nematic cell gap by spectral and split-beam interferometric methods. *Journal of Applied Physics*, (67):5, 1990.

[167] S.T. Tang and H.S. Kwok. A new method to measure the twist angle and cell gap of liquid crystal cells. In *SID International Symposium Digest of Technical Papers*, Vol XXIX, pages 552–555, Anaheim, California, USA, May 1998. SID.

[168] S.T. Tang and H.S. Kwok. Transmissive liquid crystal cell parameters measurement by spectroscopic ellipsometry. *Journal of Applied Physics*, 89(1):80–85, 2001.

[169] D. Tanooka. Measurement method for cell gap and twist angle of reflective LCD. In *Proceedings of the 9nth International Display Workshops*, pages 105–108, Hiroshima, Japan, December 2002. ITE, SID.

[170] S.F.J Appleyard, S.R. Day, R.D. Pickford, and M.R. Willis. Organic electroluminescent devices: enhanced carrier injections using SAM derivatized ITO electrodes. *Journal of Materials Chemistry*, 10:169 – 173, 2000.

[171] I.D. Park. *Journal of Applied Physics*, (75):1656, 1994.

[172] C. W. Oseen. *Arkiv før Matematik, Astronomi och Fysik A*, 19(9), 1925.

[173] F. C. Franck. *Discussion of the Faraday Society*, 25(19), 1958.

[174] G. Haas, M. Fritsch, H. Wöller, and D. Mlynski. Simulation of reverse-tilt disclinations in LCDs. In *SID International Symposium Digest of Technical Papers*, Vol XXI, pages 102–105, Las Vegas, Nevada, USA, May 1990. SID.

[175] S. Dickmann, J. Eschler, O. Cossalter, and D. Mlynski. Simulation of LCDs including anistropy and inhomogeneous fields. In *SID International Symposium Digest of Technical Papers*, Vol XXIV, pages 638–641, Seattle, Washington, USA, May 1993. SID.

[176] D. Berreman and S. Meiboom. Tensor representation of Oseen-Franck strain energy in uniaxial cholesterics. *Physical Review A*, 30(4), 1984.

[177] K. Schiele and S. Trimper. *Phys. Status Solidi B*, 118(267), 1983.

[178] J. Anderson, P. Watson, and P.J. Bos. Shortcomings of the Q tensor method for modelling liquid crystal devices. In *SID International Symposium Digest of Technical Papers*, Vol XXX, pages 198–201, San Jose, California, USA, May 1999. SID.

[179] C. Z. van Doorn. Dynamic behaviour of twisted nematic liquid-crystal layers in switched fields. *Journal of Applied Physics*, 46:3738–3745, 1975.

[180] D. W. Berreman. Dynamics of liquid-crystal twist cells. *Journal of Applied Physics*, 25:12–15, 1974.

[181] G. Haas. *Simulation zweidimensionaler Feldeffekte in Flüssigkristalzellen.* PhD Dissertation, Universität Fridericiana Karlsruhe, Fakultät fur Elektrotechnik, Institut fur Theoretische Elektrotechnik und Meβtechnik, February 1991.

[182] E.H. Stupp and M.S. Brennesholtz. *Light-valve and light-amplifier system architectures*, chapter 10. Projection Displays. John Wiley and Sons Ltd., 1999.

[183] B. A. Jacobson, R. D. Gengelbach, C. N. Stewart, and D. M. Rutan. Metal halide lighting systems and optics for high efficiency compact LCD projectors. In Ming H. Wu, editor, *Projection Displays IV*, Vol 3296, pages 38–45, San Jose, California, USA, January 1998. IS&T.

[184] P. Candry. LCD projection technologies and applications. In *Proceedings of the 15th International Display Research Conference*, Vol XXI, pages 75–78. SID, 1995.

[185] R. D. Sterling and W.P. Bleha. D-ILA technology for electronic cinema. In *SID International Symposium Digest of Technical Papers*, Vol XXI, pages 310–313, Las Vegas, Nevada, USA, May 1990. SID.

[186] J. Bowron and T. Schmidt. A new high resolution reflective liquid crystal light valve projector. In Ming H. Wu, editor, *Projection Displays IV*, Vol 3296, San Jose, California, USA, January 1998. IS&T.

[187] A.E. Rosenbluth, D. Dove, and F. Doany. Contrast losses in projection displays from depolarization by tilted beam splitter coatings. In *Proceedings of the 17nd International Display Research Conference*, pages 226–229, 1997.

[188] *Materials Science and Engineering Handbook*, page 64. CRC.

[189] *Mechanics of Materials*, (23):314, 1996.

[190] *Journal of Materials Research*, 12(1):59, 1997.

[191] *Thin Solid Films*, (283):13, 1996.

[192] *Applied Surface Science*, (106):433, 1996.

[193] *Thin Solid Films*, (209–291):363, 1996.

Index